Διδακτορική Διατριβή

με τίτλο

“Φαινόμενα Κλίμακας σε Ημι-ψαθυρά Υλικά και Θεωρίες Βαθμοελαστικότητας με Εφαρμογή στο Σκυρόδεμα”

του

Αντώνιου Τριανταφύλλου

Τμήμα Πολιτικών Μηχανικών
Πολυτεχνική Σχολή, Πανεπιστήμιο Θεσσαλίας
Βόλος

Επιβλέπων: Καθηγητής Φίλιππος Κ. Περδικάρης

Επταμελής Εξεταστική Επιτροπή

Φίλιππος Κ. Περδικάρης, Καθηγητής *(επιβλέπων και μέλος 3μελούς)*,
Τμήμα Πολιτικών Μηχανικών, Παν. Θεσσαλίας

Αντώνιος Γιαννακόπουλος, Καθηγητής *(συνεπιβλέπων και μέλος 3μελούς)*,
Τμήμα Πολιτικών Μηχανικών, Παν. Θεσσαλίας

Μαρίνα Μωρέττη, Επίκουρη Καθηγήτρια *(μέλος 3μελούς)*,
Τμήμα Πολιτικών Μηχανικών, Παν. Θεσσαλίας

Γεώργιος Βογιατζής, Καθηγητής
Τμήμα Πολιτικών και Περιβαλλ/γων Μηχανικών, Πολιτειακό Παν. Λουϊζιάνας

Χαράλαμπος Γεωργιάδης, Καθηγητής
Σχολή Εφαρμ. Μαθηματικών και Φυσ. Επιστημών, Εθν. Μετσόβιο Πολυτεχνείο

Δημοσθένης Πολύζος, Καθηγητής
Τμήμα Μηχανολόγων Μηχανικών, Παν. Πάτρας

Παναγιώτης Τσόπελας, Αναπληρωτής Καθηγητής
Σχολή Εφαρμ. Μαθηματικών και Φυσ. Επιστημών, Εθν. Μετσόβιο Πολυτεχνείο

Ευρωπαϊκή Ένωση
Ευρωπαϊκό Κοινωνικό Ταμείο
ΕΠΙΧΕΙΡΗΣΙΑΚΟ ΠΡΟΓΡΑΜΜΑ
ΕΚΠΑΙΔΕΥΣΗ ΚΑΙ ΔΙΑ ΒΙΟΥ ΜΑΘΗΣΗ
επένδυση στην κοινωνία της γνώσης
ΥΠΟΥΡΓΕΙΟ ΠΑΙΔΕΙΑΣ ΚΑΙ ΘΡΗΣΚΕΥΜΑΤΩΝ
ΕΙΔΙΚΗ ΥΠΗΡΕΣΙΑ ΔΙΑΧΕΙΡΙΣΗΣ
Με τη συγχρηματοδότηση της Ελλάδας και της Ευρωπαϊκής Ένωσης
ΕΣΠΑ 2007-2013
πρόγραμμα για την ανάπτυξη
ΕΥΡΩΠΑΪΚΟ ΚΟΙΝΩΝΙΚΟ ΤΑΜΕΙΟ

Ιανουάριος, 2015

Institutional Repository - Library & Information Centre - University of Thessaly
15/10/2023 05:52:39 EEST - 167.114.118.212

PhD dissertation
on

"Size Effects in Semi-brittle Materials and Gradient Theories with Application to Concrete"

by

Antonios Triantafyllou

Department of Civil Engineering
School of Engineering, University of Thessaly
Volos, Greece

Advisor: Prof. Philip C. Perdikaris

Submitted for review to the

Examining Committee

Professor Philip C. Perdikaris, *(advisor, member of advising committee)*,
Department of Civil Engineering, Univ. of Thessaly, Volos, Greece

Professor Antonios Giannakopoulos *(co-advisor, member of advising committee)*,
Department of Civil Engineering, Univ. of Thessaly, Volos, Greece

Assistant Professor Marina Moretti *(member of the advising committee)*,
Department of Civil Engineering, Univ. of Thessaly, Volos, Greece

Professor George Voyiadjis,
Department of Civil & Environ. Engineering, State Univ. of Louisiana, U.S.A.

Professor Charalampos Georgiadis,
School of Applied Mathematical & Phys. Sciences, Nat. Tech. Univ. of Athens, Greece

Professor Dimosthenis Polyzos,
Department of Mechanical Engineering, Univ. of Patras, Greece

Associate Professor Panos Tsopelas,
School of Applied Mathematical & Phys. Sciences, Nat. Tech. Univ. of Athens, Greece

European Union
European Social Fund
OPERATIONAL PROGRAMME
EDUCATION AND LIFELONG LEARNING
investing in knowledge society
MINISTRY OF EDUCATION & RELIGIOUS AFFAIRS
MANAGING AUTHORITY
Co-financed by Greece and the European Union
NSRF 2007-2013
programme for development
EUROPEAN SOCIAL FUND

January, 2015

Institutional Repository - Library & Information Centre - University of Thessaly
15/10/2023 05:52:39 EEST - 167.114.118.212

PREFACE - ACKNOWLEDGMENTS

Upon agreeing on a research assistantship offer by Prof. Philip Perdikaris in order to study size effects in cementitious materials, in reality I did not know much of these subjects. Four years have passed since then and this thesis is the outcome of what I learned from two people: Prof. Philip Perdikaris and Prof. Antonios Giannakopoulos who supervised my PhD thesis.

For the first two years I worked mainly with Prof. A. Giannakopoulos trying to grasp the concepts of strain gradient elasticity and damage. During this period most of the theoretical work was finalized. The following year was devoted to the experimental program. It was during this time that I worked exclusively with Prof. P. Perdikaris. Within a time period of ten months (January to November 2013), the experimental setup details were organized and the final setup was constructed, eight castings of various cementitious materials were performed and a total of one hundred and ninety (190) beam specimens were tested. Afterwards, every modelling detail had to be scrutinized in light of the experimental results, many issues had to be resolved and lengthy discussions took place with both supervisors.

During these four years, I was stationed in the Laboratory of “Reinforced Concrete Technology and Structures” of the Department of Civil Engineering at the University of Thessaly. The coexistence with Mr. Theocharis Papatheocharis, a Ph.D. candidate, and the technicians Mr. Alekos Koutselinis and Mr. Dimitris Karaberopoulos only helped to solve problems I faced and never created a single one. Their help in the research undertaken was substantial in many ways. I couldn’t have asked for better colleagues. Also, the contribution of Dr. K. Tzaros regarding programming issues in the thesis is gratefully acknowledged.

The Maranoglou and Panayiotopoulos machine shop was responsible for manufacturing the experimental setup components and their suggestions helped in improving the design of the setup. The facilities of the Regional Public Works Laboratory in Volos, Greece, were used for sawing some of the specimens and the author is grateful to the personnel for their useful advice in handling the machinery. The author is also thankful to Ms. O. Nikitaki, head of quality control for of Lafarge Ltd. in northern Greece for her extra effort in meeting our concrete mix specifications and needs.

Finally, this work was made possible by the financial support of “Herakleitos II” research project of the Greek Ministry of National Education for basic research on “Size Effects Phenomena of Concrete” and was co-financed by the European Union (European Social Fund) and Greek National funds through the Operational Program "Education and Lifelong Learning" of the National Strategic Reference Framework.

Institutional Repository - Library & Information Centre - University of Thessaly
15/10/2023 05:52:39 EEST - 167.114.118.212

CONTENTS

		PAGE
I.	**INTRODUCTION**	**1**
	1. Scope	1
	2. Microstructure and dipolar elasticity	1
	3. Microcracking and damage	4
	4. Experimental program	6
	5. Numerical predictions	8
	6. Size effects	10
II.	**GRADIENT LENGTH VIA HOMOGENIZATION OF HETEROGENEOUS MATERIALS**	**11**
	1. Introduction	11
	2. Effective Material Properties of Transversely Isotropic Materials	12
	3. Classical Elasticity Solutions	16
	4. Gradient Elasticity Solutions for the Annulus Problem	20
	5. Estimation of Internal Length	27
	6. Remote Uniaxial Tension	32
	7. Application to Fiber-Reinforced Concrete	35
	8. Conclusions	36
III.	**STRUCTURAL ANALYSIS USING A DIPOLAR ELASTIC TIMOSHENKO BEAM – APPLICATION TO MICROCANTILEVERS**	**37**
	1. Introduction	37
	2. Governing Equations and Boundary Conditions	40
	3. Examples	47
	4. Non-Local Timoshenko Beam Models	55
	5. Experimental Evidence on Microcantilevers	57
	6. Conclusions	61
IV.	**A GRADIENT ELASTO-DAMAGE MODEL FOR SEMI-BRITTLE MATERIALS WITH EVOLVING INTERNAL LENGTH – CONCRETE BEAMS UNDER 4 POINT BENDING**	**62**
	1. Introduction	62
	2. Thermodynamic Formulation	63
	3. Energy Dissipated for Microcrack Extension	71
	4. Proposed Model for Concrete Beams under 4-Point Bending	73
	5. Objectivity of the Proposed Model	76
	6. Midspan Deflection for 4-Point Bending Based on Gradient Elasticity	78
	7. Conclusions	80

Institutional Repository - Library & Information Centre - University of Thessaly
15/10/2023 05:52:39 EEST - 167.114.118.212

PAGE

V. EXPERIMENTAL PROGRAM 81

1. Materials 81
2. Classical Mechanical Properties 82
3. Split Cylinder Tests 86
4. 4-Point Bending Tests 90

VI. SIZE EFFECT OF CEMENTITIOUS MATERIALS IN ELASTICITY 93

1. Introduction 93
2 Elastic Stiffness and Curvature 93
3. Discussion of the Results 100
4. Conclusions 105

VII. SIZE EFFECT OF CEMENTITIOUS MATERIALS IN INELASTICITY 106

1. Introduction 106
2. Comparison with the Present Experimental Results 106
3. Discussion of the Results 117
4. Highly Brittle Materials 119
5. Flexural Strain Measurements 120
6. Conclusions 124

VIII. SIZE EFFECT ON STRENGTH FOR CEMENTITIOUS MATERIALS 125

1. Introduction 125
2. Size Effect on Strength 125
3. Discussion 132

MAIN CONCLUSIONS 134

REFERENCES 137

Institutional Repository - Library & Information Centre - University of Thessaly
15/10/2023 05:52:39 EEST - 167.114.118.212

CHAPTER I

INTRODUCTION

1. SCOPE

Throughout this work a simplified gradient model with one length parameter, which is the simplest case of Mindlin's Form II strain gradient elasticity theory, is employed. This automatically limits the range of considered materials to initially isotropic. The aim of the present thesis is to verify experimentally the theoretical findings for a series of problems associated with this gradient model and its application to the specific case of semi-brittle materials such as concrete.

2. MICROSTRUCTURE AND DIPOLAR ELASTICITY

All materials have a microstructure which is visible under specific magnification. The influence of microstructure on the macrostructural response is typically neglected under the assumption that the material is homogenous. Isotropic homogeneous materials are defined by two material constants, the Young's modulus and Poisson's ratio and these constants are determined experimentally from uniaxial tests. However, in many cases when classical elasticity predictions are applied to structural problems, a stiffer response than the one predicted by classical elasticity depending on the member size, is measured. A possible physically justifiable explanation for the source of this size effect is the existence of a microstructure which has not been accounted in the analysis. Gradient theories attempt to account for the presence of a microstructure by assuming that there is an additional material constant with dimensions of length.

The simplest definition of a composite material is that of inclusions embedded inside a matrix material. Knowledge of the properties of the different phases and of the inclusion volume fraction is the minimum input information required to model the composite microstructure. Therefore the first issue to be addresses is how changes in the microstructure of a composite affect the internal length assumed by gradient theories. This is explored in Chapter II. It is apparent from these theoretical results that the internal length is best viewed as a measure of the heterogeneity of the composite and that heterogeneity can not be simply defined by the size of inclusions. It is the inclusions size and elastic mismatch combined that determine the magnitude of heterogeneity of a composite.

Concrete is a multi-scale material. At the micrometer scale (10^{-6} m) cement grains are distinguished and in its hardened state cement calcium and silicate hydrates as well as pores are

Institutional Repository - Library & Information Centre - University of Thessaly
15/10/2023 05:52:39 EEST - 167.114.118.212

formed. At the meso-scale (10^{-3} m), sand and aggregate particles can be distinguished and concrete can be viewed as a composite consisting of a matrix material and inclusions. The laboratory scale (10^{+0} m) is the beginning of the macro-scale concerning structural use of concrete. At the meso-scale, concrete is a 3-phase material consisting of the hardened cement paste (hcp), the aggregates and the interfacial transition zone (ITZ) between the hcp and the aggregates. The thickness of ITZ is typically 50μm but despite its small dimensions, it greatly affects micro-stress concentration because it is the weakest link of the bond between the matrix material and the aggregates. However, the particle structure is the most important at the meso-scale. At the macro-scale of any structural member, at which material constants are assumed in order to model its structural response, the material is by definition assumed to be a continuum. Gradient theories do not depart from this assumption, since stresses and strains continue to be specified at every material point. Gradient theories are continuum theories which introduce an additional constant associated with presence of heterogeneity in what otherwise is assumed to be a homogeneous material. The fact that the matrix material and the inclusions have different properties is the source of heterogeneity. On that respect concrete can be viewed as a model material in order to study size effect in elasticity.

Concrete's heterogeneity is three dimensional and contains various size aggregates of irregular shapes in different volume fractions. Hence, its composite nature deviates significantly from the idealized case of either circular or spherical inclusions. However, two aspects of its mix proportions are of particular interest. One is the maximum aggregate size and the other the strength of the matrix material which can be increased by reducing the water-to-cement ratio. In the experimental program undertaken, the concrete mixes used had the same maximum aggregate and approximately the same volume fraction of aggregates but the relative stiffness of matrix and inclusions varied. As a result, in some mixes crack propagated bypassing the aggregates and in others aggregate fracture occurred along the crack path. Cement mortar was also employed mainly for comparison purposes since this material can be viewed as completely homogeneous.

Institutional Repository - Library & Information Centre - University of Thessaly
15/10/2023 05:52:39 EEST - 167.114.118.212

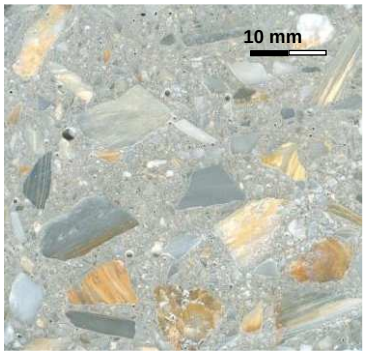

(a)

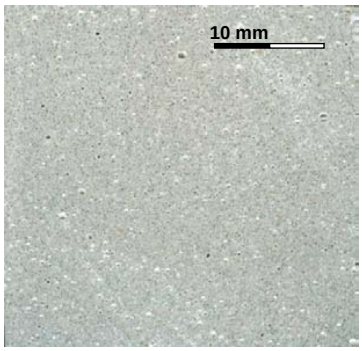

(b)

Cementitious composites:

(a) *Concrete (heterogeneous) with max. aggregate size d_{max}=32 mm.*

(b) *Cement mortar (homogeneous with max. aggregate size d_{max}=1 mm*

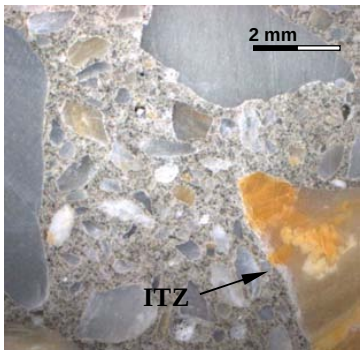

(c)

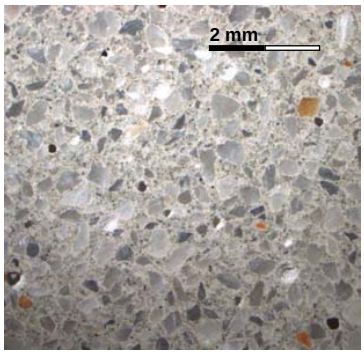

(d)

Microstructure details:

(c) *Concrete: presence of ITZ at the interface of hydrated cement paste and aggregate*

(d) *Cement mortar: composite nature becomes visible at higher magnification*

The internal length is a function of the microstructure but the microstructure's influence is manifested if triggered by the applied stress. This is due to the fact that the internal length, g, is introduced in association with the gradient of the strain:

$$\bar{\boldsymbol{\varepsilon}} = \boldsymbol{\varepsilon} - g^2 \nabla^2 \boldsymbol{\varepsilon}$$

Therefore, in the absence of gradient as for example in the case of uniaxial stresses, even a heterogeneous material is predicted to behave as a homogeneous one. This allows extracting the two classical material constants from a uniaxial test and use flexure tests, where the gradient is significant, to quantify the internal length.

In order to estimate the internal length from flexure experiments, the associated structural problem must be solved using gradient elasticity. This is done in Chapter III. Naturally, any solution to a boundary value problem relies on the correct choice of boundary conditions. Gradient theories are essentially higher-order theories in the sense that they extend the continuity assumed to the second spatial derivative of the strain. This extension of continuity introduced through the constitutive equation results in additional boundary conditions whose physical interpretation is less straightforward. However, there is way to bypass the ambiguity of the non-local boundary

Institutional Repository - Library & Information Centre - University of Thessaly
15/10/2023 05:52:39 EEST - 167.114.118.212

conditions since in all cases for a zero value of the internal length the classical result should be recovered. This must be true for all the classical kinematic variables and not just the deflections since a certain set of non-local boundary conditions can yield the correct asymptotic behavior for deflections but not for the slope or curvature. A unique set of boundary conditions exist which has the correct asymptotic behavior for all classical kinematic variables.

The above discussion is the basis for the study of size effects in elasticity for the concrete mixes considered, which is described in Chapter VI.

3. MICROCRACKING AND DAMAGE

Material's response can be described as the initial one where once the excitation is removed the deformation disappears (elasticity) and another one where upon removal of the cause, the material does not return to its original state (inelasticity). Semi-brittle materials exhibit microcracking once their elastic limit is exceeded. A macrocrack is formed after microcracking has been localized but microcracking will continue to occur while the macrocrack propagates. Microcracking and macrocracks should not be confused. Microcracking is characterized by randomness which by definition is not the case for a macrocrack. Microcracking is the source of softening whereas a macrocrack represents points with zero-transfer capability. Essentially, a macrocrack refers to complete damage at a material point whereas microcracking refers to softening experienced at this point. During softening, stresses and strains continue to be specified at each material point and this is done by assuming a stress-strain law for the material. However, damage also implies that the initial stiffness is reduced. This is revealed upon unloading once the elastic limit has been exceeded. The initial stiffness of an uncracked material is always greater than that of unloading-reloading. Therefore, since damage can be viewed as a process which reduces the initial stiffness it is linked with elasticity by definition.

The tensile strength of concrete is far less than its compressive strength, hence failure initiates from tensile stresses when plain concrete is tested under flexure. Of course, it is a known fact that failure also occurs under a compressive stress which is in apparent contradiction to the second law of thermodynamics that requires that cracks open only under tension. However, this can be explained if the composite nature of concrete is considered since even under compressive stresses, a composite with inclusions may develop tensile stresses around these inclusions. The composite nature of concrete also affects macrocrack propagation. If the inclusions' response is stiffer than that of the matrix material failure will occur there, hence the crack path becomes more tortuous. The more brittle the composite, the less tortuous the crack path would be. On the other

Institutional Repository - Library & Information Centre - University of Thessaly
15/10/2023 05:52:39 EEST - 167.114.118.212

hand, the term semi-brittle refers to the fact that concrete is not perfectly brittle, that is, it maintains its stress bearing capacity to some extend after the peak stress is reached. This softening behavior (microcracking) is also affected by the degree of heterogeneity of the material. The so-called fracture process zone (FPZ) which refers to the degree of localization of microcracking increases as inclusion dimensions increase. If inclusions are negligibly small as for example for cement mortar, the size of FPZ should be much smaller than the one measured in concrete.

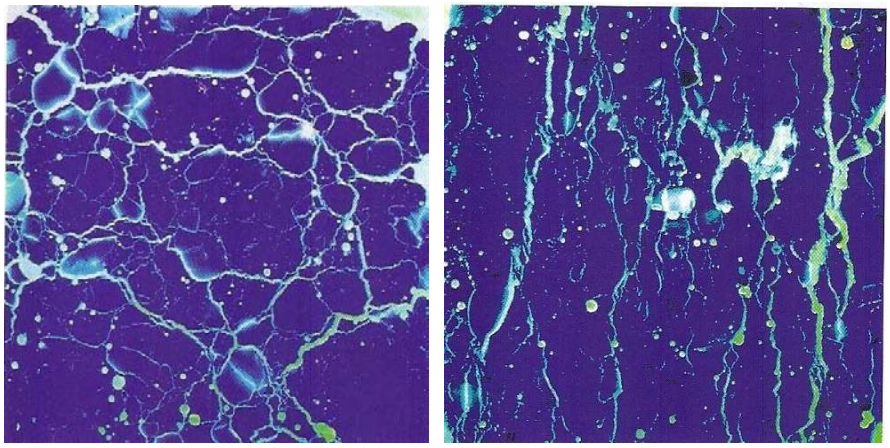

(a) **(b)**

Microcracking:

Crack patterns from fluorescent epoxy impregnation tests on cube specimens under uniaxial compression. Cut shown is:

(a) *parallel and*
(b) *perpendicular to the direction of loading.*

(Photography RA Vonk. Reprinted from the book ''Fracture Processes of Concrete'')

The irreversible character of damage implies that the initial heterogeneity of a composite is altered. Homogenization procedures have been applied to microcracked continuums and it has been found that the stiffness associated with the Cauchy strains (local stiffness) reduces but the stiffness associated with the gradient of the strains (non-local stiffness) increases with increasing degree of microcracking. In the context of gradient theories, this implies that the initial value of an internal length based on the elastic response of the material should increase with increasing damage. A thermodynamic proof for this is included in Chapter IV. This also implies that damage characterization should be local, that is a local parameter should be used to determine the level of damage. The alternative choice of using a non-local parameter such as the total strain or the total stress within the context of gradient theories has been shown to lead to incorrect damage characterization.

The experimental program undertaken in this work also aims to address the issue of how the internal length increases with damage or in other words which is the particular form of the relationship between damage and the internal length. An exponential evolution law is proposed of the form:

Institutional Repository - Library & Information Centre - University of Thessaly
15/10/2023 05:52:39 EEST - 167.114.118.212

$$g = g_0 e^{nD}$$

where $g_0 =$ initial value of the internal length (elasticity), $D =$ damage parameter ($0 \leq D \leq 1$) and $n =$ positive constant.

The choice for this particular expression for the evolution law of the gradient internal length is rooted in the correlation between damage and deflection. The inclusion of an internal length in the formulation affects the predicted deflection at a given load level. The relation of damage and deflection increase resembles that of an exponential law whereas the relation between damage and load decrease is approximately linear. Furthermore, since the initial value of the internal length is determined from the elastic response of the material, there is only one parameter to be calibrated based on the experimental results in the inelastic region. This evolution law is applied in order to study size effects in the inelastic range of the concrete mixes considered in Chapter VII. It is shown that with increasing brittleness of the composite, n increases. Note that the opposite is true for the initial value of the internal length, since as the material becomes more homogeneous the size effect in elasticity would be negligibly small. Correlation between the brittleness of the concrete mixes and evolution law parameter n is also discussed in Chapter VII.

4. EXPERIMENTAL PROGRAM

All experiments were carried out in the Laboratory of “Reinforced Concrete Technology and Structures” of the Civil Engineering Department at the University of Thessaly. However, not all experiments are reported in the present thesis. Experimental results on un-notched fiber-reinforced concrete and notched medium-strength concrete beam specimens are not within the scope of this work.

Experimental results on un-notched low-, normal- and medium-strength plain concrete and cement mortar beam specimens are presented. Three types of tests were carried out for each mix: uniaxial compression on cylinder and cube specimens, splitting on cylinder specimens and 4-point bending on un-notched plain concrete beam specimens of 3 different sizes with complete geometric similarity. The classical material properties of Young’s modulus and Poisson’s ratio were measured in both the uniaxial and split cylinder tests based on strain gage (SG) measurements. Typically, concrete is assumed to be initially isotropic and this hypothesis was verified by comparing the Young’s modulus estimates based on the uniaxial compression tests with the Young’s modulus estimated values in the split cylinder tests. Similar values where obtained for each cementicious mix (see Chapter V).

Institutional Repository - Library & Information Centre - University of Thessaly
15/10/2023 05:52:39 EEST - 167.114.118.212

The geometrically similar un-notched beam specimens with sizes of 100x100x300 (width x height x span) mm, 150x150x450 mm and 200x200x600 mm were tested under midspan deflection control. SG's were used extensively also in the flexural tests. The aim was to determine the midspan curvature and deflection through strain measurements and, independently verify any size effect in elasticity. Strain gradient theories are able to predict a size effect in the stiffness because essentially they assume that for a given level of stress the corresponding strain is less than that predicted by classical elasticity. Based on the measured stiffer response compared to the classical elasticity predictions (in terms of both stiffness and curvature), an internal length estimate for each mix was determined. It is also shown that the use of SG's can yield meaningful measurements for the inelastic response, as well. SG measurements for the neutral axis location at high damage levels and plastic strains measured upon unloading were compared with the proposed model predictions and good agreement was found. This discussion is presented in Chapters VI and VII.

In order to establish the relationship between the internal length predictions based on the flexural test results and the microstructural details of the concrete mix, selected beam specimens were sawed and their microstructure was mapped. The aim was to estimate the average inclusion size of the given concrete mix. Gradient theories attempt to account for the presence of microstructure in an average sense since they model the detail of the microstructure through a single length scale parameter. The internal length value for each cementitious mix was compared with the average inclusion size estimate in Chapter VI.

Institutional Repository - Library & Information Centre - University of Thessaly
15/10/2023 05:52:39 EEST - 167.114.118.212

Experimental program:

(a) *4-point bending specimen and testing setup*

(b) *specimen casting*

(c) *uniaxial cube compression test*

(d) *uniaxial cylinder compression test*

(e) *split cylinder test*

(a) **(b)**

(c) **(d)** **(e)**

5. NUMERICAL PREDICTIONS

Experimental results are compared with numerical predictions in Chapter VII. Under 4-point bending, the middle part of the beam experiences pure bending and, therefore, an assumed stress-strain law in tension and compression is sufficient for damage characterization in this region. Since the tensile strength of concrete is far less than its compressive strength, the compressive zone of the

Institutional Repository - Library & Information Centre - University of Thessaly
15/10/2023 05:52:39 EEST - 167.114.118.212

cross-section under pure bending remains elastic. The stress-strain law chosen, besides the value for the Young's modulus which is measured experimentally, requires an assumed uniaxial tensile strength and a positive non-dimensional parameter defining the degree of softening. The flexural strength predictions under 4-point bending and the corresponding deflections are influenced by these two parameters. The split cylinder tests can provide indicative values of the direct tensile strength. Thus, the uniaxial stress-strain law used was calibrated based on the experimental data of the 4-point bending tests performed in this study.

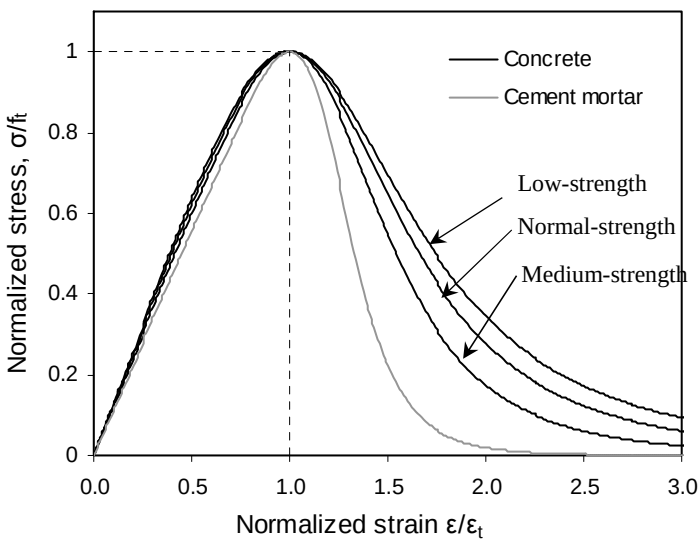

Materials exhibiting softening:
Assumed stress-strain law in tension for the concrete and cement mortar mixes (Popovics, 1973):

$$\frac{\sigma}{f_t} = \frac{\beta_t(\varepsilon/\varepsilon_t)}{\beta_t - 1 + (\varepsilon/\varepsilon_t)^{\beta_t}}$$

The constitutive law in the form of the expression $\sigma / f_i = (\beta_i(\varepsilon/\varepsilon_i))/(\beta_i - 1 + (\varepsilon/\varepsilon_i)^{\beta_i})$, proposed by Popovics (1973) for numerical modeling of the uniaxial stress-strain response in tension or compression of cementitious materials, is very versatile since by altering a single parameter one can model a response from perfectly brittle to perfectly plastic. In other words, it can model cement mortar, concrete and fiber-reinforced concrete, thus, covering the entire range from very brittle to very ductile softening materials. In examining inelasticity of cementitious materials this allows for a unified treatment of the problem.

Once a stress-strain law is assigned, through a simple iteration procedure the moment vs. curvature prediction for a cross-section can be determined. Applied bending moment is translated into applied force through equilibrium and curvature is translated into deflection by using a kinematic relation. The kinematic relation can be obtained in closed-form from the solution of the boundary value problem in elasticity. The influence of the internal length on the classical predictions is then considered by scaling the curvature and by using the kinematic relation furnished

Institutional Repository - Library & Information Centre - University of Thessaly
15/10/2023 05:52:39 EEST - 167.114.118.212

by the gradient solution to the same boundary value problem. The numerical predictions essentially rely on the assumed stress-strain law and on the gradient solution of the structural problem of 4-point bending. The predictions of the local and non-local model are numerical in nature but closed-form solutions are used and their objectivity is demonstrated in Chapter IV.

6. SIZE EFFECTS

Size effect in cementitious materials does not manifest itself only in deformation-related issues such as stiffness but also in strength-related such as flexural strength. The adopted strain gradient theory with a minus sign in the strain gradient cannot predict size effect in strength. Gradient theories with a plus sign in the gradient have been shown to predict size effect in strength but there is very little physical justification for these models and furthermore when applied to elasticity, they predict the opposite of what is observed experimentally in composites with inclusions stiffer than the matrix material. The issue of how the present strain gradient model can be improved with the inclusion of an additional constitutive parameter in order to be able to predict size effect in the flexural strength as well is beyond the scope of this thesis. If the principle of superposition is applicable in this case, it can be said that the present findings concerning the internal length, g, should still hold true. The problem would then simplify to the experimental calibration of this 4th constitutive parameter. This 4th constant could be physically associated with microstress concentration due to the composite nature of the material since as the scale decreases the redistribution of microstresses in the composite becomes more limited.

The experimental program undertaken in this work included specimen sizes of a rather limited scale range (1:1.5:2) concerning the study of size effects in the flexural strength. Nevertheless, the present experimental results on flexural strength are discussed in detail in Chapter VIII. Fracture mechanics and statistical size effects are the two main sources of size effect in strength which has been shown experimentally to occur. However, their predictions do not offer a satisfactory explanation of the observed behavior when the present experimental results are reviewed. Size effect in strength is closely related with the fact that a tensile strength is assigned to the material. When un-notched specimens are tested failure initiates at a location which is known to differ from the bulk material. The so-called wall effect is unavoidable since concrete is cast in plywood molds and the material in close proximity to the molds is altered to some effect. This is not accounted in the present study since a single stress-strain law is assumed for each mix but its presence may explain some of the experimental findings.

Institutional Repository - Library & Information Centre - University of Thessaly
15/10/2023 05:52:39 EEST - 167.114.118.212

CHAPTER II

STRAIN GRADIENT LENGTH VIA HOMOGENIZATION OF HETEROGENEOUS ELASTIC MATERIALS

1. INTRODUCTION

The novelty of gradient elasticity theories is the inclusion of an intrinsic length parameter or internal length in the constitutive equations that describe the mechanical behavior of the material. The inclusion of this parameter allows these theories to explain the size effect that has been shown experimentally to exist in heterogeneous materials. The two simplest and well studied gradient elasticity theories are the couple stress elasticity (or Cosserat theory)[1,2] and the dipolar elasticity theory (or grade-two theory)[3,4]. The main difference between these two theories is that in the assumed strain-energy density function the first associates the internal length with the gradient of the rotations, whereas the second with the gradient of the strains. However, in both theories the internal length is associated with the microstresses that are developed due to the microstructure of the material. In the present work, the simplest possible dipolar model of just one additional length parameter is employed. This model based on a one length parameter appears to be adequate for predicting size effects in elasticity while it is difficult to verify experimentally models incorporating more than one internal length parameters.

A typical composite material consists of a matrix and inclusions. The macroscopic material properties of the composite depend on the individual properties of these two phases. The aim of homogenization is to replace the composite material with an equivalent material of uniform macroscopic properties. Micro-mechanical models have been developed for both cases of particulate and fiber-reinforcement. Among the many homogenization methods that have been proposed are the Mori-Tanaka method[5], the Self Consistent method[6,7], the Generalized Self Consistent method[8] and the Differential method[9,10]. All these methods aim at deriving the material properties of elasticity which in the case of isotropy are the modulus of elasticity and the Poisson’s ratio. However, when gradient theories are considered, an additional material parameter, the internal length, must be added. Nevertheless, the same strategy of homogenization can be used to yield an estimate for this new parameter.

In the present work, the elastic energy of the heterogeneous Cauchy-elastic material will be compared with that of the homogeneous strain gradient elastic material and the characteristic length

Institutional Repository - Library & Information Centre - University of Thessaly
15/10/2023 05:52:39 EEST - 167.114.118.212

will be estimated as function of the inclusion radius, volume fraction and elastic constants. The analysis will be limited to the two-dimensional (2D) case of circular inclusions.

2. EFFECTIVE MATERIAL PROPERTIES OF TRANSVERSELY ISOTROPIC MATERIALS

The following relationships for the effective material properties are derived with the Generalized Self Consistent method for the specific case of cylindrical inclusions, as predicted in [11]. It is noted that subscript m stands for the heterogeneous matrix material and subscript i stands for the inclusion. The symbols without subscript are the effective material properties of the homogeneous material. The overall elastic behavior is that of a transversely isotropic homogeneous material, requiring five material constants with two of them (μ, ν) describing the isotropy of the plane (x_2, x_3) which is of interest in this thesis work.

The in-plane shear modulus, μ, is given by:

$$A\left(\frac{\mu}{\mu_m}\right)^2 + 2B\left(\frac{\mu}{\mu_m}\right) + C = 0 \tag{1}$$

with

$$\begin{aligned}
A &= 3c(1-c)^2\left(\frac{\mu_i}{\mu_m}-1\right)\left(\frac{\mu_i}{\mu_m}+n_i\right) \\
&\quad + \left[\frac{\mu_i}{\mu_m}n_m + n_m n_i - \left(\frac{\mu_i}{\mu_m}n_m - n_i\right)c^3\right]\left[c n_m\left(\frac{\mu_i}{\mu_m}-1\right) - \left(\frac{\mu_i}{\mu_m}n_m + 1\right)\right] \\
B &= -3c(1-c)^2\left(\frac{\mu_i}{\mu_m}-1\right)\left(\frac{\mu_i}{\mu_m}+n_i\right) \\
&\quad + \frac{1}{2}\left[n_m\frac{\mu_i}{\mu_m} + \left(\frac{\mu_i}{\mu_m}-1\right)c + 1\right]\left[(n_m-1)\left(\frac{\mu_i}{\mu_m}+n_i\right) - 2\left(\frac{\mu_i}{\mu_m}n_m - n_i\right)c^3\right] \\
&\quad + \frac{c}{2}(n_m+1)\left(\frac{\mu_i}{\mu_m}-1\right)\left[\frac{\mu_i}{\mu_m}+n_i + \left(\frac{\mu_i}{\mu_m}n_m - n_i\right)c^3\right] \\
C &= 3c(1-c)^2\left(\frac{\mu_i}{\mu_m}-1\right)\left(\frac{\mu_i}{\mu_m}+n_i\right) \\
&\quad + \left[n_m\frac{\mu_i}{\mu_m} + \left(\frac{\mu_i}{\mu_m}-1\right)c + 1\right]\left[\frac{\mu_i}{\mu_m}+n_i + \left(\frac{\mu_i}{\mu_m}n_m - n_i\right)c^3\right]
\end{aligned} \tag{2}$$

$$\begin{aligned}
n_m &= 4 - 3\nu_m \\
n_i &= 4 - 3\nu_i
\end{aligned} \tag{3}$$

Institutional Repository - Library & Information Centre - University of Thessaly
15/10/2023 05:52:39 EEST - 167.114.118.212

where c is the volume fraction of the inclusions and ν denotes the Poisson's ratio.

The in-plane bulk modulus K is:

$$K = K_m + \frac{\mu_m}{3} + \frac{c}{\dfrac{1}{K_i - K_m + (1/3)(\mu_i - \mu_m)} + \dfrac{1-c}{K_m + (4/3)\mu_m}} \quad , \tag{4}$$

the axial modulus E_1 (in the x_1 direction, normal to the (x_2, x_3) plane) is:

$$E_1 = cE_i + (1-c)E_m + \frac{4c(1-c)(\nu_i - \nu_m)^2 \mu_m}{(1-c)\left(\dfrac{\mu_m}{K_i + \mu_i/3}\right) + c\left(\dfrac{\mu_m}{K_m + \mu_m/3}\right) + 1} \quad , \tag{5}$$

the axial Poisson's ratio ν_1 is:

$$\nu_1 = c\nu_i + (1-c)\nu_m + \frac{c(1-c)(\nu_i - \nu_m)\left[\dfrac{\mu_m}{K_m + \mu_m/3} - \dfrac{\mu_m}{K_i + \mu_i/3}\right]}{(1-c)\left(\dfrac{\mu_m}{K_i + \mu_i/3}\right) + c\left(\dfrac{\mu_m}{K_m + \mu_m/3}\right) + 1} \tag{6}$$

and the in-plane Poisson's ratio, ν, is given by[12]:

$$\nu = \frac{K - \psi\mu}{K + \psi\mu} \tag{7}$$

where

$$\psi = 1 + \frac{4K\nu_1^{\,2}}{E_1} \tag{8}$$

The above solution can be simplified for the two extreme cases of rigid inclusions and porous materials. The limiting case of a porous material can be derived directly from the general case represented by Eqs. (1) to (8), if we set $\mu_i = \nu_i = 0$.

For the case of fibers much stiffer than the matrix, only the coefficients of the μ_i terms in A, B, C of Eq. (2) need be retained with the other being vanishing small. Hence, the A, B, C coefficients, when inclusions are much stiffer than the matrix, take the form:

$$\begin{aligned} A &= 3c(1-c)^2 + n_m^{\,2}(1-c^3)(c-1) \\ B &= -3c(1-c)^2 + (1/2)(n_m + c)(n_m - 1 - 2n_m c^3) + (c/2)(n_m + 1)(1 + n_m c^3) \\ C &= 3c(1-c)^2 + (n_m + c)(1 + n_m c^3) \end{aligned} \tag{9}$$

If $\mu_i \to \infty$ is assumed, the rest of the solution for the case of rigid inclusions is found and Eqs. (4) to (8) are modified, accordingly.

Institutional Repository - Library & Information Centre - University of Thessaly
15/10/2023 05:52:39 EEST - 167.114.118.212

These results have been shown to give good estimates not only for the case of dilute composition but also for the limiting case of full packing of the inclusion phase ($c \to 1$). In addition to the physical consistency of the results, it should be noted that the Generalized Self Consistent method is the only complete, exact, closed-form solution for the 2D case of cylindrical inclusions.

The normalized composite shear modulus ratio, μ/μ_m, for elastic cylindrical inclusions for inclusion to matrix shear modulus ratio values ranging from 1.5 to 15 is shown in Fig. 1. The assumed matrix and inclusion Poisson's ratio for all cases considered are 0.2 and 0.25, respectively.

The limiting cases of rigid fibers and porous materials are shown in a semi-logarithmic plot in Fig. 2 and Fig. 3, respectively. Both results depend (weakly) only on the Poisson's ratio of the matrix and four cases are plotted corresponding to matrix Poisson's ratios of 0.1, 0.15, 0.2 and 0.25. A comparison between three cases with a matrix Poisson's ratio of 0.2 is shown in Fig. 4. The shear modulus ratio for the elastic inclusion case is $\mu_i/\mu_m = 2$. The rigid inclusion and the void solution are upper and lower bounds for μ_i/μ_m, respectively.

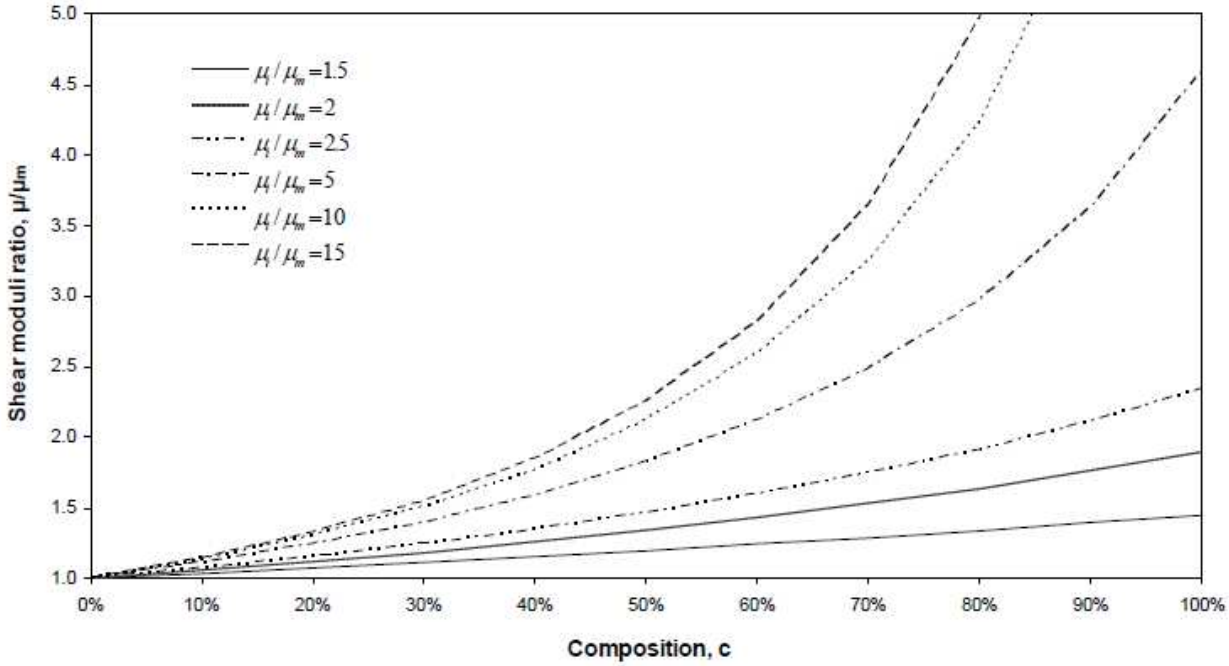

Fig. 1. Effective shear modulus ratios for the case of elastic cylindrical inclusions for inclusion to matrix shear modulus ratio values, μ_i/μ_m = 1.5, 2, 2.5, 5, 10, 15 (Poisson's ratio for matrix, $\nu_m = 0.2$, and for inclusions, $\nu_i = 0.25$).

Institutional Repository - Library & Information Centre - University of Thessaly
15/10/2023 05:52:39 EEST - 167.114.118.212

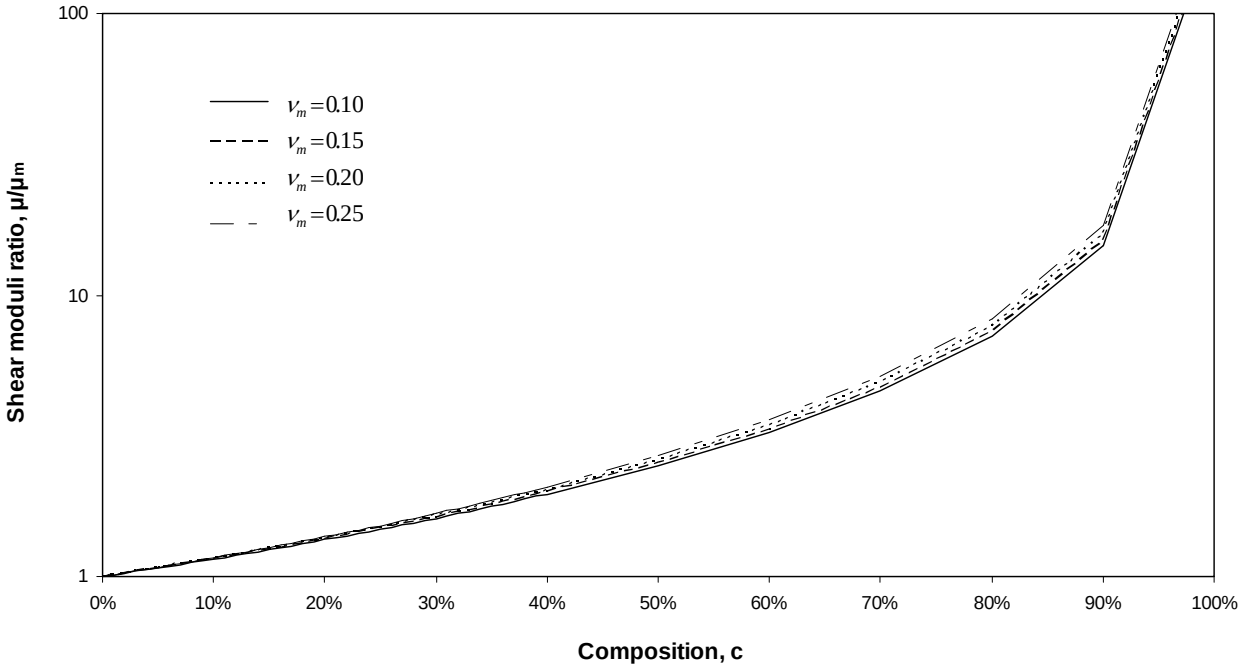

Fig. 2. Effective shear modulus ratio for the case of cylindrical inclusions much stiffer than the matrix for matrix Poisson's ratio values, $\nu_m = 0.1$, 0.15, 0.2, and 0.25.

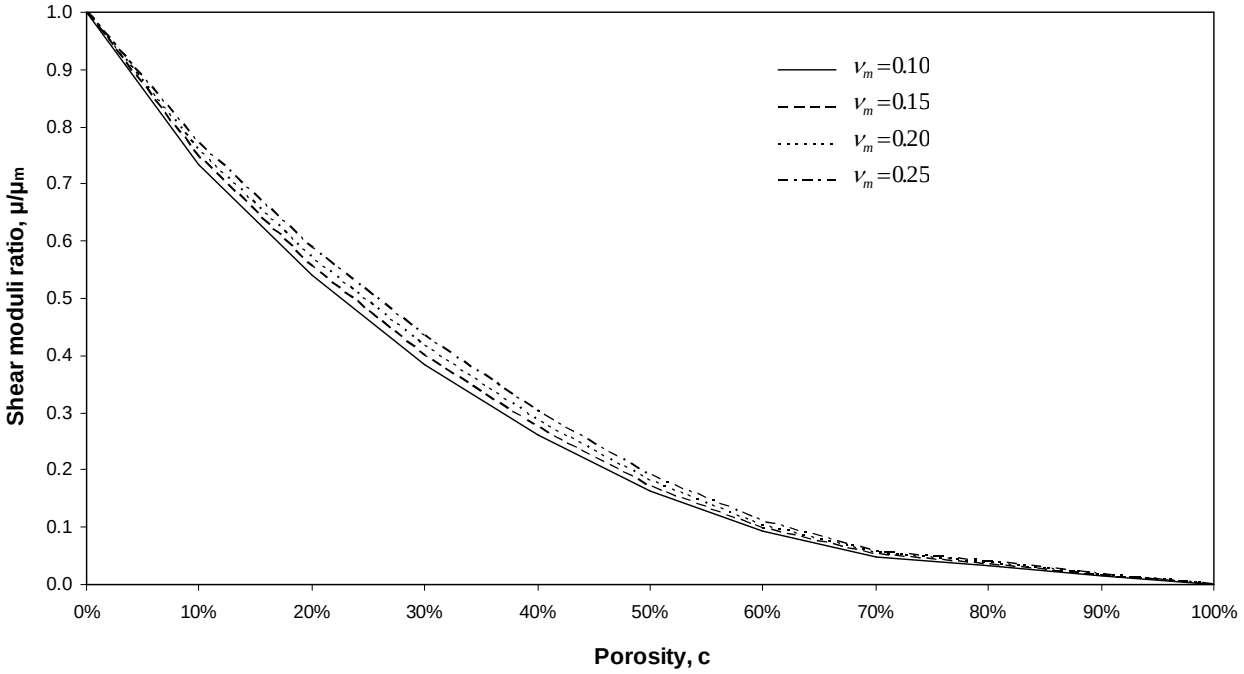

Fig. 3. Effective shear modulus ratio for the case of a porous material ($\mu_f = \nu_f = 0$) for matrix Poisson's ratio values, $\nu_m = 0.1$, 0.15, 0.2, and 0.25.

Institutional Repository - Library & Information Centre - University of Thessaly
15/10/2023 05:52:39 EEST - 167.114.118.212

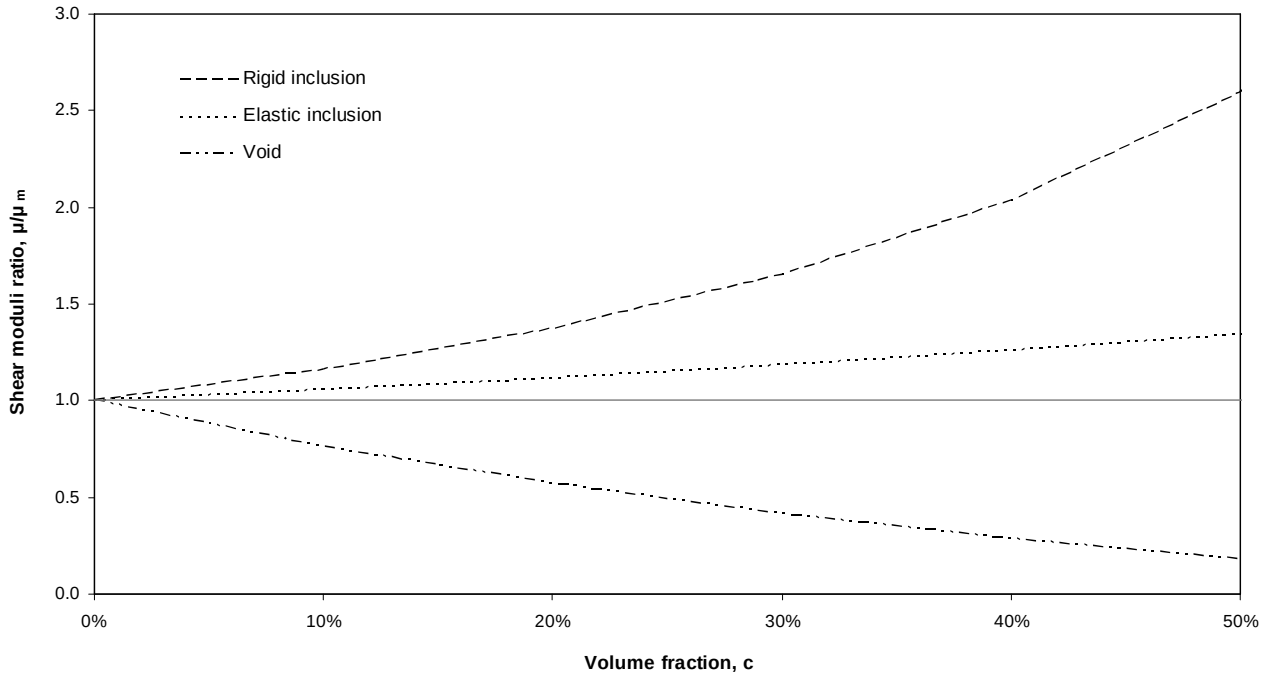

Fig. 4. Comparison between the cases of a porous and elastic matrix material with rigid or elastic inclusions ($\mu_i / \mu_m = 2$) for $\nu_m = 0.2$.

3. CLASSICAL ELASTICITY SOLUTIONS

The solution of a circular ring under plain strain conditions subjected to uniform pressure p applied at the outer boundary $r = b$ and to uniform pressure q applied at the inner boundary $r = a$ is[13, 14] (see Fig. 5):

$$u_r = \frac{1}{2\mu_m (b^2 - a^2)} \left\{ b^2 a^2 (q - p) \frac{1}{r} + (1 - 2\nu_m)(qa^2 - pb^2) r \right\} \tag{10}$$
$$u_\theta = 0$$

$$\sigma_{rr} = \frac{(p-q) b^2 a^2}{b^2 - a^2} \frac{1}{r^2} + \frac{qa^2 - pb^2}{b^2 - a^2}$$
$$\sigma_{\theta\theta} = -\frac{(p-q) b^2 a^2}{b^2 - a^2} \frac{1}{r^2} + \frac{qa^2 - pb^2}{b^2 - a^2} \tag{11}$$
$$\sigma_{r\theta} = 0$$

where u_r is the radial displacement , σ_{rr} the radial stress, $\sigma_{\theta\theta}$ the hoop stress, ν_m the Poisson's ratio and μ_m the shear modulus of elasticity. Subscripts r and θ denote radial and circumferential directions of the ring.

The elastic energy is:

Institutional Repository - Library & Information Centre - University of Thessaly
15/10/2023 05:52:39 EEST - 167.114.118.212

$$U_{cl} = 2\pi\int_{\alpha}^{b}\frac{r}{2}(\sigma_{rr}\varepsilon_{rr} + \sigma_{\theta\theta}\varepsilon_{\theta\theta})dr \tag{12}$$

The expressions for the strains can be found directly from those of the stresses assuming plane-strain constitutive equations[14]. The constitutive expressions of the non-zero strains are:

$$\begin{aligned}\varepsilon_{rr} &= \frac{1}{2\mu_m}\{(1-\nu)\sigma_{rr} - \nu\sigma_{\theta\theta}\}\\ \varepsilon_{\theta\theta} &= \frac{1}{2\mu_m}\{(1-\nu)\sigma_{\theta\theta} - \nu\sigma_{rr}\}\end{aligned} \tag{13}$$

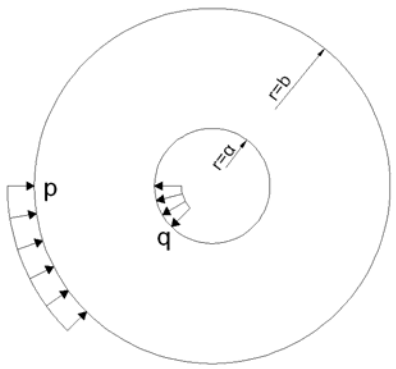

Fig. 5. Circular ring subjected to uniform external and internal pressure.

Rigid inclusions

The above general solution of the annulus problem can be modified to yield the solution for the case of a rigid inclusion of radius a. In this case, the displacements at the inner boundary must be zero. By using (10) and setting $u_r(r=a)=0$, we obtain a relation between the inner and outer pressures that satisfies this condition. The inner pressure q must be:

$$q = \frac{2b^2(1-\nu_m)p}{b^2 + a^2(1-2\nu_m)} \tag{14}$$

If we substitute this specific value of q back to (10) and (11), we will have the solution for the problem of a circular ring with a rigid inclusion.

The elastic energy U_{cl1} would then be:

$$U_{cl1} = \frac{\pi(1-c)p^2a^2(1-\nu_m - 2\nu_m{}^2)}{2\mu_m(1+\nu_m)c(1+c-2c\nu_m)} \tag{15}$$

where c is the composition value equal to $c = a^2/b^2$ for the 2D case.

We can rearrange (15) to become:

Institutional Repository - Library & Information Centre - University of Thessaly
15/10/2023 05:52:39 EEST - 167.114.118.212

$$U_{cl1} = \frac{\pi(1-c)p^2\ell^2\left(\frac{b}{\ell}\right)^2(1-\nu_m-2\nu_m{}^2)}{2\mu_m(1+\nu_m)(1+c-2c\nu_m)} = \pi\times\ell^2\times p^2\times f_1(\mu_m,\nu_m,c,\frac{b}{\ell}) \tag{16}$$

where ℓ is an internal length used to normalize the expression of elastic energy. The inclusion of this parameter might appear unnecessary at the moment since it does not affect the solution but its usefulness will become apparent in Section II.4

The first derivative of u_r at $r = b$ is:

$$\left.\frac{\partial u_r}{\partial r}\right|_{r=b} = -\frac{(1+c)p(1-2\nu_m)}{2\mu_m(1+c(1-2\nu_m))} = u^0_{rrr} \tag{17}$$

Porous material (voids)

The general solution for the case of pores is directly obtained from the general results of (10) and (11), if we set $q = 0$. The elastic energy is then:

$$U_{cl2} = \frac{\pi p^2 b^2(1+c-2\nu_m)}{2\mu_m(1-c)} \tag{18}$$

and if we normalize the expression of the elastic energy with the internal length ℓ, we obtain:

$$U_{cl2} = \frac{\ell^2\pi p^2\left(\frac{b}{\ell}\right)^2(1+c-2\nu_m)}{2\mu_m(1-c)} = \pi\ell^2p^2f_2(\mu_m,\nu_m,c,\frac{b}{\ell}) \tag{19}$$

The first derivative of u_r at $r = b$ is in this case:

$$\left.\frac{\partial u_r}{\partial r}\right|_{r=b} = -\frac{p(1-c-2\nu_m)}{2\mu_m(1-c)} = u^0_{rrr} \tag{20}$$

Elastic inclusions

The solution for this case can be obtained by superimposing the solution of two sub-problems following the well-known Eshelby methodology[15]. We first remove the inclusion and assume an internal pressure q acting at the inner boundary $(r = a)$. By solving this problem we obtain the displacement $u(r = a) = u_1$. We then assume a solid circle with the inclusion properties of radius α under normal pressure q. By solving this problem, we obtain the displacement $u(r = a) = u_2$. The two sub-problems are shown in Fig. 1.6. The solutions to both of these problems can be obtained from the general solution represented by (10) and (11) applying the necessary simplifications for the second sub-problem.

Institutional Repository - Library & Information Centre - University of Thessaly
15/10/2023 05:52:39 EEST - 167.114.118.212

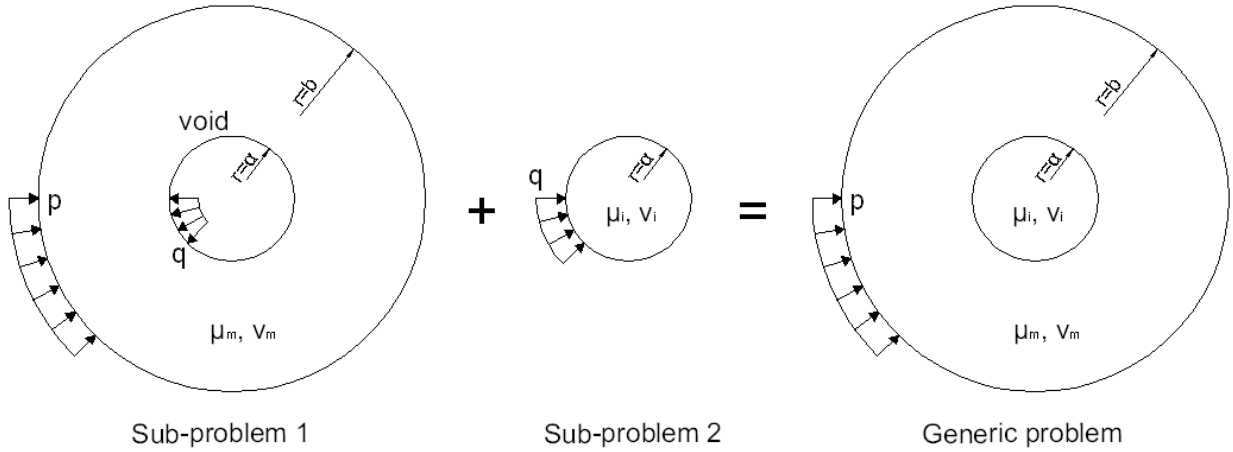

Fig. 6. Superposition of sub-problems 1 and 2 yields the generic case of an annulus with elastic circular inclusions.

The radial displacement u_1 at $r = a$ of the sub-problem 1, is:

$$u_1 = \frac{a\left[q(1+c-2c\nu_m)-2p(1-\nu_m)\right]}{2\mu_m(1-c)} \tag{21}$$

The radial displacement u_2 at $r = a$ of the sub-problem 2, is:

$$u_2 = -\frac{qa(1-2\nu_i)}{2\mu_i} \tag{22}$$

The boundary condition of the generic problem demands $u_1 = u_2$. Using (21) and (22), we obtain the value of q as a function of the outer pressure p and the material properties of the matrix and inclusion. The pressure q must be:

$$q = \frac{2p\mu_i(1-\nu_m)}{\mu_m(1-c)(1-2\nu_i)+\mu_i(1+c-2c\nu_m)} \tag{23}$$

If we feed this value of q back to the solution of the two sub-problems, we obtain the solution of the annulus with a circular inclusion. The elastic energy of the matrix would then be:

$$\begin{aligned} U_{cl3_m} = {} & \frac{a^2(1-c)p^2\pi}{2c\mu_m\left[(1-c)\mu_m(1-2\nu_i)+\mu_i(1+c-2c\nu_m)\right]^2}\times \\ & \times\left[\mu_m{}^2(1-2\nu_i)^2(1+c-2\nu_m)+2(1-c)\mu_i\mu_m(1-2\nu_i)(1-2\nu_m)+\mu_i{}^2(1-2\nu_m)(1+c(1-2\nu_m)\right] \end{aligned} \tag{24}$$

and, if we normalize the expression of the elastic energy with the internal length ℓ, we obtain:

Institutional Repository - Library & Information Centre - University of Thessaly
15/10/2023 05:52:39 EEST - 167.114.118.212

$$U_{cl3_m} = \frac{\left(\frac{b}{\ell}\right)^2 (1-c)p^2\ell^2\pi}{2\mu_m\left[(1-c)\mu_m(1-2\nu_i)+\mu_i(1+c-2c\nu_m)\right]^2} \times$$
$$\times\left[\mu_m{}^2(1-2\nu_i)^2(1+c-2\nu_m)+2(1-c)\mu_i\mu_m(1-2\nu_i)(1-2\nu_m)+\mu_i{}^2(1-2\nu_m)(1+c(1-2\nu_m)\right] \quad (25)$$
$$= \pi\times\ell^2\times p^2\times f_{3_m}(\mu_m,\nu_m,\mu_i,\nu_i,c,\frac{b}{\ell})$$

The elastic energy of the inclusions is:

$$U_{cl3_i} = \frac{2a^2p^2\pi\mu_i(1-2\nu_i)(1-\nu_m)^2}{\left[(1-c)\mu_m(1-2\nu_i)+\mu_i(1+c-2c\nu_m)\right]^2} \quad (26)$$

and, if we normalize the expression of the elastic energy with the internal length ℓ, we obtain:

$$U_{cl3_i} = \frac{2c\left(\frac{b}{\ell}\right)^2\ell^2p^2\pi\mu_i(1-2\nu_i)(1-\nu_m)^2}{\left[(1-c)\mu_m(1-2\nu_i)+\mu_i(1+c-2c\nu_m)\right]^2} = \pi\times\ell^2\times p^2\times f_{3_i}(\mu_m,\nu_m,\mu_i,\nu_i,c,\frac{b}{\ell}) \quad (27)$$

Therefore, the total elastic energy of an annulus with an elastic circular inclusion is:

$$U_{cl3} = U_{cl3_m} + U_{cl3_i} = \pi\times\ell^2\times p^2\times\left[f_{3_m}(\mu_m,\nu_m,\mu_i,\nu_i,c,\frac{b}{\ell}) + f_{3_i}(\mu_m,\nu_m,\mu_i,\nu_i,c,\frac{b}{\ell})\right] \quad (28)$$

and the first derivative of u_r at $r = b$ is:

$$\left.\frac{\partial u_r}{\partial r}\right|_{r=b} = \frac{-p\left[(1+c)\mu_i(1-2\nu_m)+\mu_m(1-2\nu_i)(1-c-2\nu_m\right]}{2\mu_m\left[(1-c)\mu_m(1-2\nu_i)+\mu_i(1+c-2c\nu_m)\right]} = u^0_{rrr} \quad (29)$$

Note that Eq. (29) gives Eq. (20) in the case of a porous material ($\mu_i = 0, \nu_i = 0$) and for rigid inclusions ($\mu_i \to \infty$), Eq. (29) becomes Eq. (17).

4. GRADIENT ELASTICITY SOLUTION FOR THE ANNULUS PROBLEM

Eshel and Rosenfeld[16] were the first to provide the outline of the gradient elasticity solution for the annulus problem. The problem was solved analytically by Aravas[17] and Gao and Park[18] for plain strain conditions. The key points of the solution of the annulus problem (see Fig. 5) are presented next.

The material is an in-plane isotropic, compressible, homogeneous, linear elastic material and is described by an elastic strain energy density function W which incorporates strain gradient effects:

$$W(\varepsilon,\kappa) = \mu\left[\varepsilon_{ij}\varepsilon_{ij} + \frac{\nu}{1-2\nu}\varepsilon_{ij}\varepsilon_{ij} + \ell^2(\kappa_{ijk}\kappa_{ijk} + \frac{\nu}{1-2\nu}\kappa_{ijj}\kappa_{ikk})\right] \quad (30)$$

Institutional Repository - Library & Information Centre - University of Thessaly
15/10/2023 05:52:39 EEST - 167.114.118.212

where is ℓ is a material length, $\boldsymbol{\varepsilon}$ is the infinitesimal strain tensor and $\boldsymbol{\kappa}$ the strain gradient 3rd order tensor. Note that the deformation in the out-of-plane direction x_3 is zero ($u_3 = 0$) and also $\varepsilon_{33} = 0$, $\kappa_{33k} = 0$.

The Cauchy stress and double stress quantities $\boldsymbol{\tau}$ and $\boldsymbol{\lambda}$ are defined as follows:

$$\tau_{ij} = \frac{\partial W}{\partial \varepsilon_{ij}} = 2\mu\left[\varepsilon_{ij} + \frac{\nu}{1-2\nu}\varepsilon_{ij}\delta_{ij}\right] \text{ and } \lambda_{ijk} = \frac{\partial W}{\partial \kappa_{ijk}} = 2\mu\ell^2\left[\kappa_{ijk} + \frac{\nu}{1-2\nu}\kappa_{ipp}\delta_{jk}\right] \tag{31}$$

The following relations also hold true:

$$\boldsymbol{\lambda} = \ell^2\nabla\boldsymbol{\tau} \ (\lambda_{ijk} = \ell^2\,\partial\tau_{ij}/\partial x_k) \text{ and } \boldsymbol{\kappa} = \nabla\boldsymbol{\varepsilon} \ (\kappa_{ijk} = \partial\varepsilon_{ij}/\partial x_k) \tag{32}$$

The dynamic boundary conditions required by the principal of virtual work, are the Cauchy (P_r) and the double stress tractions (R_r) in the radial direction:

$$P_r(r) = \pm\left\{\frac{c_1}{2} - \frac{c_6}{2r^2} - c_2\frac{\ell}{r}\left[\nu K_1\left(\frac{r}{\ell}\right) - (1-2\nu)K_2\left(\frac{r}{\ell}\right)\right] + c_3\frac{\ell}{r}\left[\nu I_1\left(\frac{r}{\ell}\right) - (1-2\nu)I_2\left(\frac{r}{\ell}\right)\right] - \frac{c_6}{2}\frac{\ell^2}{r^4}\right\} \tag{33}$$

$$R_r(r) = -c_2\ell\left[(1-\nu)K_1\left(\frac{r}{\ell}\right) + (1-2\nu)K_2\left(\frac{r}{\ell}\right)\right] + c_3\ell\left[(1-\nu)I_1\left(\frac{r}{\ell}\right) - (1-2\nu)I_2\left(\frac{r}{\ell}\right)\right] \tag{34}$$

where K and I are modified Bessel functions of the 1st and 2nd kind (the subscript indicates the order) and c_1, c_2, c_3 and c_6 are unknown constants to be determined from the following boundary conditions:

$$P_r(a) = -q,\ R_r(a) = 0 \text{ at } r = a$$
$$P_r(b) = -p,\ R_r(b) = 0 \text{ at } r = b \tag{35}$$

The radial displacements are:

$$u_r(r) = \frac{1}{2\mu}\left\{\frac{(1-2\nu)c_1}{2}r + \frac{c_6}{2r} - (1-2\nu)\ell\left[c_2K_1\left(\frac{r}{\ell}\right) - c_3I_1\left(\frac{r}{\ell}\right)\right]\right\} \tag{36}$$

and the rest of the solution is:

$$\tau_{rr}(r) = \tau_{rr}^0(r) + \frac{1}{2}\left(c_7 - \frac{c_8}{r^2}\right) + \frac{c_2}{2}\left[K_0\left(\frac{r}{\ell}\right) + (1-2\nu)K_1\left(\frac{r}{\ell}\right)\right] + \frac{c_3}{2}\left[I_0\left(\frac{r}{\ell}\right) + (1-2\nu)I_1\left(\frac{r}{\ell}\right)\right] \tag{37}$$

$$\tau_{\theta\theta}(r) = \tau_{\theta\theta}^0(r) + \frac{1}{2}\left(c_7 + \frac{c_8}{r^2}\right) + \frac{c_2}{2}\left[K_0\left(\frac{r}{\ell}\right) - (1-2\nu)K_1\left(\frac{r}{\ell}\right)\right] + \frac{c_3}{2}\left[I_0\left(\frac{r}{\ell}\right) - (1-2\nu)I_1\left(\frac{r}{\ell}\right)\right] \tag{38}$$

and

Institutional Repository - Library & Information Centre - University of Thessaly
15/10/2023 05:52:39 EEST - 167.114.118.212

$$\varepsilon_{rr}(r)=\varepsilon_{rr}^{0}(r)+\frac{1}{2\mu}\left\{\frac{(1-2\nu)}{2}c_7-\frac{c_8}{2r^2}\right.$$
$$\left.+(1-2\nu)\left\{c_2\left[K_0\left(\frac{r}{\ell}\right)+\frac{\ell}{r}K_1\left(\frac{r}{\ell}\right)\right]+c_3\left[I_0\left(\frac{r}{\ell}\right)-\frac{\ell}{r}I_1\left(\frac{r}{\ell}\right)\right]\right\}\right\} \tag{39}$$

$$\varepsilon_{\theta\theta}(r)=\varepsilon_{\theta\theta}^{0}(r)+\frac{1}{2\mu}\left\{\frac{(1-2\nu)}{2}c_7+\frac{c_8}{2r^2}-(1-2\nu)\frac{\ell}{r}\left[c_2K_1\left(\frac{r}{\ell}\right)-c_3I_1\left(\frac{r}{\ell}\right)\right]\right\} \tag{40}$$

where τ_{rr}^{0}, $\tau_{\theta\theta}^{0}$, ε_{rr}^{0} and $\varepsilon_{\theta\theta}^{0}$ represent the classical linear isotropic elasticity solution , (i.e. $\ell=0$).

$$\tau_{rr}^{0}=A+\frac{B}{r^2},\tau_{\theta\theta}^{0}=A-\frac{B}{r^2}\ \text{and}\ u_{rr}^{0}=\frac{1}{2\mu}\left[(1-2\nu)Ar-\frac{B}{r}\right] \tag{41}$$

with

$$A=\frac{qa^2-pb^2}{b^2-a^2},\ B=(p-q)\frac{a^2b^2}{b^2-a^2} \tag{42}$$

and

$$c_1=c_7+2A,\ c_6=c_8-2B \tag{43}$$

The solution of interest corresponds to $a\to 0$. The constants c_2 and c_6 must be zero in order for the displacements to be finite and zero at $r=0$. Therefore, the unknown constants reduce to just two, c_3 and c_7. However, when trying to calculate the values of these two constants from traction type boundary conditions, they both vanish and the gradient solution reduces to the classical elasticity solution. This is not surprising because in order for the gradient effects to participate in the solution, they must be triggered somehow by the boundary conditions. This is in agreement with the finding of Bigoni and Drugan[19] who considered corresponding results for Cosserat materials.

In order to overcome this, a kinematic boundary condition is assumed at $r=b$:

$$\left.\frac{\partial u_r}{\partial r}\right|_{r=b}=u_{rrr}^{0} \tag{44}$$

This condition implies that the 2D gradient elastic material representing the composite, assumes a homogeneous gradient of the radial displacement. Eq. (44) together with the traction type condition $P_r(b)=-p$ will be used. Thus, the gradient material is loaded with tractions and displacements gradients that are the same with these of the inhomogeneous classic composite system.

The constants now become:

$$c_8=c_2=B=0,\ A=-p \tag{45}$$

and

Institutional Repository - Library & Information Centre - University of Thessaly
15/10/2023 05:52:39 EEST - 167.114.118.212

$$c_3 = \frac{2b[(1-2\nu)p + 2\mu \times u^0_{rrr}]}{(1-2\nu)\left[b\left(I_0\left(\frac{b}{\ell}\right) + I_2\left(\frac{b}{\ell}\right)\right) - 2\ell\left(I_2\left(\frac{b}{\ell}\right) + \nu I_1\left(\frac{b}{\ell}\right) - 2\nu I_2\left(\frac{b}{\ell}\right)\right)\right]} \tag{46}$$

$$c_7 = \frac{-4\ell\left[I_2\left(\frac{b}{\ell}\right) + \nu I_1\left(\frac{b}{\ell}\right) - 2\nu I_2\left(\frac{b}{\ell}\right)\right]\left[(1-2\nu)p + 2\mu \times u^0_{rrr}\right]}{(1-2\nu)\left[b\left(I_0\left(\frac{b}{\ell}\right) + I_2\left(\frac{b}{\ell}\right)\right) - 2\ell\left(I_2\left(\frac{b}{\ell}\right) + \nu I_1\left(\frac{b}{\ell}\right) - 2\nu I_2\left(\frac{b}{\ell}\right)\right)\right]}, \tag{47}$$

The elastic energy of the gradient solution U_{gr} is:

$$U_{gr} = \pi\int_0^b r\left(\tau_{rr}\varepsilon_{rr} + \tau_{\theta\theta}\varepsilon_{\theta\theta} + \lambda_{rrr}\kappa_{rrr} + \lambda_{\theta\theta\theta}\kappa_{\theta\theta\theta}\right)dr$$

or
$$U_{gr} = \pi\ell^2\int_0^{b/\ell}\frac{r}{\ell}\left(\tau_{rr}\varepsilon_{rr} + \tau_{\theta\theta}\varepsilon_{\theta\theta} + \lambda_{rrr}\kappa_{rrr} + \lambda_{\theta\theta\theta}\kappa_{\theta\theta\theta}\right)d\frac{r}{\ell} \tag{48}$$

The values of **κ** and **λ** are obtained after substituting Eqs. (37) to (40) into (32). After substituting all the quantities and integrating, the gradient elastic energy becomes:

$$\begin{aligned}
U_{gr} = \frac{\pi(-1+2\nu)p^2\ell^2}{4\mu}\Bigg\{ & -\frac{1}{2}\left(\frac{c_7}{p} - 2\right)^2\left(\frac{b}{\ell}\right)^2 - \frac{1}{2}\left(\frac{c_3}{p}\right)^2\left(\frac{b}{\ell}\right)^2\left[I_0^{\,2}\left(\frac{b}{\ell}\right) - I_1^{\,2}\left(\frac{b}{\ell}\right)\right] \\
& -\frac{1}{2}\left(\frac{c_3}{p}\right)^2\left(\frac{b}{\ell}\right)^2\left[I_1^{\,2}\left(\frac{b}{\ell}\right) - I_0\left(\frac{b}{\ell}\right)I_2\left(\frac{b}{\ell}\right)\right] - \frac{c_3}{p}\left(\frac{c_7}{p} - 2\right)\left(\frac{b}{\ell}\right)^2 HG\Gamma\left[2, \frac{1}{4}\left(\frac{b}{\ell}\right)^2\right] \\
& +\frac{1}{2}\left(\frac{c_3}{p}\right)^2\left(-1 + HG\left[\left\{\frac{1}{2}\right\}, \{1,1\}, \left(\frac{b}{\ell}\right)^2\right]\right) - \left(\frac{c_3}{p}\right)^2\left(-1 + HG\left[\left\{\frac{1}{2}\right\}, \{1,2\}, \left(\frac{b}{\ell}\right)^2\right]\right) \\
& -3\left(\frac{c_3}{p}\right)^2\frac{b}{\ell}(1+2\nu)HG\left[\left\{\frac{1}{2}\right\}, \{2,2\}, \left(\frac{b}{\ell}\right)^2\right] + \left(\frac{c_3}{p}\right)^2\frac{b}{\ell}(1-2\nu)HG\left[\left\{\frac{1}{2}\right\}, \{2,3\}, \left(\frac{b}{\ell}\right)^2\right] \\
& +2\left(\frac{c_3}{p}\right)^2\frac{b}{\ell}(1-2\nu)HG\left[\left\{\frac{1}{2}, \frac{1}{2}\right\}, \left\{1,1,\frac{3}{2}\right\}, \left(\frac{b}{\ell}\right)^2\right] \\
& -\frac{1}{3}\left(\frac{c_3}{p}\right)^2\left(\frac{b}{\ell}\right)^3(1+2\nu)HG\left[\left\{\frac{3}{2}, \frac{3}{2}\right\}, \left\{2,2,\frac{5}{2}\right\}, \left(\frac{b}{\ell}\right)^2\right] \\
& +\frac{1}{4}\left(\frac{c_3}{p}\right)^2\left(\frac{b}{\ell}\right)^3(1-2\nu)HG\left[\left\{\frac{3}{2}, \frac{3}{2}\right\}, \left\{2,\frac{5}{2},3\right\}, \left(\frac{b}{\ell}\right)^2\right]\Bigg\}
\end{aligned} \tag{49}$$

or
$$U_{gr} = \pi \times \ell^2 \times p^2 \times g\left(\mu, \nu, c_3, c_7, c, \frac{b}{\ell}\right)$$

Institutional Repository - Library & Information Centre - University of Thessaly
15/10/2023 05:52:39 EEST - 167.114.118.212

where HG is a generalized hypergeometric function and HGΓ is a regularized confluent hypergeometric function[20]. Both functions are described as:

$$HG[\{a_1,...,a_p\},\{b_1,...,b_q\},x]={}_pF_q(a;b;x)=\sum_{k=0}^{\infty}(a_1)_k...(a_p)_k/(b_1)_k...(b_q)_k\frac{x^k}{k!}$$

and $HG\Gamma[a,x]={}_0F_1(a;x)/\Gamma(a)$,

where Γ(α) is the Euler gamma function.

Alternatively, the gradient elastic energy can be found from the external work. The elastic energy is then equal to:

$$U_{gr}=\pi b\{P_r(b)u_r(b)+R_r(b)u_r'(b)\} \tag{50}$$

where prime denotes derivative with respect to r.

Substituting the value of u^0_{rrr} from (29) into (46) and (47), the gradient elasticity solutions can be equated with the classic elasticity solutions for the three cases of rigid inclusion, porous material and elastic inclusions discussed in Section II.3. This approach is similar to that of Bigoni and Drugan[19]for Cosserat gradient elastic materials.

Thus, we obtain the constants c_3 and c_7 for each case separately:

For the case of **rigid inclusions** (Fig. 7), the constants become:

$$c_{3_1}=\frac{2\frac{b}{\ell}p\left[(1-2\nu)-\frac{\mu}{\mu_m}\frac{(1+c)(1-2\nu_m)}{1+c(1-2\nu_m)}\right]}{(1-2\nu)\left[\frac{b}{\ell}\left(I_0\left(\frac{b}{\ell}\right)+I_2\left(\frac{b}{\ell}\right)\right)-2\left(I_2\left(\frac{b}{\ell}\right)+\nu I_1\left(\frac{b}{\ell}\right)-2\nu I_2\left(\frac{b}{\ell}\right)\right)\right]} \tag{51}$$

$$c_{7_1}=\frac{-4p\left[I_2\left(\frac{b}{\ell}\right)+\nu I_1\left(\frac{b}{\ell}\right)-2\nu I_2\left(\frac{b}{\ell}\right)\right]\left[(1-2\nu)-\frac{\mu}{\mu_m}\frac{(1+c)(1-2\nu_m)}{1+c(1-2\nu_m)}\right]}{(1-2\nu)\left[\frac{b}{\ell}\left(I_0\left(\frac{b}{\ell}\right)+I_2\left(\frac{b}{\ell}\right)\right)-2\left(I_2\left(\frac{b}{\ell}\right)+\nu I_1\left(\frac{b}{\ell}\right)-2\nu I_2\left(\frac{b}{\ell}\right)\right)\right]} \tag{52}$$

For the case of **porous materials** (Fig. 8), the constants become:

$$c_{3_2}=\frac{2\frac{b}{\ell}p\left[(1-2\nu)-\frac{\mu}{\mu_m}\frac{(1-c-2\nu_m)}{(1-c)}\right]}{(1-2\nu)\left[\frac{b}{\ell}\left(I_0\left(\frac{b}{\ell}\right)+I_2\left(\frac{b}{\ell}\right)\right)-2\left(I_2\left(\frac{b}{\ell}\right)+\nu I_1\left(\frac{b}{\ell}\right)-2\nu I_2\left(\frac{b}{\ell}\right)\right)\right]} \tag{53}$$

Institutional Repository - Library & Information Centre - University of Thessaly
15/10/2023 05:52:39 EEST - 167.114.118.212

$$c_{7_2} = \frac{-4p\left[I_2\left(\frac{b}{\ell}\right) + \nu I_1\left(\frac{b}{\ell}\right) - 2\nu I_2\left(\frac{b}{\ell}\right)\right]\left[(1-2\nu) - \frac{\mu}{\mu_m}\frac{(1-c-2\nu_m)}{(1-c)}\right]}{(1-2\nu)\left[\frac{b}{\ell}\left(I_0\left(\frac{b}{\ell}\right) + I_2\left(\frac{b}{\ell}\right)\right) - 2\left(I_2\left(\frac{b}{\ell}\right) + \nu I_1\left(\frac{b}{\ell}\right) - 2\nu I_2\left(\frac{b}{\ell}\right)\right)\right]} \tag{54}$$

For the case of **elastic inclusions** (Fig. 9), the constants become:

$$c_{3_3} = \frac{2\frac{b}{\ell}p\left[(1-2\nu) - \frac{\mu\left[(1+c)\mu_i(1-2\nu_m) + \mu_m(1-2\nu_i)(1-c-2\nu_m)\right]}{\mu_m\left[(1-c)\mu_m(1-2\nu_i) + \mu_i(1+c-2c\nu_m)\right]}\right]}{(1-2\nu)\left[\frac{b}{\ell}\left(I_0\left(\frac{b}{\ell}\right) + I_2\left(\frac{b}{\ell}\right)\right) - 2\left(I_2\left(\frac{b}{\ell}\right) + \nu I_1\left(\frac{b}{\ell}\right) - 2\nu I_2\left(\frac{b}{\ell}\right)\right)\right]} \tag{55}$$

$$c_{7_3} = \frac{-4p\left[I_2\left(\frac{b}{\ell}\right) + \nu I_1\left(\frac{b}{\ell}\right) - 2\nu I_2\left(\frac{b}{\ell}\right)\right]\left[(1-2\nu) - \frac{\mu\left[(1+c)\mu_i(1-2\nu_m) + \mu_m(1-2\nu_i)(1-c-2\nu_m)\right]}{\mu_m\left[(1-c)\mu_m(1-2\nu_i) + \mu_i(1+c-2c\nu_m)\right]}\right]}{(1-2\nu)\left[\frac{b}{\ell}\left(I_0\left(\frac{b}{\ell}\right) + I_2\left(\frac{b}{\ell}\right)\right) - 2\left(I_2\left(\frac{b}{\ell}\right) + \nu I_1\left(\frac{b}{\ell}\right) - 2\nu I_2\left(\frac{b}{\ell}\right)\right)\right]} \tag{56}$$

Note that for all expressions of the constants c_3 and c_7, the internal length appears only in the normalized form b/ℓ. By substituting c_{3_i} and c_{7_i} $(i = 1,\ 2,\ 3)$ in (49), we obtain three expressions for the gradient elastic energy, U_{gr1}, U_{gr2} and U_{gr3}, respectively.

Institutional Repository - Library & Information Centre - University of Thessaly
15/10/2023 05:52:39 EEST - 167.114.118.212

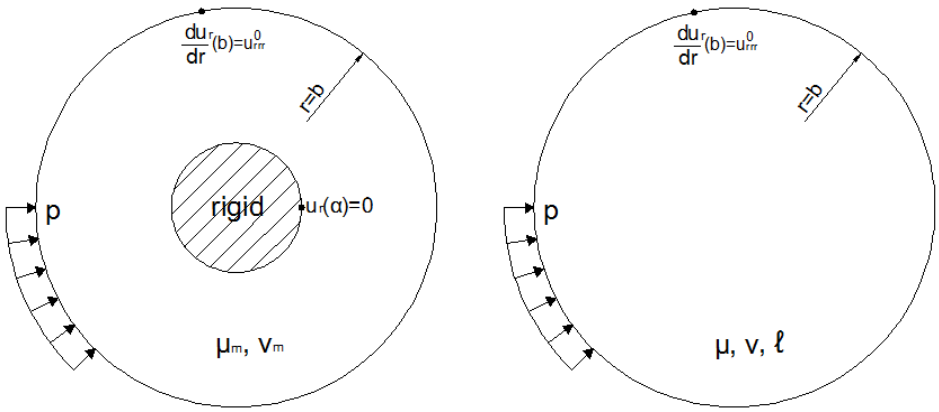

(a) (b)

Fig. 7. Homogenization procedure of a material containing rigid inclusions: (a) Heterogeneous Cauchy material; (b) Homogeneous gradient material.

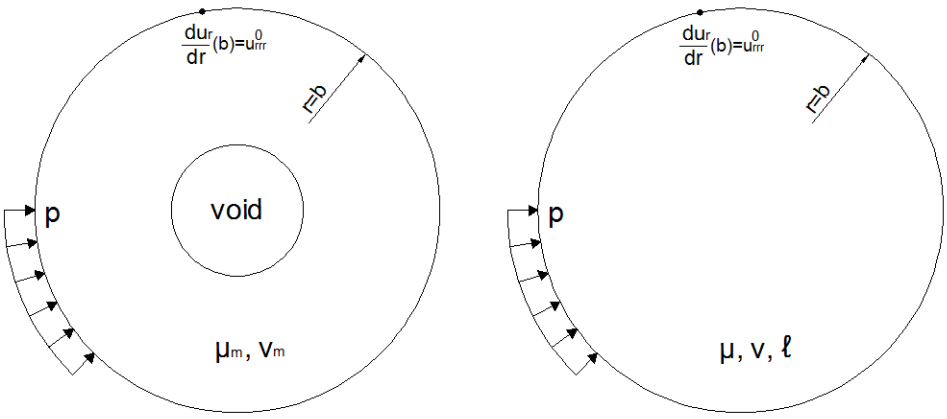

(a) (b)

Fig. 8. Homogenization procedure of a porous material: (a) Heterogeneous Cauchy material; (b) Homogeneous gradient material.

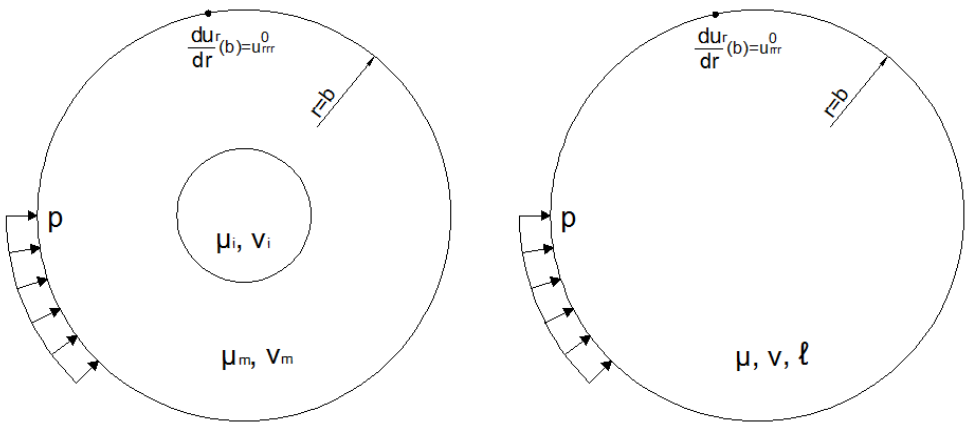

(a) (b)

Fig. 9. Homogenization procedure of a material containing elastic inclusions: (a) Heterogeneous Cauchy material; (b) Homogeneous gradient material.

Institutional Repository - Library & Information Centre - University of Thessaly
15/10/2023 05:52:39 EEST - 167.114.118.212

5. ESTIMATION OF INTERNAL LENGTH

The energy for a heterogeneous material shown in Section II.3 and that for a gradient homogeneous material shown in Section II.4 were determined based on the same boundary conditions. By equating the two energies, we can derive an estimation of the internal length for a gradient material as a function of the inclusion radius a, the composition value ratio c and the elastic material constants of the matrix and the inclusion ($\mu_i/\mu_m, \nu_i, \nu_m$). However, before proceeding, we must face the problem of how to settle with the other two material properties of the gradient material which in the general case will not be equal to the matrix material properties.

The problem has three unknowns, namely, the internal length ℓ, the in-plane shear modulus μ and Poisson's ratio ν and there is only one equation to work with, namely:

$$U_{cl} = U_{gr} \tag{57}$$

One approach is to limit the solution of diluting the concentration of inclusions and hence assume that the material properties of the matrix and composite material remain the same. It is noted that the results of Bigoni and Drugan[19] were derived using this assumption. However, another engineering approach is to extract the two material properties of shear modulus and Poisson's ratio from a classical composite model suitable to the problem under consideration and substitute them to Eq. (57). By doing so, there is only one unknown left, the internal length ℓ, which can then be determined. This approach is justified by the fact that the gradient material should always reduce to the classical material if the gradient effect is neglected, i.e. $\ell = 0$. Therefore the effective material properties predicted by the classical homogenization schemes hold true for the composite gradient material as well. Estimates of the effective material properties of the homogeneous gradient material that correspond to our problem are given in Section II.2.

The expression of U_{gr} is highly non-linear and can not be solved explicitly with respect to ℓ. It can, however, be solved numerically through an iteration process for different values of all the parameters. The solution path is shown schematically in Fig.10. Throughout the calculations, a 5-digit accuracy was maintained. The numerical integration of the curves presented in Fig. 11-13 converges as the interpolation order is increased.

Institutional Repository - Library & Information Centre - University of Thessaly
15/10/2023 05:52:39 EEST - 167.114.118.212

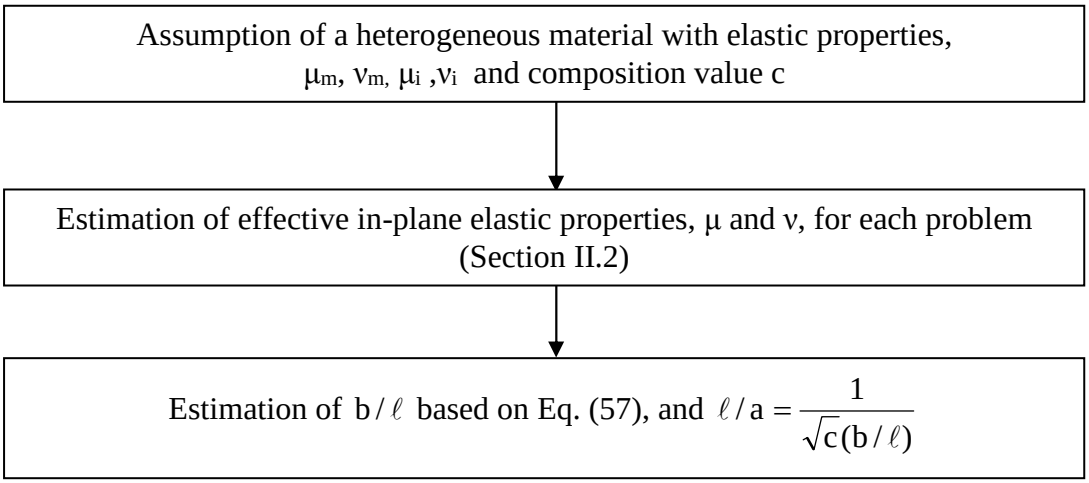

Fig. 10. Iteration process for estimating the internal length as a function of the composition value, c, and the inclusion radius, a .

Rigid Inclusions

Estimation for the internal length for rigid inclusions is derived by equating the two associated energies, $U_{cl1} = U_{gr1}$ (see Fig.7). The variation of the gradient internal length, ℓ, normalized by the radius of the inclusion, a , with a composition value ratio c is shown in Fig. 11 in a semi-logarithmic plot for ν_m values of 0.1, 0.15, 0.2 and 0.25. The results are also presented in Table 1. It can be seen that the internal length increases with increasing value of the matrix's Poisson's ratio.

Institutional Repository - Library & Information Centre - University of Thessaly
15/10/2023 05:52:39 EEST - 167.114.118.212

Table 1. Estimated normalized gradient internal length values for the case of rigid inclusions.

c	b/ℓ				ℓ/α*			
	ν_m=0,1	ν_m=0,15	ν_m=0,2	ν_m=0,25	ν_m=0,1	ν_m=0,15	ν_m=0,2	ν_m=0,25
0.1%	4.6	4.5	4.5	4.7	6.802	7.088	7.058	6.707
1%	7.2	5.4	4.9	5.0	1.390	1.844	2.028	2.017
5%	17.1	9.6	7.0	6.1	0.262	0.468	0.640	0.732
10%	27.8	14.7	10.2	7.8	0.114	0.214	0.309	0.408
20%	47.9	26.4	16.7	12.0	0.047	0.085	0.134	0.186
30%	71.7	42.0	26.7	18.6	0.025	0.043	0.068	0.098
40%	106.2	66.1	43.1	29.6	0.015	0.024	0.037	0.053
50%	163.0	107.3	72.3	50.0	0.009	0.013	0.020	0.028
60%	268,2	186.3	130.2	91.7	0.005	0.007	0.010	0.014
70%	495.5	362.2	263.6	191.0	0.002	0.003	0.005	0.006
80%	1140.7	875.8	664.8	498.6	0.001	0.001	0.002	0.002
90%	4583.1	3685.0	2921.5	2277.0	0.000	0.000	0.000	0.000

* the composition value $c = a^2 / b^2$ for the 2D case

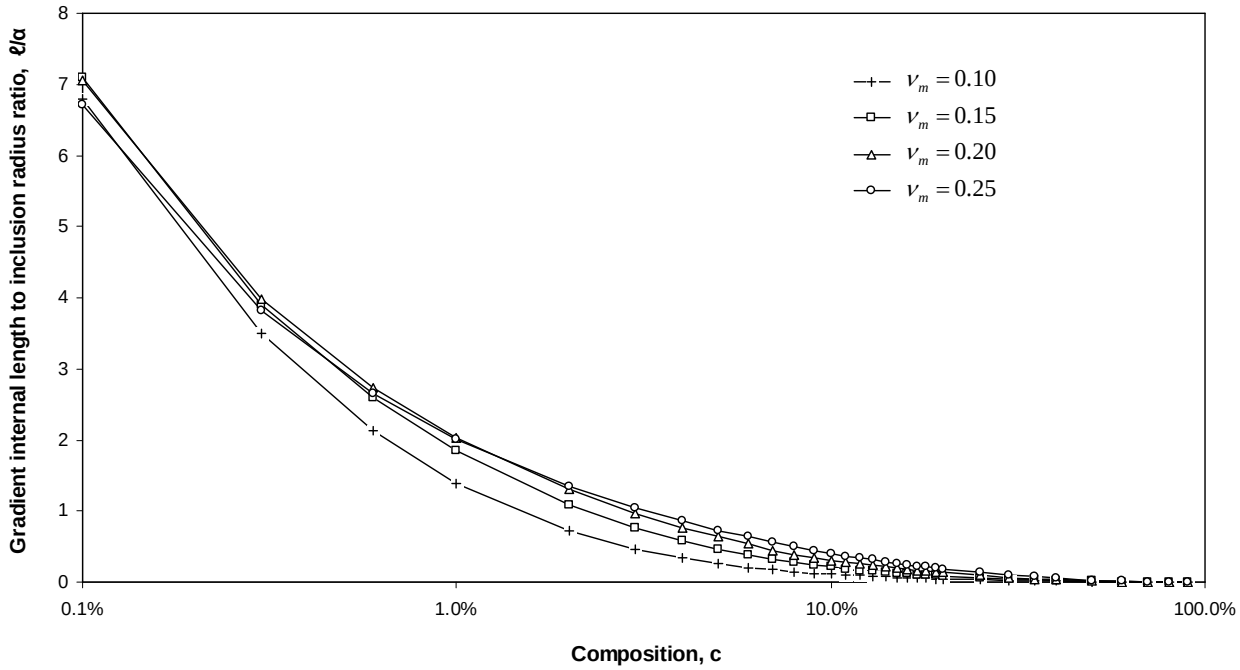

Fig. 11. Variation of the gradient internal length to inclusion radius ratio value, ℓ/α, with respect to the composition value c for the case of rigid cylindrical inclusions.

Institutional Repository - Library & Information Centre - University of Thessaly
15/10/2023 05:52:39 EEST - 167.114.118.212

Elastic Inclusions

Estimation for the internal length for the case of elastic inclusions is derived by equating the two associated energies, $U_{cl3} = U_{gr3}$ (see Fig. 9). The variation of the gradient internal length, ℓ, normalized by the radius of the inclusion, α, with respect to the composition value ratio c is shown in Fig. 12 in a semi-logarithmic plot for inclusion to matrix shear modulus ratio, μ_i/μ_m, values of 2, 2.5, 5, 10 and 15 ($\nu_m = 0.2, \nu_i = 0.25$). For comparison purposes, the rigid case with $\nu_m = 0.2$ is plotted as well. These results are also presented in Table 2. The rigid inclusion case of $\mu_i/\mu_m \to \infty$ gives the upper bound of ℓ/α and ℓ/α increases monotonically for $\mu_i/\mu_m > 1$. The normalized internal length, ℓ/α, is a decreasing function of the composition value c, with $\ell/\alpha \to 0$ as $c \to 1$. It is noted that in all cases, when $c \to 0$ then $\ell/\alpha \to \infty$ with $\int_0^1 \frac{\ell}{\alpha} dc$ finite. Note also that when μ_i/μ_m =1 and ν_i/ν_m =1, no physically meaningful prediction was found as expected, because this case is essentially the case of a homogeneous material. The same was found to be true when the inclusion is less stiff than the matrix.

Table 2. Variation of the normalized gradient internal length value for the case of elastic inclusions.

c	b/ℓ (*)					ℓ/α (**)				
	μ_i/μ_m=2	μ_i/μ_m=2.5	μ_i/μ_m=5	μ_i/μ_m=10	μ_i/μ_m=15	μ_i/μ_m=2	μ_i/μ_m=2.5	μ_i/μ_m=5	μ_i/μ_m=10	μ_i/μ_m=15
0.1%	52.5	44.1	16.6	9.4	7.5	0.602	0.717	1.909	3.350	4.193
1%	55.5	36.8	16.4	9.8	8.0	0.180	0.272	0.611	1.018	1.252
5%	54.6	38.5	18.6	12.0	10.2	0.082	0.116	0.240	0.372	0.440
10%	57.3	41.7	21.8	15.0	13.1	0.055	0.076	0.145	0.210	0.241
20%	64.3	49.4	29.4	22.4	20.3	0.035	0.045	0.076	0.100	0.110
30%	72.5	58.9	39.6	32.5	30.5	0.025	0.031	0.046	0.056	0.060
40%	82.5	70.7	54.0	47.9	46.1	0.019	0.022	0.029	0.033	0.034
50%	93.9	85.4	74.9	72.4	72.0	0.015	0.017	0.019	0.020	0.020
60%	106.7	103.5	106.0	113.6	117.7	0.012	0.012	0.012	0.011	0.011
70%	121.2	125.4	153.1	187.4	205.7	0.010	0.010	0.008	0.006	0.006
80%	136.4	152.1	227.2	332.6	398.5	0.008	0.007	0.005	0.003	0.003
90%	164.5	185.9	-	674.2	938.2	0.006	0.006	-	0.002	0.001

(*) Poisson's ratio for matrix and inclusions is 0.2 and 0.25, respectively.

(**) composition value $c = a^2/b^2$ for the 2D case

Institutional Repository - Library & Information Centre - University of Thessaly
15/10/2023 05:52:39 EEST - 167.114.118.212

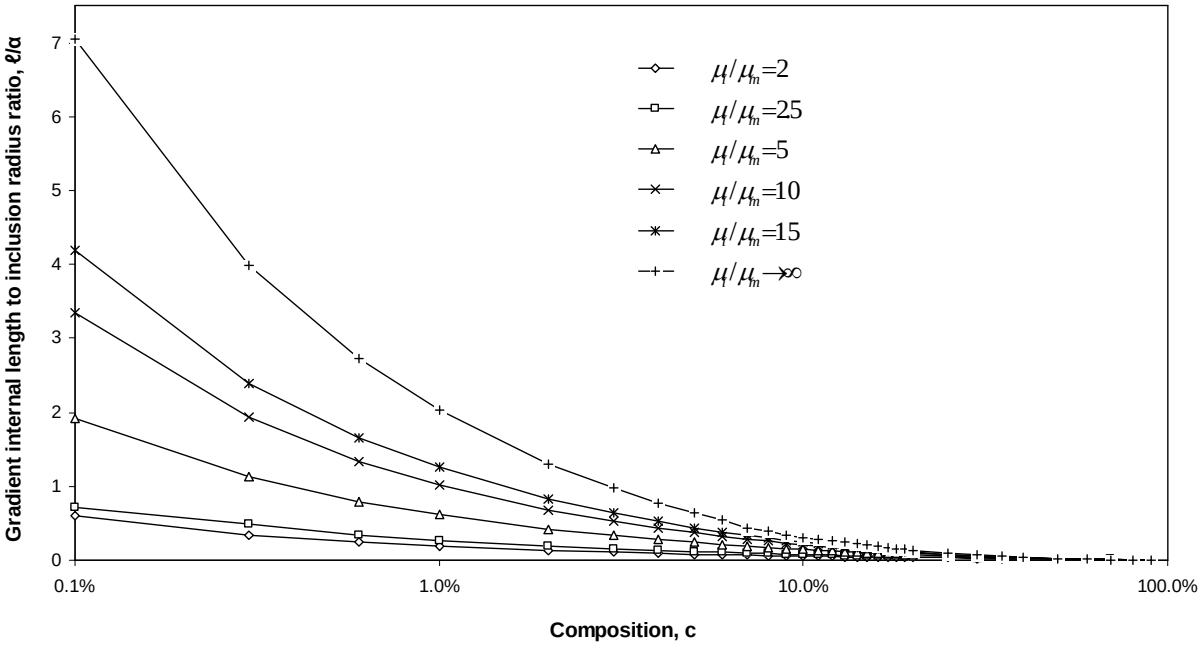

Fig. 12. Variation of the normalized gradient internal length to inclusion radius ratio with respect to the composition value, c, for the case of elastic cylindrical inclusions ($\nu_m = 0.2, \nu_i = 0.25$).

Porous material

Estimation for the internal length for the case of voids present in a material is derived by equating the two associated energies, $U_{cl2} = U_{gr2}$ (see Fig.8). The estimate of the normalized internal length, b/ℓ, for the case of porous materials is either in the order of 10^{-8} or negative. This is not acceptable since it lacks physical justification. In other words, it is not possible to predict an internal length for the case of porous materials or generally when the inclusions are less stiff than the matrix. When inclusions are less stiff than the matrix, the micro-structural load path changes and strain gradient theories may be no longer applicable. This is in agreement with Bigoni and Drugan[19] who proved that predicting the Cosserat microstructural length when particles are stiffer than the matrix is not feasible. It could be argued that the present results are complementary to those of Bigoni and Drugan[19] who were interested in gradients of rotations and not of strains as in the present work.

Micromechanical explanation of the results

The internal length predictions in this work showed that as the composition value is increased, the internal length estimate decreases. The internal length is associated with the microstresses that develop due to the microstructure of the composite. However, when composition value increases the distance between particles, decreases. Instead of having an inclusion embedded in a continuum, the

Institutional Repository - Library & Information Centre - University of Thessaly
15/10/2023 05:52:39 EEST - 167.114.118.212

problem resembles that of a particle with a thin layer around it. It has been shown[21] that when this occurs, the strain gradients reduce drastically.

The estimates shown above were based on an axisymmetric type of loading. In order to verify that these predictions hold true for other loading cases, a different loading system that removes this symmetry is considered next. This loading case corresponds to a remote uniaxial tension and the details of the solutions are presented in Section II.6. The limiting case of rigid inclusions was considered only and it was found that the material length predictions obtained for both loading cases are identical.

6. REMOTE UNIAXIAL TENSION

The problem of a circular inclusion of radius, a, in an infinite isotropic plate under remote uniform uniaxial tension, P, is considered, as shown in Fig. 13. Outside the inclusion, the gradient solution for the radial and angular displacements, respectively, are[21]:

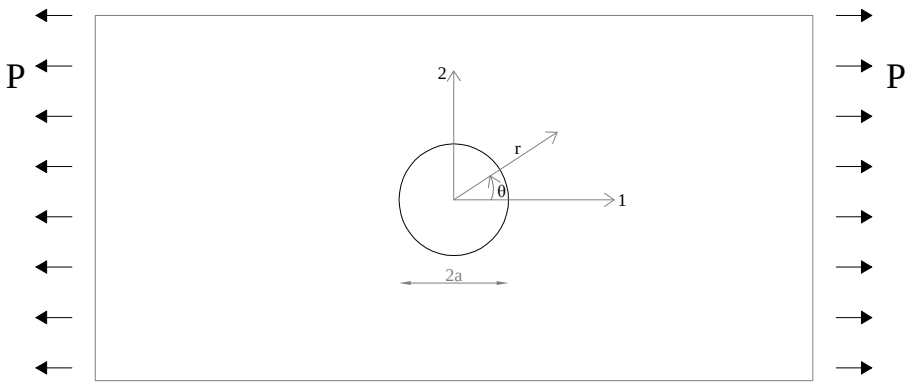

Fig. 13. Inclusion of radius, a, in an infinite plate subjected to uniform uniaxial tension, P.

$$u_r(r,\theta) = u_r^0(r,\theta) + \frac{P}{\mu}\left\{\begin{array}{l}\left[A_1\frac{a}{r} + A_3\frac{a}{r} + A_5\frac{a}{\ell}K_1\left(\frac{r}{\ell}\right)\right] \\ +\left[A_1\frac{a}{r} + A_2\frac{\ell}{r}K_2\left(\frac{r}{\ell}\right) + A_4\left(\frac{a}{r}\right)^3 + A_6\left(\frac{a}{r}K_2\left(\frac{r}{\ell}\right) + \frac{a}{2\ell}K_1\left(\frac{r}{\ell}\right)\right)\right]\cos(2\theta)\end{array}\right\} \tag{58}$$

$$u_\theta(r,\theta) = u_\theta^0(r,\theta) + \frac{P}{\mu}\left\{-\frac{1-2\nu}{2(1-\nu)}A_1\frac{a}{r} + A_2\left(\frac{\ell}{r}K_2\left(\frac{r}{\ell}\right) + \frac{1}{2}K_1\left(\frac{r}{\ell}\right)\right) + A_4\left(\frac{a}{r}\right)^3 + A_6\frac{a}{r}K_2\left(\frac{r}{\ell}\right)\right\}\sin(2\theta) \tag{59}$$

Institutional Repository - Library & Information Centre - University of Thessaly
15/10/2023 05:52:39 EEST - 167.114.118.212

where $A_{1...6}$ are unknown coefficients and $u_r^0(r,\theta)$ and $u_\theta^0(r,\theta)$ are the classical expressions of radial and angular displacements.

The classical expressions of the displacements outside the inclusion for the case of rigid inclusions are[21]:

$$u_r^0(r,\theta) = \frac{Pa}{8\mu}\left\{\left[(k_0-1)\frac{r}{a}+2\gamma\frac{a}{r}\right]+\left[2\frac{r}{a}+\beta(k_0+1)\frac{a}{r}+2\delta\left(\frac{a}{r}\right)^3\right]\cos(2\theta)\right\} \tag{60}$$

$$u_\theta^0(r,\theta) = \frac{Pa}{8\mu}\left\{-2\frac{r}{a}-\beta(k_0+1)\frac{a}{r}+2\delta\left(\frac{a}{r}\right)^3\right\}\sin(2\theta) \tag{61}$$

It is demanded that the gradient displacements are equal to the classical predictions for every θ at $r=a$ and $r=b$ ($b>a$):

$$\begin{aligned} u_r(a,\theta) &= u_r^0(a,\theta) \ \ \forall\theta \\ u_\theta(a,\theta) &= u_\theta^0(a,\theta) \ \ \forall\theta \end{aligned} \tag{62}$$

Eqs. (62) describe a system of 6 equations that can be solved for the six unknowns $A_{1...6}$. The coefficients should be:

$$A_2 = A_5 = A_6 = 0 \tag{63}$$

Therefore, the gradient solution reduces to the classical solution but this does not mean that the gradient effect disappears as in the case of axisymmetric loading. In essence, the same kinematic admissible field for either a gradient homogeneous material or classical heterogeneous material is applied. Obviously, this kinematic field is the same only for $r \geq a$, but for the case of dilute composites ($a << b$) the total elastic energy calculated for $b \geq r \geq a$ is approximately the same with the total elastic energy calculated for $b \geq r \geq 0$.

The expression for the total classical elastic energy is:

$$U_{cl} = 4\int_0^{\pi/2}\int_a^b \frac{1}{2} r\left(\tau_{rr}\varepsilon_{rr}+\tau_{\theta\theta}\varepsilon_{\theta\theta}+2\tau_{r\theta}\varepsilon_{r\theta}\right)drd\theta \tag{63}$$

and that for the total gradient elastic energy is:

$$U_{gr} = 4\int_0^{\pi/2}\int_a^b \frac{1}{2} r\begin{pmatrix}\tau_{rr}\varepsilon_{rr}+\tau_{\theta\theta}\varepsilon_{\theta\theta}+2\tau_{r\theta}\varepsilon_{r\theta} \\ +\lambda_{rrr}k_{rrr}+\lambda_{r\theta\theta}k_{r\theta\theta}+2\lambda_{rr\theta}k_{rr\theta}+\lambda_{\theta rr}k_{\theta rr}+\lambda_{\theta\theta\theta}k_{\theta\theta\theta}+2\lambda_{\theta r\theta}k_{\theta r\theta}\end{pmatrix}drd\theta \tag{64}$$

It is reminded that for the case of cylindrical coordinates the following relations hold true:

Institutional Repository - Library & Information Centre - University of Thessaly
15/10/2023 05:52:39 EEST - 167.114.118.212

$$\nabla = \mathbf{e}_r \frac{\partial}{\partial r} + \mathbf{e}_\theta \frac{1}{r}\frac{\partial}{\partial \theta}, \qquad \begin{aligned} \nabla \boldsymbol{\tau} = & \frac{\partial \tau_{rr}}{\partial r}\mathbf{e}_{rrr} + \frac{\partial \tau_{\theta\theta}}{\partial r}\mathbf{e}_r\mathbf{e}_\theta\mathbf{e}_\theta + \frac{\partial \tau_{r\theta}}{\partial r}\mathbf{e}_r(\mathbf{e}_r\mathbf{e}_\theta + \mathbf{e}_\theta\mathbf{e}_r) \\ & + \frac{1}{r}\left(\frac{\partial \tau_{rr}}{\partial \theta} - 2\tau_{r\theta}\right)\mathbf{e}_\theta\mathbf{e}_r\mathbf{e}_r + \frac{1}{r}\left(\frac{\partial \tau_{\theta\theta}}{\partial \theta} + 2\tau_{r\theta}\right)\mathbf{e}_\theta\mathbf{e}_\theta\mathbf{e}_\theta \\ & + \frac{1}{r}\left(\frac{\partial \tau_{r\theta}}{\partial \theta} + \tau_{rr} - \tau_{\theta\theta}\right)\mathbf{e}_\theta(\mathbf{e}_r\mathbf{e}_\theta + \mathbf{e}_\theta\mathbf{e}_r) \end{aligned} \tag{65}$$

Under the assumption of dilute composition, equality of the two energies can be demanded since both systems have the same kinematic field. The other two material properties, i.e. in-plane shear modulus and Poisson's ratio for the gradient material, are extracted from Christensen's predictions (see Section II.2). In Fig. 14, the prediction for rigid inclusions is plotted assuming that the matrix Poisson's ratio is $\nu = 0.2$. The solid line corresponds to loading case 1 (see Fig. 7) and the diamond symbols correspond to loading case 2 (Fig. 13). The predictions for loading case 2 were derived under the assumption of dilute concentration of inclusions and hence only the predictions for $c < 5\%$ are plotted. As it can be seen, the agreement for the two estimates is very good for values of c up to 1% while the deviation between the two predictions increases for higher values.

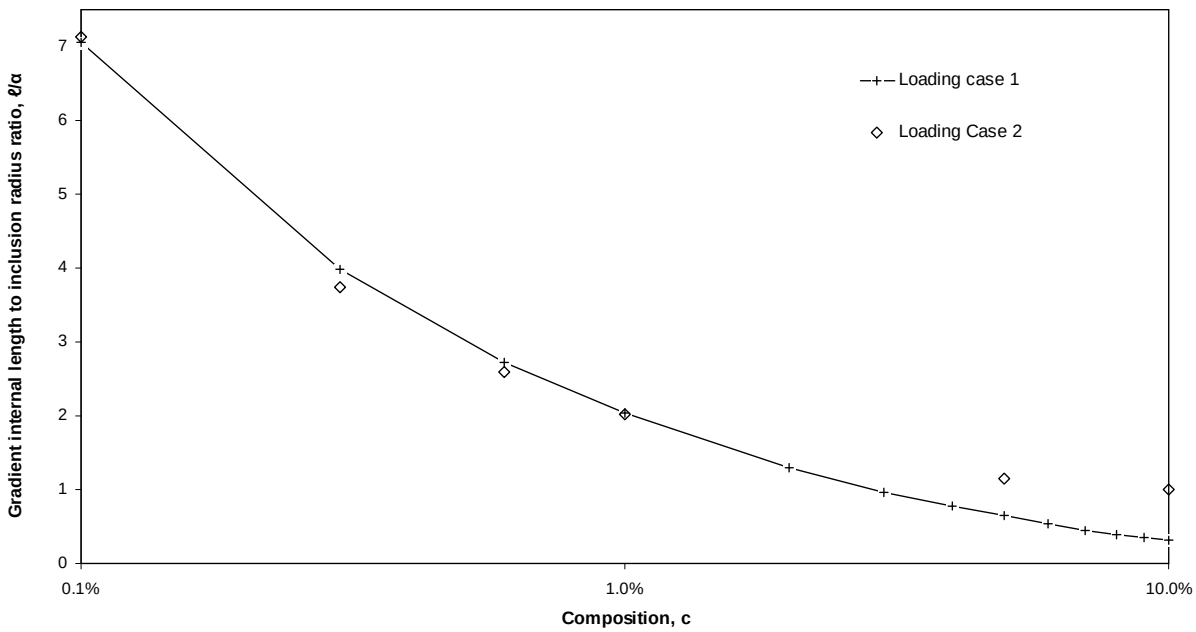

Fig. 14. Variation of the normalized gradient internal length to inclusion radius ratio, ℓ/α, vs. the composition value c for the case of rigid cylindrical inclusions and two loading cases ($\nu_m = 0.2$).

Institutional Repository - Library & Information Centre - University of Thessaly
15/10/2023 05:52:39 EEST - 167.114.118.212

7. APPLICATION TO FIBER-REINFORCED CONCRETE

In order to obtain an estimate of the internal length for fiber-reinforced concrete (FRC), one can use either the assumption of elastic or that of rigid inclusions. In this study, a typical FRC mix[22] with hooked-end steel fibers and the following properties, $E_m = 40\,\text{GPa}$, $\nu_m = 0.2$, $E_i = 210\ \text{GPa}$, $\nu_i = 0.3$ and $c = 0.8\%$ used for retrofitting RC structures is considered. The steel fibers have a circular cross-section with a 5-mm diameter and the fibers to cement matrix shear modulus ratio is $\mu_i / \mu_m = 4.85$. The density for the cement matrix and the "fiber" inclusions is $\rho_m = 2350\ \text{kg/m}^3$ and $\rho_i = 7850\,\text{kg/m}^3$, respectively.

The normalized internal length, ℓ/a, and internal length, ℓ, estimate according to the proposed model for the assumption of elastic and rigid "fiber" inclusions is $\ell / a = 0.6$ ($\ell = 1.50$ mm) and $\ell / a = 2.3$ ($\ell = 5.75$ mm), respectively. It is noted that this specific FRC mix was designed to be used as a 3- to 5-cm thick jacket to existing RC columns.

The Ben-Amoz model[23] for predicting the internal length parameter is based on a dynamic analysis of the micro- and macro-structure. It is noted that, in the absence of the dynamic conditions imposed, the validity of this model becomes questionable. Nevertheless, the Ben-Amoz model is the only model in the literature that can predict the strain gradient internal length parameter and for this reason it is interesting to compare its predictions with the proposed model predictions. The key points of Ben-Amoz model are described next.

A normalized scale parameter, L/d, which can be seen as a measure of the strength of heterogeneity, is introduced as follows:

$$L / d = \left[\rho_\upsilon (\lambda + 2\mu)_\upsilon / \rho_R (\lambda + 2\mu)_R\right]^{1/2} \tag{66}$$

where $d = 2b$ for the 2D case and subscripts υ and R denote the Voigt and Reuss averaging quantities, respectively, which are defined as follows:

$$\begin{aligned} (\ )_\upsilon &= c_m (\ )_m + c_i (\ )_i \\ \frac{1}{(\ )_R} &= \frac{c_m}{(\ )_m} + \frac{c_i}{(\ )_i} \end{aligned} \tag{67}$$

where c is the volume fraction of the inclusions and subscripts m and i denote the matrix and "fiber" inclusion material, respectively. It is noted that this scale parameter is derived by assuming that the strain energy and kinetic energy are of the same order of magnitude but this assumption is not always true..

Institutional Repository - Library & Information Centre - University of Thessaly
15/10/2023 05:52:39 EEST - 167.114.118.212

The internal length parameters of Mindlin's work for the long wave-length approximation, ℓ_1 and ℓ_2 (pp. 69 in [4]) are then associated with the scale parameter L by the following equations for the shear and dilatation modes:

$$\ell_1^{\,2} = \frac{L^2}{4}\left[1 - \frac{\mu_i - \mu_m}{\mu_\upsilon}(c_i - 4I_i)\right]$$
$$\ell_2^{\,2} = \frac{L^2}{4}\left[1 - \frac{(\lambda + 2\mu)_i - (\lambda + 2\mu)_m}{(\lambda + 2\mu)_\upsilon}(c_i - 4I_i)\right] \tag{68}$$

where $I_i = (a/b)^4 = c_i^{\,2}$ for the 2D case.

Applying the simplifications of the simplified strain gradient theory used throughout this thesis, that is $\hat{a}_1 = \hat{a}_3 = \hat{a}_5 = 0$, $\hat{a}_2 = (\lambda/2)\ell^2$ and $\hat{a}_4 = \mu\ell^2$ (see [4], pp. 73), the Mindlin's internal length parameters become $\ell_1 = \ell_2 = \ell$. Hence, the Ben-Amoz model gives two different estimates for the internal length parameter, which for small values of the composition value c are approximately the same. The Ben-Amoz predictions, for the specific FRC mix considered here, are:

$\ell/a = 11.28$ and $\ell = 28.2\,\text{mm}$, for the shear mode,

and $\ell/a = 11.22$ and $\ell = 28.05\,\text{mm}$, for the dilatation mode

The predicted internal length estimates for the same FRC material of the present (about 6 mm) and the Ben-Amoz model (about 28 mm) are significantly different. A definite answer as to which model is more appropriate would require the estimation of an internal length for an FRC mix independently based on flexure tests.

8. CONCLUSIONS

A homogenization of a plane-strain heterogeneous Cauchy-elastic material was performed and the internal length parameter assumed in the strain gradient theory was estimated for the case of elastic inclusions stiffer than the matrix in the case of fiber-reinforced composites. The internal length was found to be 0.5 to 7 times the inclusion radius for very small values of $c \cong 0.1\%$ depending on the inclusion to matrix shear modulus ratio. The internal length estimate decreases rather rapidly as the composition value c is increased and is approximately zero for $c > 70\%$. No prediction was possible for inclusions less stiff than the matrix and for the extreme case of porous materials.

Institutional Repository - Library & Information Centre - University of Thessaly
15/10/2023 05:52:39 EEST - 167.114.118.212

CHAPTER III

STRUCTURAL ANALYSIS USING A DIPOLAR ELASTIC TIMOSHENKO BEAM - APPLICATION TO MICROCANTILEVERS

1. INTRODUCTION

A term so-called "size effect'' is usually used to describe the effect of the microstructure on the mechanical behavior of a member which for different sizes deviates from that expected based on similitude laws. When the dimensions of the microstructure (grain size, inclusion size, lattice distance etc.) becomes comparable with the dimensions of the member itself, the assumption of a homogeneous medium of classical elasticity and its implication concerning the very definition of stress and strain no longer suffice. In other words, as structures are scaled down their behavior becomes increasingly dominated by the inhomogeneous nature of the material itself. The need to model such behavior without modeling the full detail of the microstructure has led to the development of enriched continuum models. This is done in an average sense by introducing length scale parameters in the constitutive equations that account for the effect that the microstructure has on the deformation process. By doing so, these theories have the advantage over classical elasticity of explaining why scaled down structures are stiffer and stronger. However, in their original form[1,2,3,4] these theories become unpractical since it is impossible to quantify all these new length scale parameters with the available experimental data, i.e. static or dynamic flexural tests. Nevertheless, by simplifying these theories and keeping just one length scale parameter (for static cases), calibration becomes rather straight forward and at the same time the key novelty of such theories which is the prediction of size effect is preserved. For this reason, in this work, a simplified (dipolar) isotropic strain gradient theory is used with just one material length scale parameter, g, in addition to the two classical elasticity parameters, that is the elastic modulus, E, and the Poisson's ratio, ν.

Quite small structural elements that are used in the design of micro-electromechanical systems (MEMS) are often in the form of beams (e.g. sensors and actuators) and their design requires them to deform within their elastic domain[5]. Although the stiffness of such micro-devices is essential information for their design, in many cases their stiffness is determined experimentally and is found to be higher than that predicted by classical elasticity. Salvetat et al.[6] performed flexural experiments on single-wall carbon nanotube beams with both ends fixed arranged in a close-packed lattice with dimensions of 1.4 nm and used rope diameters from 3 to 20 nm in flexural tests. They found that as

Institutional Repository - Library & Information Centre - University of Thessaly
15/10/2023 05:52:39 EEST - 167.114.118.212

the diameter decreased the nanotubes exhibited a much stiffer response. The same behavior was observed in carbon nanotubes by Poncharal et al.[7]. Ding et al.[8] tested polysilicon microcantilevers with grain size in the order of 0.2 μm, thickness of 2.4 μm and variable aspect ratios and although the authors attributed the stiffness differences in the beams to measurement errors, a closer look at their results suggests the existence of a size effect. Lam et al.[9] performed bending tests on epoxy polymeric microcantilevers with thickness values varying from 20 to 115 μm and showed that as the thickness decreased the stiffness increased beyond the predictions of classical elasticity. Although no information about the microstructure of the PP microcantilevers is included in this work, high crosslink-density regions with a diameter of 6 to 104 nm have been observed in cross-linked resins forming on that scale a heterogeneous rather than a homogeneous material[10,11]. McFarland and Colton[12] tested polypropylene (PP) microcantilevers which have a nonhomogeneous microstructure due to their semi-crystalline nature and found that the microcantilevers with a thickness of 15 and 29 μm exhibited a much stiffer response which cannot be explained by any of the possible error sources associated with the experiments. It is noted that the nonhomogeneous nature of PP is due to the formation of spherical particles called spherulites during its manufacturing process. The authors did not provide any information about the size of the spherulites in their material but typically their size can be up to 10 μm when the specimen is manufactured via injection molding[13]. Hong et al.[14] tested copper (Cu) microcantilevers with a thickness of 10.5 and 2.8 μm under flexure and reported a stiffer response for the thinner films. Grain size of copper films manufactured by electroplating and annealed in vacuum can be up to[15] 1 μm. Yang et al.[16] tested native and cross-linked type I collagen fibrils with diameters ranging from 187 to 424 nm and found that the stiffness increased as the diameter of the fibrils decreased. Note that collagen fibrils are assembled of parallel collagen molecules arranged with a longitudinal stagger and also contain mineral particles (typically flat and elongated) with the elongated dimension reaching values up to[17] 100 nm. It is also worth mentioning the work of Namazu et al.[18] and Liu et al.[19] who carried out flexure experiments on single-crystal silicon beams which have a continuous crystal lattice (no grain boundaries) and hence can be seen as completely homogeneous and found absence of size effect in stiffness as the specimens ranged from a nano- to a mm scale. Size effect in strength, however, was significant. This review of the available experimental evidence is not meant to be exhaustive but only indicative of the phenomenon which the current work attempts to explain, which is that size effect in the elastic deformation range of beams is to be expected when the scale of the structure becomes comparable with the scale of the microstructure.

Institutional Repository - Library & Information Centre - University of Thessaly
15/10/2023 05:52:39 EEST - 167.114.118.212

The need to quantify the departure from the classical elasticity predictions and offer the designer of MEMS a theoretical tool in the form of closed-form solutions for predicting size effect is one of the motivations in this work. Of interest is the solution of a Timoshenko beam[20] loaded statically. Papargyri-Beskou et al.[21] have used the same simplified strain gradient theory using surface energy[22] to solve the bending and buckling of the Bernoulli-Euler beam. Their model has been investigated further by Giannakopoulos and Stamoulis[23] for the case of a cantilever beam under flexure and a cracked bar under tension. Nevertheless, the Bernoulli-Euler beam is only applicable to slender beams where shear forces have a negligible influence on the deformations of the beam.

In the present work using the Timoshenko beam kinematics it is examined how the gradient solution is affected when the shear forces are included in the analysis. It is noted here that the same strain gradient elasticity theory has been used by Wang et al.[24] and Lazopoulos and Lazopoulos[25] for the case of Timoshenko beam kinematics. Both these works employ Fourier series to solve the boundary value problem, whereas in the present work closed-form solutions are provided. Furthermore, none of these works address the issue of indeterminate members and how they should be treated and only refer to the isostatic case of a simply-supported beam. As it would become apparent, by solving the problem in a closed-form, a methodology for treating more complex structural problems (hyperstatic beams, frames etc.) emerges. However, it is beyond the scope of this work to explore all beam configurations and only the example of a doubly-clamped beam is considered in detail. More differences exist if the solution in the present model is compared to that of Wang et al.[24] and Lazopoulos and Lazopoulos[25] and those are discussed in detail in Section III.4. Finally, other non-local theories for the case of Timoshenko beam kinematics have also been considered by Lam et al.[9], Reddy[26], Ma et al.[27], Asghari et al.[28], Ramezani et al.[29]. These works employ different gradient elasticity theories than the presented one and are briefly discussed in Section III.4. Models that are based on integral (strong) non-local theories will not be examined in this work.

Concerning the structure of the present chapter, Section III.2 includes the governing equations and boundary conditions for the Timoshenko beam, while in Section III.3 the proposed model is applied to the specific problem of a cantilever beam with a point load at its free end and the details of the solution are investigated. An indeterminate beam is also investigated, i.e. a beam clamped at both ends, loaded by a point load at midspan. In Section III.4, the present approach is compared with the various Timoshenko beam theories in the literature. Finally, in Section III.5,

Institutional Repository - Library & Information Centre - University of Thessaly
15/10/2023 05:52:39 EEST - 167.114.118.212

available experimental data on microcantilevers in the literature are used to compare the predictions of the length parameter for the strain gradient elasticity with those for the micropolar elasticity.

2. GOVERNING EQUATIONS AND BOUNDARY CONDITIONS

We consider a straight prismatic beam subjected to a static lateral load $q(x)$ distributed along the longitudinal axis x of the beam, as shown in Fig. 1(a). The loading plane coincides with the xz plane and the cross-section of the beam is parallel to the yz plane and symmetric with respect to the xz plane. The displacement field following the Timoshenko beam kinematics can be described by the following relations:

$$\begin{aligned} u_x &= z\,\psi(x) \\ u_y &= 0 \\ u_z &= w(x) \end{aligned} \tag{1}$$

where $\psi(x)$ is the rotation angle of the cross-section with respect to the z-direction and $w(x)$ is the z component of the displacements along the axis x. Note that the Timoshenko kinematics allow the boundary conditions to be only defined on the beam's cross-section at the two ends keeping the 1D character of the solution. It is beyond the scope of this work to solve analytically the true 3D problem. The important question is whether such approach is justified and this question is addressed by comparing the predictions of the present model with the 2D finite element results, which suffice for the case of beams (see Fig. 8).

Using the geometric relations (Eqs. (1)), the non-zero axial and shear strains are equal to:

$$\begin{aligned} \varepsilon_{xx} &= \frac{\partial u_x}{\partial x} = z\frac{d\psi}{dx} \\ \gamma_{xz} &= 2\varepsilon_{xz} = \frac{\partial u_x}{\partial z} + \frac{\partial u_z}{\partial x} = \frac{dw}{dx} + \psi \end{aligned} \tag{2}$$

The material is a homogeneous, linear elastic material and thus the non-zero Cauchy stresses are equal to:

$$\bar{\sigma}_{xx} = E\varepsilon_{xx} \tag{3a}$$

$$\bar{\sigma}_{xz} = kG\gamma_{xz} \tag{3b}$$

where k is a correction[30] factor which depends on the shape of the beam's cross-section, ν is the Poisson's ratio introduced to account for the non-uniformity of the shear strain over the beam's cross-section, E is the Young's modulus of elasticity and G the shear modulus which for an isotropic material is $G = E/2(1+\nu)$. Note that Eq. (3a) is based on the assumption that the Poisson's ratio ν is

Institutional Repository - Library & Information Centre - University of Thessaly
15/10/2023 05:52:39 EEST - 167.114.118.212

zero. Equation (3a) can be modified to account for the effect of isotropic Poisson's ratio, as in Ma et al.[27], if $E^* = \frac{1-\nu}{(1+\nu)(1-2\nu)}E$ is used instead of E. The simplified form of Eq. (3a) will be kept but throughout the manuscript the numerical results are derived using E^*.

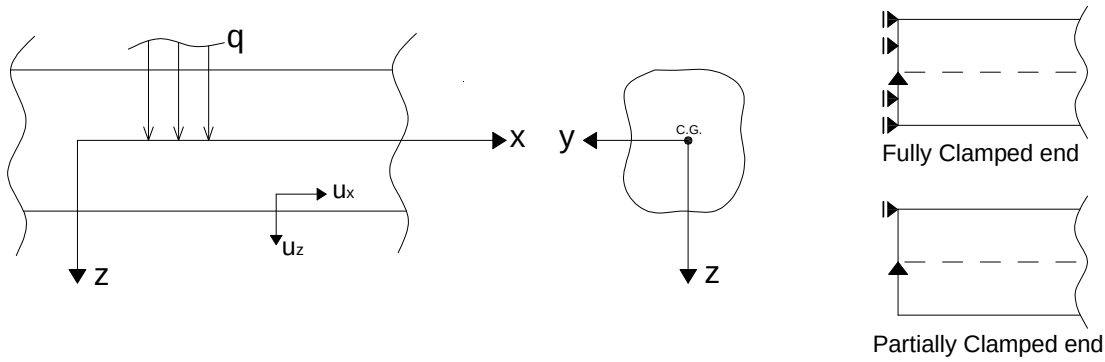

(a) **(b)**

Fig. 1. (a) Beam configuration and coordinate system (C.G. = center of gravity), (b) Clamped-end configurations.

The employed strain gradient theory is a simplification of Mindlin's[1] form II gradient theory, using just one material length scale parameter. In this case, the non-zero total axial and shear stresses can be expressed with respect to the Cauchy stresses, as:

$$\begin{aligned} \sigma_{xx} &= (1-g^2\nabla^2)\bar{\sigma}_{xx} \\ \sigma_{xz} &= (1-g^2\nabla^2)\bar{\sigma}_{xz} \end{aligned} \tag{4}$$

where g is the strain gradient material length, the over-bar quantities are the Cauchy stresses (see Eqs. (3)) and $\nabla^2 = \partial^2/\partial x^2 + \partial^2/\partial z^2$ is the Laplace operator.

The total internal elastic strain energy for the beam is:

$$U_{tot} = U_{cl} + U_{gr} \tag{5}$$

where U_{cl} is the internal elastic strain energy of a classical beam given by:

$$U_{cl} = \frac{1}{2}\iiint_V \left(\bar{\sigma}_{xx}\varepsilon_{xx} + 2\bar{\sigma}_{xz}\,\varepsilon_{xz} \right) dxdydz \tag{6}$$

and U_{gr} is the internal elastic strain energy of a purely gradient beam given by:

$$U_{gr} = \frac{1}{2}g^2 \iiint_V \left(\frac{\partial\bar{\sigma}_{xx}}{\partial x}\frac{\partial\varepsilon_{xx}}{\partial x} + 2\frac{\partial\bar{\sigma}_{xz}}{\partial x}\frac{\partial\varepsilon_{xz}}{\partial x} + \frac{\partial\bar{\sigma}_{xx}}{\partial z}\frac{\partial\varepsilon_{xx}}{\partial z} \right) dxdydz \tag{7}$$

Institutional Repository - Library & Information Centre - University of Thessaly
15/10/2023 05:52:39 EEST - 167.114.118.212

The variation of the total elastic strain energy for a beam of length L is:

$$\delta U_{tot} = \int_0^L \left\{ \begin{array}{l} \delta\psi\left(-EI\left(1-g^2\frac{d^2}{dx^2}\right)\frac{d^2\psi}{dx^2} + kAG\left(1-g^2\frac{d^2}{dx^2}\right)\left(\frac{dw}{dx}+\psi\right) - EAg^2\frac{d^2\psi}{dx^2}\right) \\ +\delta w\left(-kAG\left(1-g^2\frac{d^2}{dx^2}\right)\left(\frac{d^2w}{dx^2}+\frac{d\psi}{dx}\right)\right) \end{array} \right\} dx$$
$$+\left[\delta\psi\left(EI\left(1-g^2\frac{d^2}{dx^2}\right)\frac{d\psi}{dx} + kAGg^2\left(\frac{d^2w}{dx^2}+\frac{d\psi}{dx}\right) + EAg^2\frac{d\psi}{dx}\right)\right]_0^L$$
$$+\left[\delta w\left(kAG\left(1-g^2\frac{d^2}{dx^2}\right)\left(\frac{dw}{dx}+\psi\right)\right)\right]_0^L \tag{8}$$
$$+\left[\delta\psi'\left(g^2EI\frac{d^2\psi}{dx^2}\right)\right]_0^L$$
$$+\left[\delta w'\left(kAGg^2\left(\frac{d^2w}{dx^2}+\frac{d\psi}{dx}\right)\right)\right]_0^L$$

where δ indicates variation, $I = \iint z^2 dydz$ is the moment of inertia about the z-axis and $A = \iint dydz$ is the cross-sectional area. Eq. (8) is obtained from Eq. (5), using Eqs. (6) and (7) by expressing all quantities in terms of the independent kinematic variables w, ψ, w' and ψ' and applying integration by parts. Note that classical analysis uses only w and ψ as independent kinematic variables.

The variation of the work δW done by the distributed forces, $q(x)$, the classical and non-classical boundary shear forces Q and Y, respectively, and the classical and non-classical bending moments M and m, respectively, is:

$$\delta W = \int_0^L q\delta w dx + [Q\delta w]_0^L + [M\delta\psi]_0^L + [Y\delta w']_0^L + [m\delta\psi']_0^L \tag{9}$$

while the principle of minimum potential energy states that,

$$\delta(U_{tot} - W) = 0 \tag{10}$$

It is recalled that in classical elasticity, the bending moment $\overline{M}$ and shear forces $\overline{Q}$ are equal to:

$$\begin{aligned} \overline{M} &= \iint_A \overline{\sigma}_{xx} z dA = EI\frac{d\psi}{dx} \\ \overline{Q} &= \iint_A \overline{\sigma}_{xz} dA = kAG\left(\frac{dw}{dx}+\psi\right) \end{aligned} \tag{11}$$

Institutional Repository - Library & Information Centre - University of Thessaly
15/10/2023 05:52:39 EEST - 167.114.118.212

Substituting Eqs (8) and (9) into Eq. (10) and using Eqs. (11), the following governing equations (see Eqs. 12) and boundary conditions (see Eqs. 13) are derived for the gradient Timoshenko beam:

$$\left(1+\frac{A}{I}g^2-g^2\frac{d^2}{dx^2}\right)\frac{d\overline{M}}{dx}=\left(1-g^2\frac{d^2}{dx^2}\right)\overline{Q} \tag{12a}$$

$$\left(1-g^2\frac{d^2}{dx^2}\right)\frac{d\overline{Q}}{dx}=-q \tag{12b}$$

$$\left[\left\{Q-\left(\left(1-g^2\frac{d^2}{dx^2}\right)\overline{Q}\right)\right\}\delta w\right]_0^L=0 \tag{13a}$$

$$\left[\left\{Y-\left(g^2\frac{d\overline{Q}}{dx}\right)\right\}\delta w'\right]_0^L=0 \tag{13b}$$

$$\left[\left\{M-\left(\left(1-g^2\frac{d^2}{dx^2}\right)\overline{M}+\frac{A}{I}g^2\overline{M}+g^2\frac{d\overline{Q}}{dx}\right)\right\}\delta\psi\right]_0^L=0 \tag{13c}$$

$$\left[\left\{m-\left(g^2\frac{d\overline{M}}{dx}\right)\right\}\delta\psi'\right]_0^L=0 \tag{13d}$$

Note that all the above relations reduce to the classical Timoshenko beam expressions in the absence of gradient, i.e. $g=0$. Also note that the coefficient A/I in Eqs. (12a) and (13c) stems directly from the cross-term $(\partial\bar{\sigma}_{xx}/\partial z)(\partial\varepsilon_{xx}/\partial z)$ in the expression of the strain gradient elastic energy (Eq. (7)). Considering only the leading gradient shear term, i.e. $(\partial\bar{\sigma}_{xz}/\partial x)(\partial\varepsilon_{xz}/\partial x)$, will not capture this additional scaling effect for shear. Therefore, for a complete gradient Timoshenko beam solution both terms must be considered.

The boundary conditions (Eqs. (13)) are mutually exclusive. This means that one can prescribe the following:

either $\quad Q = (1-g^2\frac{d^2}{dx^2})\ \overline{Q} \quad$ or $\quad w$ (14a)

Institutional Repository - Library & Information Centre - University of Thessaly
15/10/2023 05:52:39 EEST - 167.114.118.212

$$Y = g^2 \frac{d\overline{Q}}{dx} \quad \text{or} \quad w' \tag{14b}$$

$$M = 1 \quad g^2 \frac{d^2}{dx^2} \overline{M} + \frac{A}{I} g^2 \overline{M} + g^2 \frac{d\overline{Q}}{dx} \quad \text{or} \quad \psi \tag{14c}$$

$$m = g^2 \frac{d\overline{M}}{dx} \quad \text{or} \quad \psi' \tag{14d}$$

The end conditions and continuity requirements that stem from the boundary conditions (Eqs. 14a-d) for a gradient Timoshenko beam are summarized in Table 1. This table is of utmost importance for solving beam systems with various end conditions and connectivity, both statically determinate and indeterminate. The issue of the appropriateness of the non-classical boundary conditions recommended in Table 1 is discussed in Section III.3 where the finite element solution of a cantilever beam is considered (see comments made regarding Fig. 8). The physical implication for $\psi' = 0$ is that a fully-clamped condition is accounted for, i.e. preventing deformation in all directions at the clamped end. This brings into consideration the actual implementation of "clamping''. For example, it is true that $\psi' \neq 0$ for a partially clamped end support, as shown in Fig. 1(b).

Table 1. Beam boundary conditions and continuity requirements for the gradient Timoshenko beam.

End Condition	**Boundary Conditions**		**Continuity Requirements**
	Classical	**Non-Classical**	
End Hinge	$w=0,\ M=0$	$Y=0,\ m=0$	-
Clamped End	$w=0,\ \psi=0$	$w'=0,\ \psi'=0$	-
Free End	$Q=0,\ M=0$	$Y=0,\ m=0$	-
Internal Hinge	$M=0$	$m=0$	$w^+=w^-,\ w'^+=w'^-,\ w''^+=w''^-,\ \psi^+=\psi^-$
Internal Roller	$w=0$	-	$\psi^+=\psi^-, \psi'^+=\psi'^-, \psi''^+=\psi''^-, w'^+=w'^-,$ $w''^+=w''^-,\ w'''^+=w'''^-$

Note: In the case of concentrated moments or forces, the BC's should be modified accordingly. This also applies to the case of intermediate supports such as springs.

To illustrate the details of the general solution, Eqs. (11) are substituted back into Eqs. (12) to obtain the two differential equations for the $w(x)$ and $\psi(x)$ functions describing the solution. The differential equations are:

$$EI\left(1+\frac{A}{I}g^2 - g^2\frac{d^2}{dx^2}\right)\frac{d^2\psi}{dx^2} = kAG\left(1-g^2\frac{d^2}{dx^2}\right)\left(\frac{dw}{dx}+\psi\right) \tag{15a}$$

and $$kAG\left(1-g^2\frac{d^2}{dx^2}\right)\left(\frac{d^2w}{dx^2}+\frac{d\psi}{dx}\right) = -q \tag{15b}$$

Institutional Repository - Library & Information Centre - University of Thessaly
15/10/2023 05:52:39 EEST - 167.114.118.212

In order to solve the 4th-order differential equations, it is convenient to set:

$$\Omega(x) = \frac{dw}{dx} + \psi \tag{16}$$

So, Eqs. (15) become:

$$\left(1 - \ell^2 \frac{d^2}{dx^2}\right)\frac{d^2\psi}{dx^2} = \frac{kAG}{EI}\left(\frac{\ell}{g}\right)^2\left(1 - g^2 \frac{d^2}{dx^2}\right)\Omega \tag{17a}$$

$$\left(1 - g^2 \frac{d^2}{dx^2}\right)\frac{d\Omega}{dx} = -\frac{q}{kAG} \tag{17b}$$

where ℓ is a length, which can be seen as the shear gradient internal length equal to:

$$\ell = g\sqrt{\frac{1}{1 + (A/I)g^2}} \tag{18}$$

Note that when $g = 0$, then $\ell = 0$ and $\ell / g = 1$. Also, if $(A/I)g^2 << 1$, then $\ell = g$ and $\ell / g = 1$. Therefore, for all cases it is true that $0 < \ell / g \le 1$.

For a constant q, Eq. (17b) has a general solution of the form:

$$\Omega(x) = -\frac{q}{kAG}x + c_1 e^{x/g} - c_2 e^{-x/g} + c_3 \tag{19}$$

Substituting Eq. (19) into Eq. (17a), the general solution is obtained for ψ:

$$\psi(x) = -\frac{q}{6EI}\left(\frac{\ell}{g}\right)^2 x^3 + \frac{kAG}{2EI}\left(\frac{\ell}{g}\right)^2 c_3 x^2 + d_1 \ell^2 e^{x/\ell} + d_2 \ell^2 e^{-x/\ell} + d_3 + d_4 x \tag{20}$$

Also, substituting Eq. (20) back to Eq. (16), the general solution is obtained for w:

$$w(x) = \left\{\begin{array}{l} (c_3 - d_3)x - \frac{d_4}{2}x^2 + c_4 + d_2 \ell^3 e^{-x/\ell} - d_1 \ell^3 e^{x/\ell} + c_1 g^2 e^{x/g} + c_2 g^2 e^{-x/g} \\ + \frac{q}{24EI}\left(\frac{\ell}{g}\right)^2 x^4 - \frac{q}{2kAG}x^2 - \frac{c_3 kAG}{6EI}\left(\frac{\ell}{g}\right)^2 x^3 \end{array}\right\} \tag{21}$$

Equations (20) and (21) contain a total of 8 constants, c_i and d_i $(i = 1...4)$. These constants can be obtained from the 4 boundary conditions, which allow for 8 independent boundary conditions (Eqs. 14a to 14d).

It is interesting to examine the physical implication of the shear gradient length, ℓ, since is a function of the cross-sectional shape and the internal length, g. The shear gradient length, for a rectangular and a circular cross-section, respectively, is:

Institutional Repository - Library & Information Centre - University of Thessaly
15/10/2023 05:52:39 EEST - 167.114.118.212

$$\frac{\ell_{\text{rect}}}{g} = \sqrt{\frac{1}{1+12\left(\frac{g}{h}\right)^2}}, \quad \text{and} \quad \frac{\ell_{\text{circ}}}{g} = \sqrt{\frac{1}{1+16\left(\frac{g}{D}\right)^2}} \tag{22}$$

where D is the diameter of the circular cross-section and h is the height of the rectangular cross-section.

The normalized internal length parameter, ℓ / g, is plotted vs. the ratio g/h and g/D for the case of rectangular and circular cross-section, respectively, in Fig. 2. It is observed that the shape of cross-section has a minor effect on the normalized internal length.

Also, the ratio $\ell_{\text{circ}} / \ell_{\text{rect}}$ (circular vs. rectangular cross-section) is plotted vs. the ratio h/D in Fig. 3 for different values of the internal length, g. As noted above, as g becomes very small, the ratio $\ell_{\text{circ}} / \ell_{\text{rect}}$ approaches asymptotically the value of one. Therefore, as g becomes very small the influence of the shear gradient length is not greatly affected by the shape of the cross-section. Furthermore, there is an interception point of the curves for different g/h values at $h = 0.86D$, the same for all values of g, for which it is true that $\ell_{\text{circ}} = \ell_{\text{rect}}$. It is noted that when $\ell_{\text{circ}} > \ell_{\text{rect}}$ the circular cross-section is stiffer than the rectangular one and vice versa.

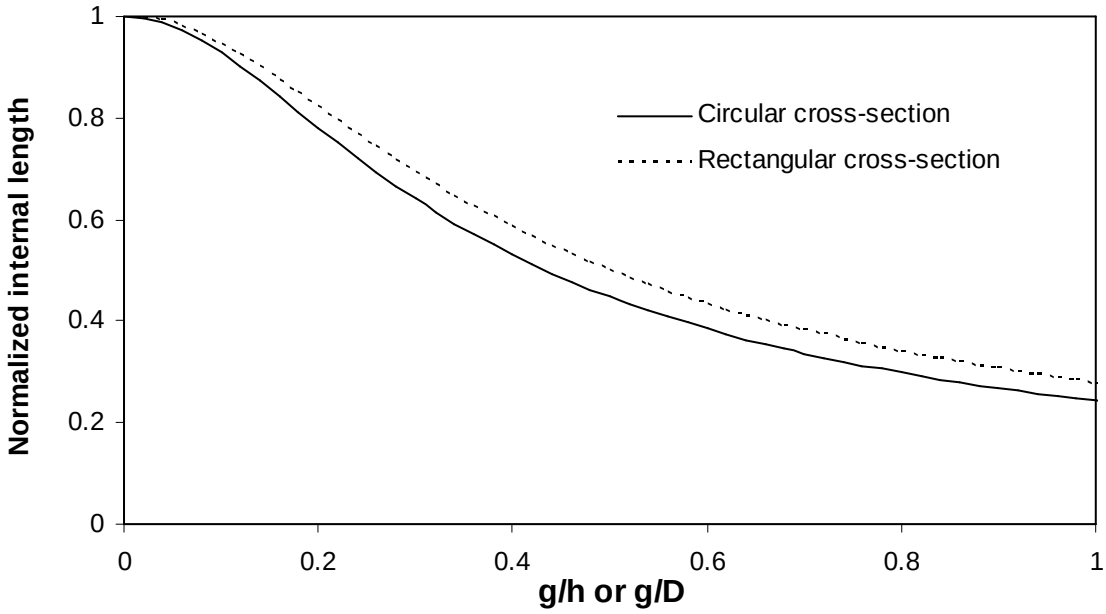

Fig. 2. Influence of g/h or g/D, on the ratio ℓ / g for the case of rectangular and circular cross-section, respectively.

Institutional Repository - Library & Information Centre - University of Thessaly
15/10/2023 05:52:39 EEST - 167.114.118.212

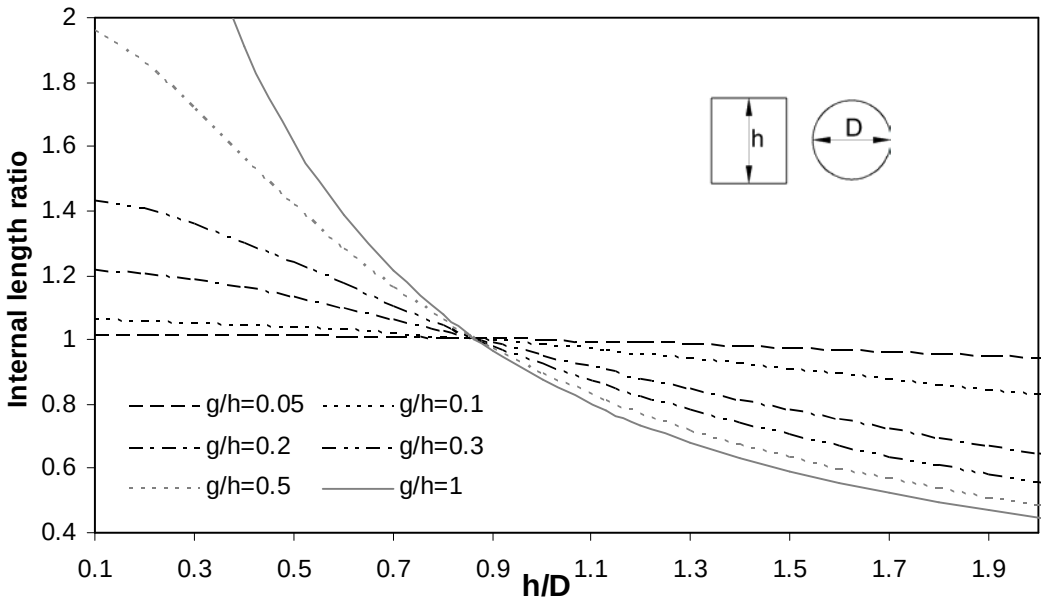

Fig. 3. Internal length ratio of circular vs. rectangular cross-section, $\ell_{circ} / \ell_{rect}$, vs. h/D and the gradient length, g .

3. EXAMPLES

Determinate beam: cantilever with a point load at the free-end

We consider a cantilever beam of length L, loaded by a point load at its free-end, as shown in Fig. 4. The beam has a rectangular cross-section with a width, b, and height, h, and $k = (5\nu + 5)/(6\nu + 6)$ [30].

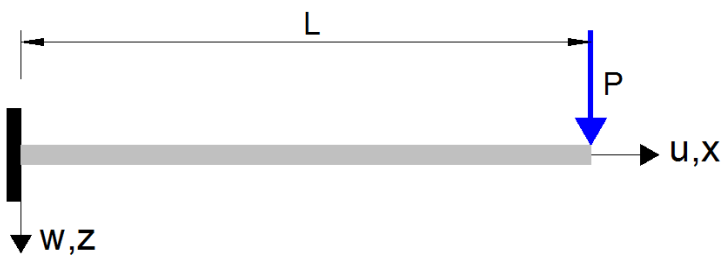

Fig. 4. Clamped beam of length L, loaded by a point load, P, at its free-end.

The classical boundary conditions are:

$$w(0) = 0\,,\ \psi(0) = 0\,,\ Q(L) = P\,,\ M(L) = 0 \tag{23}$$

The non-classical boundary conditions are assumed to be:

$$\left.\frac{dw}{dx}\right|_{x=0} = 0\,,\ \left.\frac{d\psi}{dx}\right|_{x=0} = 0\,,\ m(L) = 0\,,\ Y(L) = 0 \tag{24}$$

Institutional Repository - Library & Information Centre - University of Thessaly
15/10/2023 05:52:39 EEST - 167.114.118.212

The first two non-classical conditions imply that the beam achieves maximum flexural and shear stiffness without enforcing m and Y at the fixed-end. The last two conditions imply that there are no double bending moments and double shear forces at the free-end. The above conditions define a set of 8 linear algebraic equations that can be solved for the 8 unknown coefficients of Eqs. (20) and (21). The coefficients for the case of fixed-end beam loaded by a point load at its free-end are:

$$c_1 = -\frac{P}{kAGg\left(1+e^{2L/g}\right)},\ c_2 = \frac{P}{kAGg}\left(\frac{e^{2L/g}}{1+e^{2L/g}}\right),\ c_3 = \frac{P}{kAG},$$

$$c_4 = \frac{P\left(kAL\ell^4(1+e^{2L/g}) - 2(1+\nu)g^3 I(e^{2L/g}-1)\right)}{kAg^2 EI(1+e^{2L/g})},\ d_1 = -\frac{P\ell(\ell e^{L/\ell} - L)}{EIg^2(1+e^{2L/\ell})}, \tag{25}$$

$$d_2 = -\frac{P\ell e^{L/\ell}(Le^{L/\ell}+\ell)}{EIg^2(1+e^{2L/\ell})},\ d_3 = \frac{P\ell^3(Le^{2L/\ell}+2\ell e^{L/\ell}-L)}{EIg^2(1+e^{2L/\ell})},\ d_4 = -\frac{PL\ell^2}{EIg^2}$$

The deflection at the free end of the gradient Timoshenko beam is:

$$w_{gr}(x=L) = \frac{PL^3}{3EI}\left(\frac{\ell}{g}\right)^2 \begin{pmatrix} 1+3\left(\frac{\ell}{L}\right)\frac{1-e^{2L/\ell}}{1+e^{2L/\ell}} \\ +3\left(\frac{\ell}{L}\right)^2 \frac{1+e^{2L/\ell}-4e^{L/\ell}}{1+e^{2L/\ell}} \\ +3\left(\frac{\ell}{L}\right)^3 \frac{e^{2L/\ell}-1}{e^{2L/\ell}+1} \end{pmatrix} + \frac{PL}{kAG}\left(1+\left(\frac{g}{L}\right)\frac{1-e^{2L/g}}{1+e^{2L/g}}\right) = w_{gr}^b + w_{gr}^s \tag{26}$$

where w_{gr}^b is the flexural part and w_{gr}^s the shear part of the deflection.

Note that Eq. (26) predicts the classical Timoshenko beam elasticity solution (including the influence of shear) in the limit that $g \to 0$ ($\ell/g \to 1$):

$$w_{cl} = w(x=L, g=0) = \frac{PL^3}{3EI} + \frac{PL}{kAG} = w_{cl}^b + w_{cl}^s \tag{27}$$

where w_{cl}^b is the flexural part and w_{cl}^s the shear part of the deflection. Note that as $G \to \infty$, then $w_{cl} = w_{cl}^b$ and $w_{gr} = w_{gr}^b$, which is similar to the Bernoulli-Euler solution.

The deflection at the free end of the beam predicted by the gradient Bernoulli-Euler solution (see Eq. (9) in Giannakopoulos and Stamoulis[23]) is:

$$w_{gr_BE}(x=L) = \frac{PL^3}{3EI}\begin{pmatrix} 1-3\left(\frac{g}{L}\right)^2\left(\cosh\left(\frac{L}{g}\right)+\frac{1}{\cosh(L/g)}+\left(\frac{L}{g}\right)\tanh\left(\frac{L}{g}\right)-1\right) \\ +3\left(\frac{g}{L}\right)^3\left(\tanh\left(\frac{L}{g}\right)+\left(\frac{L}{g}\right)\sinh\left(\frac{L}{g}\right)\tanh\left(\frac{L}{g}\right)\right) \end{pmatrix} = w_{gr_BE}^b \tag{28}$$

Institutional Repository - Library & Information Centre - University of Thessaly
15/10/2023 05:52:39 EEST - 167.114.118.212

The normalized flexural deflection, w_{gr}^{b} / w_{cl}^{b}, is plotted in Fig. 5 against the normalized parameter, g/L, for both the Timoshenko and Bernoulli-Euler gradient solutions assuming that $g = \ell$. This is true when $g/h << 0.3$ (see Eq. 18). The two solutions then become identical and yield the same prediction for the beam deflections. Therefore, the Timoshenko solution reduces to the Bernoulli-Euler solution when: (a) $G \to \infty$ and (b) the scaling influence on g through the length ℓ is neglected.

The normalized deflection, w_{gr} / w_{cl}, is plotted in Fig. 6 against the normalized parameter g/h, assuming $L/h = 3$ and $\nu = 0$. As g/h increases, i.e. as the dimensions of the cross-section of geometrically similar beams become smaller, the beam becomes stiffer. Unlike the gradient Bernoulli-Euler solution, which can account only for the influence of g/L on the deflections, the gradient Timoshenko solution is able to capture the additional stiffening effect of the ratio g/h. On the contrary, the Bernoulli-Euler prediction remains the same for the same span but different cross-section. Also, the normalized shear deflection, w_{gr}^{s} / w_{cl}^{s}, is plotted in Fig. 7 against the normalized parameter g/L for $L/h = 3$ and $\nu = 0$. The shear stiffness increases as g/L increases, but the increase in the shear stiffness is less significant than that observed in the flexural part of the deflections.

In order to compare the present model against the results from a 2D finite element model by Giannakopoulos et al.[32], a complete expression for the deflections of the gradient Timoshenko beam is used the finite element results were derived assuming $\nu = 0.26$ and are shown in Fig. 8 (triangle symbols). The present model (gradient Timoshenko beam) matches overall the finite elements results much better than the gradient Bernoulli-Euler solution, as expected. The finite element results support the present choice of boundary conditions, since considering alternative non-classical boundary conditions resulted in a considerable deviation from the finite element results. For quite short beams, the error is of the order of about 40% and comparable to that for the Bernoulli-Euler beam. The error is rooted in the Timoshenko kinematics (see Eq. (1)) which neglect the prismatic surface boundary layers. Taking a Poisson's ratio value of $\nu = 0$ brings the FEM results for a very short beam closer to the Timoshenko approximation.

Institutional Repository - Library & Information Centre - University of Thessaly
15/10/2023 05:52:39 EEST - 167.114.118.212

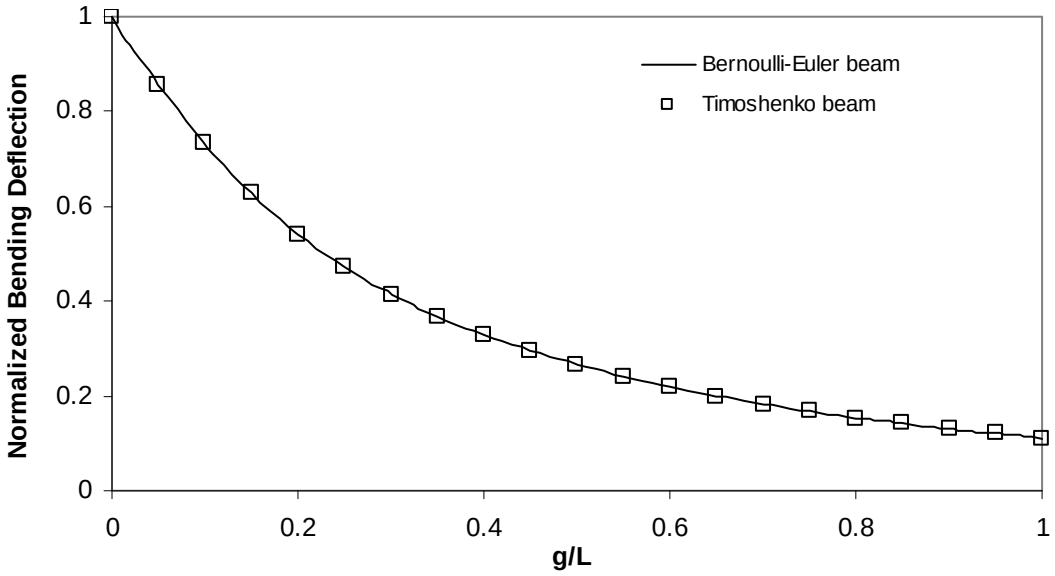

Fig. 5. Influence of g/L on the normalized bending deflection, w_{gr}^{b}/w_{cl}^{b}, at the free-end of a cantilever beam for the gradient Timoshenko and Bernoulli-Euler prediction ($g=\ell$, $\nu=0$).

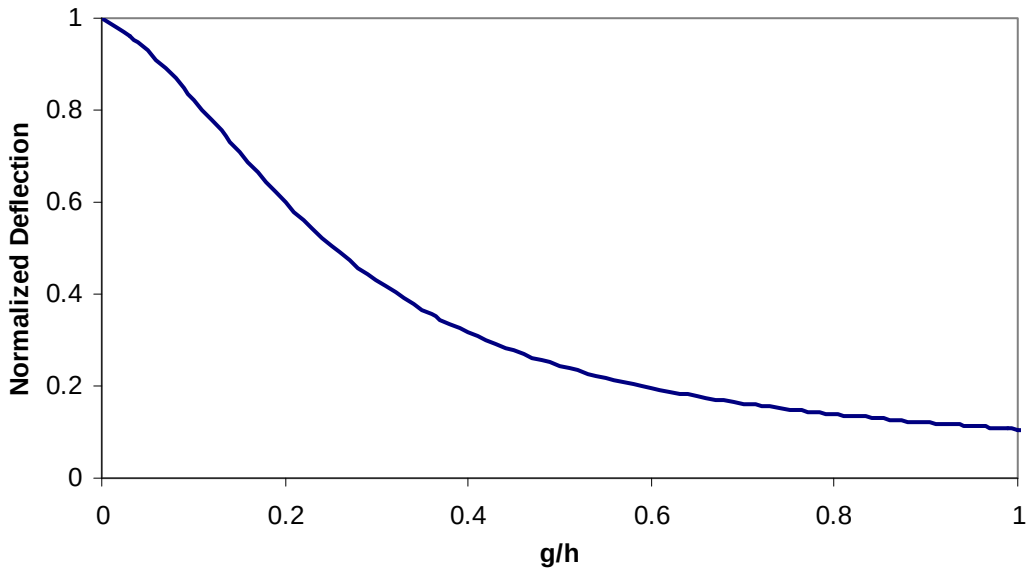

Fig. 6. Influence of g/h on the normalized deflection, w_{gr}/w_{cl}, at the free- end of a cantilever beam with $L/h=3$, $\nu=0$ for the gradient Timoshenko prediction.

Institutional Repository - Library & Information Centre - University of Thessaly
15/10/2023 05:52:39 EEST - 167.114.118.212

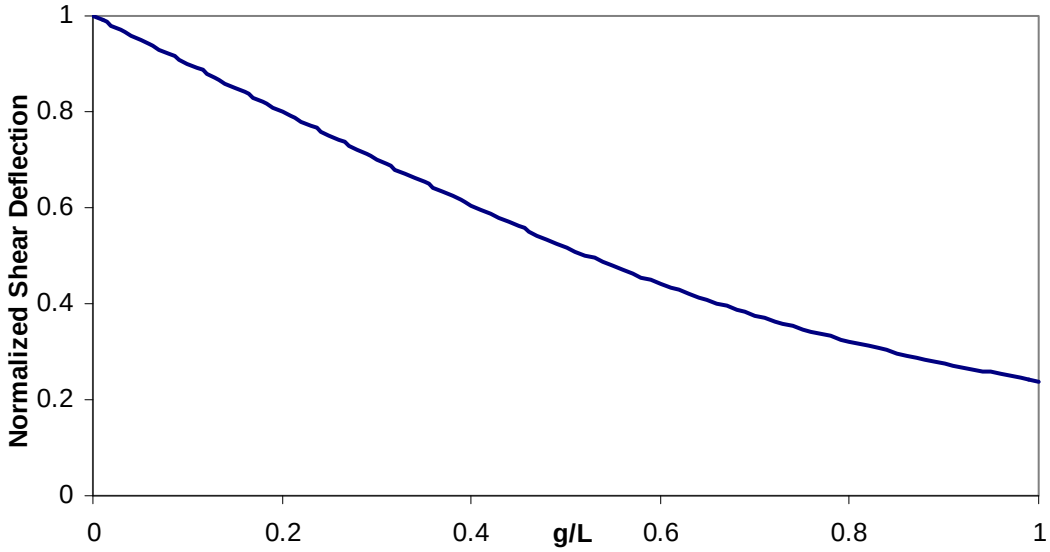

Fig. 7. Influence of g/L on the normalized shear deflection, w^s_{gr}/w^s_{cl}, at the free-end of a cantilever beam with $L/h = 3$, $\nu = 0$ for the gradient Timoshenko predictions.

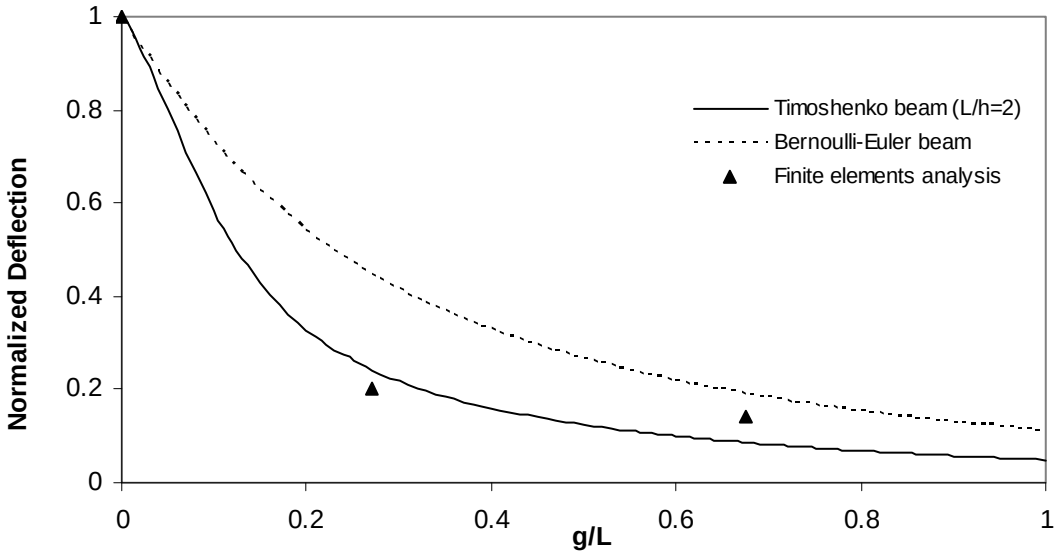

Fig. 8. Comparison of the finite element analysis results (plane-strain, $u_y = 0$) for the 2D gradient model by Giannakopoulos et al.[31] with the gradient Timoshenko ($L/h = 2$, $\nu = 0.26$) and gradient Bernoulli-Euler beam predictions.

Next, the variation of the axial and shear strains along the length of the beam is considered. The axial strain at the extreme fiber of the cross-section, ε_{xx}, is:

Institutional Repository - Library & Information Centre - University of Thessaly
15/10/2023 05:52:39 EEST - 167.114.118.212

$$\varepsilon_{xx}(x)=\varepsilon_0\left(\frac{\ell}{g}\right)^2\left[\begin{array}{l}1-\dfrac{x}{L}-\dfrac{e^{-(x/L)(L/\ell)}\left(e^{2L/\ell}+e^{2(x/L)(L/\ell)}\right)}{1+e^{2L/\ell}}\\ +\left(\dfrac{\ell}{L}\right)\dfrac{e^{(L/\ell)(1-(x/L))}\left(e^{2(x/L)(L/\ell)}-1\right)}{1+e^{2L/\ell}}\end{array}\right] \tag{29}$$

where ε_0 is the maximum strain as predicted by classical Bernoulli-Euler beam analysis and is equal to:

$$\varepsilon_0=\frac{PL}{Ebh^2} \tag{30}$$

The shear strain γ_{xz} is:

$$\gamma_{xz}(x)=\gamma_0\left[1-\frac{e^{(2L/g)-(x/L)(L/g)}+e^{(x/L)(L/g)}}{1+e^{2L/g}}\right] \tag{31}$$

where γ_0 is the shear strain as predicted by classical Timoshenko beam analysis and equal to:

$$\gamma_0=\frac{P}{kAG} \tag{32}$$

The normalized axial strain, $\varepsilon_{xx}/\varepsilon_0$, is plotted vs. the non-dimensional distance x/L in Fig. 9 for the gradient Timoshenko beam for different values of the normalized parameter g/L and $L/h=3$, $\nu=0$ (the diamond symbols correspond to the classical Bernoulli-Euler beam predictions). The solution for small values of g/L approaches asymptotically the classical Bernoulli-Euler prediction ($\varepsilon_{xx}\to\varepsilon_0$). As g/L increases the departure from the classical solution becomes more significant ($\varepsilon_{xx}\to 0$). As observed in the gradient Bernoulli-Euler solution, the maximum strain does not occur at the fixed end of the beam (see Fig. 3 in Giannakopoulos and Stamoulis[23]). However, unlike the gradient Bernoulli-Euler solution, the gradient Timoshenko beam has approximately zero axial strain at the free end, even for large values of g/L. The fact that the maximum strain does not occur at the clamped end of the beam is due to the imposed boundary conditions, $\psi'\big|_{x=0}=0$. Actual measurements of strains on the microcantilever's clamped end, to the best of our knowledge, do not exist in the literature. Such measurements are hard to obtain due to the scale of the problem. A definite answer on whether a boundary layer exists is an issue still to be explored. However, it is interesting to note that recent fatigue tests on microcantilevers with dimensions comparable to the dimensions of the microstructure have shown that the fracture location does not occur at the fixed end[32,33,34] of the cantilever. On the other hand, a fatigue test on

Institutional Repository - Library & Information Centre - University of Thessaly
15/10/2023 05:52:39 EEST - 167.114.118.212

microcantilevers with a fully homogeneous microstructure results in a failure at the fixed end of the beam[19,36].

The normalized shear strain, γ_{xz}/γ_0, is plotted against the non-dimensional distance x/L in Fig. 10 for the gradient Timoshenko cantilever beam for different values of the normalized parameter g/L (diamond symbols correspond to the classical Timoshenko beam predictions). The solution for large g/L values approaches asymptotically the classical Timoshenko beam predictions ($\gamma_{xz} \to \gamma_0$). This is the opposite to what was observed for the normalized axial strains. For very small g/L values shear can be neglected ($\gamma_{xz} \to 0$), but, as it was pointed out above, it does not mean that the gradient Bernoulli-Euler solution is recovered. Furthermore, as g/L increases, shear becomes important, which is true when the slenderness is decreased or when the microstructural average scale is of the same order of magnitude as the dimensions of the beam.

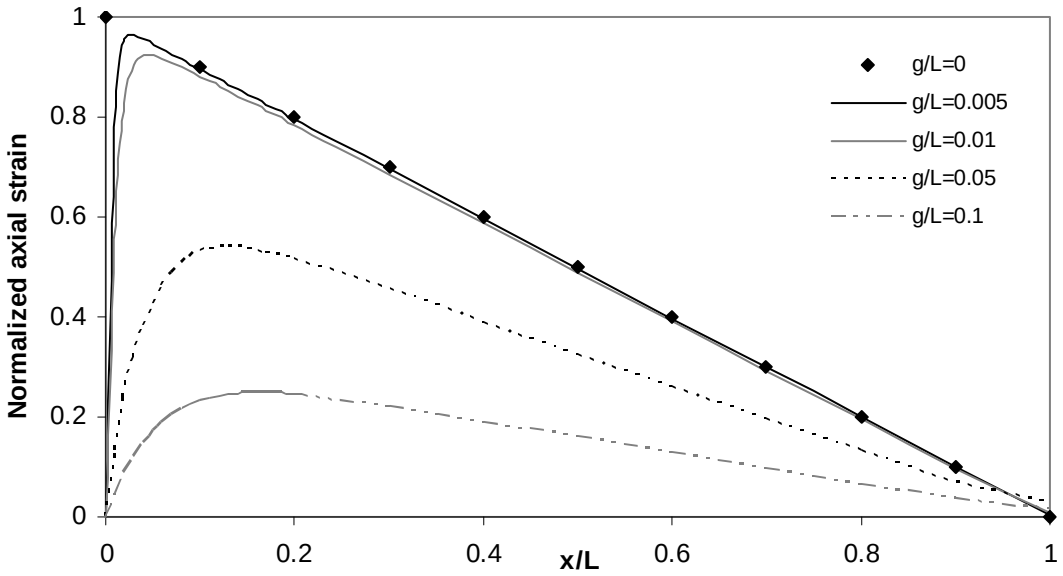

Fig. 9. Influence of the normalized parameter, g/L, on the normalized axial strain, $\varepsilon_{xx}/\varepsilon_0$, along the length of a cantilever beam with $\nu = 0$ and $L/h = 3$.

Institutional Repository - Library & Information Centre - University of Thessaly
15/10/2023 05:52:39 EEST - 167.114.118.212

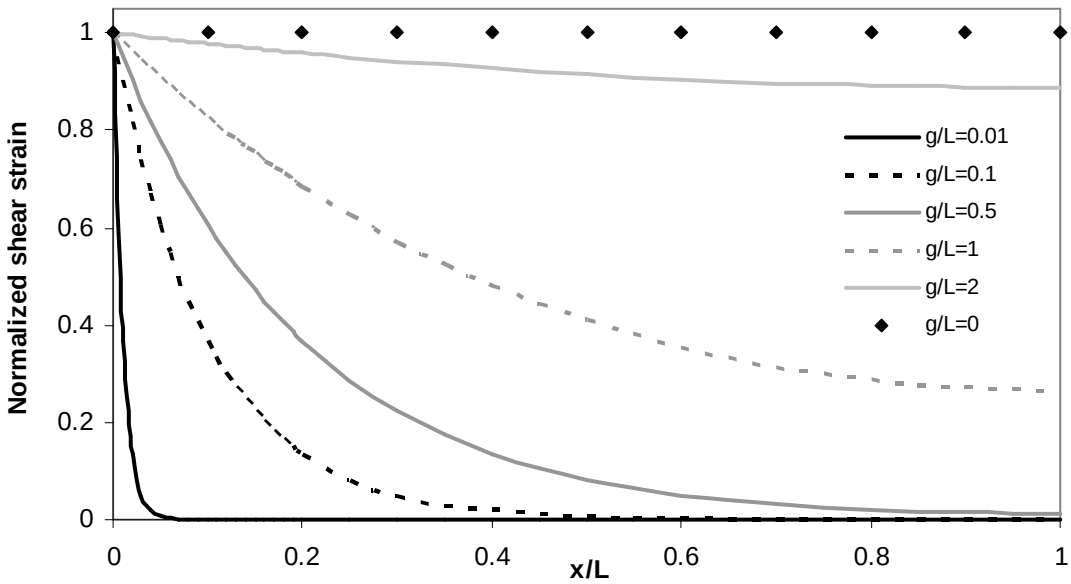

Fig. 10. Influence of the normalized parameter, g/L, on the normalized shear strain, γ_{xz}/γ_0, along the length of a cantilever beam with $\nu = 0$ and $L/h = 3$.

Indeterminate beam: beam with both ends fixed

Little attention has been given to the solution of statically indeterminate structural problems within the framework of gradient elasticity. In order to demonstrate how the gradient Timoshenko beam solution can be applied to such problems, a beam of span L and both ends fixed loaded by a point load P at midspan is considered, as shown in Fig. 11. It is noted that this beam configuration can be found in nanoscale elements (see Salvetat et al.[6]; Ni and Li[36]).

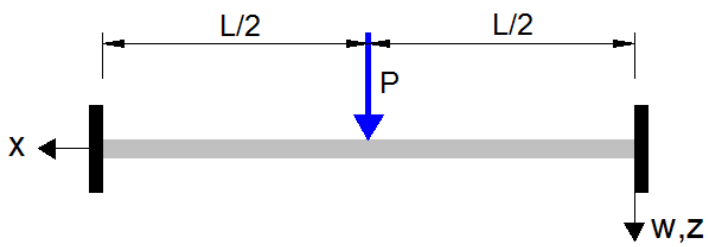

Fig. 11. Beam of span L with both ends clamped loaded by a point load P at midspan.

Making use of the symmetry of the problem, only half of the beam is modeled. The boundary conditions at the fixed end at the left support are:

$$w(0) = 0\,,\ \psi(0) = 0\,,\ \left.\frac{dw}{dx}\right|_{x=0} = 0\,,\ \left.\frac{d\psi}{dx}\right|_{x=0} = 0 \tag{33}$$

Institutional Repository - Library & Information Centre - University of Thessaly
15/10/2023 05:52:39 EEST - 167.114.118.212

The 4 additional conditions in order to define the solution at midspan are:

$$Q(L/2) = -P/2\,,\ \psi(L/2) = 0\,,\ \left.\frac{dw}{dx}\right|_{x=L/2} = 0\,,\ \left.\frac{d\psi}{dx}\right|_{x=L/2} = 0\,, \tag{34}$$

The conditions at midspan imply that the beam is in essence fixed but allowed to deflect vertically. The coefficients for this case are:

$$c_1 = \frac{P}{2kAGg\left(1+e^{L/2g}\right)},\qquad c_2 = \frac{Pe^{L/2g}}{2kAGg(1+e^{L/2g})},\qquad c_3 = \frac{PL}{2kAG},\qquad d_1 = \frac{PL\ell}{8EIg^2(1-e^{L/2\ell})}$$

$$c_4 = \frac{P}{8kAg^2EI(1+e^{L/2g})}\left(8I(1+\nu)g^3 - 8Ie^{L/2g}(1+\nu)g^3 + kAL\ell^4(1+e^{L/2g})\right), \tag{35}$$

$$d_2 = \frac{PL\ell e^{L/2\ell}}{8EIg^2(1-e^{L/2\ell})},\ d_3 = \frac{PL\ell^3(e^{L/2\ell}+1)}{8EIg^2(e^{L/2\ell}-1)},\ d_4 = -\frac{PL\ell^2(L^2+2\ell^2)}{8EIg^2}$$

The plots and details of the solution will not be repeated here as in Section III.1 since all comments and remarks hold true regardless of the loading and support conditions. The prediction for the maximum deflection at midspan will be simply presented as:

$$w_{gr}(x = L/2) = \frac{PL^3}{192EI}\left(\frac{\ell}{g}\right)^2\left(\begin{array}{l}1+12\left(\frac{\ell}{L}\right)\frac{1+e^{L/2\ell}}{1-e^{L/2\ell}}\\ +24\left(\frac{\ell}{L}\right)^2\frac{1+2e^{L/2g}}{1+e^{L/2g}}\end{array}\right) + \frac{PL}{4kAG}\left(1+4\left(\frac{g}{L}\right)\frac{1-e^{L/2g}}{1+e^{L/2g}}\right) \tag{36}$$

In the limit, $g \to 0$, the classical Timoshenko beam solution is recovered:

$$w_{cl} = w(x = L, g = 0) = \frac{PL^3}{192EI} + \frac{PL}{4kAG} \tag{37}$$

If, it is also true that $G \to \infty$, the classical Bernoulli-Euler solution, $PL^3/(192EI)$ is obtained.

4. NON-LOCAL TIMOSHENKO BEAM MODELS

It is interesting to compare our solution with other gradient Timoshenko beam solutions available in the bibliography. Non-local Timoshenko beam models have been proposed by Lam et al.[9], Ma et al.[27], Wang et al.[24], Asghari et al.[28] and Lazopoulos and Lazopoulos[25]. An epoxy beam with material properties, $E = 1.44\,\text{GPa}$, $\nu = 0.38$ and $g = 17.6\,\mu\text{m}$ is considered as an example. The beam's length, width and height are $L = 10h$, $b = 2h$ and $h = 2g$, respectively. The applied load is $P = 50\,\mu\text{N}$. Note that most of the above authors have considered a similar case of a simply supported beam loaded by a point load at midspan. The maximum deflection of the cantilever beam is equal to the maximum deflection of a simply supported beam if we set the applied load and span of the simply supported

Institutional Repository - Library & Information Centre - University of Thessaly
15/10/2023 05:52:39 EEST - 167.114.118.212

beam to be double of those for the cantilever beam (i.e. for the simply supported beam $P = 100\,\mu N$ and $L = 20h$). It is noted that only Lam et al.[9], Asghari et al.[28] and the present work have solved the problem in closed-form. The other works use Fourier series to describe the solution to the problem. The normalized maximum deflection predictions for each model are listed in Table 2.

All models assume the same Timoshenko kinematic assumptions and all can capture the size effect in stiffness. As it can be seen in Table 2, dipolar elasticity models give stiffer response than both the micropolar and couple stress models, as they should. Furthermore, micropolar elasticity models give stiffer response than the couple stress models, as expected.

Two other Timoshenko beam models have been reported by Lazopoulos and Lazopoulos[25] and Wang et al.[24] using the same dipolar strain gradient theory. In particular, Wang et al.[24] used three material lengths (ℓ_0, ℓ_1, ℓ_2) that are taken equal in their numerical examples. Lazopoulos and Lazopoulos[25] have correctly used the principle of minimum potential energy and have come up with 4 boundary conditions (BC), as in the present work. However, instead of enforcing $M = m = 0$ at the hinge supports, they used $\psi = \psi' = 0$ (see the recommendations of Table 1 and Eqs. (25) in Lazopoulos and Lazopoulos[25]).

Although the variational principle allows their choice of these BC's, a hinge support implies absence of bending moment and, in the case of a gradient beam, absence of double bending moment as well, something which is not satisfied by choosing $\psi = \psi' = 0$. In the case of Wang et al.[24], in their minimization principle, the term associated with $\delta w'$, was attributed to the work done by the bending moment M and not by the double shear forces Y, as has been also done in this work. Actually, they do not prescribe at all the double shear force quantity in the expression of the external work done and, by doing so, the term $\delta\psi$ in the strain energy has no equivalent in the expression of the external work (see Eqs. (27) and (30) in Wang et al.[24]). It is believed that since the inclusion of axial stress gradient results in double bending moment, the inclusion of shear gradients should results in double shear forces. Furthermore, double shear forces should be treated as a separate quantity to the classical bending moment, although their dimensions are the same. For this reason, although their formulation requires four (4) BC's, one of them, i.e. the BC steaming from $\delta\psi$ is suppressed (see Eqs. (35) in Wang et al.[24]). Regarding their choice of BC's, they assumed the same BC's with the couple stress model of Ma et al.[24], but this is possible for the particular choice of the Fourier series expansion for w and ψ that was assumed in their work.

Institutional Repository - Library & Information Centre - University of Thessaly
15/10/2023 05:52:39 EEST - 167.114.118.212

Next, the three works (present, Lam et al.[9] and Asghari et al.[28]) that solve the problem in closed-form are considered and their predictions in the case of a less slender beam are compared. The same example as before is considered but for a length of $L = 5h$. The w_{cl} / w_{gr} ratio for the three models becomes 4.42, 2.19 and 12.35, respectively. Assuming a slenderness value equal to one-half of the original value didn't affect the Lam et al.[9] predictions since this model accounts only for the influence of the g/h ratio. If g/h is kept the same, any changes in the slenderness of the beam will not affect the Lam's prediction. Both, the present and the Asghari et al.[28] models predict higher flexural stiffness values than the classical model. However, the Asghari et al.[28] model predicts surprisingly high increases in the stiffness values, since it predicts that the stiffness for g/L=0.1 is eight times that for g/L=0.05.

The aforementioned comparisons assumed the same value for the internal length. Clearly, all theories can be forced to give the same stiffness, if the material length is taken appropriately. How appropriate each theory is depends on the material system. Consistency for a theory requires testing independent beam configurations for the same material. To the best of our knowledge such tests do not exist.

Table 2. Maximum prediction values for different non-local Timoshenko beam models for the case of an epoxy beam (internal length is assumed the same in all cases).

Non-local Timoshenko models	w_{cl}/w_{gr}
Dipolar elasticity	
Proposed model	4.12
Lazopoulos and Lazopoulos[25]	3.85
Wang et al.[24]	3.00
Micropolar elasticity	
Lam et al.[9]	2.19
Couple stress elasticity	
Ma et al.[27]	1.58
Asghari et al.[28]	1.59

5. EXPERIMENTAL EVIDENCE ON MICROCANTILEVERS

In this Section, experimental results on microcantilevers available in the bibliography are used in order to explain the size effect observed. Furthermore, the predictions of the present model for the microstructural length are compared with the predictions of micropolar elasticity in order to illustrate another import issue concerning the validity of non-local models.

Micropolar elasticity[9] predicts that the stiffness of a cantilever beam, $K = dP / dw_{gr}$, is:

Institutional Repository - Library & Information Centre - University of Thessaly
15/10/2023 05:52:39 EEST - 167.114.118.212

$$K = K_{cl}\left[1+\left(\frac{\hat{b}_h}{h}\right)^2\right] \tag{38}$$

where K_{cl} is the classical prediction and $\hat{b}_h$ is a length parameter equal to:

$$\hat{b}_h{}^2 = (10.6 - 15.4\nu)\lambda^2 \tag{39}$$

where λ is the micropolar elasticity length, if all the material length scale parameters are assumed to be the same.

McFarland and Colton[12] tested polypropylene (PP, Basel/Montell ProFax 6323) microcantilever beams manufactured by injection molding with two different mold geometries and compared the measured stiffness of the beams. The geometry of the microcantilevers and the experimental to classical model stiffness ratio values, K_{exp}/K_{cl}, are summarized in Table 3. The last two columns of Table 3, list the internal length estimate according to the gradient Timoshenko beam solution and micropolar elasticity, respectively.

Table 3. Geometry and results for polypropylene microcantilever tests by McFarland and Colton[12].

E (GPa)	**ν**	**L** (μm)	**b** (μm)	**h** (μm)	K_{exp}/K_{cl}	**g** [(a)] (μm)	**λ** [(b)] (μm)
3.3	0.3	836	125	29.37	5.075	16.87	24.24
3.1		398	123	15.85	4.347	8.23	11.86

[(a)] strain gradient Timoshenko solution
[(b)] micropolar elasticity solution

Lam et al.[9] tested epoxy polymeric (Bisphenol-A epichlorohydrin resin with 20phr diethylenetriamine hardener) casted microcantilevers of the same slenderness ratio and four different thicknesses. The geometry of the microcantilevers and their stiffness ratios, K_{exp}/K_{cl}, are summarized in Table 4 (Fig. 12 in Lam et al.[9]). The last two columns of Table 4 include the gradient Timoshenko beam and micropolar elasticity internal length estimates. The proposed model predicts an internal length value of 6.73 ±15% μm while the micropolar elasticity a value of 10.61 ±17% μm.

Table 4. Geometry and results for the epoxy polymeric microcantilevers tested by Lam et al.[9]

E (GPa)	**ν**	**h** (μm)	Slenderness **L/h**	K_{exp}/K_{cl}	**g** [(a)] (μm)	**λ** [(b)] (μm)
1.5	0.3	20	10	2.357	6.41	9.53
		38		1.321	5.72	8.80
		75		1.143	7.27	11.60
		115		1.071	7.51	12.53

[(a)] strain gradient Timoshenko solution
[(b)] micropolar elasticity solution

Institutional Repository - Library & Information Centre - University of Thessaly
15/10/2023 05:52:39 EEST - 167.114.118.212

Ding et al.[8] tested LPCVD polysilicon microcantilevers with constant thickness and varying the L/h ratio. Based on these flexure tests they derived an estimate for the modulus of elasticity, E, using classical elasticity. However, in a separate paper[38], the same authors tested the same material in tension and found a different value for the modulus of elasticity. The modulus of elasticity estimate derived by the tension experiments was used in this work to interpret the flexure experiments and it was found that the beams exhibit a stiffer response than that predicted by classical elasticity. The geometry of the microcantilevers and their relative stiffness (K_{exp}/K_{cl}) are summarized in Table 5. The last two columns of Table 5, list the estimates of the internal length obtained from the gradient Timoshenko beam solution and micropolar elasticity, respectively. Our model predicts a value for the internal length of $0.29 \pm 13\%\,\mu m$ while micropolar elasticity predicts a value of $0.42 \pm 14\%\,\mu m$.

Table 5. Geometry and results for the LPCVD polysilicon microcantilevers tested by Ding et al.[8]

E [(c)] (GPa)	**ν**	**L** (μm)	**b** (μm)	**h** (μm)	K_{exp}/K_{cl}	**g** [(a)] (μm)	**λ** [(b)] (μm)
164	0.23	16	50	2.4	1.215	0.278	0.425
		34	40		1.209	0.295	0.413
		31	40		1.154	0.248	0.354
		18	10		1.276	0.324	0.475

[(a)] strain gradient Timoshenko solution
[(b)] micropolar elasticity solution
[(c)] derived from tension experiments (see Ding et al.[37])

Hong et al.[14] tested Cu microcantilevers keeping the same width and varying the L/h ratio. They also used the flexure experiments to derive an estimate for the modulus of elasticity, E, using classical elasticity. Hunag and Spaepen[38] conducted uniaxial tensile experiments on thin Cu films and reported a Young's modulus value. The value based on the uniaxial tests was used in this work and the experimental stiffness reported with the one predicted by classical elasticity were compared. The geometry and the relative stiffness, K_{exp}/K_{cl}, of the microcantilevers are summarized in Table 6. The last two columns of Table 6, list the estimates of the internal length obtained from the gradient Timoshenko beam solution and micropolar elasticity.

Institutional Repository - Library & Information Centre - University of Thessaly
15/10/2023 05:52:39 EEST - 167.114.118.212

Table 6. Geometry and results for the copper (Cu) microcantilevers tested by Hong et al.[14]

E [(c)] (GPa)	**ν**	**L** (μm)	**b** (μm)	**h** (μm)	K_{exp} / K_{cl}	**g** [(a)] (μm)	**λ** [(b)] (μm)
102	0.31	129	50	10.5	1.021	0.361	0.630
		104	50	2.8	1.177	0.351	0.497

[(a)] strain gradient Timoshenko solution
[(b)] micropolar elasticity solution
[(c)] derived from tension experiments (see Huang and Spaepen[38])

Obviously, all non-local theories can predict a microstructural length and the magnitude of this length will vary depending on the theory used. Nevertheless, consistency of a theory requires this prediction to be the same for different geometries but for the same material. Both non-local theories predict an average value with approximately the same error. Furthermore, both theories are able to explain the size effect measured in the experiments, and quantify the departure form the classical elasticity predictions. The main difference is in the magnitude of the internal length predicted by the two theories. The micropolar length is approximately 50% greater than the dipolar length ($\lambda \approx 1.5g$).

As mentioned in the introduction (Section III.1), the microstructural length parameter is associated with the microstructure of the material in an average sense. In other words, the exact physical correlation between the internal length and the dominant feature of a material's microstructure is a topic still wide open. The simplest correlation would be for the internal length to be equal to the size of the dominant feature of the microstructure. From the experimental results presented in this Section, only Ding et al.[8] provide information about the microstructure of the material used in the experiments under flexure (grain size of polysilicon in the order of 0.2 μm). The present model predicts an internal length value of $0.29 \pm 13\%\ \mu m$, whereas micropolar elasticity predicts a value of $0.42 \pm 14\%\ \mu m$. It seems that the proposed model successfully predicts the size effect dependence on the microstructure's scale in this particular case. Concerning the other three experimental works, information concerning the microstructure is not provided by the authors. The predictions of both theories fall within the typical range of values for the microstructure scale for these materials. In the absence of the explicit information for the material used in the experiments, no conclusion can be made on which theory is more accurate.

The correlation between the dominant feature of the microstructure and the internal length may be more complex. For example, size effect has been also observed on ZnO nanobelts with the structures being stiffer as the diameter of the cross-section decreased from 40 nm to 10 nm[36]. Although the ZnO nanobelts are single crystalline (quartzite-structured) and can be seen as

Institutional Repository - Library & Information Centre - University of Thessaly
15/10/2023 05:52:39 EEST - 167.114.118.212

homogeneous materials, their source of size effect is somehow geometric. Essentially, as the scale decreases, the surface-to-volume ratio increases considerably and this results in more atoms being at the surface than in the bulk. When deformation occurs, the surface reconstruction affects the mechanical properties of the nanowire. This was sufficiently explained by molecular dynamics[40] simulations, but can be equivalently explained in the context of gradient elasticity, if an internal length is assumed. Obviously this line of thinking is rather speculative at this point, but as structures are pushed to the limit, surface effects could provide explanation on why materials that are homogeneous in the atomic level will exhibit size effects.

Finally, the difference between the predicted internal length values leads to another important observation regarding the limitation of both theories. Although the formulae allow for any value of the internal length, it is tacitly presupposed that the microstructural length is of the same order or less than the dimensions of the cross-section, otherwise the assumption of a continuum is compromised. In other words, the prediction must satisfy that g/h or λ/h is less than or equal to 1. Son et al.[41] performed cantilever flexure tests on thin films of aluminum and gold with grain size to thickness ratios close to 1 and in some cases greater than 1. In this extreme limit, it is questionable whether isotropic gradient theories are still applicable. Micropolar elasticity reaches this threshold for smaller stiffness rations than the present strain gradient Timoshenko model.

6. CONCLUSIONS

The governing equations and boundary conditions for the proposed model were derived for a strain gradient Timoshenko beam using a simplified (dipolar) strain gradient theory assuming only one additional material length. The problem was solved in closed-form and a methodology was described for solving more complex beam problems, i.e. indeterminate beam configurations. This model reduces to the gradient Bernoulli-Euler solution and to the classical Timoshenko solution, when the necessary simplifications and limits are considered and also is in good agreement with the 2D finite element model. Furthermore, the proposed model was used to interconnect the size effect observed in experiments of microcantilevers, obtaining good results regarding the material length. Finally, the proposed model was compared with the micropolar elasticity model and it was found that both can capture the size effect in a consistent manner, while the proposed model predicts approximately 50% smaller values for the internal length than that predicted by micropolar elasticity.

Institutional Repository - Library & Information Centre - University of Thessaly
15/10/2023 05:52:39 EEST - 167.114.118.212

CHAPTER IV

A GRADIENT ELASTO-DAMAGE MODEL FOR SEMI-BRITTLE MATERIALS WITH EVOLVING INTERNAL LENGTH – BEAMS UNDER 4-POINT BENDING

1. INTRODUCTION

The aim of this work is to present a new approach which is based on a strain gradient damage constitutive law for modeling semi-brittle materials and composites. There are two reasons that justify such an effort. Materials which exhibit strain softening are size sensitive[1] and their inelastic response manifesting itself through microcracking should be described using a non-local model[2]. In other words, a length parameter is necessary not only for modeling any size effect present but also for ensuring that damage is not localized. A strain gradient theory can include such a length parameter and can address these issues in a physically consistent manner. Gradient theories can also address the issue of size effect in elasticity.

Elasticity and inelasticity for the case of softening materials are coupled by the very nature of the problem since damage is defined as a loss of the initial (elastic) stiffness due to material degradation. In this work, a weak type non-local formulation based on strain gradient elasticity is used and damage is seen as a process affecting the gradient internal length.

The first issue addressed is whether the gradient internal length should evolve with damage. A constant internal length is assumed by a number of existing non-local damage theories[3-15] but there is strong evidence that this length is not constant. Geers et al.[16] considered a finite element formulation of a gradient damage model and concluded that an evolving internal length with an upper bound limit is necessary in order to predict a damage zone of a finite width. Pijaudier-Cabot et al.[17] used acoustic emission experimental results and micromechanical arguments to justify that the internal length increases with damage starting from an initial value. Aggelis and Shiotani[18,19] considering Rayleigh wave propagation in cementitious materials with thin inclusions simulating prescribed levels of damage, found increasingly stronger dispersion of the Rayleigh waves with increasing damage. This, in the context of a gradient elastic damage model, can be explained by assuming an internal length increasing with damage[20]. Li[21] and Li et al.[22] arrived at the same conclusion by using a homogenization procedure in order to derive a strain gradient constitutive law for the case of linear-elastic materials with microcracks. In the present work, a thermodynamic formulation is employed to confirm this. However, it has been shown that, based on

Institutional Repository - Library & Information Centre - University of Thessaly
15/10/2023 05:52:39 EEST - 167.114.118.212

thermodynamics[23] and experimental evidence on aluminum and nickel micro-breams[24], this length should decrease with accumulated plastic strain. This is due to the inherent differences in the physics of gradient plasticity and damage theory (see Fig. 1).

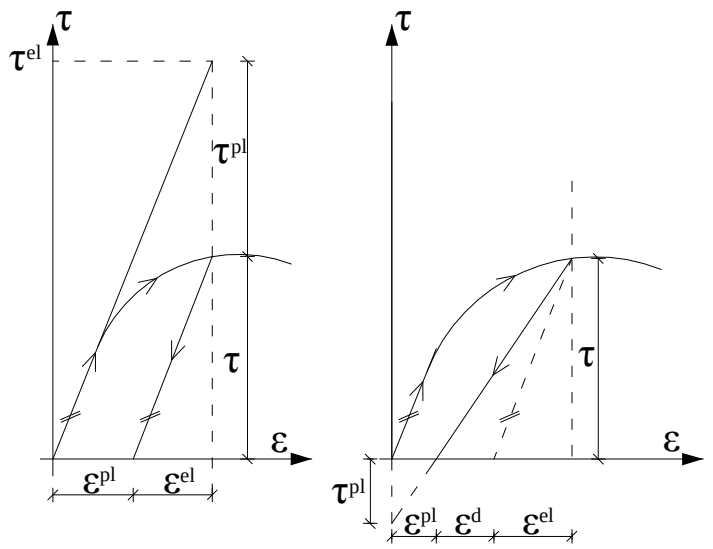

(a) Plasticity **(b)** Damage

Fig.1. Stress-strain diagram illustrating a loading-unloading cycle: (a) plasticity and (b) damage ("el", "pl" and "d" denote elastic, plastic and damage, respectively).

2. THERMODYNAMIC FORMULATION

A thermodynamic formulation of a classical damage model based on the Helmholtz free energy was proposed by Mazars and Pijaudier-Cabot[25], Murakami and Kamiya[26], Wu et al.[27] and many others. However, in the present work, the approach of Ortiz[28] based on Gibbs energy is followed (implying isothermal conditions). Ortiz's model for concrete was extended to include strain gradient effects by employing a simplified model with only one length parameter, g, which is the simplest case of Mindlin's[29] Form II strain gradient elasticity theory.

Gibb's energy density for isothermal process within the framework of strain gradient elasticity in a Cartesian frame (x_k) is:

$$G = \frac{1}{2}\boldsymbol{\tau} : \mathbf{C} : \boldsymbol{\tau} + \frac{1}{2}\boldsymbol{\lambda} \therefore \mathbf{B} : \boldsymbol{\lambda} - A^c \tag{1}$$

where, $\boldsymbol{\tau}$ (τ_{ij}) is the Cauchy stress, $\mathbf{C}$ (C_{ijkl}) the 4th-order elasticity tensor, $\boldsymbol{\lambda}$ (λ_{ijk}) the double-stress taken as $\boldsymbol{\lambda} = g^2 \nabla \boldsymbol{\tau}$ ($\lambda_{kij} = g^2 \partial \tau_{ij} / \partial x_k$), $\mathbf{B}$ the 4th-order tensor taken as $\mathbf{B} = (1/g^2)\mathbf{C}$ and A^c the free

Institutional Repository - Library & Information Centre - University of Thessaly
15/10/2023 05:52:39 EEST - 167.114.118.212

energy density for microcrack formation. The symbols (:) and ($\therefore$) denote the two- and three-index product, respectively, i.e. $(B{:}\lambda)_{ijk} = B_{ijmn}\lambda_{kmn}$, $\boldsymbol{\lambda} \therefore \mathbf{B} : \boldsymbol{\lambda} = \lambda_{ijk}B_{ijmn}\lambda_{kmn}$, $(C{:}\tau)_{ij} = C_{ijkl}\tau_{kl}$, $\boldsymbol{\tau} : \mathbf{C} : \boldsymbol{\tau} = \tau_{ij}C_{ijkl}\tau_{kl}$, and repeated indices imply summation from 1 to 3.

The stress-strain relations corresponding to Gibb's energy density (Eq. (1)) are given by $\boldsymbol{\varepsilon} = \partial G / \partial \boldsymbol{\tau} = \mathbf{C} : \boldsymbol{\tau} = \boldsymbol{\varepsilon}^{\mathbf{e}} + \boldsymbol{\varepsilon}^{\mathbf{i}}$ and $\boldsymbol{\kappa} = \partial G / \partial \boldsymbol{\lambda} = \mathbf{C} : \nabla \boldsymbol{\tau} = \nabla \boldsymbol{\varepsilon} = \nabla(\boldsymbol{\varepsilon}^{\mathbf{e}} + \boldsymbol{\varepsilon}^{\mathbf{i}})$, where $\boldsymbol{\varepsilon}(\varepsilon_{ij})$ is the infinitesimal strain tensor and $\boldsymbol{\kappa} = \nabla\boldsymbol{\varepsilon}(\kappa_{kij} = \partial\varepsilon_{ij}/\partial x_k)$ the strain gradient 3rd-order tensor. Also, the total stress is $\boldsymbol{\sigma} = \boldsymbol{\tau} - \nabla\boldsymbol{\lambda} = \boldsymbol{\tau} - \mathbf{g}^2\nabla^2\boldsymbol{\tau}$. The equilibrium equations and the kinematic boundary conditions originating from the total stress expression can be found in Georgiadis and Grentzelou[30]. The stress-strain time rate relations are given by $\dot{\boldsymbol{\varepsilon}} = \mathbf{C} : \dot{\boldsymbol{\tau}} + \dot{\mathbf{C}} : \boldsymbol{\tau} = \dot{\boldsymbol{\varepsilon}}^{\mathbf{e}} + \dot{\boldsymbol{\varepsilon}}^{\mathbf{i}}$ and $\dot{\boldsymbol{\kappa}} = \nabla\dot{\boldsymbol{\varepsilon}}^{\mathbf{e}} + \nabla\dot{\boldsymbol{\varepsilon}}^{\mathbf{i}} = \dot{\boldsymbol{\kappa}}^{\mathbf{e}} + \dot{\boldsymbol{\kappa}}^{\mathbf{i}}$, where $(\dot{\ }) = \partial / \partial t$ and the superscript "e" and "i" denotes the elastic and inelastic rate of deformation due to degradation of the elastic material properties, respectively.

Microcracking can be physically viewed as added flexibility to the initial flexibility of an uncracked material. Following Ortiz[28], the elastic compliance tensor is taken as a characterization of the state of material damage. Therefore, the elastic compliance can be described by an additive formulation:

$$\mathbf{C} = \mathbf{C}^0 + \mathbf{C}^c \tag{2}$$

where $\mathbf{C}^0$ is the elasticity tensor of the uncracked material initially assumed as isotropic and $\mathbf{C}^c$ is the added flexibility due to microcrack opening under the current applied stress field.

In essence, the inelastic flexibility is the sum of the initial plus the additional flexibility due to the presence of distributed microcracking in the material which is justifiable in terms of the softening and is in line with self-consistent calculations of the overall elastic compliance of elastic media with distributed cracking[29-31]. Hence, the total strain and strain gradient due to cracking can be written as:

$$\begin{aligned} \boldsymbol{\varepsilon} &= (\mathbf{C}^0 + \mathbf{C}^c) : \boldsymbol{\tau} = \boldsymbol{\varepsilon}^0 + \boldsymbol{\varepsilon}^c \\ \boldsymbol{\kappa} &= \nabla\boldsymbol{\varepsilon}^0 + \nabla\boldsymbol{\varepsilon}^c = \boldsymbol{\kappa}^0 + \boldsymbol{\kappa}^c \end{aligned} \tag{3}$$

Opening and closing of microcracks

Cracks in concrete, as well as in other quasi-brittle materials, can develop even under compressive stress conditions. Also, opened cracks can close and not propagate further. The closing of cracks

Institutional Repository - Library & Information Centre - University of Thessaly
15/10/2023 05:52:39 EEST - 167.114.118.212

and the resulting stiffening of the material explains the characteristic S-shaped hysteretic loops that for example are observed experimentally in flexural members subjected to cyclic loading.

In order to mathematically model opening or closed microcracks, the positive and negative orthogonal projections $\mathbf{P}^+$ and $\mathbf{P}^-$ of the strain space onto the positive and negative cones C^+ and C^- are introduced. This operator assigns to every state of strain $\boldsymbol{\varepsilon}$ its point $\mathbf{P}^+\boldsymbol{\varepsilon}$ and $\mathbf{P}^-\boldsymbol{\varepsilon}$ on C^+ and C^-, respectively. If $\varepsilon^{(a)}$ and $d^{(a)}$ ($a = 1,2,3$) denote the eigenvalues and eigenvectors of the total strain $\boldsymbol{\varepsilon}$, respectively, so that: $\varepsilon_{ij} = \sum_{a=1}^{3} \varepsilon^{(a)} d_i^{(a)} d_j^{(a)}$, then, the positive projection of $\boldsymbol{\varepsilon}$ is given by: $(P^+\varepsilon)_{ij} = \varepsilon_{ij}^+ = \sum_{a=1}^{3} \langle \varepsilon^{(a)} \rangle d_i^{(a)} d_j^{(a)}$, where $\langle x \rangle = (x + |x|)/2$ is the Macauley bracket, and the negative projection is $\mathbf{P}^- = \mathbf{I} - \mathbf{P}^+$ ($\mathbf{I}$ =identity tensor).

For a given state of stress $\boldsymbol{\tau}$ consistent with the closing mode of microcracks, the following minimization problem must be satisfied:

$$\text{minimize: } \frac{1}{2}\boldsymbol{\varepsilon} : \left(\mathbf{C}^0 + \overline{\mathbf{C}}^c\right)^{-1} : \boldsymbol{\varepsilon} - \boldsymbol{\tau} : \boldsymbol{\varepsilon} \text{ subject to: } \varepsilon^{c\,(a)} \geq 0 \tag{4}$$

where $\overline{\mathbf{C}}^c$ is the added flexibility due to opening of all microcracks and $\varepsilon^{c\,(a)}$ are the eigenvalues of the inelastic strain, $\boldsymbol{\varepsilon}^c = \boldsymbol{\varepsilon} - \mathbf{C}^0 : \boldsymbol{\tau}$. For a given state of stress gradient $\nabla\boldsymbol{\tau}$, the minimization problem is:

$$\text{minimize: } \frac{1}{2}\nabla\boldsymbol{\varepsilon} \therefore \left(\mathbf{C}^0 + \overline{\mathbf{C}}^c\right)^{-1} : \nabla\boldsymbol{\varepsilon} - \nabla\boldsymbol{\tau} \therefore \nabla\boldsymbol{\varepsilon} \text{ subject to: } \nabla\varepsilon^{c\,(a)} \geq 0 \tag{5}$$

The solution to problems (4) and (5) can be approximated respectively as:

$$\boldsymbol{\varepsilon} \approx \mathbf{C}^0 : \boldsymbol{\tau} + \mathbf{P}^+(\overline{\mathbf{C}}^c : \boldsymbol{\tau}^+) \text{ and } \nabla\boldsymbol{\varepsilon} \approx \mathbf{C}^0 : \nabla\boldsymbol{\tau} + \mathbf{P}^+(\overline{\mathbf{C}}^c : (\nabla\boldsymbol{\tau})^+) \tag{6}$$

where $\tau_{ij}^+ = P^+(\tau_{ij}) = \sum_{a=1}^{3} \langle \tau^{(a)} \rangle q_i^{(a)} q_j^{(a)}$, $\tau^{(a)}$ and $\mathbf{q}^{(a)}$ the eigenvalues and eigenvectors of $\boldsymbol{\tau}$ and $(\nabla\tau)_{ijk}^+ \approx \sum_{a=1}^{3} \left(\partial\langle \tau^{(a)} \rangle / \partial x_i\right)^+ q_j^{(a)} q_k^{(a)}$ (for Eq. (6a) see Ortiz[28]). In order the stress-strain relations are consistent with Eqs. (6), then $\boldsymbol{\varepsilon}^c = \mathbf{C}^c : \boldsymbol{\tau} = \mathbf{P}^+(\overline{\mathbf{C}}^c : \boldsymbol{\tau}^+)$ and $\nabla\boldsymbol{\varepsilon}^c = \mathbf{C}^c : \nabla\boldsymbol{\tau} = \mathbf{P}^+(\overline{\mathbf{C}}^c : (\nabla\boldsymbol{\tau})^+)$ should hold true.

Finally, the added flexibility tensor due to the opening of microcracks can be approximated as:

$$\mathbf{C}^c = \mathbf{P}^+ : \overline{\mathbf{C}}^c : \mathbf{P}^+ \quad (C^c{}_{ijkl} = P^+{}_{ijmn}\, \overline{C}^c{}_{mnpq}\, P^+{}_{pqkl}) \tag{7}$$

Institutional Repository - Library & Information Centre - University of Thessaly
15/10/2023 05:52:39 EEST - 167.114.118.212

Recalling also that $\boldsymbol{\varepsilon}^c = \mathbf{C}^c : \boldsymbol{\tau}$, the positive and negative strain projections based on the positive and negative stress projections can be approximated as $\mathbf{P}^+(\boldsymbol{\varepsilon}^c) = \mathbf{P}^+\left(\overline{\mathbf{C}}^c : \mathbf{P}^+(\boldsymbol{\tau})\right) = \mathbf{P}^+\left(\overline{\mathbf{C}}^c : \boldsymbol{\tau}^+\right)$ and $\mathbf{P}^-(\boldsymbol{\varepsilon}^c) = \mathbf{P}^-\left(\overline{\mathbf{C}}^c : \boldsymbol{\tau}^-\right)$, respectively.

To further illustrate the necessity of the above mathematical manipulations, a microcrack normal to a unit vector $\mathbf{n}$ is considered. Any stress acting upon a planar microcrack can be analyzed in any of the four possible loading configurations depicted in Fig.2. Cases (b) and (d) refer to nonzero positive projections ($\boldsymbol{\tau} = \boldsymbol{\tau}^+$) while cases (a) and (c) to nonzero negative projections ($\boldsymbol{\tau} = \boldsymbol{\tau}^-$). The orientation of the stress in cases (b) and (c) is normal to the crack plane, that is $\mathbf{n} \cdot \boldsymbol{\tau}^+ \cdot \mathbf{n} = 0$ and $\mathbf{n} \cdot \boldsymbol{\tau}^- \cdot \mathbf{n} = 0$, respectively, preventing crack propagation. Therefore, microcrack opening occurs due to a tensile stress in case (d) and a compressive stress in case (a). These two cases correspond to a tensile and a compressive opening mode I_T and I_C, respectively. Thus, the added flexibility tensor due to microcrack opening can be decomposed as $\overline{\mathbf{C}}^c = \overline{\mathbf{C}}^c_{I_T} + \overline{\mathbf{C}}^c_{I_C}$, and the inelastic deformation due to microcracking can be expressed as $\boldsymbol{\varepsilon}^c = \boldsymbol{\varepsilon}^c_{I_T} + \boldsymbol{\varepsilon}^c_{I_C}$. Microcrack opening under mode I_T and I_C implies that: $\boldsymbol{\varepsilon}^c_{I_T} \geq 0$ and $\boldsymbol{\varepsilon}^c_{I_C} \leq 0$, respectively.

Summarizing, the Gibbs energy becomes:

$$G = \begin{cases} \frac{1}{2}\boldsymbol{\tau} : \mathbf{C}^0 : \boldsymbol{\tau} + \frac{1}{2}\boldsymbol{\tau}^+ : \overline{\mathbf{C}}^c_{I_T} : \boldsymbol{\tau}^+ + \frac{1}{2}\boldsymbol{\tau}^- : \overline{\mathbf{C}}^c_{I_C} : \boldsymbol{\tau}^- + \\ \frac{1}{2}g^2 \nabla\boldsymbol{\tau} \therefore \mathbf{C}^0 : \nabla\boldsymbol{\tau} + \frac{1}{2}g^2 (\nabla\boldsymbol{\tau})^+ \therefore \overline{\mathbf{C}}^c_{I_T} : (\nabla\boldsymbol{\tau})^+ - A^c \end{cases} \tag{8}$$

It is true that the stress gradient in Eq. (8) induces only mode I_T crack opening since there are no terms of the type $(\nabla\boldsymbol{\tau})^-$. This is further clarified in Section IV.3.

Institutional Repository - Library & Information Centre - University of Thessaly
15/10/2023 05:52:39 EEST - 167.114.118.212

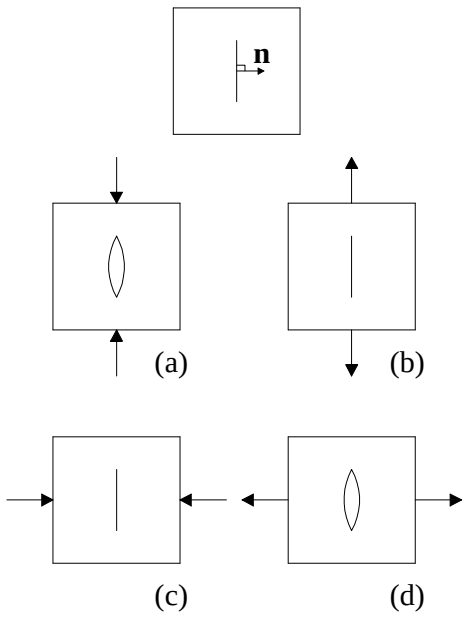

Fig. 2. State of microcracks: (a) and (d) opening mode; (b) and (c) closing mode (Ortiz, 1985).

Damage rules

The evolution of the tensorial damage parameter $\mathbf{C}^c$ (Eq. (2)) can be described based on the evolution of $\overline{\mathbf{C}}^c$ according to a damage rule of the general form $\dot{\overline{\mathbf{C}}}^c = \dot{\overline{\mathbf{C}}}^c_{I_T} + \dot{\overline{\mathbf{C}}}^c_{I_C}$ (Ortiz[28]) with:

$$\dot{\overline{\mathbf{C}}}^c_{I_T} = \dot{\mu}\mathbf{R}_{I_T}(\boldsymbol{\tau}) \text{ and } \dot{\overline{\mathbf{C}}}^c_{I_C} = \dot{\mu}\mathbf{R}_{I_C}(\boldsymbol{\tau}) \tag{9}$$

where $\mathbf{R}_{I_T}(\boldsymbol{\tau})$, $\mathbf{R}_{I_C}(\boldsymbol{\tau})$ are material response functions (4th-order dimensionless tensors) which determine the direction in which damage should occur and μ is an internal scalar parameter (dimensions “area/force”), which may be regarded as a measure of the cumulative damage resulting in a decrease of the unloading elastic modulus. In plasticity theory, the parameter μ resembles the accumulated equivalent plastic strain. A localization analysis for the case of uniaxial tension is included in Section IV.5, where it is shown that the proposed non-local model leads to objective and mesh-independent results if used in a FEM analysis.

Initially, the material is assumed to be uncracked ($\mu = 0$) and initial conditions reign. The proposed damage rules presented include only the Cauchy (local) part of the total stress. The proposed model will be calibrated through experimental strain data and hence the damage rules will be associated with the energetically conjugate quantity of strain, that is the Cauchy part of the total stress. It should be emphasized that this assumption has a physical justification since the damage surface of a quasi-brittle material is established through experimental results of uniaxial tests and in

Institutional Repository - Library & Information Centre - University of Thessaly
15/10/2023 05:52:39 EEST - 167.114.118.212

the case of uniform loading there in no gradient effect. The choice of local stress in Eq. (9) can be further justified from the work of Simone et al.[34] who showed that the use of a non-local dissipation-driving state variable (i.e. the total stress or total strain of the gradient formulation) leads to an incorrect failure characterisation in terms of damage initiation and propagation ahead of a macro-crack. In the proposed approach, the inelastic strains are used for the tensorial characterization of damage. A similar approach was used by Bui[35], introducing a mixed (local and non-local) formulation for damage characterization.

The irreversible character of damage necessitates that, $\dot{\mu} \geq 0$. The condition $\dot{\mu} > 0$ refers to active damage mechanisms, while $\dot{\mu} = 0$ refers to elastic behavior. Therefore, $\mathbf{R}_{I_T}(\boldsymbol{\tau})$ and $\mathbf{R}_{I_C}(\boldsymbol{\tau})$ must be positive definite. Furthermore, the internal length of the material, g, is assumed to be a function of the damage level, that is $g = g(\mu)$, and the rate of change of the internal length is, $\dot{g} = \dot{\mu}(dg/d\mu)$.

It should be emphasized that the present work is based on gradient elasticity, while inelasticity (damage) is treated as a process affecting the parameters of gradient elasticity, the internal length and the classical elastic properties[36]. In this thermodynamic formulation there are two internal variables, the damage parameter, μ, and the internal length, g, with a constraint demand for the internal length to be a function of the damage parameter. Based on these assumptions, the energy density dissipation inequality (see Eq. (1)) can be expressed as:

$$d = \frac{1}{2}\boldsymbol{\tau} : \dot{\overline{\mathbf{C}}}^c : \boldsymbol{\tau} + \frac{1}{2} g^2 \nabla\boldsymbol{\tau} \therefore \dot{\overline{\mathbf{C}}}^c : \nabla\boldsymbol{\tau} + \frac{1}{2}\left(\dot{g^2}\right)(\nabla\boldsymbol{\tau})^+ \therefore \overline{\mathbf{C}}^c : (\nabla\boldsymbol{\tau})^+ - \dot{A}^c \geq 0 \tag{10}$$

where d signifies the rate of energy dissipation density.

Substituting Eqs.(9) in Eq. (10), the rate of energy dissipation becomes:

$$d = \begin{pmatrix} \frac{1}{2}\boldsymbol{\tau}^+ : \mathbf{R}_{I_T} : \boldsymbol{\tau}^+ + \frac{1}{2}\boldsymbol{\tau}^- : \mathbf{R}_{I_C} : \boldsymbol{\tau}^- + \frac{1}{2} g^2 (\nabla\boldsymbol{\tau})^+ \therefore \mathbf{R}_{I_T} : (\nabla\boldsymbol{\tau})^+ \\ + g\frac{dg}{d\mu}(\nabla\boldsymbol{\tau})^+ \therefore \overline{\mathbf{C}}^c : (\nabla\boldsymbol{\tau})^+ \end{pmatrix} \dot{\mu} - \dot{A}^c \geq 0 \tag{11}$$

The rate of energy dissipation should be positive according to the 2nd law of thermodynamics. Since, $\mathbf{R}_{I_T}$, $\mathbf{R}_{I_C}$, $\mathbf{C}^c_{I_T}$ and $\mathbf{C}^c_{I_C}$ are positive definite and $\dot{\mu} \geq 0$, it follows that

$$dg/d\mu \geq 0 \tag{12}$$

is true. This shows that if the internal length is allowed to evolve with damage, then it must increase or remain constant with increasing damage.

Institutional Repository - Library & Information Centre - University of Thessaly
15/10/2023 05:52:39 EEST - 167.114.118.212

The inelastic free energy density, A^c, associated with microcrack formation is a function of μ. The rate of the free energy coincides with the energy release rate per unit microcrack length. Using a micromechanical model of fracture, as a justification (see Section IV.3 for diluted microcracking), the rate of the inelastic free energy is defined as:

$$\dot{A}^c = \dot{\mu}\frac{dA^c}{d\mu} = \left(\frac{\pi}{2}t(\mu)^2 + \frac{1}{3}\left(\frac{\partial t(\mu)}{\partial \omega}\xi(\mu)\right)^2\right)\dot{\mu} \tag{13}$$

where $t(\mu)$ is a critical stress for damage extension and ω is the direction normal to the critical stress (along the microcrack). Note that $\xi(\mu)$ is half the microcrack length and Eq. (13) requires two tests: a uniaxial test ($\partial t(\mu)/\partial\omega = 0$) to establish $t(\mu)$ and a pure bending test to establish $\partial t(\mu)/\partial\omega$.

Substituting Eq. (13) into Eq. (12), it yields:

$$d = \begin{pmatrix} \frac{1}{2}\boldsymbol{\tau}^+ : \mathbf{R}_{I_T} : \boldsymbol{\tau}^+ + \frac{1}{2}\boldsymbol{\tau}^- : \mathbf{R}_{I_C} : \boldsymbol{\tau}^- - \frac{\pi}{2}t(\mu)^2 + \frac{1}{2}g^2(\nabla\boldsymbol{\tau})^+ \therefore \mathbf{R}_{I_T} : (\nabla\boldsymbol{\tau})^+ \\ + g\frac{dg}{d\mu}(\nabla\boldsymbol{\tau})^+ \therefore \overline{\mathbf{C}}^c : (\nabla\boldsymbol{\tau})^+ - \frac{1}{3}\left(\frac{\partial t(\mu)}{\partial\omega}\xi(\mu)\right)^2 \end{pmatrix}\dot{\mu} \geq 0 \tag{14}$$

Since $\dot{\mu} \geq 0$, Eq. (15) necessitates:

$$\frac{1}{2}\boldsymbol{\tau}^+ : \mathbf{R}_{I_T} : \boldsymbol{\tau}^+ + \frac{1}{2}\boldsymbol{\tau}^- : \mathbf{R}_{I_C} : \boldsymbol{\tau}^- - \frac{\pi}{2}t(\mu)^2 \geq 0\text{, and} \tag{15a}$$

$$\frac{1}{2}g^2(\nabla\boldsymbol{\tau})^+ \therefore \mathbf{R}_{I_T} : (\nabla\boldsymbol{\tau})^+ + g\frac{dg}{d\mu}(\nabla\boldsymbol{\tau})^+ \therefore \overline{\mathbf{C}}^c : (\nabla\boldsymbol{\tau})^+ - \frac{1}{3}\left(\frac{\partial t(\mu)}{\partial\omega}\xi(\mu)\right)^2 \geq 0 \tag{15b}$$

The effects of stress gradient and damage which influence the inelastic response can be treated separately in Eqs. (15a) and (15b). Eq. (15a) corresponds to the case of $g = 0$ and Eq. (15b) addresses the influence of the internal length, g, and consequently of the stress gradient. In the absence of the stress gradient effect in Gibb's energy, Ortiz's model[28] is recovered using Eq. (15a).

Next, a stress function F is defined, in the form:

$$F(\boldsymbol{\tau}) = \frac{1}{2}\boldsymbol{\tau}^+ : \mathbf{R}_{I_T} : \boldsymbol{\tau}^+ + \frac{1}{2}\boldsymbol{\tau}^- : \mathbf{R}_{I_C} : \boldsymbol{\tau}^- = F_{I_T} + F_{I_C} \tag{16}$$

Substituting Eq. (16) into Eq. (15a), a damage function Φ is obtained as:

$$\Phi(\boldsymbol{\tau}, \mu) = F(\boldsymbol{\tau}) - \frac{\pi}{2}t(\mu)^2 \geq 0, \tag{17}$$

and if inequality in Eq. (17) is not satisfied the material behaves elastically. Also, for further damage to occur, the equality must be satisfied in expression (17) (see Fig. 3). Therefore,

Institutional Repository - Library & Information Centre - University of Thessaly
15/10/2023 05:52:39 EEST - 167.114.118.212

$F(\boldsymbol{\tau}) = (\pi/2)t(\mu)^2$ defines the elasto-damage boundary in the local stress space. Thus, the onset of damage is characterized by the criteria:

$$\Phi(\boldsymbol{\tau},\mu) = F(\boldsymbol{\tau}) - \frac{\pi}{2}t(\mu)^2 = 0 \text{ and } (\partial\Phi/\partial\boldsymbol{\tau}):\dot{\boldsymbol{\tau}} = (\partial F/\partial\boldsymbol{\tau}):\dot{\boldsymbol{\tau}} > 0 \tag{18}$$

These relations imply that for further damage the stress point must lie on the current damage surface and the stress increment must point outwards of the elastic domain. A stress point inside the current damage surface will imply gradient elasticity.

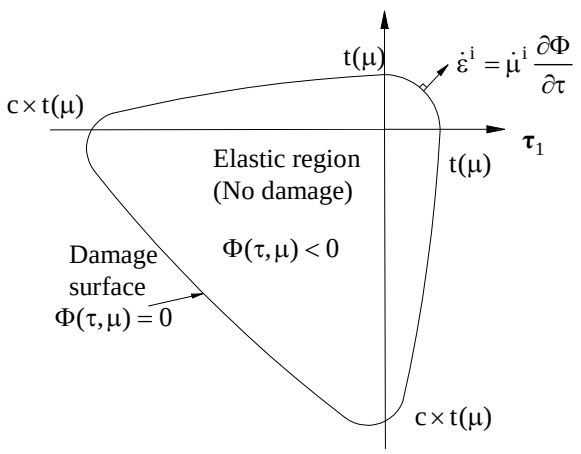

Fig. 3. Damage surface and damage criterion in the local principal stress space.

Associated damage rule

The damage rule is associated, if the following relations hold true for the damage direction tensors:

$$\mathbf{R}_{I_T} = \frac{\partial F_{I_T}}{\partial\boldsymbol{\tau}^+\partial\boldsymbol{\tau}^+} \text{ and } \mathbf{R}_{I_C} = \frac{\partial F_{I_C}}{\partial\boldsymbol{\tau}^-\partial\boldsymbol{\tau}^-} \tag{19}$$

This assumption reduces the calibration to the determination of the scalar functions F rather than the tensorial quantities $\mathbf{R}_{I_T}$ and $\mathbf{R}_{I_C}$. Furthermore, the inelastic strain rate tensor due to damage is:

$$\dot{\boldsymbol{\varepsilon}}^{\mathbf{i}} = \dot{\mathbf{C}}:\boldsymbol{\tau} = \dot{\mathbf{C}}^c:\boldsymbol{\tau} = \left(\mathbf{P}^+:\dot{\overline{\mathbf{C}}}^c:\mathbf{P}^+\right):\boldsymbol{\tau} = \dot{\mu}\left(\mathbf{R}_{I_T}:\boldsymbol{\tau}^+ + \mathbf{R}_{I_C}:\boldsymbol{\tau}^-\right) \quad , \tag{20}$$

which, using Eqs. (19), can be written as:

$$\dot{\boldsymbol{\varepsilon}}^{\mathbf{i}} = \dot{\mu}\left(\frac{\partial\mathbf{F}_{I_T}}{\partial\boldsymbol{\tau}^+} + \frac{\partial\mathbf{F}_{I_C}}{\partial\boldsymbol{\tau}^-}\right) = \dot{\mu}\partial F/\partial\boldsymbol{\tau} = \dot{\mu}\partial\Phi/\partial\boldsymbol{\tau} \tag{21}$$

Eq. (21) implies that the inelastic part of the strain rate tensor points outwards and in a normal direction to the damage surface (see Fig. 3). In the context of a rate independent damage formulation, as suggested by Ortiz (1983), it is true that

Institutional Repository - Library & Information Centre - University of Thessaly
15/10/2023 05:52:39 EEST - 167.114.118.212

$$\mathbf{R}_{I_T} = \frac{\boldsymbol{\tau}^+ \otimes \boldsymbol{\tau}^+}{(\boldsymbol{\tau}^+ : \boldsymbol{\tau}^+)} \text{ and } \mathbf{R}_{I_C} = c\frac{\boldsymbol{\tau}^- \otimes \boldsymbol{\tau}^-}{(\boldsymbol{\tau}^- : \boldsymbol{\tau}^-)} \tag{22}$$

where c_e is the "cross-effect" coefficient governing the level of damage under compression ($c_e = 0$ for no cross-effect), $(\tau \otimes \tau)_{ijkl} = \tau_{ij}\tau_{kl}$ the dyadic product tensor and $(\boldsymbol{\tau} : \boldsymbol{\tau}) = \tau_{ij}\tau_{ij}$ the trace of the $(\boldsymbol{\tau} \otimes \boldsymbol{\tau})$ tensor. The value of the critical stress $t(\mu)$ and the "cross-effect" coefficient, c_e, can be determined from uniaxial test results. Then, the damage surface simplifies to:

$$\Phi = \frac{1}{2}\boldsymbol{\tau}^+ : \boldsymbol{\tau}^+ + \frac{1}{2}c_e\boldsymbol{\tau}^- : \boldsymbol{\tau}^- - \frac{\pi}{2}t^2(\mu) \tag{23}$$

It is worth noting that according to the present approach since the effect of microcracking is directly linked with the elasticity tensor, an initially isotropic material would become anisotropic with damage. In the case of non-associative damage evolution and/or initially anisotropic elastic behavior, as observed in rocks, microcracking may not occur along the principal stress trajectories but localizes along specific weak surfaces in the material[37]. Any existing directionality of microcrack opening, can be included in the response functions $\mathbf{R}_{I_T}$ and $\mathbf{R}_{I_C}$.

3. ENERGY DISSIPATION DURING MICROCRACK EXTENSION

Two 2D isotropic cases are considered, as shown in Fig. 4. Case (a) depicts a microcrack subjected to a uniform tensile stress and case (b) a microcrack under a stress gradient. The model predictions in this study do not assume interaction between the microcracks and elastic anisotropy.

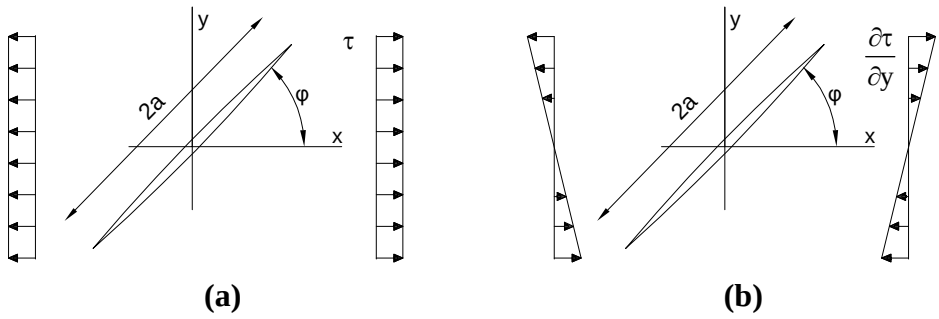

Fig. 4. A crack with a length of 2a under: (a) uniaxial tension and (b) pure bending.

For a crack of length 2a, loaded by a uniform tensile stress, τ, as shown in Fig. 4(a), neglecting mode III the stress intensity factors for modes I and II are[38]: $K_I = \tau\sqrt{\pi a}\sin^2\varphi$ and

Institutional Repository - Library & Information Centre - University of Thessaly
15/10/2023 05:52:39 EEST - 167.114.118.212

$K_{II} = \tau\sqrt{\pi a}\sin\varphi\cos\varphi$, and the energy release rate is: $G = \left(K_I^2 + K_{II}^2\right)/E^*$, where $E^* = E$ for plane stress and $E^* = E/(1-\nu^2)$ for plane strain, E is the elastic modulus and ν the Poisson's ratio.

The crack can occur at an arbitrary angle value φ assuming the same probability of occurrence at all possible angle values. Therefore, the 2D average energy release rate per unit microcrack length extension, is

$$\left\langle \frac{dG}{da} \right\rangle = \frac{\pi\tau^2}{E^*}\frac{1}{\pi}\int_{-\pi/2}^{\pi/2}\sin^2(\varphi)d\varphi = \frac{\pi\tau^2}{2E^*} \tag{24}$$

where $\langle\ \rangle$ denotes the average of the quantity enclosed in the brackets.

For a crack of length 2a, under pure bending, as shown in Fig. 4(b), the stress intensity factors for mode I and II is[39] $K_I = (d\tau/dy)(2a/3)^{3/2}\sin^3(\varphi)$ and $K_{II} = (d\tau/dy)(2a/3)^{3/2}\sin^2(\varphi)\cos(\varphi)$, respectively. The average 2D energy release rate per unit microcrack length, a, for all possible angles, is:

$$\left\langle \frac{dG}{da} \right\rangle = \frac{2}{E^*}\left(\frac{d\tau}{dy}\right)^2\left(\frac{2a}{3}\right)^2\frac{1}{\pi}\int_{-\pi/2}^{\pi/2}\sin^4(\varphi)d\varphi = \frac{1}{3E^*}\left(\frac{d\tau}{dy}a\right)^2 \tag{25}$$

Crack propagation under a non-uniform stress field has been considered by Stallybrass[40] and used by Huang and Detournay[41] to improve the accuracy of crack propagation predictions in quasi-brittle materials subjected to an indentation.

Damage can be introduced in different ways depending on the damage parameter definition. The damage parameter, μ, is associated to the damage parameter D through Eq. (31) and differentiating both parts yields:

$$d(E^*\mu) = \frac{dD}{(1-D)^2} \tag{26}$$

Accounting for the effect of damage on the Young's modulus, the free energy density required to form microcracks should be:

$$A_c = \frac{1}{1-D}\left\langle \frac{dG}{da} \right\rangle \tag{27}$$

Thus, the energy dissipated during microcrack propagation is:

$$\frac{dA_c}{dD} = \frac{1}{(1-D)^2}\left\langle \frac{dG}{da} \right\rangle \tag{28}$$

Making use of Eq. (26), the energy dissipated during crack propagation can be expressed with respect to μ as:

Institutional Repository - Library & Information Centre - University of Thessaly
15/10/2023 05:52:39 EEST - 167.114.118.212

$$\frac{dA_c}{d\mu} = (1-D)^2 E^* \frac{dA_c}{dD} = E^* \left\langle \frac{dG}{da} \right\rangle = \frac{\pi}{2}\tau^2 + \frac{1}{3}\left(\frac{d\tau}{dy} a\right)^2 \tag{29}$$

Obviously, the crack length, a, and the internal length, g, are a function of the damage parameter. Therefore, $g = g(\mu) = \psi(a)$ and $a = \psi^{-1}(g) = \xi(\mu)$. It should be noted that a stress gradient cannot induce crack opening under a compressive mode (see Fig. 4). The stress gradient is essentially a bending moment and thus, one-half of the crack length will be under a compressive stress and the other half under a tensile stress. The latter corresponds to a tensile opening mode I_T, whereas the former to case (c) of Fig. 2, which does not induce crack extension.

4. APPLICATION TO PLAIN CONCRETE

The proposed model is applied to plain concrete beams subjected to 4-point bending, with damage occurring in the middle part of the beam subjected to pure bending, where since axial normal stresses are principal and a uniaxial law for the concrete is assumed to be sufficient for damage characterization.

Uniaxial Response

The uniaxial response of plain concrete under tension or compression is assumed to be of the form:

$$\tau_i = E_{0i}\varepsilon_i, \text{ for } \varepsilon_i \le \varepsilon_{0i}, \text{ and, } \tau_i = (1-D_i)E_{0i}\varepsilon_i = \frac{E_{0i}\varepsilon_i}{1+E_{0i}\mu_i}, \text{for } \varepsilon_i > \varepsilon_{0i} \tag{30}$$

where E_{0i} is the Young's modulus of elasticity of the uncracked material, ε_{0i} the strain value depicting the end of a perfectly elastic response and initiation of damage and D_i (dimensionless), μ_i (stress^{-1}) are two equivalent damage parameters. The index $i = c, t$ is a subscript denoting compression or tension, respectively.

In a thermodynamic formulation, μ is used to avoid imposing the additional constraint $D \le 1$. However, both damage parameters can be used, since:

$$D = 1 - \frac{1}{1+E_0\mu} \tag{31}$$

It is obvious from Eq. (31) that if $\mu = 0$, then $D = 0$ and if $\mu \to \infty$, then $D \to 1$. In other words, both μ and D describe the initiation and the evolution of damage in the same way but the limit for complete damage is bounded in the case of D, but this is not true for μ. There is a one-to-one correspondence between D and μ and $dD/d\mu|_{\mu=0} = E_0$.

Institutional Repository - Library & Information Centre - University of Thessaly
15/10/2023 05:52:39 EEST - 167.114.118.212

If a relationship of the form:

$$\tau_i = f_i \frac{\beta_i(\varepsilon/\varepsilon_i)}{\beta_i - 1 + (\varepsilon/\varepsilon_i)^{\beta_i}} \tag{32}$$

is assumed for the stress-strain response of plain concrete[42], where f_i is the maximum stress, ε_i the strain at maximum stress and β_i a material parameter defining the steepness of the softening branch, a damage law for compression ($i = c$) and tension ($i = t$) can be derived based on Eqs. (30) and (32):

$$D_i = 0 \text{ for } \varepsilon < \varepsilon_{0i}, \text{ and } D_i = 1 - \frac{\beta_i - 1 + (\varepsilon_{0i}/\varepsilon_i)^{\beta_i}}{\beta_i - 1 + (\varepsilon/\varepsilon_i)^{\beta_i}} \quad \text{for } \varepsilon \geq \varepsilon_{0i} \tag{33}$$

where the Young's modulus, E_{0i}, is equal to:

$$E_{0i} = \frac{\beta_i f_i}{\left(\beta_i - 1 + (\varepsilon_{0i}/\varepsilon_i)^{\beta_i}\right)\varepsilon_i} \tag{34}$$

The threshold strain values, ε_{0t} and ε_{0c}, for uniaxial tension and compression, respectively, are assumed to occur at a stress[43] $\tau_t = 0.8 f_t$ and $\tau_c = 0.4 f_c$, respectively. Therefore, the critical strain, ε_{0i}, signifying the onset of damage can be determined using Eq. (32). Furthermore, assuming that the Young's modulus is the same in uniaxial tension and compression, an estimate for the tensile to compressive strain ratio at the peak stress (Eq. (35)) is obtained as follows:

$$\frac{\varepsilon_t}{\varepsilon_c} = \frac{\beta_t f_t \left(\beta_c - 1 + (\varepsilon_{0c}/\varepsilon_c)^{\beta_c}\right)}{\beta_c f_c \left(\beta_t - 1 + (\varepsilon_{0t}/\varepsilon_t)^{\beta_t}\right)} \tag{35}$$

Flexural response

The local normal longitudinal strains in the part of the concrete beam specimens under pure bending are assumed to be linearly distributed along the depth of the beam's cross-section (z-axis), $\varepsilon_{xx} = \varepsilon_m + kz$, where ε_m is the strain at $z = 0$ and k is the curvature. In the elastic region of the beam $\varepsilon_m = 0$ and beyond the elastic limit the neutral axis shifts upwards ($\varepsilon_m \neq 0$).

For a given value of k, and using the assumed law for uniaxial tension and compression, the value of ε_m which satisfies equilibrium is determined through an iteration procedure. This implies a 1D discretization of the cross-section to strips of depth dz in order to evaluate numerically the integral, $N = b\int_{-h/2}^{h/2} \sigma_{xx} dz = 0$. Essentially, in the proposed model, the input parameter is the curvature

Institutional Repository - Library & Information Centre - University of Thessaly
15/10/2023 05:52:39 EEST - 167.114.118.212

at midspan and the output is the bending moment capacity, $M = b\int_{-h/2}^{h/2}\sigma_{xx} z dz$, corresponding to the assumed linear axial strain distribution along the height of the cross-section. The number of strips used to discretize the cross-sectional area is chosen based on a convergence requirement of a mesh refinement so that when the number of strips is doubled there is a change of less than 10^{-5} kNm in the predicted value of M. It is noted that the output of this procedure is a local M vs. k prediction curve which is size independent, since it is only a function of the assumed uniaxial stress-strain response. A 2D mesh refinement study is also included in Section IV.5. The non-local M vs. k prediction curve is obtained by scaling the local curvature estimate using Eq. (44) for 4-point bending (see Section IV.6). This implies that predicting size effect for ultimate strength is not feasible for the proposed non-local model.

The local M vs. k response prediction can be transformed to a force vs. midspan deflection curve by solving the boundary value problem for a simply supported Timoshenko beam under 4-poind bending (see Section IV.6). Using Eqs. (44) and (46), a local kinematic expression for the midspan deflection δ_m is obtained in terms of the curvature k_m, $\delta_m = 0.13611\, L^2 k_m$, where δ_m is the midspan deflection corresponding to the curvature k_m. The non-local force vs. midspan deflection curve is determined by imposing a similar kinematic relation between curvature and deflection, based on the gradient solution of the boundary problem (Eqs. 41 and 45). Unlike, the local (classical) predictions, the non-local kinematic relation is affected by the internal length, g, which evolves with damage. Therefore, this kinematic relation is computed for the current value of g, which evolves with damage.

Regarding the evolution law for the gradient length, an exponential expression is assumed of the form:

$$g = g_0 e^{nD}, \text{ for } nD > 0 \tag{36}$$

where g_0 is the initial internal length, D the damage parameter and n a positive constant which defines the ratio of the gradient value g_1 (at D=1) to the initial gradient internal length g_0 (at D=0). Since the initial value of the gradient internal length is based on elasticity, there is only a single unknown parameter, n, to be determined based on experimental data in the inelastic region. It is worth noting that, according to Le Bellego et al.[44], attempting to calibrate a gradient damage model assuming a constant internal length (independent of the damage level) resulted in a lack of objectivity when experimental data from geometrical similar notched beam specimens were

Institutional Repository - Library & Information Centre - University of Thessaly
15/10/2023 05:52:39 EEST - 167.114.118.212

considered. This could be partially remedied if an increasing value for the internal length is assumed with damage.

5. OBJECTIVITY OF THE PROPOSED MODEL PREDICTIONS

The total strain, $\boldsymbol{\varepsilon}$, is related to the total displacement, $\mathbf{u}$ ($\varepsilon_{ij} = (\partial u_i / \partial x_j + \partial u_j / \partial x_i)/2$), where ε_{ij} is the gradient enriched strain. The damage rules of Eq. (9) provide the stiffness evolution as functions of the Cauchy stress $\boldsymbol{\tau}$, which in turn relates to the total strain as: $\boldsymbol{\tau} = \mathbf{C}^{-1} : \boldsymbol{\varepsilon}$. For a 1D case, the equilibrium equation ($\partial\sigma / \partial x = 0$) within the framework of the proposed gradient model becomes:

$$\frac{\partial\sigma}{\partial\varepsilon}\frac{\partial\varepsilon}{\partial x} + \frac{\partial\sigma}{\partial\varepsilon_{,xx}}\frac{\partial\varepsilon_{,xx}}{\partial x} = \frac{\partial\sigma}{\partial\varepsilon}\frac{\partial^2 u}{\partial x^2} + \frac{\partial\sigma}{\partial\varepsilon_{,xx}}\frac{\partial^4 u}{\partial x^4} = 0 \tag{38}$$

The constitutive law assumed in this work can be expressed as:

$$\sigma(\varepsilon, \varepsilon_{,xx}) = (1 - D(\varepsilon))E(\varepsilon - g^2\varepsilon_{,xx}) \tag{39}$$

where $D(\varepsilon) = [\varepsilon_u(\varepsilon - \varepsilon_i)]/[\varepsilon(\varepsilon_u - \varepsilon_i)]$ is the damage loading function for uniaxial tension (ε_i the strain signifying end of elastic behavior, ε_u the strain signifying complete damage and ε the applied uniform axial tensile strain equal to ε_{t0}.

Assuming a harmonic perturbation for the displacement, $u = A\cos(\phi x)$, where ϕ = wave number and A = amplitude, Eq. (38) becomes:

$$\frac{E\varepsilon_i}{\varepsilon_u - \varepsilon_i}\left[\left(\frac{\varepsilon_u}{\varepsilon_{t0}} - 1)\right)g^2\phi^2 - 1]\right] = 0 \tag{40}$$

It can be seen that Eq. (40) yields a real wave number with a critical value of $\phi_{crit} = \frac{1}{g}\sqrt{\frac{\varepsilon_{t0}}{\varepsilon_u - \varepsilon_{t0}}}$, which is identical to that in Rodriguez-Ferran et al.[36]. Such a result renders a non-local model suitable for regularization if employed in a FEM analysis.

A 2D mesh refinement study of the presented model for the beam specimen with dimensions 200x200x600 mm at a load level of $0.84P_{peak}$ in the post-peak softening branch is shown in Fig. 10. The numerical results are derived assuming that f_c=38 MPa, $\beta_c = 3.89$, $f_t = 3.09$ MPa, $\beta_t = 6.5$ ($c_e = 12.313$), E= 34 GPa, $\nu = 0.2$ and ε_c=0.0015. Based on the 1D-discretized midspan cross-section (strips of depth dz), this load level of $0.84P_{peak}$ corresponds to the first detection of a damage value of D=0.95. Three sizes for an “xyz” grid with a width of b=200 mm are used: (a) 20 x 200 x 20 mm, (b) 10 x 200 x 10 mm and (c) 5 x 200 x 5 mm. It can be seen that mesh-independent

Institutional Repository - Library & Information Centre - University of Thessaly
15/10/2023 05:52:39 EEST - 167.114.118.212

damage predictions are obtained along the beam's length. The calculated damage levels are the same for both local and non-local $\overline{P}$ vs. $\overline{\delta}$ predictions (see Fig. 8c). A damage value of $D \geq 0.95$, corresponding practically to zero stress transfer capability, may signify major crack development. The present model's prediction that a major crack forms at a load level of about $0.84P_{peak}$ in the post-peak softening branch is in agreement with acoustic emission findings for concrete beams under flexure[46] and uniaxial tension[47]. Also, it is noted that a non-zero midspan damage value $\overline{D}$ is computed at $0.74P_{peak}$ in the ascending branch of response. A damage value of D>0, signifying softening under uniaxial tension, can be associated with microcracking activity. Acoustic emission measurements on notched and un-notched concrete beam specimens tested under flexure have shown that microcracking activity becomes detectable before the peak applied load is reached and at load level of 70% to 80% of the peak load[46,48].

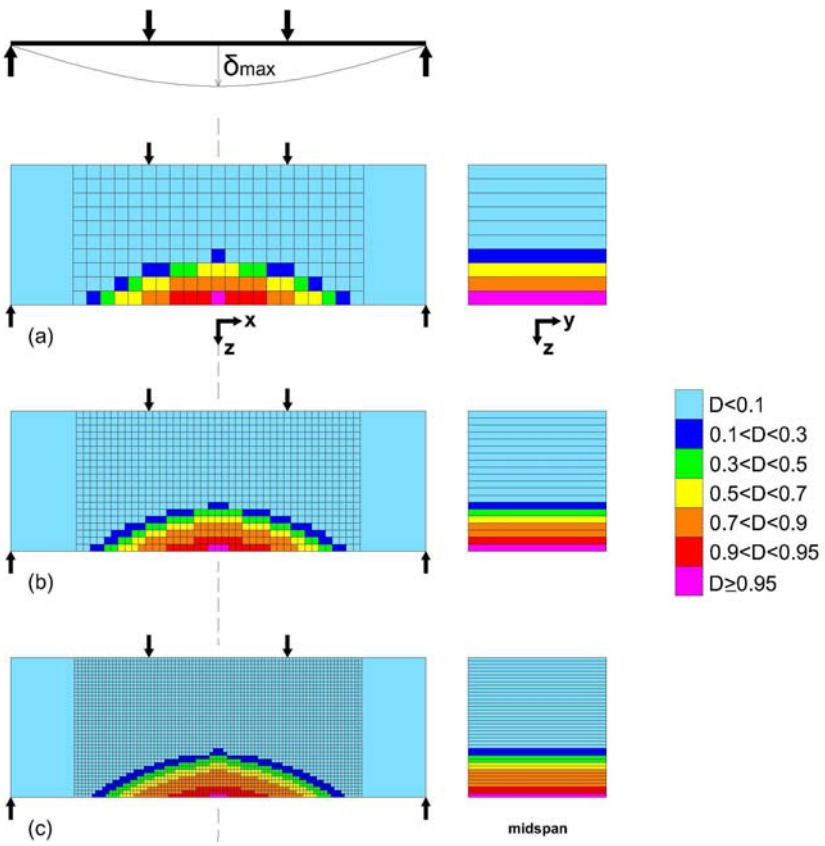

Fig. 10. Numerical damage level predictions of a 2D mesh refinement study of the proposed model for specimen size S3 (200x200x600 mm) at $0.84P_{peak}$ in the post-peak softening branch: (a) grid of 20x20 mm, (b) grid of 10x10 mm and (c) grid of 5x5 mm.

Institutional Repository - Library & Information Centre - University of Thessaly
15/10/2023 05:52:39 EEST - 167.114.118.212

6. MIDSPAN DEFLECTION FOR 4-POINT BENDING BASED ON GRADIENT ELASTICITY

The boundary value problem for a dipolar elastic Timoshenko simply supported beam has been solved in closed-form by Triantafyllou and Giannakopoulos[49] and only the relevant work is included here.

The expression for the midspan deflection of a simply supported beam with an orthogonal cross-section subjected to two equal concentrated loads, P/2, at a distance L/3 from the supports is:

$$\delta = \frac{23PL^3}{1296\overline{E}I}\left(\frac{\ell}{g}\right)^2\left(\left(1-f_b\right)+\frac{216}{115}\left(\frac{h}{L}\right)^2\left(\frac{g}{\ell}\right)^2\left(\frac{1-\nu}{1-2\nu}\right)\left(1-f_{sh}\right)\right) \tag{41}$$

where P is the applied load by the actuator, $\overline{E} = \left[(1-\nu)/(1+\nu)(1-2\nu)\right]E_0$, E_0 = Young's modulus of elasticity, $\ell = g\sqrt{1/(1+(A/I)g^2)}$ is a "shear" gradient internal length, and f_b, f_{sh} are non-dimensional functions of the internal length g, see Eqs. (42) and (43),

$$f_{sh} = -\frac{g}{L}\frac{\left(\begin{array}{l} e^{\frac{11L}{6g}}\left(6\frac{g}{L}-2\right)+3e^{\frac{4L}{3g}}-e^{\frac{2L}{g}}+2e^{\frac{L}{6g}}\left(3\frac{g}{L}+1\right) \\ -2e^{\frac{7L}{6g}}\left(3\frac{g}{L}+1\right)+e^{\frac{5L}{6g}}\left(2-6\frac{g}{L}\right)+1-3e^{\frac{2L}{3g}} \end{array}\right)}{\left(2\left(1-e^{\frac{2L}{g}}\right)\frac{g}{L}+\left(1+e^{\frac{2L}{3g}}+e^{\frac{4L}{3g}}+e^{\frac{2L}{g}}\right)\right)} \tag{42}$$

$$f_b = \frac{\alpha_1}{\Delta_1}+\frac{\alpha_2+\alpha_3+\alpha_4+\alpha_5+\alpha_6+\alpha_7}{\Delta} \tag{43}$$

where

$$\alpha_1 = 32\left(\frac{g}{L}\right)\left(1-e^{\frac{L}{6g}}-e^{\frac{5L}{6g}}+e^{\frac{7L}{6g}}+e^{\frac{11L}{6g}}-e^{\frac{2L}{g}}\right),\ \alpha_2 = 96\left(\frac{\ell}{L}\right)\left(1+e^{\frac{2L}{3g}}+e^{\frac{4L}{3g}}+e^{\frac{2L}{g}}\right)\left(-1+e^{\frac{2L}{\ell}}\right)$$

$$\alpha_3 = 96\left(\frac{\ell}{L}\right)\left(\frac{g}{L}\right)\left(1-e^{\frac{L}{g}}\right)\left(e^{\frac{2L}{3g}}-1\right)\left(\begin{array}{l} 3-e^{\frac{L}{6g}}-e^{\frac{5L}{6g}}+3e^{\frac{L}{g}}-4e^{\frac{L}{6}\left(\frac{5}{g}+\frac{4}{\ell}\right)}-e^{\frac{L}{6}\left(\frac{5}{g}+\frac{8}{\ell}\right)}+6e^{\frac{L}{g}+\frac{2L}{3\ell}} \\ +3e^{\frac{L}{g}+\frac{4L}{3\ell}}+6e^{\frac{2L}{3\ell}}+3e^{\frac{4L}{3\ell}}-4e^{\frac{L(4g+\ell)}{6g\ell}}-e^{\frac{L(8g+\ell)}{6g\ell}} \end{array}\right)$$

$$\alpha_4 = 288e^{\frac{L}{6g}}\left(\frac{g}{L}\right)\left(\frac{\ell}{L}\right)^2\left(e^{\frac{L}{g}}-1\right)\left(\begin{array}{l} 2+2e^{\frac{L}{6g}}-4e^{\frac{L}{6}\left(\frac{1}{g}+\frac{1}{\ell}\right)}+2e^{L\left(\frac{1}{g}+\frac{1}{\ell}\right)}+4e^{\frac{L}{6}\left(\frac{5}{g}+\frac{3}{\ell}\right)}+4e^{\frac{L}{6}\left(\frac{5}{g}+\frac{7}{\ell}\right)} \\ -4e^{\frac{L}{6}\left(\frac{5}{g}+\frac{9}{\ell}\right)}-7e^{\frac{L}{g}+\frac{L}{2\ell}}+2e^{\frac{L}{g}+\frac{2L}{3\ell}}-7e^{\frac{L}{g}+\frac{7L}{6\ell}}+2e^{\frac{L}{g}+\frac{5L}{3\ell}} \\ -7e^{\frac{L}{2\ell}}+2e^{\frac{2L}{3\ell}}+2e^{\frac{L}{\ell}}-7e^{\frac{7L}{6\ell}}+2e^{\frac{5L}{3\ell}}+4e^{\frac{L(3g+\ell)}{6g\ell}} \\ +4e^{\frac{L(7g+\ell)}{6g\ell}}-4e^{\frac{L(9g+\ell)}{6g\ell}}-4e^{\frac{L(g+5\ell)}{6g\ell}} \end{array}\right)$$

Institutional Repository - Library & Information Centre - University of Thessaly
15/10/2023 05:52:39 EEST - 167.114.118.212

$$\alpha_5 = 144\left(\frac{\ell}{L}\right)^2 \left(\begin{array}{l} 3e^{\frac{2L}{3}\left(\frac{3}{g}+\frac{1}{\ell}\right)} - 2e^{\frac{L}{6}\left(\frac{4}{g}+\frac{1}{\ell}\right)} + 4e^{\frac{L}{3}\left(\frac{4}{g}+\frac{1}{\ell}\right)} + 4e^{\frac{L}{3}\left(\frac{6}{g}+\frac{1}{\ell}\right)} + 4e^{\frac{L}{3}\left(\frac{2}{g}+\frac{5}{\ell}\right)} - 2e^{\frac{L}{6}\left(\frac{4}{g}+\frac{5}{\ell}\right)} \\ + 4e^{\frac{L}{3}\left(\frac{4}{g}+\frac{5}{\ell}\right)} - 2e^{\frac{L}{6}\left(\frac{8}{g}+\frac{5}{\ell}\right)} - 2e^{\frac{L}{6}\left(\frac{4}{g}+\frac{7}{\ell}\right)} - 2e^{\frac{L}{6}\left(\frac{8}{g}+\frac{7}{\ell}\right)} - 2e^{\frac{L}{6}\left(\frac{4}{g}+\frac{11}{\ell}\right)} - 2e^{\frac{L}{6}\left(\frac{8}{g}+\frac{11}{\ell}\right)} \\ - 2e^{\frac{2L}{g}+\frac{L}{6\ell}} - 2e^{\frac{2L}{g}+\frac{5L}{6\ell}} - 2e^{\frac{2L}{g}+\frac{7L}{6\ell}} + 3e^{\frac{2L}{g}+\frac{4L}{3\ell}} + 4e^{\frac{2L}{g}+\frac{5L}{3\ell}} - 2e^{\frac{2L}{g}+\frac{11L}{6\ell}} - 2e^{\frac{L}{6\ell}} \\ + 4e^{\frac{L}{3\ell}} + 3e^{\frac{2L}{3\ell}} - 2e^{\frac{5L}{6\ell}} - 2e^{\frac{7L}{6\ell}} + 3e^{\frac{4L}{3\ell}} + 4e^{\frac{5L}{3\ell}} - 2e^{\frac{11L}{6\ell}} + 3e^{\frac{2L(g+\ell)}{3g\ell}} + 3e^{\frac{4L(g+\ell)}{3g\ell}} \\ + 3e^{\frac{2L(2g+\ell)}{3g\ell}} + 4e^{\frac{L(g+2\ell)}{3g\ell}} + 3e^{\frac{2L(g+2\ell)}{3g\ell}} - 2e^{\frac{L(g+8\ell)}{6g\ell}} \end{array} \right)$$

$$\alpha_6 = 432\left(\frac{\ell}{L}\right)^3\left(\frac{g}{L}\right) \left(\begin{array}{l} 2 + e^{\frac{L}{6g}} + e^{\frac{5L}{6g}} - e^{\frac{7L}{6g}} - e^{\frac{11L}{6g}} - 2e^{\frac{2L}{g}} + 2e^{2\left(\frac{L}{g}+\frac{L}{\ell}\right)} - 2e^{\frac{2}{3}\left(\frac{3L}{g}+\frac{L}{\ell}\right)} + 2e^{\frac{1}{2}\left(\frac{4L}{g}+\frac{L}{\ell}\right)} - 3e^{\frac{1}{6}\left(\frac{5L}{g}+\frac{4L}{\ell}\right)} \\ + 3e^{\frac{1}{6}\left(\frac{7L}{g}+\frac{4L}{\ell}\right)} + 3e^{\frac{1}{6}\left(\frac{11L}{g}+\frac{4L}{\ell}\right)} + 3e^{\frac{1}{6}\left(\frac{5L}{g}+\frac{8L}{\ell}\right)} - 3e^{\frac{1}{6}\left(\frac{7L}{g}+\frac{8L}{\ell}\right)} - 3e^{\frac{1}{6}\left(\frac{11L}{g}+\frac{8L}{\ell}\right)} - 2e^{\left(\frac{2L}{g}+\frac{5L}{6\ell}\right)} \\ + 2e^{\left(\frac{2L}{g}+\frac{7L}{6\ell}\right)} + 2e^{\left(\frac{2L}{g}+\frac{4L}{3\ell}\right)} - 2e^{\left(\frac{2L}{g}+\frac{3L}{2\ell}\right)} - e^{\left(\frac{L}{6g}+\frac{2L}{\ell}\right)} - e^{\left(\frac{5L}{6g}+\frac{2L}{\ell}\right)} + e^{\left(\frac{7L}{6g}+\frac{2L}{\ell}\right)} + e^{\left(\frac{11L}{6g}+\frac{2L}{\ell}\right)} \\ - 2e^{\frac{L}{2\ell}} + 2e^{\frac{2L}{3\ell}} + 2e^{\frac{5L}{6\ell}} - 2e^{\frac{7L}{6\ell}} - 2e^{\frac{4L}{3\ell}} + 2e^{\frac{3L}{2\ell}} - 2e^{\frac{2L}{\ell}} - 3e^{\frac{1}{6}\left(\frac{L}{g}+\frac{4L}{\ell}\right)} + 3e^{\frac{1}{6}\left(\frac{L}{g}+\frac{8L}{\ell}\right)} \end{array} \right)$$

$$\alpha_7 = 216\left(\frac{\ell}{L}\right)^3 \left(\begin{array}{l} 3 + 3e^{\frac{2L}{3g}} + 3e^{\frac{4L}{3g}} + 3e^{\frac{2L}{g}} - e^{\frac{2}{3}\left(\frac{3L}{g}+\frac{L}{\ell}\right)} - 2e^{\frac{1}{2}\left(\frac{4L}{g}+\frac{L}{\ell}\right)} - 3e^{\frac{2}{3}\left(\frac{L}{g}+\frac{3L}{\ell}\right)} - 2e^{\frac{1}{6}\left(\frac{4L}{g}+\frac{3L}{\ell}\right)} - 2e^{\frac{1}{6}\left(\frac{8L}{g}+\frac{3L}{\ell}\right)} \\ + 2e^{\frac{1}{6}\left(\frac{4L}{g}+\frac{5L}{\ell}\right)} + 2e^{\frac{1}{6}\left(\frac{8L}{g}+\frac{5L}{\ell}\right)} - 2e^{\frac{1}{6}\left(\frac{4L}{g}+\frac{7L}{\ell}\right)} - 2e^{\frac{1}{6}\left(\frac{8L}{g}+\frac{7L}{\ell}\right)} + 2e^{\frac{1}{6}\left(\frac{4L}{g}+\frac{9L}{\ell}\right)} + 2e^{\left(\frac{8L}{g}+\frac{9L}{6\ell}\right)} + 2e^{\left(\frac{2L}{g}+\frac{5L}{6\ell}\right)} \\ - 2e^{\left(\frac{2L}{g}+\frac{7L}{6\ell}\right)} + 2e^{\left(\frac{2L}{g}+\frac{4L}{3\ell}\right)} + 2e^{\left(\frac{2L}{g}+\frac{3L}{2\ell}\right)} - 3e^{\left(\frac{4L}{3g}+\frac{2L}{\ell}\right)} - 2e^{\frac{L}{2\ell}} - 2e^{\frac{2L}{3\ell}} + 2e^{\frac{5L}{6\ell}} - 2e^{\frac{7L}{6\ell}} \\ + e^{\frac{4L}{3\ell}} + 2e^{\frac{3L}{2\ell}} - 3e^{\frac{2L}{\ell}} - e^{\frac{2}{3}\left(\frac{L}{g}+\frac{L}{\ell}\right)} + e^{\frac{4}{3}\left(\frac{L}{g}+\frac{L}{\ell}\right)} - 3e^{2\left(\frac{L}{g}+\frac{L}{\ell}\right)} + e^{\frac{2}{3}\left(\frac{L}{g}+\frac{2L}{\ell}\right)} - e^{\frac{2}{3}\left(\frac{2L}{g}+\frac{L}{\ell}\right)} \end{array} \right)$$

$$\Delta_1 = 23\left(\left(1 + e^{\frac{2L}{3g}} + e^{\frac{4L}{3g}} + e^{\frac{2L}{g}}\right) + 2\left(\frac{g}{L}\right)\left(1 - e^{\frac{2L}{g}}\right)\right), \quad \Delta = \left(1 + e^{\frac{2L}{3\ell}} + e^{\frac{4L}{3\ell}} + e^{\frac{2L}{\ell}}\right)\Delta_1$$

Note that in Eq. (41), the effect of the Poisson's ratio on the Young's modulus is taken into account. In the absence of gradient, i.e. $g = 0$ ($\ell / g = 1$), Eq. (41) reduces to the classical elasticity solution:

$$\delta = \frac{23PL^3}{1296\bar{E}I}\left(1 + \frac{216}{115}\left(\frac{h}{L}\right)^2\left(\frac{1-\nu}{1-2\nu}\right)\right) \tag{44}$$

The expression for the normal axial strain of the beam at midspan at a distance z from the n.a. is given by:

$$\varepsilon_{xx} = kz = \frac{PL}{6\bar{E}I}\left(\frac{\ell}{g}\right)^2\left(1 - \frac{2e^{\frac{L}{6\ell}}\left(2 + 2e^{\frac{L}{\ell}} + 3\frac{\ell}{L}e^{\frac{L}{3\ell}} - 3\frac{\ell}{L}e^{\frac{2L}{3\ell}}\right)}{3\left(1 + 4e^{\frac{4L}{3\ell}}\right)}\right)z \tag{45}$$

Institutional Repository - Library & Information Centre - University of Thessaly
15/10/2023 05:52:39 EEST - 167.114.118.212

where k = beam's curvature and $-h/2 \le z \le h/2$. Of course, in the absence of gradient, i.e. $g = 0$, Eq. (45) reduces to the classical expression for the axial strains:

$$\varepsilon_{xx_cl} = k_{cl} z = \frac{PL}{6\bar{E}I} z \tag{46}$$

7. CONCLUSIONS

In the present study, a strain gradient damage theory is proposed based on the influence of the stress gradient on Gibb's energy. It was shown that, if a microstructural internal length is related to the level of damage, then this length should be either increasing with damage or remaining constant. Furthermore, a simple continuous damage model was proposed for the case of 4-point bending.

Institutional Repository - Library & Information Centre - University of Thessaly
15/10/2023 05:52:39 EEST - 167.114.118.212

CHAPTER V

EXPERIMENTAL PROGRAM

1. MATERIALS

Five (5) cementitious mixes were used for the beam specimens tested: low-strength concrete (LC), normal-strength concrete (NC), medium-strength concrete (MC1, MC2) and cement mortar (CM). The mix proportions are shown in Table 1 and the sieve analysis for the aggregates used is described in Table 2.

Table 1. Concrete and cement mortar mix proportioning.

Mix	Quantities (Kg/m^3)				Dry density (kg/m^3)	Slump (cm)	Air-content [(d)] (%)
	Cement [(a)]	Aggregates [(b)]	w/c ratio	Additives [(c)]			
CM	450	1350	293 (0.65)	3.6	2100	- [(e)]	2.5
LC	208	1980	162 (0.78)	1.6	2335	25	3.0
NC	276	2080	176 (0.64)	1.5	2365	10	2.5
MC1	448	1720	204 (0.45)	4.0	2410	22.4	2.0
MC2	447	1640	207 (0.46)	6.0	2440	15.6	2.0

[(a)] cement type CEM II/42.5
[(b)] crushed limestone (compressive strength 100 MPa)
[(c)] plasticizer Sika® Viscocrete® for M, MC1, MC2; Sika®Sikament® for NC; Sika®Plastimen® for LC
[(d)] air content of fresh mix (Gilson HM-30 pressure meter)
[(e)] not measured

Table 2. Sieve analysis of the aggregates used in the cementicious mixes.

Sieve opening (mm)	% passing				
	LC	NC	MC1	MC2	CM
32	100	100	100	100	-[(a)]
16	85.8	84.1	80.6	78.7	-
8	70.7	67.8	60.0	57.7	-
4	62.7	59.7	49.6	49.1	-
2	45.4	43.3	35.7	35.5	-
1	29.6	28.2	23.3	23.2	100
0.5	-	-	-	-	30
0.25	12.9	12.3	10.2	10.1	-
0.075	8.0	7.6	6.3	6.3	-

[(a)] not measured

Institutional Repository - Library & Information Centre - University of Thessaly
15/10/2023 05:52:39 EEST - 167.114.118.212

2. CLASSICAL MECHANICAL PROPERTIES

The classical mechanical properties of the five (5) cementicious mixes were determined based on uniaxial compression and split cylinder tension tests. The cylinder (150x300 mm) and cube (150x150x150 mm) specimens were tested under uniaxial compression using a DMG 3000kN testing machine. The tests were performed following the ASTM recommendations[1,2] and the determination of the Young's modulus and Poisson's ratio from the compression test was obtained using four strain gages (SG) placed at mid-height (two SG's at 90° on each diametrically opposite location). The Young's modulus (E_{sp}^{c} and E_{sp}^{t}) and Poisson's ratio were also estimated from the split cylinder tension tests based on SG measurements of two SG's attached on each of the flat faces of the cylinder specimens (see Fig. 1) and using the elasticity solution of a disc subjected to diametrically opposite compression[3,4]. The split cylinder test data except to an estimate for the Poisson's ratio also provide a second independent estimate of the Young's modulus (E_{sp}^{t}) based on the two tensile measured strains, in addition to the estimate based on the compressive strain measurements of the uniaxial compression test (E_{sp}^{c}) (see Section V.4). Loading rates ranging from 0.7 to 1 MPa/min were used for this test[4]. The measured mechanical properties are summarized in Table 3.

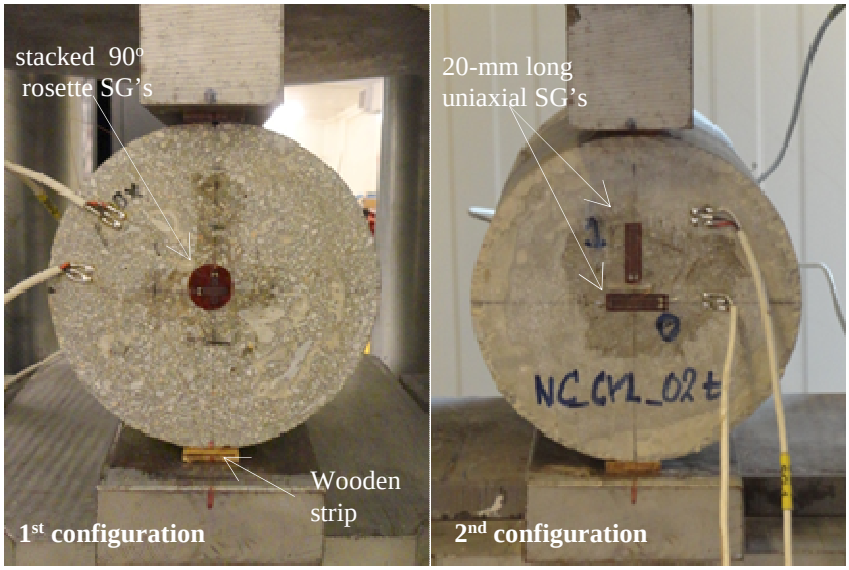

Fig. 1 – Split cylinder tension test setup and strain gage instrumentation.

Institutional Repository - Library & Information Centre - University of Thessaly
15/10/2023 05:52:39 EEST - 167.114.118.212

Table 3 – Measured mechanical properties for the LC, NC, MC1, MC2 and CM mixes.

Mechanical properties	LC	NC	MC1	MC2	CM
Uniaxial compression of cubes *(150x150x150 mm)*					
f_{28day}, MPa	19.96 ± 0.4 (3) [(a)]	26.48 ± 0.8 (3)	45.05 ± 1.1 (3)	48.48 ± 0.7 (3)	30.54 ± 0.1 (3)
f, MPa [(b)]	21.63 ± 0.4 (3)	29.76 ± 0.5 (3)	52.59 ± 1.0 (4)	54.69 ± 0.7 (3)	- [(d)]
Uniaxial compression of cylinders *(150x300 mm)*					
f_c , MPa[(b)]	15.92 ± 0.4 (5)	20.51 ± 2.1 (4)	34.67 ± 2.5(3)	38.01 ± 3.6 (4)	32.42 ± 2.4 (4)
E, GPa [(b)]	25.40 ± 2.1 (4)	30.68 ± 1.5 (3)	33.63 ± 4.3 (3)	34.53 ± 0.6 (3)	22.10 ± 1.1 (3)
ν [(b)]	0.22 ± 0.01 (4)	0.23 ± 0.02 (3)	0.21 ± 0.01 (2)	0.23 ± 0.04 (2)	0.23 ± 0.01 (3)
Split cylinder tension *(150x300 mm cylinders)*					
f_{sp}, MPa [(b)]	2.67 ± 0.3 (3)	3.06 ± 0.4 (3)	3.38 ± 0.1 (4)	3.43 ± 0.1 (3)	2.87 ± 0.1 (2)
E^t_{sp} ,GPa[(b),(c)]	22.17 ± 1.4 (3)	30.84 ± 1.1 (3)	31.68 ± 1.4 (3)	31.82 ± 1.1 (3)	22.38 (1)
E^c_{sp} ,GPa[(b),(c)]	26.20 ± 1.4 (3)	31.92 ± 3.4 (2)	32.75 ± 0.8 (3)	35.93 ± 0.6 (3)	25.41 (1)
ν [(b)]	0.23 ± 0.04 (3)	0.17(1)	0.21 ± 0.02 (3)	0.21 ± 0.06 (2)	0.25 (1)

[(a)] number in parenthesis denotes the number of tested specimens considered for the reported average value.
[(b)] tests performed after 1 month for LC, NC, MC1, MC2 and after 8.5 months for CM.
[(c)] estimated Young's modulus for $\nu = 0.2$ (see Section V.3).
[(d)] not measured

The Young's modulus and Poisson's ratio values obtained from the uniaxial compression and split cylinder tension tests for all mixes are shown versus the compressive strength in Figs. 2 and 3, respectively. The 95% confidence limit for the Young's modulus of elasticity (in MPa) from reported experiments data[5] corresponding to a $\pm 20\%$ deviation of the value predicted by the empirical formula of Eq. (3)[5], is also shown in Fig. 2,

$$E = 1.7832 \times 10^{-3} \gamma^2 f_c^{1/3} \tag{3}$$

where f_c is the cylinder compressive strength (in MPa), γ is the specific weight (in kg/m^3). It is noted that Eq. (3) is applicable to concretes with limestone aggregates and normal additives[5].

The majority of the experimental values for the Young's modulus fall within the expected range as represented by the limits of Eq. (3). As expected, the Young's modulus of the concrete mixes considered in this study is higher than that of the cement mortar. It is known that the Young's modulus of limestone varies from 50 to70 GPa[6] and hence limestone aggregates should be stiffer than the matrix material at least for a normal- and medium-strength concrete resulting in a higher Young's modulus value.

The experimental values for Poisson's ratio range from 0.16 to 0.27 and apparently seem to be independent of the compressive strength. This is in agreement with the findings of others[7-9].

Institutional Repository - Library & Information Centre - University of Thessaly
15/10/2023 05:52:39 EEST - 167.114.118.212

Furthermore, similar values for the Poisson's ratio were obtained for both concrete and cement mortar mixes since the range of the Poisson's ratio value for limestone (0.15 to 0.30)[10] is similar to that of cement paste. Hence, the limestone aggregates inclusions have a negligible effect on the Poisson's ratio of the composite.

The compressive strains obtained from the uniaxial compression cylinder test at 40% and 55% of the peak stress are plotted versus the compressive strength in Fig. 4. It can be seen that as the compressive strength of the material increases, the strain values for the same level of stress increase as well. This is a due to the fact that the Young's modulus increases with increasing compressive strength. Also, the difference in strains for the two assumed stress levels remains approximately the same with increasing compressive strength. This observed behavior renders[11] a constitutive law expressed in a normalized form particularly suitable for cementitious materials.

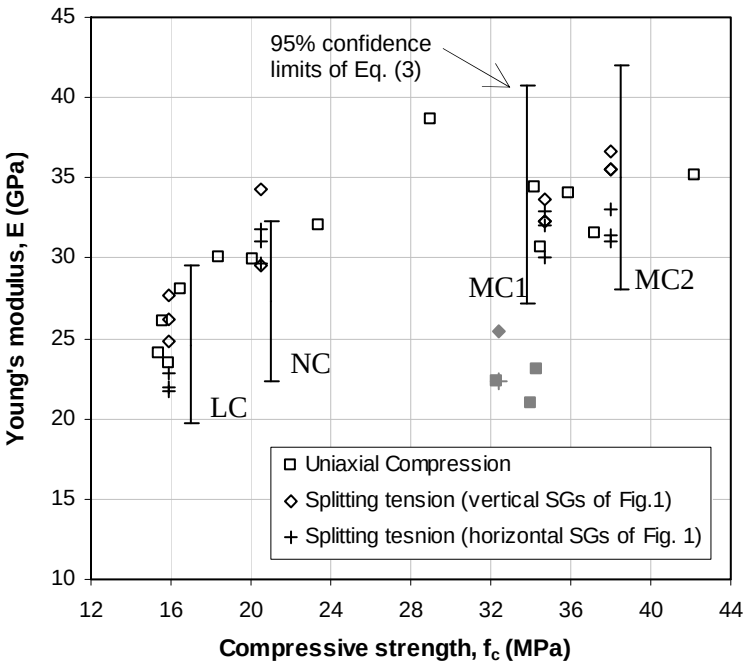

Fig. 2. Measured Young's modulus vs. compressive strength for mixes LC, NC, MC1, MC2 and CM (solid symbols are for CM mix).

Institutional Repository - Library & Information Centre - University of Thessaly
15/10/2023 05:52:39 EEST - 167.114.118.212

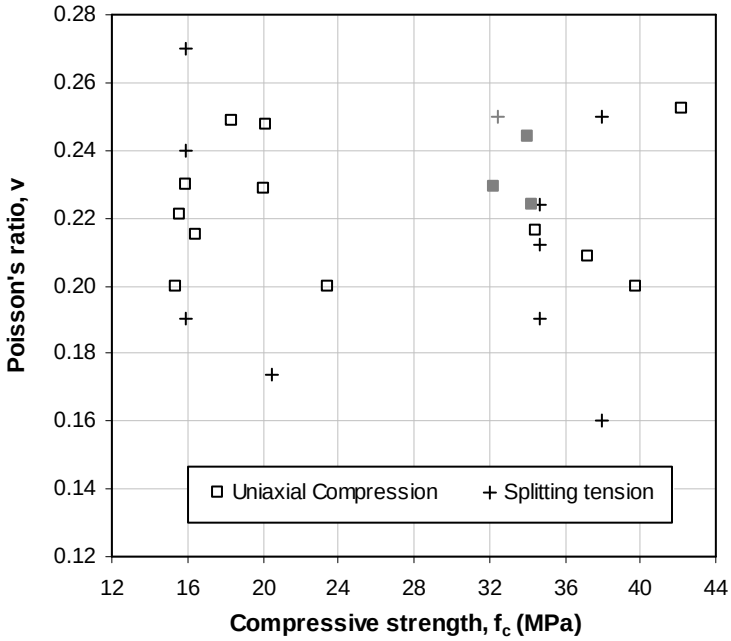

Fig. 3. Measured Poisson's ratio vs. compressive strength for mixes LC, NC, MC1, MC2 and CM (solid symbols are for CM mix).

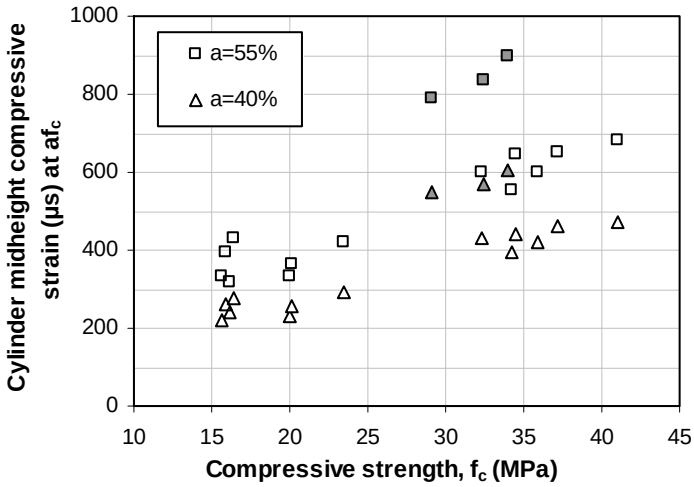

Fig. 4. Measured compressive strain at 40% and 55% of the peak stress vs. compressive strength (solid symbols are for CM mix).

Mechanical properties used in the analysis

The Poisson's ratio of concrete ranges typically between 0.14 and 0.26[12]. In this work, a similar value range was observed with the majority of the data being greater or equal to 0.2. This can be attributed to the stress limit chosen for deriving these estimates[1], i.e. 40% of the peak stress, since the Poisson's ratio of concrete appears to increase with the load level from about 0.15 for a

Institutional Repository - Library & Information Centre - University of Thessaly
15/10/2023 05:52:39 EEST - 167.114.118.212

relatively low stress level to about 0.25 at a load level close to 70% of the peak stress[13]. It is widely accepted that a reasonable value for the Poisson ratio of concrete to be used in an analysis is 0.2. The measured values for the two classical material properties used in Eqs. (1b) and (2b) for each mix in order to compare their experimental flexural response to the classical elasticity predictions are presented in Table 4.

Table 4. Measured material parameters used in the analysis.

Mix	**LC**	**NC**	**MC1**	**MC2**	**CM**
E (GPa)	25.0	30.70	32.7	34.0	22.3
ν			0.2		

Based on the predictions of Eq. (1b) and (2b) for a beam specimen with L/h=3, a deviation of ± 1 GPa in the Young's modulus value translates to a $\pm 5\%$ difference in both the flexural stiffness and the curvature predictions, while a deviation of ± 0.01 in the Poisson's ratio value translates to a less than $\pm 1\%$ and $\pm 1.5\%$ difference in the flexural stiffness and curvature prediction, respectively. Thus, it is reasonable to assume that a deviation of the measured flexural stiffness and curvature values from the classical predictions of up to about 10% can be attributed to the expected variation of the E and ν values.

3. SPLIT CYLINDER TESTS

The stresses for the 2D problem of a disc subjected to diametrically opposite uniformly distributed compression (see Fig. 5a) are[3]:

$$\sigma_r(\bar{r},\theta) = \frac{-p}{\pi}\left(A_1 + A_2 + B_1 + B_2 + \Phi\right) \tag{4}$$

$$\sigma_\theta(\bar{r},\theta) = \frac{-p}{\pi}\left(-A_1 - A_2 + B_1 + B_2 + \Phi\right) \tag{5}$$

$$\tau_{r\theta}(\bar{r},\theta) = \frac{p}{\pi}\left(C_1 - C_2\right) \tag{6}$$

with

$$A_1 = \frac{\left(1-\bar{r}^2\right)\sin 2(\alpha+\theta)}{\bar{r}^4 + 1 - 2\bar{r}^2\cos 2(\alpha+\theta)},\ A_2 = \frac{\left(1-\bar{r}^2\right)\sin 2(\alpha-\theta)}{\bar{r}^4 + 1 - 2\bar{r}^2\cos 2(\alpha-\theta)},$$

Institutional Repository - Library & Information Centre - University of Thessaly
15/10/2023 05:52:39 EEST - 167.114.118.212

$$B_1 = \tan^{-1}\left(\frac{1+\bar{r}^2}{1-\bar{r}^2}\tan(\alpha+\theta)\right),\ B_1 = \tan^{-1}\left(\frac{1+\bar{r}^2}{1-\bar{r}^2}\tan(\alpha-\theta)\right)\ C_1 = \frac{\left(1-\bar{r}^2\right)\left(-\bar{r}^2+\cos 2(\alpha-\theta)\right)}{\bar{r}^4+1-2\bar{r}^2\cos 2(\alpha-\theta)},$$

$$C_2 = \frac{\left(1-\bar{r}^2\right)\left(-\bar{r}^2+\cos 2(\alpha+\theta)\right)}{\bar{r}^4+1-2\bar{r}^2\cos 2(\alpha+\theta)},\ \Phi = \begin{cases} 0 \text{ for } 0 \le \theta \le \pi/2-\alpha \\ \pi \text{ for } \pi/2-\alpha \le \theta \le \pi/2 \end{cases}$$

where σ_r = the normal stress in the r-direction, σ_θ = the normal stress in the θ-direction, $\tau_{r\theta}$ = the shear stress in the r-θ plane, p = the applied uniform pressure, 2α = the angle at the disc's centre that defines the part of the disc's circumference under compression, R = the radius of the disc and $\bar{r} = r/R$ is the normalized radial coordinate.

For a loading width of 20 mm and a radius of 75 mm ($\alpha = 7.64^o$), the maximum stresses at the center of the disc ($\theta = 0$ and $\bar{r} = 0$) are:

$$\sigma_r(0,0) = \sigma_x = f_{sp} = 0.976\sigma \text{ and } \sigma_\theta(0,0) = \sigma_y = -2.976\sigma \tag{7}$$

where $\sigma = 2P/\pi LD$, P =total load, L= cylinder's length and $D = 2R$ = disc's diameter. Note that when $\alpha \to 0$, then $\sigma_x(0,0) = \sigma$ and $\sigma_y(0,0) = -3\sigma$, which corresponds to the idealized case of a disc subjected to a point load.

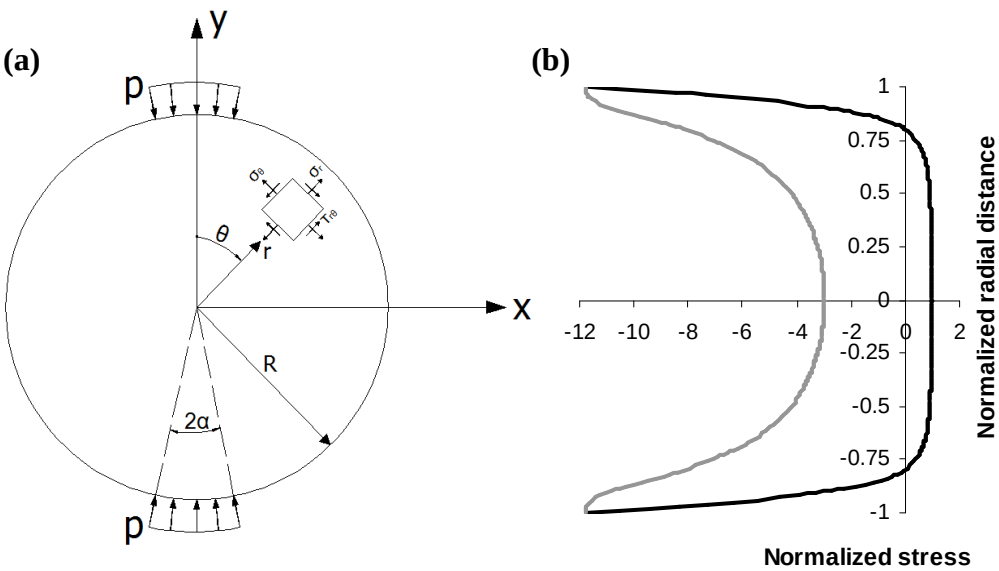

Fig. 5 (a) Disc subjected to diametrically opposite compression (b) Normalized principal stress distribution along the y-axis for σ_y/σ and σ_x/σ .

Institutional Repository - Library & Information Centre - University of Thessaly
15/10/2023 05:52:39 EEST - 167.114.118.212

The principal stresses are shown in Fig. 5b and the corresponding strains along the x- and y-axis assuming plane-stress conditions, are[10]:

$$\varepsilon_r(\bar{r},\theta=\pi/2)=\varepsilon_x=-\frac{\sigma}{E}\frac{D}{d}\left(-(1+\nu)\frac{(1-\bar{r}^2)\sin 2\alpha}{\bar{r}^4+1-2\bar{r}^2\cos 2\alpha}+(1-\nu)\cot^{-1}\left(\frac{1+\bar{r}^2}{1-\bar{r}^2}\cot\alpha\right)\right) \quad (8)$$

$$\varepsilon_r(\bar{r},\theta=0)=\varepsilon_y=-\frac{\sigma}{E}\frac{D}{d}\left((1+\nu)\frac{(1-\bar{r}^2)\sin 2\alpha}{\bar{r}^4+1-2\bar{r}^2\cos 2\alpha}+(1-\nu)\tan^{-1}\left(\frac{1+\bar{r}^2}{1-\bar{r}^2}\tan\alpha\right)\right) \quad (9)$$

where E =Young's modulus, ν =Poisson's ratio and d =loading width.

For the strain measurements on each flat face of the cylinder specimens, the ratio $\varepsilon_y/\varepsilon_x$ yields an estimate for the Poisson's ratio, ν and for an assumed value of ν (ν=0.2 was assumed in the present study) the ratios σ/ε_x and σ/ε_y yield two independent estimates for the Young's modulus of elasticity, E_{sp}^{t} and E_{sp}^{c}, respectively (see Fig. 6, experimental results using the 1st configuration shown in Fig. 1). It is noted that the split cylinder test has also been used by others[15-17] to determine a value for Young's modulus and Poisson's ratio.

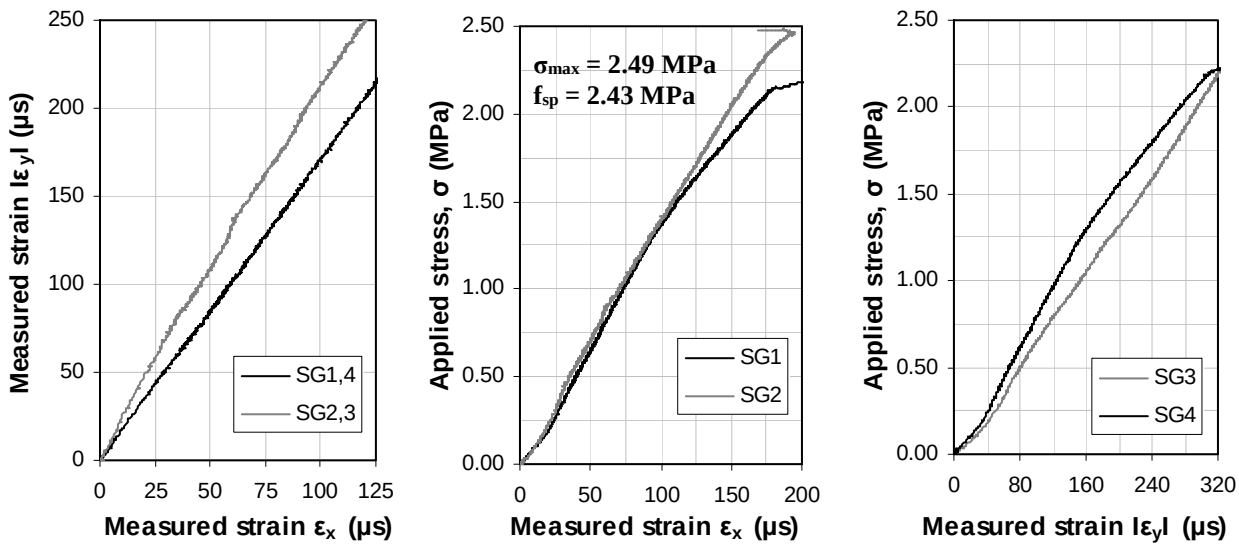

Fig. 6. Split cylinder test tensile strain SG measurements on the flat cylinder faces for the LC mix: (a) ε_y vs. ε_x, (b) σ vs. ε_x and (c) σ vs. ε_y.

A number of studies[18-20] have examined the failure mechanism of concrete under the biaxial stress state present in a split cylinder test by monitoring the evolution of microcracking. They found that cracking starts at approximately 70% of the peak load and that the geometry and that the test

Institutional Repository - Library & Information Centre - University of Thessaly
15/10/2023 05:52:39 EEST - 167.114.118.212

setup may significantly affect this value. In the present study, the Young's modulus and Poisson's ratio estimates were determined based on the slope of the principal stress-strain curve between a stress at a tensile strain of 30 μs and a stress at 50% of the peak stress, since non-linearity was apparent around 60% of the peak tensile stress (see Fig. 5b). The tensile and compressive strains that correspond to 50% of the peak values are plotted against the splitting tensile strength in Fig. 7. It is interesting to notice that the strain values corresponding to the 50% of the peak load are approximately the same for both concrete and cement mortar mixes and are not significantly affected from the material's strength.

The measured splitting to compressive strength ratio together with the results of empirical formulae[21-23] are plotted versus the compressive strength for each mix in Fig. 8 (f_c and f_{sp} values are shown in Table 3). Good agreement with the empirical equations is observed for the normal- and medium-strength concrete and less so for the low-strength concrete although the deviation is not significant. The empirical equations are not applicable to cement mortar which is also included in Fig. 8.

Finally, it is noted that a gradient elasticity solution to any problem reduces to the classical solution if the internal length is zero ($g = 0$) or if the stress gradient is zero ($\partial\sigma_{ij} / \partial x_k = 0$). In the split cylinder test, the stress distribution is approximately uniform near the center of the cylinder where the measurements are made (see Fig. 5b) resulting in a negligibly small stress gradient ($\partial\sigma_{r\theta} / \partial r \cong 0$). This implies that the measured Young's modulus and Poisson's ratio from the split cylinder test can be seen as independent of the gradient internal length of the material as is the case for the uniaxial cylinder compression test as well.

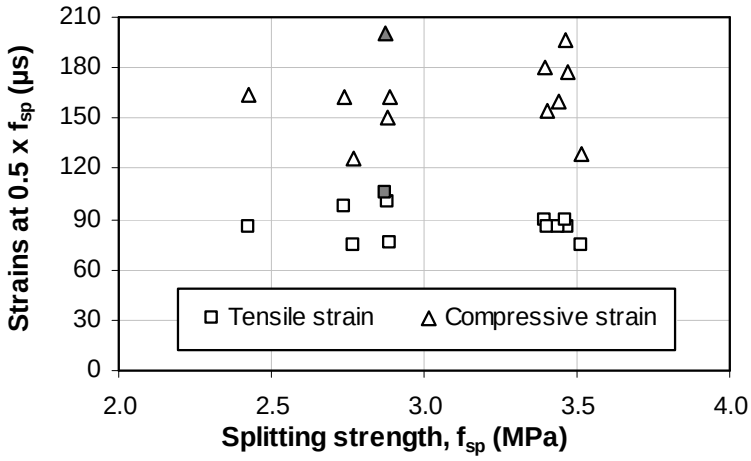

Fig. 7. Tensile and compressive strains at 50% of the splitting strength vs. splitting strength (solid symbols are for CM mix).

Institutional Repository - Library & Information Centre - University of Thessaly
15/10/2023 05:52:39 EEST - 167.114.118.212

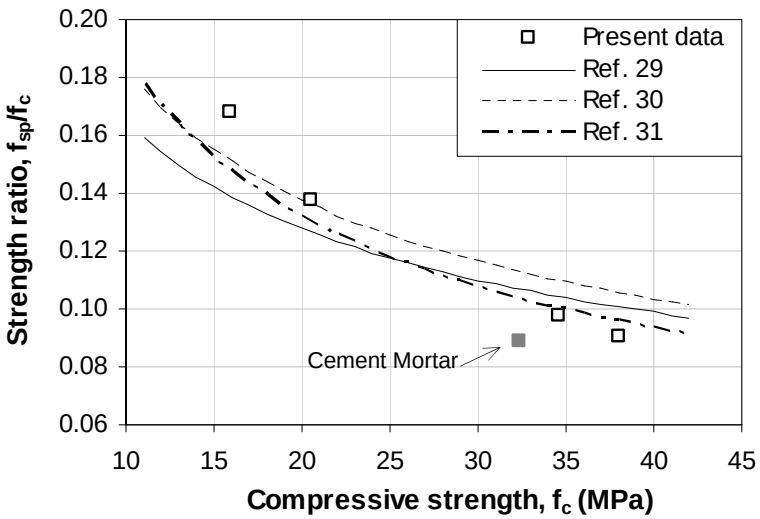

Fig. 8. Splitting to compressive strength ratio vs. compressive strength.

4. FOUR-POINT BENDING TESTS

Setup and specimens

A total of seventy-one (71) geometrically similar beam specimens with an aspect ratio of L/h=3 (see Table 5) were tested under 4-point bending. The three (3) nominal beam sizes considered have dimensions of 100x100x300 (width x height x span) mm (**S1**), 150x150x450 mm (**S2**) and 200x200x600 mm (**S3**). The specimens were tested using an MTS ± 250 kN hydraulic actuator under midspan deflection-control. The midspan deflection was the average of two DC displacement transducers (DCDT's) measurements one on each side of the specimen. Two instrumentation configurations were used for estimating the beam curvature: either using two SG's placed at midspan in the axial direction (one at the top and one at the bottom fiber of the cross-section) or four SG's placed at midspan in the axial direction (two on each side of the beam at a distance 2 or 1 cm from the top and bottom fiber). For a limited number of specimens both arrangements were used (see Fig. 11). The experimental setup is shown in Fig. 9 together with a detailed representation of the instrumentation.

The beam specimens of each mix were cured together with the cylinder and cube specimens in the same environmental conditions and the date of testing for each mix is included in Table 3. The uniaxial compression, split cylinder tension and 4-point bending tests for each mix were conducted in parallel and were completed in less than a two weeks period.

Institutional Repository - Library & Information Centre - University of Thessaly
15/10/2023 05:52:39 EEST - 167.114.118.212

Table 5. Experimental program.

Specimen size	Number of specimens tested				
	CM	**LC**	**NC**	**MC1**	**MC2**
S1	3 (3)	8 (4)	8 (4)	8 (4)	4 (3)
S2	2 (0)	7 (3)	7 (2)	8 (2)	4 (3)
S3	2 (0)	3 (1)	3 (2)	2 (0)	2 (0)

Note: Number in parenthesis denotes the number of specimens with strain gage instrumentation.

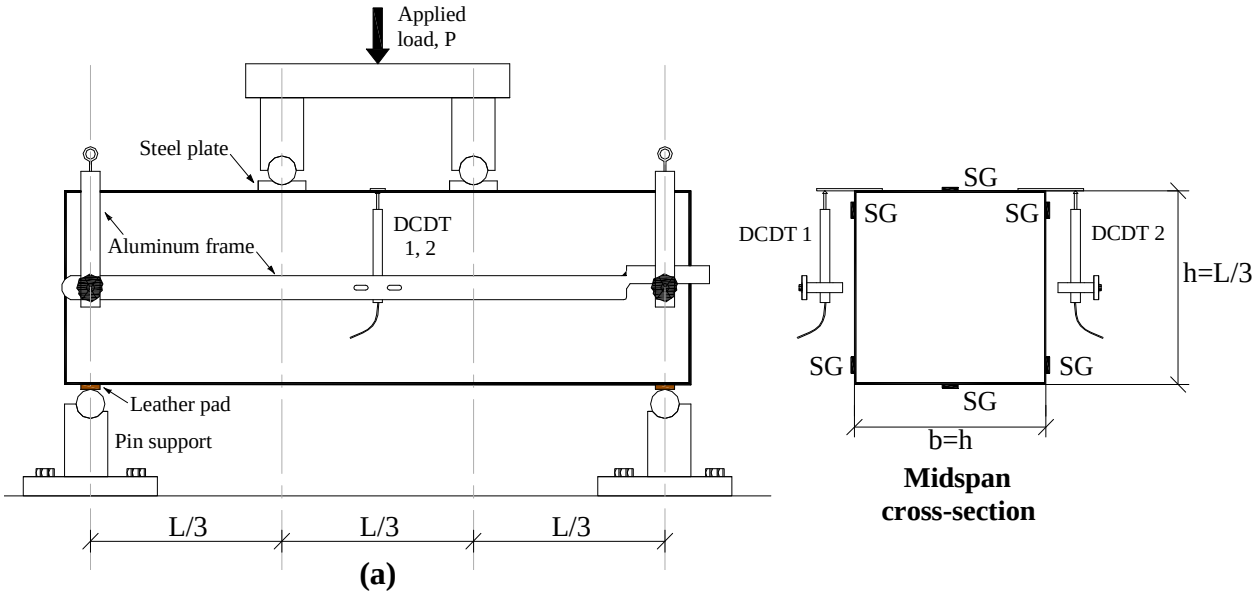

(a)

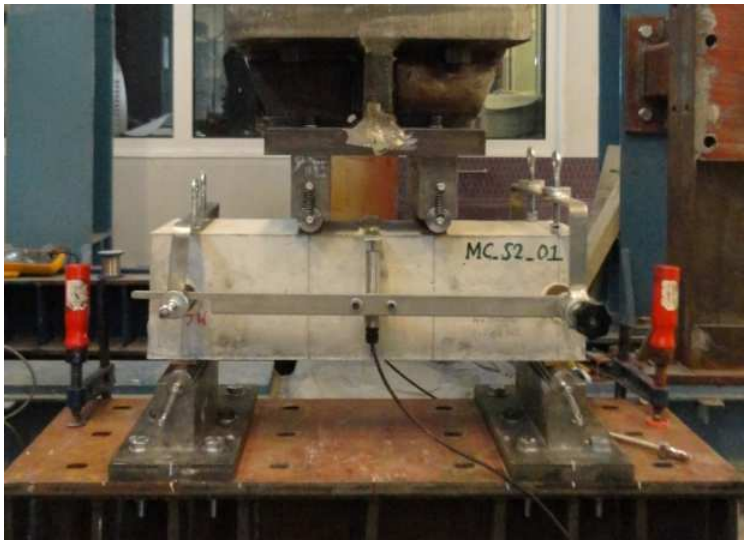

(b)

Fig. 9. Experimental setup for the 4-point bending tests: (a) schematic of the testing setup and (b) photo for size S2 beam specimen.

Institutional Repository - Library & Information Centre - University of Thessaly
15/10/2023 05:52:39 EEST - 167.114.118.212

Experimental post-peak softening response

The post-peak flexural response of the concrete beams tested under 4-point bending is captured by displacement control. A DCDT located at midspan was used as the controlling displacement sensor and all tests were performed at a constant rate of 0.001 mm/sec. However, once softening initiates, the experiment becomes unstable since energy is released back from the elastically deformed steel reaction frame where the hydraulic load actuator is attached to[8]. Before the peak load is reached the hydraulic jack is moving downwards increasing the applied load but after the peak load is reached, through the controller the jack's cylinder moves upwards resulting in unloading of the beam specimen. This is done through a Proportional-Integral-Derivative (PID) closed-loop feedback algorithm[24] of the Flex-40 MTS controller[25]. The choice of the proper PID value is essentially done through a trial and error procedure since it is specific to the experimental setup used (stiffness of the reaction frame) and the stiffness of the specimen. This procedure unavoidably resulted in the loss of the post-peak response for some of the specimens. The specimens for which a post-peak softening branch was captured successfully for each mix and specimen size considered in this work are listed in Table 6. Concerning the CM mix, although various PID values were used, the post-peak response was lost for all specimens. It appears that the response of the CM specimens in the post-peak softening branch was the most brittle, resulting in an extremely unstable crack growth. Note that for the rest of the concrete specimens, even when the post-peak response was not fully recorded, failure was not catastrophic since the specimen didn't collapse although it was almost fully cracked.

Table 6 - Number of beam specimens with recorded post-peak softening branch.

Specimen size	Mix				
	CM	**LC**	**NC**	**MC1**	**MC2**
S1	0 (3)	7 (8)	0 (8)	6 (8)	5 (5)
S2	0 (3)	6 (7)	4 (7)	8 (8)	3 (5)
S3	0 (3)	3 (3)	3 (3)	3 (3)	2 (3)

Note: number in the parenthesis denotes the total number of tested specimens

Institutional Repository - Library & Information Centre - University of Thessaly
15/10/2023 05:52:39 EEST - 167.114.118.212

CHAPTER VI

SIZE EFFECT OF CEMENTITIOUS MATERIALS IN ELASTICITY

1. INTRODUCTION

The aim of this work is to demonstrate that size effect in elasticity exists in composite materials when the size of the microstructural details is comparable with the macrostructure. On that respect, cementitious materials such as concrete are ideal since they can be viewed as composites with inclusions (aggregates, fibers etc.) embedded in a matrix material. It is noted that this simplified view of the microstructure of concrete is sufficient for the aim and purposes of gradient elasticity which attempts to introduce a new constitutive parameter (length) that accounts for the influence that the meso-scale microstructure has on the macrostructural response. So far, the attention of researchers to gradient elasticity was motivated from flexural tests on micro-beams and this field was the first actual implementation of these theories[4]. In this work, in order to test the hypothesis that for a given composite a certain microstructure can result in size effect phenomena in elasticity, four (4) concrete mixes of maximum aggregate size d_{max}=32 mm and cement mortar of d_{max}=1 mm are considered. However, the scale of the microstructure is not the only factor that affects size effect phenomena. The relative stiffness of the two phases in a composite, i.e. matrix and inclusions, is an equally significant factor[5]. To investigate this issue, similar component volume fractions and aggregate gradation is used for the four (4) concrete mixes considered, while the water to cement (w/c) of the mixes is altered from 0.78 to 0.45 (low to medium strength concrete).

2. ELASTIC STIFFNESS AND CURVATURE

The measured elastic stiffness and curvature data of the flexural response for each specimen reported here correspond to the slope between a load level of 10% and that of 50% of the peak applied load. The experimental to classical elastic flexural stiffness ratio is plotted vs. the nominal beam size in Figs. 1(a) to 1(e). The curvature estimates correspond to the stiffness ratio with the internal length estimate derived from Eq. (45) in Section IV.6 and substituted back to Eq. (41) in Section IV.6. Also, the theoretical predictions of the dipolar elasticity model for different beam sizes and for different values of the gradient internal length are shown in Fig. 1. The experimental results are also presented in Tables 1 to 5.

The experimental applied total load vs. midspan curvature results for a representative MC1-S1 specimen are shown in Fig. 2. A total of six SG's are attached to that specimen. It is noted that

Institutional Repository - Library & Information Centre - University of Thessaly
15/10/2023 05:52:39 EEST - 167.114.118.212

two types of axial SG's were used: 20-mm long (SG2, SG3, SG4, SG5) and 10-mm long SG's (SG0, SG1).

For this particular setup, the following observations were made:

i) the SG's in tension (SG0 and SG2) at the two opposite vertical beam faces record practically the same strain indicating that the concrete strain measurements appear not to be affected by the SG lengths used, while the SG at the extreme bottom tensile fiber (SG4) records higher strains than SG0 and SG2 for the same load level, as it should (see Fig. 2b),

ii) the SG at the top extreme fiber of the compression zone (SG5) records lower values than it should, practically the same as those of SG1 and SG3 on the side faces (see Fig. 2c),

iii) midspan curvature estimates derived from the SG measurements on the vertical beam faces predict a n.a. location that deviates less than 5% from the centroid of the cross-section, while if the top/bottom extreme fiber SG measurements are used the deviation is more than 15% because of the unreasonably high measured strains at the bottom extreme fiber (SG4),

iv) the measured elastic force to curvature ratio value of S=7.64 Nm for this specimen (see Fig. 2d) is based on the average of the consistent in terms of the n.a. prediction curvature measurements (SG0, SG1, SG2 and SG3).

Based on the midspan deflection and curvature measurements, the gradient internal length estimate for specimen MC1-S1 was $g_K = 10.6$ mm and $g_S = 11.6$ mm, respectively, while the overall average gradient internal length of the mix MC1 was found to be $g_{MC1} = 12.3 \pm 2.3$ mm (see Fig. 5).

Institutional Repository - Library & Information Centre - University of Thessaly
15/10/2023 05:52:39 EEST - 167.114.118.212

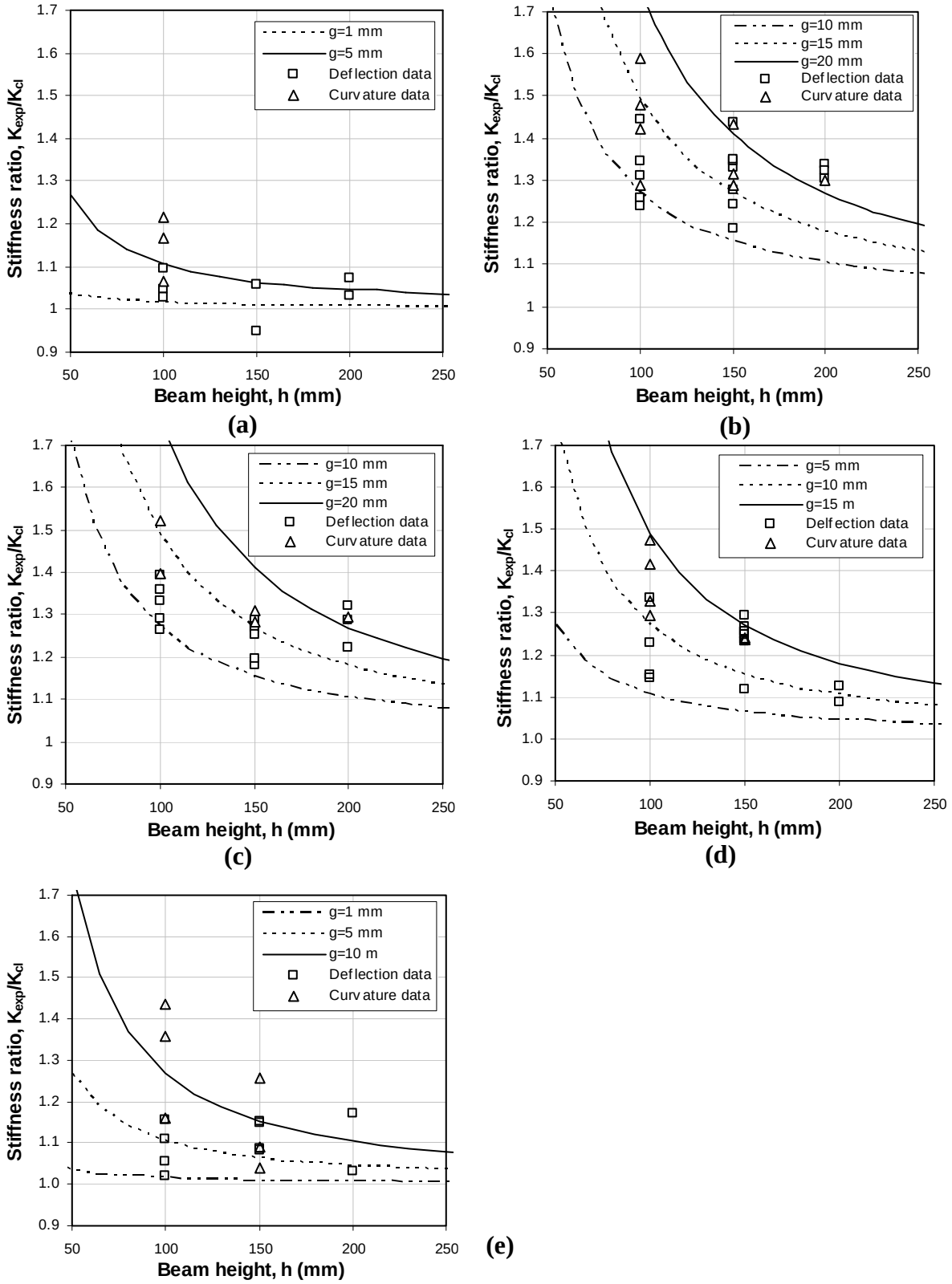

Fig. 1 – Experimental to classical elastic flexural stiffness ratio: (a) mix CM, (b) mix LC, (c) mix NC, (d) mix MC1 and (e) mix MC2.

Institutional Repository - Library & Information Centre - University of Thessaly
15/10/2023 05:52:39 EEST - 167.114.118.212

Table 1 - Experimental results in the elastic response range of CM mix.

Specimen Code	Average Dimensions		Stiffness, K = P/δ (N/m)				Curvature Coefficient, S = P/k (Nm)			
	b	h	K_{cl}	K_{exp}	K_{exp}/K_{cl}	g_K [(a)]	S_{cl}	S_{exp}	S_{exp}/S_{cl}	g_S [(b)]
	(mm)	(mm)				(mm)				(mm)
CM-S1-01	100.7	100.3	341.67	357.75	1.047	2.6	4.190	4.251	1.014	3.4
CM-S1-02	100.5	100.2	340.14	349.63	1.028	1.6	4.170	4.541	1.089	8.5
CM-S1-03	99.9	100.2	338.20	371.06	1.097	4.7	4.146	4.400	1.061	7.1
CM-S2-02	150.0	149.9	505.29	535.23	1.059	4.7	-	- (**)	-	-
CM-S2-03	150.6	150.7	514.27	487.43	0.948	0.0	-	- (**)	-	-
CM-S3-01	197.6	198.6	654.23	675.28	1.032	3.7	-	- (**)	-	-
CM-S3-02	198.6	198.6	657.54	705.00	1.072	7.3	-	- (*)	-	-

[(a)] internal length estimate based on the stiffness ratio (see Eq. 41 in section IV.6)
[(b)] internal length estimate based on the curvature coefficient ratio (see Eq. 45 in section IV.6).
[(**)] data not used, [(*)] not measured

Table 2 - Experimental results in the elastic response range of LC mix.

Specimen Code	Average Dimensions		Stiffness, K = P/δ (N/m)				Curvature Coefficient, S = P/k (Nm)			
	b	h	K_{cl}	K_{exp}	K_{exp}/K_{cl}	g_K [(a)]	S_{cl}	S_{exp}	S_{exp}/S_{cl}	g_S [(b)]
	(mm)	(mm)				(mm)				(mm)
LC-S1-01	99.4	100.9	384.89	517.50	1.345	11.9	-	- (*)	-	-
LC-S1-02	100.1	101.5	393.22	567.75	1.444	14.1	-	- (*)	-	-
LC-S1-03	99.8	101.2	388.44	485.22	1.249	9.5	-	- (*)	-	-
LC-S1-04	99.5	101.5	390.98	484.60	1.239	9.2	-	- (*)	-	-
LC-S1-05	99.7	102.0	396.21	497.74	1.256	9.7	4.896	6.881	1.405	17.2
LC-S1-06	100.2	101.4	392.58	515.56	1.313	11.1	4.839	6.277	1.297	14.8
LC-S1-07	99.6	102.1	-	- [(**)]	-	-	4.904	6.117	1.247	13.7
LC-S1-08	100.2	101.6	-	- (**)	-	-	4.869	5.553	1.141	10.6
LC-S2-01	149.3	152.3	593.59	704.94	1.188	11.7	-	N.M.	-	-
LC-S2-02	149.9	150.7	578.74	830.69	1.435	20.8	-	N.M.	-	-
LC-S2-03	150.4	152.7	592.82	788.51	1.330	17.2	-	N.M.	-	-
LC-S2-04	151.0	150.2	602.63	811.53	1.347	17.8	16.77	21.039	1.255	20.7
LC-S2-05	150.6	150.6	586.17	790.66	1.349	17.9		- (**)		
LC-S2-06	150.4	151.2	596.09	761.89	1.278	15.3	16.56	18.841	1.138	15.6
LC-S2-07	150.2	152.7	607.65	755.84	1.244	13.9	16.94	19.618	1.158	16.6
LC-S3-01	197.9	198.8	753.42	981.53	1.303	21.5	-	- (**)	-	-
LC-S3-02	199.0	200.0	738.73	989.80	1.340	23.3	36.12	41.336	1.144	21.1
LC-S3-03	199.5	199.5	749.14	992.35	1.325	22.5	-	- (**)	-	-

[(a)]Internal length estimate based on the stiffness ratio (see Eq. 41 in section IV.6)
[(b)]Internal length estimate based on the curvature coefficient ratio (see Eq. 45 in section IV.6).
[(**)]data not used, [(*)] not measured.

Institutional Repository - Library & Information Centre - University of Thessaly
15/10/2023 05:52:39 EEST - 167.114.118.212

Table 3 - Experimental results in the elastic response range of NC mix

Specimen Code	Average Dimensions		Stiffness, K = P/δ (N/m)				Curvature Coefficient, S = P/k (Nm)			
	b	h	K_{cl}	K_{exp}	K_{exp}/K_{cl}	g_K [(a)]	S_{cl}	S_{exp}	S_{exp}/S_{cl}	g_S [(b)]
	(mm)	(mm)				(mm)				(mm)
NC-S1-01	101.0	102.0	493.22	671.06	1.361	12.3	-	- (*)	-	
NC-S1-03	99.4	100.7	469.32	605.95	1.291	10.5	-	- (*)	-	
NC-S1-04	101.2	102.0	494.76	658.40	1.331	11.6	-	- (*)	-	
NC-S1-05	99.5	101.8	483.15	673.49	1.394	13.1	-	- (*)	-	
NC-S1-06	100.9	101.7	-	- (**)	-	-	6.036	7.394	1.225	13.1
NC-S1-07	99.4	102.7	-	- (**)	-	-	6.125	8.190	1.337	15.9
NC-S1-08	100.6	101.8	488.03	617.24	1.265	10.0	-	- (*)	-	-
NC-S2-01	149.3	152.3	719.76	848.85	1.179	11.3	-	- (*)	-	-
NC-S2-02	149.9	150.7	703.61	902.75	1.283	15.5	-	- (*)	-	-
NC-S2-03	150.4	152.7	730.57	940.20	1.287	15.8	-	- (*)	-	-
NC-S2-04	151.0	150.2	703.21	892.15	1.269	14.9	-	- (*)	-	-
NC-S2-05	150.6	150.6	706.43	897.31	1.270	15.0	-	- (**).	-	-
NC-S2-06	150.4	151.2	712.13	892.86	1.254	14.4	19.69	22.735	1.154	16.5
NC-S2-07	150.2	152.7	728.84	872.15	1.197	12.1	20.24	22.968	1.135	15.6
NC-S3-01	197.9	198.8	903.88	1163.3	1.287	20.6	-	- (**)	-	-
NC-S3-02	199.0	200.0	923.55	1128.8	1.222	17.3	-	- (**)	-	-
NC-S3-03	199.5	199.5	919.95	1215.6	1.321	22.4	45.03	51.529	1.144	21.1

[(a)] Internal length estimate based on the stiffness ratio (see Eq. 41 in section IV.6)
[(b)] Internal length estimate based on the curvature coefficient ratio (see Eq. 45 in section IV.6).
[(**)] data not used, [(*)] not measured

Institutional Repository - Library & Information Centre - University of Thessaly
15/10/2023 05:52:39 EEST - 167.114.118.212

Table 4 - Experimental results in the elastic response range of MC1 mix.

Specimen Code	Average Dimensions		Stiffness, K = P/δ (N/m)				Curvature Coefficient, S = P/k (Nm)			
	b	h	K_{cl}	K_{exp}	K_{exp}/K_{cl}	g_K [(a)]	S_{cl}	S_{exp}	S_{exp}/S_{cl}	g_S [(b)]
	(mm)	(mm)				(mm)				(mm)
MC1-S1-02	100.9	103.4	543.68	647.00	1.190	7.9	-	- (*)	-	-
MC1-S1-03	100.4	102.6	529.96	708.99	1.338	11.9	-	- (*)	-	-
MC1-S1-05	99.7	102.7	526.97	678.86	1.288	10.6	6.531	7.636	1.169	11.6
MC1-S1-06	100.0	103.3	537.70	660.51	1.228	9.0	6.684	7.646	1.144	10.9
MC1-S1-07	99.6	102.3	-	- (**)	-	-	6.448	8.004	1.241	13.6
MC1-S1-08	99.7	102.4	523.11	662.54	1.267	10.0	6.475	8.378	1.294	14.9
MC1-S2-01	150.6	151.4	762.85	967.82	1.269	15.0	-	- (*)	-	-
MC1-S2-02	149.6	154.3	795.08	981.83	1.235	13.8	-	- (*)	-	-
MC1-S2-03	149.8	153.4	783.51	979.52	1.250	14.4	-	- (*)	-	-
MC1-S2-04	150.5	153.1	783.30	876.87	1.119	8.3	21.783	24.02	1.103	13.8
MC1-S2-05	150.1	151.1	756.27	950.48	1.257	14.5	20.914	23.10	1.105	13.8
MC1-S2-06	150.8	153.9	795.86	998.12	1.254	14.6	-	- (**)	-	-
MC1-S2-07	150.0	153.3	783.51	970.20	1.238	13.9	-	- (*)	-	-
MC1-S2-08	150.0	153.0	779.79	1009.6	1.295	16.1	-	- (*)	-	-
MC1-S3-01	200.9	200.8	1003.7	1128.3	1.124	11.3	-	- (**)	-	-
MC1-S3-03	200.0	200.4	994.0	1081.6	1.088	8.6	-	- (**)	-	-

[(a)]Internal length estimate based on the stiffness ratio (see Eq. 41 in section IV.6)
[(b)]Internal length estimate based on the curvature coefficient ratio (see Eq. 45 in section IV.6).
[(**)]data not used, [(*)] not measured

Table 5 - Experimental results in the elastic response range of MC2 mix.

Specimen Code	Average Dimensions		Stiffness, K = P/δ (N/m)				Curvature Coefficient, S = P/k (Nm)			
	b	h	K_{cl}	K_{exp}	K_{exp}/K_{cl}	g_K [(a)]	S_{cl}	S_{exp}	S_{exp}/S_{cl}	g_S [(b)]
	(mm)	(mm)				(mm)				(mm)
MC2-S1-01	100.7	103.4	563.42	625.00	1.109	5.2	-	- (*)	-	-
MC2-S1-02	99.5	102.8	-	- (**)	-	-	6.799	8.570	1.260	14.1
MC2-S1-04	99.9	102.7	548.99	579.25	1.055	3.0	6.804	8.130	1.195	12.4
MC2-S1-05	100.2	103.3	559.97	647.10	1.156	6.9	6.961	7.343	1.055	8.9
MC2-S2-01	150.1	152.9	810.11	879.65	1.086	6.4	22.518	22.659	1.006	3.4
MC2-S2-02	150.8	152.7	811.15	935.35	1.153	10.0	-	- (*)	-	-
MC2-S2-03	150.0	153.0	810.92	878.38	1.083	6.3	22.548	23.055	1.023	6.7
MC2-S2-05	150.8	150.9	787.57	905.95	1.150	9.8	21.766	24.304	1.117	14.5
MC2-S3-01	200.3	200.8	1040.1	1217.6	1.171	14.4	-	- (**)	-	-
MC2-S3-03	199.5	200.8	1035.3	1068.5	1.032	3.7	-	- (*)	-	-

[(a)]Internal length estimate based on the stiffness ratio (see Eq. 41 in section IV.6)
[(b)]Internal length estimate based on the curvature coefficient ratio (see Eq. 45 in section IV.6).
[(**)]data not used, [(*)] not measured

Institutional Repository - Library & Information Centre - University of Thessaly
15/10/2023 05:52:39 EEST - 167.114.118.212

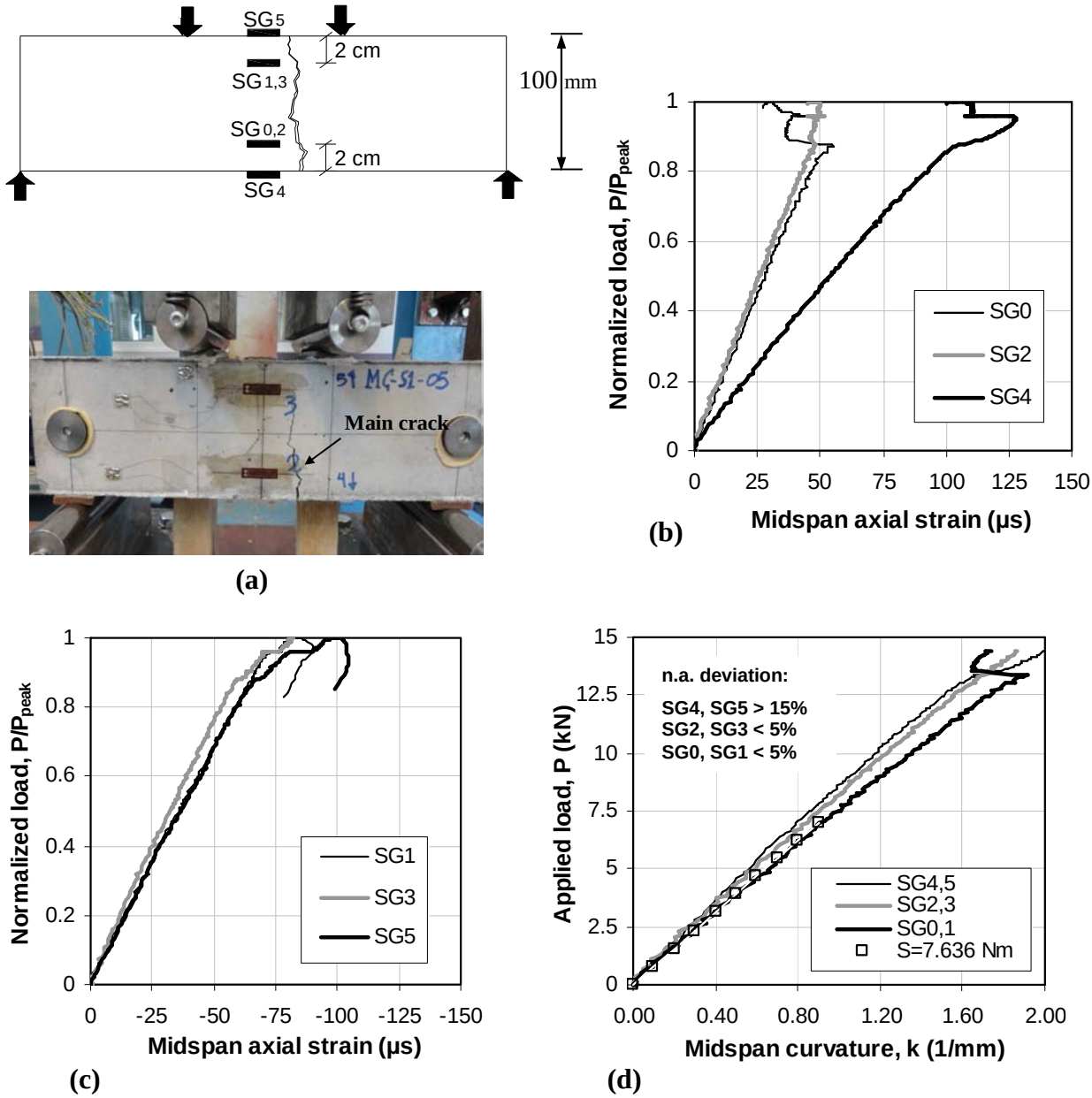

Fig. 2. Experimental data for beam size S1 of MC1 mix: (a) schematic and photo of the experimental setup, (b) normalized applied load vs. tensile axial strain, (c) normalized applied load vs. compressive axial strain and (d) applied load vs. calculated midspan curvature based on the strain measurements.

Institutional Repository - Library & Information Centre - University of Thessaly
15/10/2023 05:52:39 EEST - 167.114.118.212

3. DISCUSSION OF RESULTS

In this section, the magnitude and the observed scatter of the gradient internal length estimate is discussed with reference to the details of the material's microstructure. It is noted that for a gradient elasticity theory:

(i) the predicted internal length based on curvature and deflection experimental data should be the same for all sizes and

(ii) for a given material, a consistent model should be able to predict adequately its flexural response with an estimated internal length value independent of the specimen size.

Influence of the microstructure on the gradient internal length

The gradient internal length is an additional constitutive parameter which is introduced for modeling the details of the material's microstructure. It has the dimension of length because it is introduced in association with the strain gradient[6]. Thus, it is reasonable to assume that its magnitude is related to the dominant feature of the microstructure. However, this correlation is done in an average sense, since the microstructure incorporates many scales and this is especially true for concrete which contains inclusions of various sizes (aggregate gradation) and of different volume fractions (see Fig. 3a). Furthermore, in the case of concrete one can only control the quantities of the different constituents, but after mixing and casting the actual locations of the aggregate particles is completely random, and it is possible for a given mix to have different microstructural details in specimens of the same size. This is especially true for the beam specimen size S1 with cross-sectional dimensions only about 3 times the maximum aggregate size of d_{max}=32 mm. Thus, it is reasonable to expect a significantly higher scatter and difference between the internal length estimates based on curvature measurements and those based on deflection data for specimen size S1 than for larger sizes S2 and S3. This can be attributed to the lack of the necessary material volume for the average prevalent microstructural details of the mix to be represented at any cross-section. It is true that gradient theories are continuum theories, in which although what constitutes a representative volume element (RVE) for the material is not directly addressed, it is always presupposed in the analysis. However, in terms of consistency of the theory the influence of the RVE on the gradient internal length is ''naturally'' accounted for by the present model, since for decreasing the size the scatter in the predicted stiffness ratios is predicted to increase as well (see theoretical curves of Fig. 1).

Institutional Repository - Library & Information Centre - University of Thessaly
15/10/2023 05:52:39 EEST - 167.114.118.212

The results for the CM (cement mortar) mix, which can be perceived as almost homogeneous mix relative to the other concrete mixes (see Fig. 3b), show that even the gradient model predictions for g = 1 mm does not deviate much from the classical elasticity predictions (see Fig. 1a). Furthermore, experimental elastic stiffness ratio values higher and lower than 1 with a scatter less than 10% were obtained for the majority of the cases. The CM mix was also the most brittle of all the mixes resulting in relatively smoother crack surfaces. For the concrete mixes, on the other hand, significantly rougher crack surfaces were obtained due to the presence of larger size aggregates. In addition, as the strength of the material increases the less torturous the crack surface is expected and more aggregates will fracture along the crack path (see Fig. 4). This is due to the fact that the matrix and inclusion heterogeneity is reduced and hence a crack will not be forced to change direction. Thus, the gradient internal length value should decrease with increasing compressive strength (or Young's modulus of elasticity) and should decrease with decreasing average inclusion size[5,7].

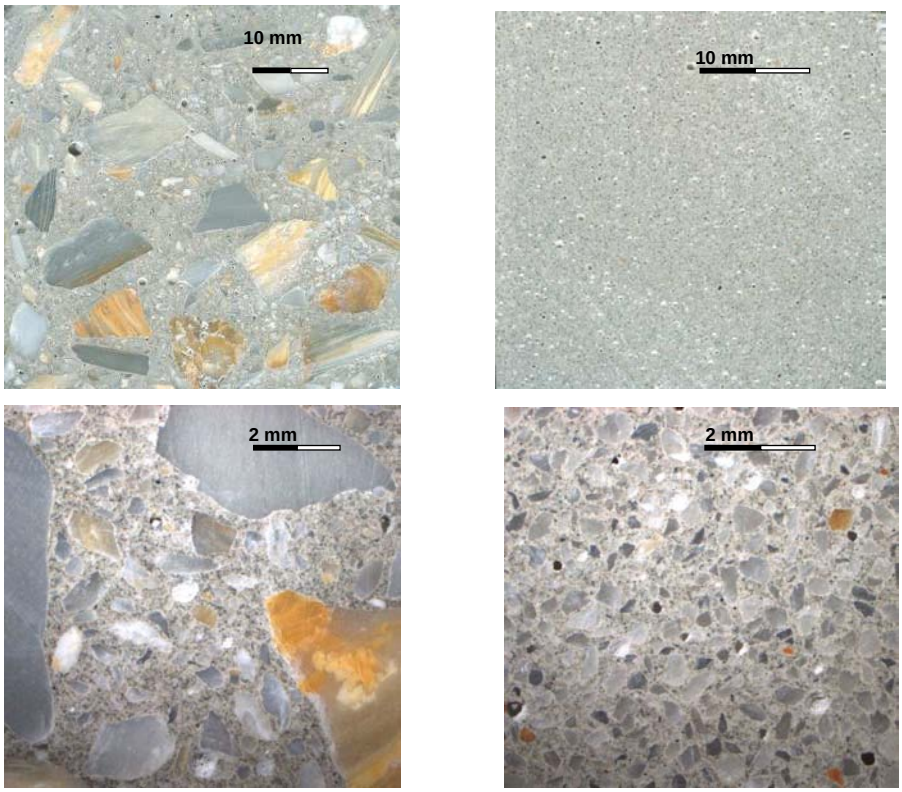

(a) **(b)**

Fig. 3 – Microstructure at different scales: (a) concrete, (b) cement mortar.

Institutional Repository - Library & Information Centre - University of Thessaly
15/10/2023 05:52:39 EEST - 167.114.118.212

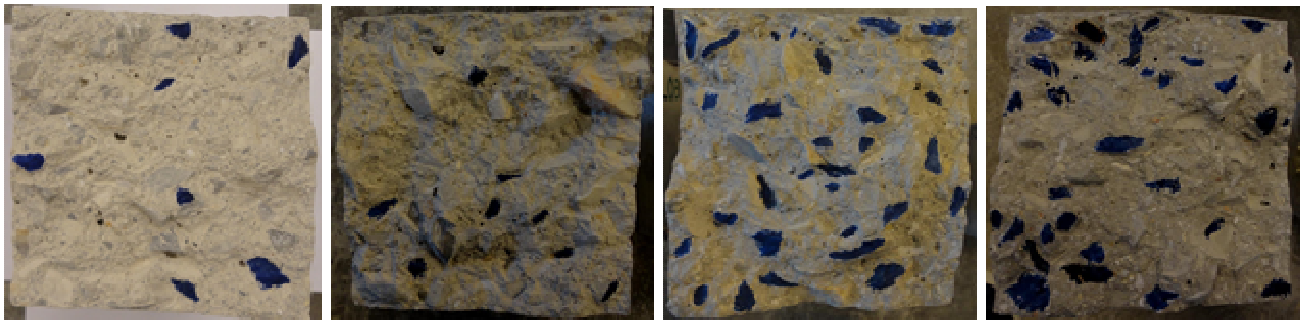

(a) **(b)** **(c)** **(d)**

Fig. 4 – Cross-sectional fracture surfaces 150x150 mm for specimen size S2 (a) mix LC, (b) mix NC, (c) mix MC1 and (d) mix MC2 (marked areas denote fractured aggregates).

The average gradient internal length estimate considering all tested specimens for each mix is plotted versus the Young's modulus of elasticity in Fig. 5. It is noted that estimates of the gradient internal length of up to 4.8 mm for size S1, 7.2 mm for size S2 and 9.6 mm for size S3 correspond to a stiffness ratio of K_{exp}/K_{cl}=1.1. Therefore, also shown with dashed line in Fig. 5, is the average gradient internal length limit value of 7.2 mm which can be seen as a lower limit for the experimental findings for size effect in elasticity. Internal length estimates lower than this value can be interpreted as proof of insignificant size effect in elasticity and vice versa. A size effect in elasticity is found only for the concrete mixes and not for the cement mortar and similar internal length values were determined for all mixes independently of the use of either the midspan deflection or the axial strain (curvature) measurements. Concerning the magnitude of the internal length of the concrete mixes, it is found to decrease with increase of the Young's modulus and is similar for mixes LC and NC. The first can be attributed to the decrease of the elastic mismatch of the mixes and the latter possibly indicates that above a specific inclusion to matrix stiffness ratio value, the internal length is less sensitive to further increasing this ratio (non-linear correlation between g and E for mixes with the same d_{max}).

Institutional Repository - Library & Information Centre - University of Thessaly
15/10/2023 05:52:39 EEST - 167.114.118.212

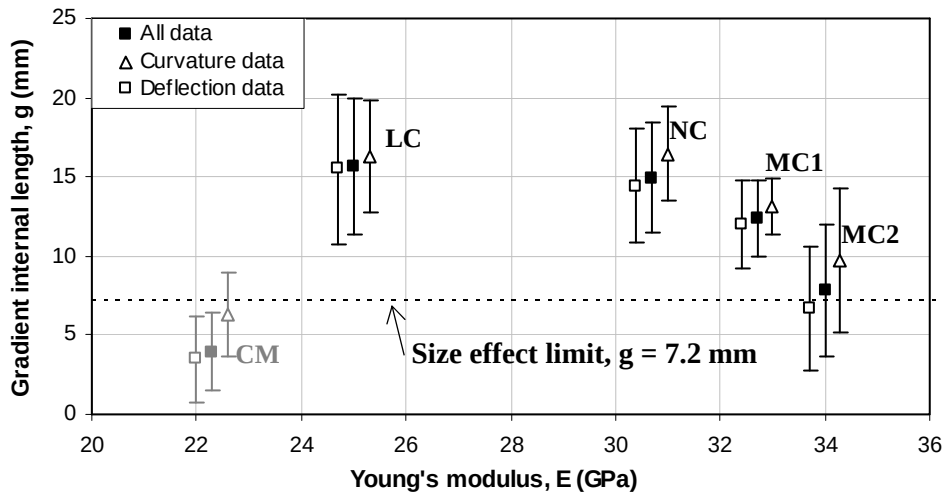

Fig. 5 – Gradient internal length estimate, g, for each mix vs. the Young's modulus of elasticity, E, based on the 4-point bending test results of geometrically similar beam specimens.

Gradient internal length and average inclusion size

The average size of the inclusions (d_{av}) for a concrete mix is difficult to define, because aggregates have irregular shapes and their average size can be easily up to 1.5 to 2 times the sieve opening used for gradation. In order to establish the average size of the material's microstructure, selected specimens of all sizes for each mix were sawed perpendicular to the beam axis at random locations. The average inclusion size was estimated using two methods. The first was to average their maximum size identified in a cross-sectional cut. The second method accounted for the irregular shape of the aggregates and the estimation of the average inclusion size was based on an average aggregate area. The shortcoming of the latter is that a nominal shape for the aggregates must be assumed in order to transform an average equivalent aggregate area on the plane of the saw-cut to an average length. Truly, heterogeneity is three-dimensional[8], while the above averaging methods are either 1D or 2D. The mapping of the microstructure for the MC1 mix for specimen size S1 using both methods is shown in Fig. 6. For this particular specimen, the first method yielded a value of $d_{av} \cong 12.9$ mm, whereas based on the second method the estimate depends on the assumed shape of the "equivalent" aggregate, i.e. for square-shaped aggregate, $d_{av} \cong 8.1$ mm, for circular-shaped, $d_{av} \cong 9.2$ and for equilateral triangular-shaped $d_{av} \cong 12.4$ mm. Given the angular shape of the aggregates used, the triangular shape seems more representative

The results on aggregate measurements from a total of twelve (12) cross-sectional cuts of the tested beam specimens are shown in Table 6. It is noted that aggregates with a maximum

Institutional Repository - Library & Information Centre - University of Thessaly
15/10/2023 05:52:39 EEST - 167.114.118.212

dimension of less than 5 mm were assumed to be part of the matrix material. It is obviously rather difficult to determine the average inclusion size for heterogeneous materials such as concrete. The measurements included in Table 6 suggest an “average” inclusion size ranging from 10 to 20 mm for all mixes, thus verifying that all concrete mixes have approximately the same microstructure (see also Tables V.1 and V.2). This “average” inclusion size range corresponds to a gradient internal length value of about 15 mm with a $\pm 30\%$ scatter. The standard deviation for the internal length estimate based on the 4-point bending test results is 27.4%, 22.8%, 19.5% and 52.6% for mixes LC, NC, MC1 and MC2, respectively (see Fig. 14). This can explain most of the scatter observed without considering the experimental errors and uncertainties accompanying the measurements. On the other hand, the apparent association of the measured average aggregate size with the gradient internal length estimates for the low- and normal-strength concrete mixes is far too good to be coincidental since the internal length value was found to be $g = 15.7 \pm 4.3$ and 14.9 ± 3.4 mm for the LC and NC mixes, respectively. It is concluded that the gradient internal length is about equal to the average inclusion size of a composite material provided that the heterogeneity is high (high of matrix and inclusions mismatch) as in the low-strength concrete. For lower values of the elastic mismatch as in the case of the higher-strength concrete mixes (MC1 and MC2), the internal length estimate based on the experimental results for MC1 and MC2 is $g = 12.3 \pm 2.4$ and 7.8 ± 4.1 mm, respectively.

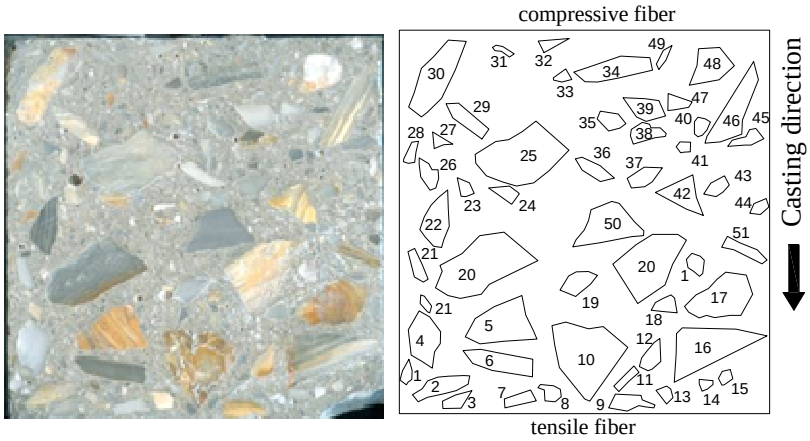

Fig. 6 – Mapping of the microstructure for estimating the “average” inclusion size in a 100 x100 mm cross-sectional cut of size S1 specimen for mix MC1.

Institutional Repository - Library & Information Centre - University of Thessaly
15/10/2023 05:52:39 EEST - 167.114.118.212

Table 6. Average inclusion size of the microstructure for particles larger than 5 mm.

Mix	d_{av} (mm) [(a)]			d_{av} (mm) [(b)]		
	S1	**S2**	**S3**	**S1**	**S2**	**S3**
LC	15.3	17.3	18.6	13.8	16.6	16.8
NC	11.8	14.7	16.8	11.5	13.7	15.4
MC1	12.9	13.2	16.4	12.4	12.7	15.8
MC2	13.5	14.7	16.0	12.5	14.2	15.0

[(a)] 1D averaging
[(b)] 2D averaging assuming equilateral triangle shape for aggregates

4. CONCLUSIONS

The size effect in elasticity was investigated using a Timoshenko dipolar elastic beam model[6] and the experimental results of un-notched geometrically similar beams of five (5) cementitious mixes (four concrete mixes with d_{max}=32 mm and one cement mortar mix with d_{max}=1 mm) tested under 4-point bending. The size effect was verified independently from both the experimental load versus midspan deflection and load versus midspan curvature data. The key findings of the present work can be summarized as follows:

1. A stiffer response than that predicted by classical elasticity theory is measured for cementitious composites with f_c up to 40 MPa in the flexural elastic response range of geometrically similar un-notched concrete beam specimens for specimen height to maximum aggregate size ratio values up to about 6.5.
2. The internal length introduced by the gradient theory and described in this work is estimated to be about equal to the average inclusion size of the material's microstructure for the lower-strength mixes considered in this study, while it is equal to about one-half of the average inclusion size for the medium-strength mixes. It appears that the internal length parameter value for a truly high-strength concrete mix with a compressive strength of above 45 MPa will be even lower.
3. The size effect in elasticity is affected by both the inclusion size and the elastic mismatch of the different phases of the composite, and it increases with increasing inclusion size and decreases with less elastic mismatch.

Institutional Repository - Library & Information Centre - University of Thessaly
15/10/2023 05:52:39 EEST - 167.114.118.212

CHAPTER VII

SIZE EFFECT OF CEMENTITIOUS MATERIALS IN INELASTICITY

1. INTRODUCTION

Size effect in elasticity was investigated and an estimate for the internal length ($g=g_0$) for the mixes considered was obtained based on a proposed gradient elasticity model. The microstructure of cementitious materials undergoes significant changes due to microcracking in the inelastic range of response. This in the context of a continuum damage formulation is defined as a degradation of the elastic material properties (softening). Therefore, the initial value of the internal length (g_0), should also be affected by this evolution of damage. Microcracking can be seen as a source of heterogeneity which augments any initial heterogeneity of the composite due to the presence of stiffer inclusions inside a matrix material (see chapter V). This implies that with increasing the accumulated microcracking activity (increasing accumulate damage), the initial value of the internal length g_0 should increase. A thermodynamic formulation of the problem[1] has shown this to be true.

The present experimental results are compared against the predictions of a gradient elasto-damage model[1] for the case of beams under flexure. Damage characterization is based on an assumed uniaxial stress-strain law for each mix and is defined in a classical manner through the use of a damage parameter D ($0 \le D \le 1$), with D=0 signifying elastic behavior and D=1 zero stress transfer capability (complete failure). The aim of this work is to examine whether sufficient experimental evidence can be found in support of the hypothesis that the internal length should increase with damage and furthermore to investigate its evolution law based on the experimental evidence.

2. COMPARISON WITH THE PRESENT EXPERIMENTAL RESULTS

Peak applied load

The uniaxial stress-strain law parameters (see Section IV.4) in tension and compression used in the analysis for each mix are summarized in Table 1. The value of axial strain, ε_c, corresponding to the uniaxial compressive strength, was determined from the SG measurements in the uniaxial compression cylinder test. A strain value of about 0.0015 for the concrete and 0.0018 for the CM specimens was measured in the present tests. Although, SG measurements are probably highly unreliable during inelastic deformations, the consistency of the measurements appears convincing

Institutional Repository - Library & Information Centre - University of Thessaly
15/10/2023 05:52:39 EEST - 167.114.118.212

for considering these values in the analysis. Furthermore, based on the present uniaxial formulation (see Section IV.4), the predicted strain values for, ε_{0t} and ε_{0c} (threshold strain value that signifies the end of a perfectly elastic response), are also included in Table 1. It can be seen in Figs. V.4 and V.7, that similar strain values were measured by SG's in the uniaxial cylinder compression and the split cylinder tests, respectively.

Table 1 - Input material parameters for each cementicious mix.

Mix	Uniaxial stress-strain law parameters								Young's modulus
	Compression				Tension				
	f_c [(a)]	ε_c	ε_{0c} [(b)]	b_c [(b)]	f_t [(c)]/ f_{sp} [(a)]	b_t [(c)]	ε_{0t} [(d)]	ε_t [(d)]	E [(a)]
	(MPa)	(x10^{-6})	(x10^{-6})	-	-	-	(x10^{-6})	(x10^{-6})	(GPa)
LC	15.9	1500	250	1.643	0.80	4.5	70	110	25.0
NC	20.5	1500	270	1.707	0.85	5.0	65	100	30.7
MC1	34.7	1500	430	3.360	0.88	6.0	80	120	32.7
MC2	38.0	1500	450	3.890	0.90	6.5	80	110	34.0
CM [(e)]	32.4	1800	600	5.183	0.95	10	130	130	22.4

[(a)] measured (see Table V.3).
[(b)] Eq. (4) and assumed elastic limit at $0.4f_c$.
[(c)] based on the 4-point bending peak load and corresponding midspan deflection.
[(d)] Eq. (5) and assumed elastic limit at $0.8f_t$.
[(e)] assumed elastic behavior up to peak stress f_t ($\varepsilon_{0t} = \varepsilon_t$).

The measured peak applied load and midspan deflection for all sizes of each mix where used in this work in order to judge which values for the uniaxial tensile stress-strain law parameters b_t and f_t were more appropriate for each mix since direct uniaxial tensile tests were not performed. Concerning the details of the present model, the effect of b_t and f_t on the predicted peak load and midspan deflection can be decomposed as follows: lowering the value f_t and keeping the same b_t results in a decrease of the predicted δ_{peak} and P_{peak}, while increasing b_t and keeping the same f_t results in a decrease of the predicted δ_{peak} and P_{peak}.

The measured peak load value for each beam size and mix is included together with the model predictions in Figs. 1(a) to 1(e). The scatter of the predicted peak load values corresponds to a $\pm 5\%$ deviation of the assumed tensile strength values. This deviation is not significant given the number of uncertainties of the assumption that the tensile strength is a material property[2]. It can be seen that with the exception of size S1 specimens of the NC and CM mixes, no size effect in the flexural strength is apparent since the predicted peak load values shown in Fig. 1, if computed as $\sigma_N = 3P/bh$, yield a size-independent flexural strength. Also, note that for all mixes specimens considered it is true that $\sigma_N > f_{sp} > f_t$, as expected[3].

Institutional Repository - Library & Information Centre - University of Thessaly
15/10/2023 05:52:39 EEST - 167.114.118.212

The measured peak load midspan deflections for all tested specimens are listed in Table 2. It can be seen that for mixes MC1 and MC2, an increase of the peak load with size is accompanied by an increase in the corresponding midspan deflection. This is not observed in mixes LC and NC, where the peak load of beam sizes S2 and S3 occurs at the same midspan deflection. A similar inconsistency is observed in the CM mix for beam sizes S1 and S2.

Table 2 - Measured midspan deflection at peak load (values in mm).

Mix	size S1	size S2	size S3
LC	0.035 ± 0.004	0.049 ± 0.010	0.049 ± 0.009
NC	0.036 ± 0.003	0.042 ± 0.004	0.045 ± 0.008
MC1	0.029 ± 0.005	0.046 ± 0.004	0.058 ± 0.004
MC2	0.034 ± 0.005	0.048 ± 0.007	0.068 ± 0.002
CM	0.053 ± 0.001	0.052 ± 0.003	0.072 ± 0.007

Institutional Repository - Library & Information Centre - University of Thessaly
15/10/2023 05:52:39 EEST - 167.114.118.212

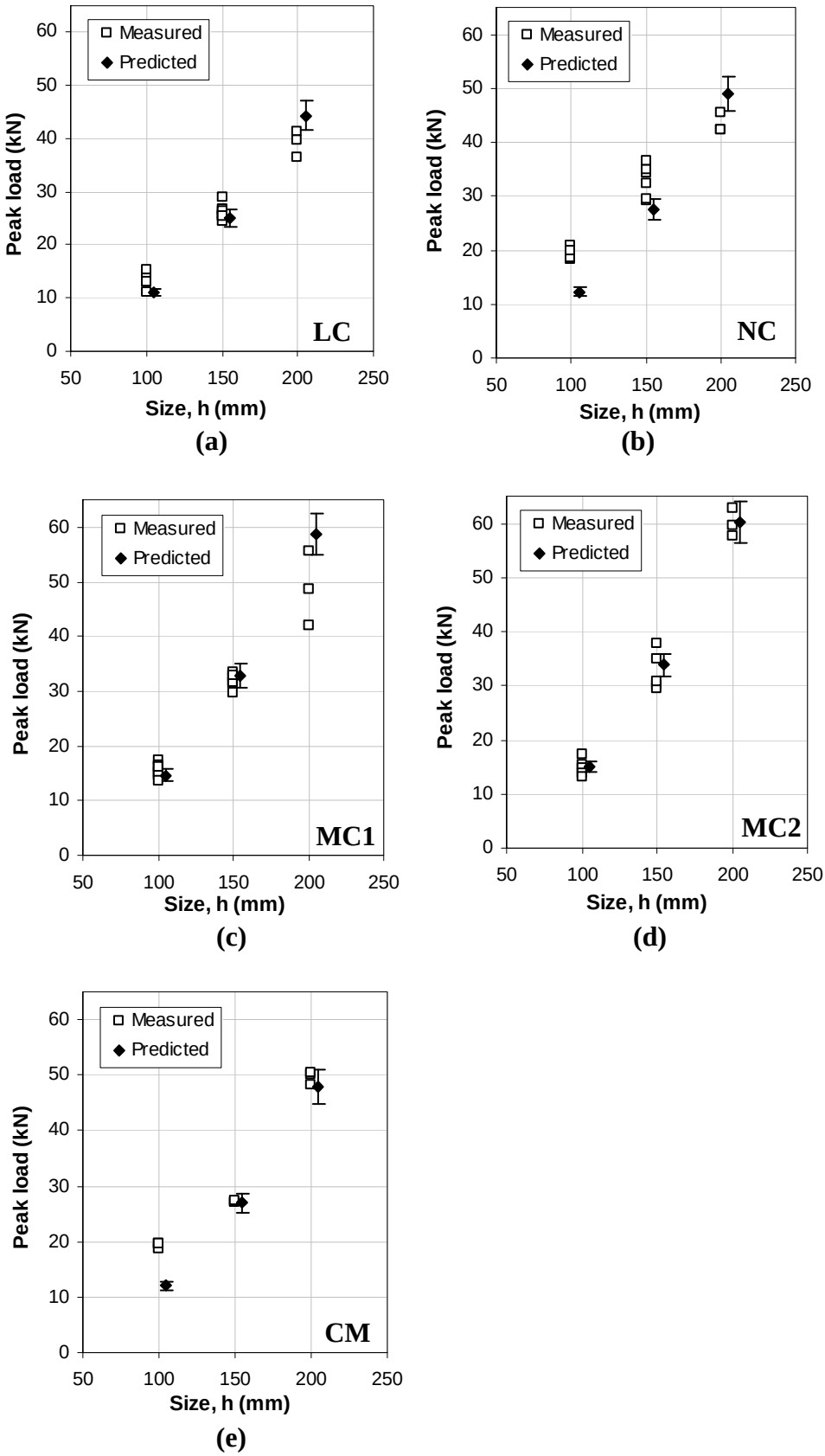

Fig. 1 – Peak load vs. size (experimental results and numerical predictions): (a) LC mix, (b) NC mix, (c) MC1 mix (d) MC2 mix and (e) CM mix.

Institutional Repository - Library & Information Centre - University of Thessaly
15/10/2023 05:52:39 EEST - 167.114.118.212

Initial softening and large deflections

The model predictions are compared with the experimental results in Figs. 2 to 5. The classical (local) and gradient (non-local) predictions are also shown. The non-local predictions were derived using the internal length parameters shown in Table 3. It can be seen that the non-local predictions are in better agreement with the experimental results than the local predictions, especially for large deflections. Furthermore, a significant scatter in the softening response is observed for the size S1 specimens for all mixes. Regarding the CM mix, this is discussed in Section VII.4.

Table 3 - Gradient internal length evolution law parameters.

Non-local parameters	**Mix**			
	LC	**NC**	**MC1**	**MC2**
Average $\mathbf{g_0}$ (mm)	17	15	12.5	8.0
n	0.90	1.30	1.65	2.00

Institutional Repository - Library & Information Centre - University of Thessaly
15/10/2023 05:52:39 EEST - 167.114.118.212

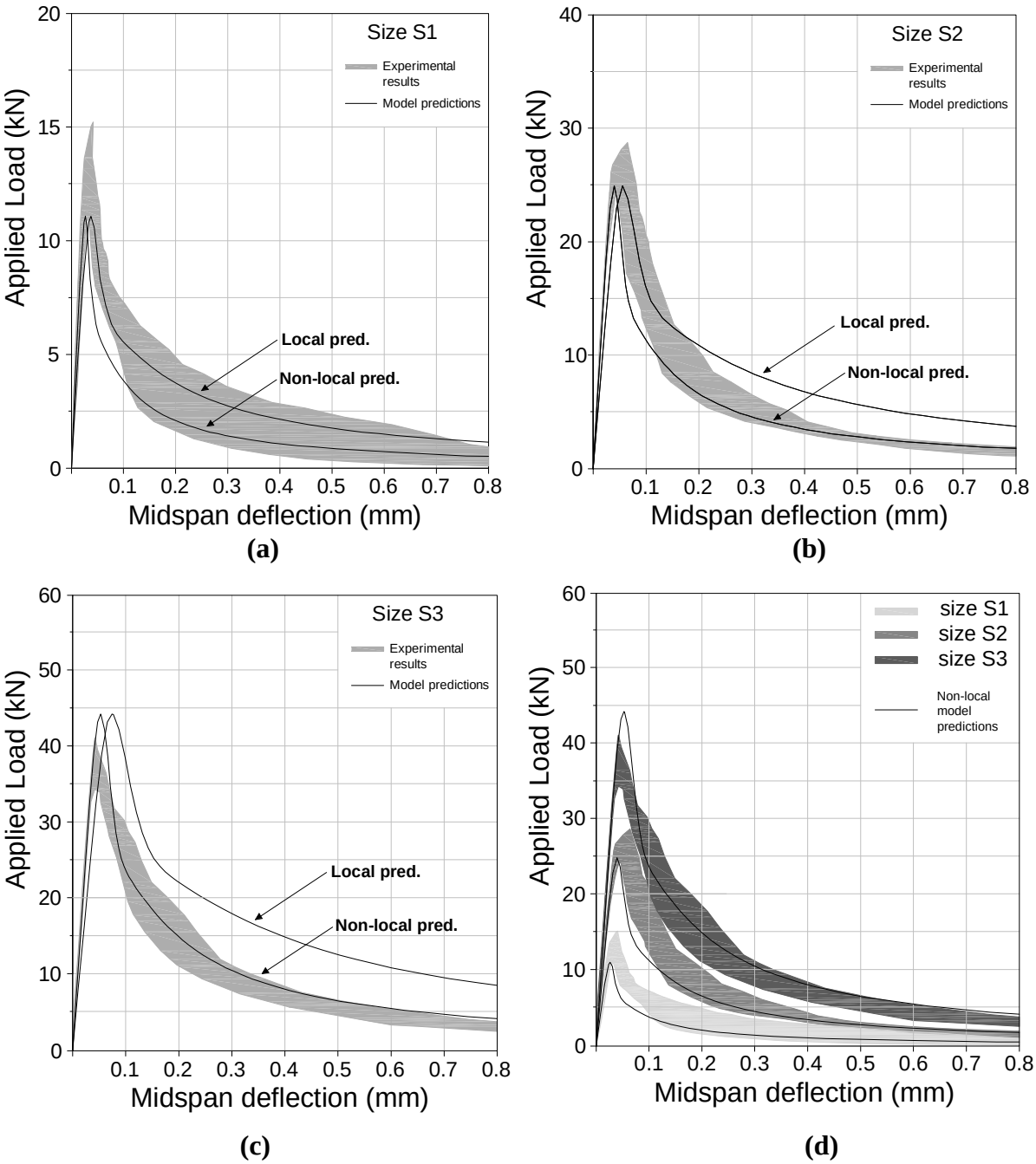

Fig. 2 – Comparison of the experimental results with numerical predictions for the LC mix: (a) size S1, (b) size S2, (c) size S3 and (d) all sizes.

Institutional Repository - Library & Information Centre - University of Thessaly
15/10/2023 05:52:39 EEST - 167.114.118.212

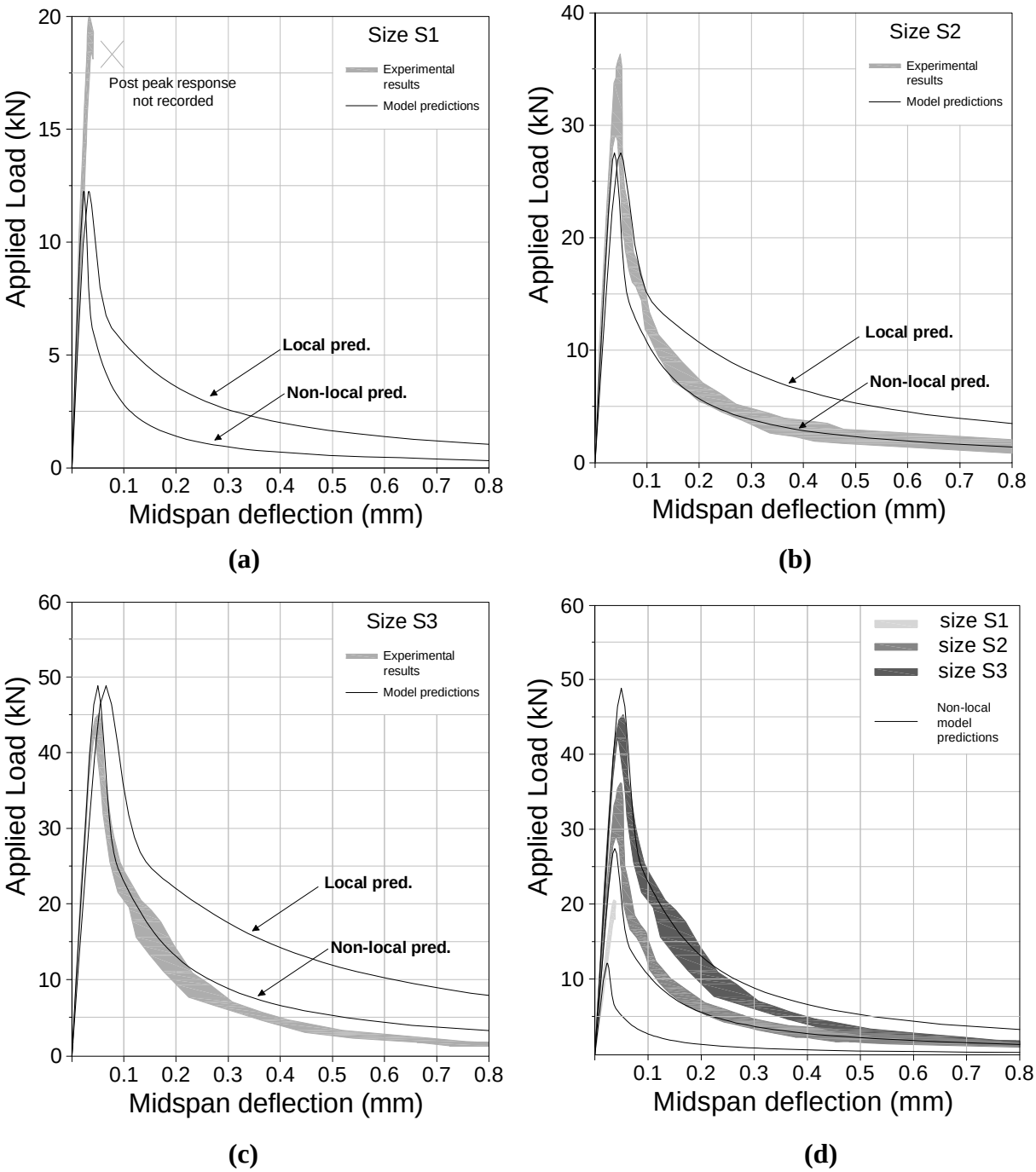

Fig. 3 – Comparison of the experimental results with numerical predictions for the NC mix: (a) size S1, (b) size S2, (c) size S3 and (d) all sizes.

Institutional Repository - Library & Information Centre - University of Thessaly
15/10/2023 05:52:39 EEST - 167.114.118.212

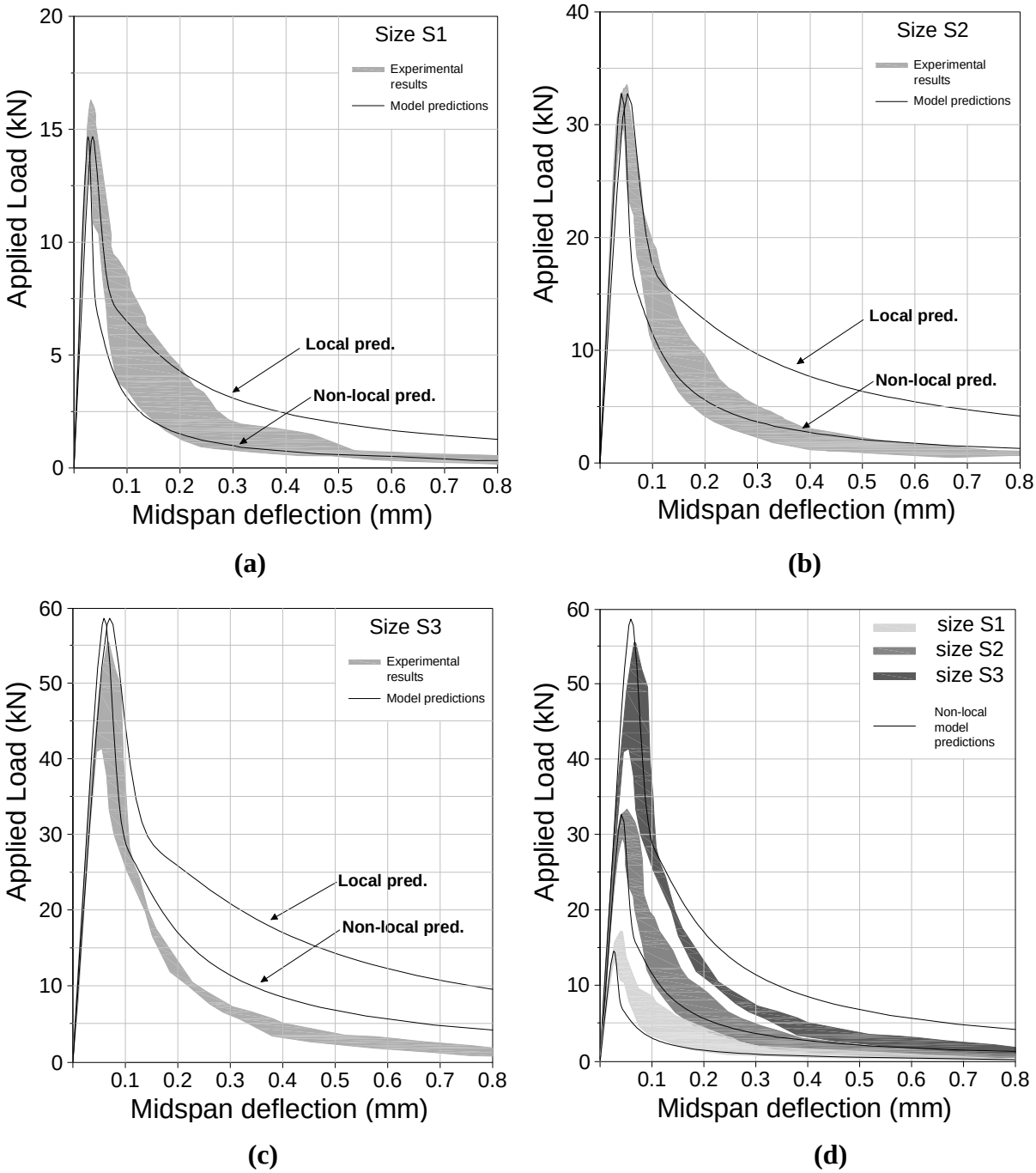

Fig. 4 – Comparison of the experimental results with numerical predictions for the MC1 mix: (a) size S1, (b) size S2, (c) size S3 and (d) all sizes.

Institutional Repository - Library & Information Centre - University of Thessaly
15/10/2023 05:52:39 EEST - 167.114.118.212

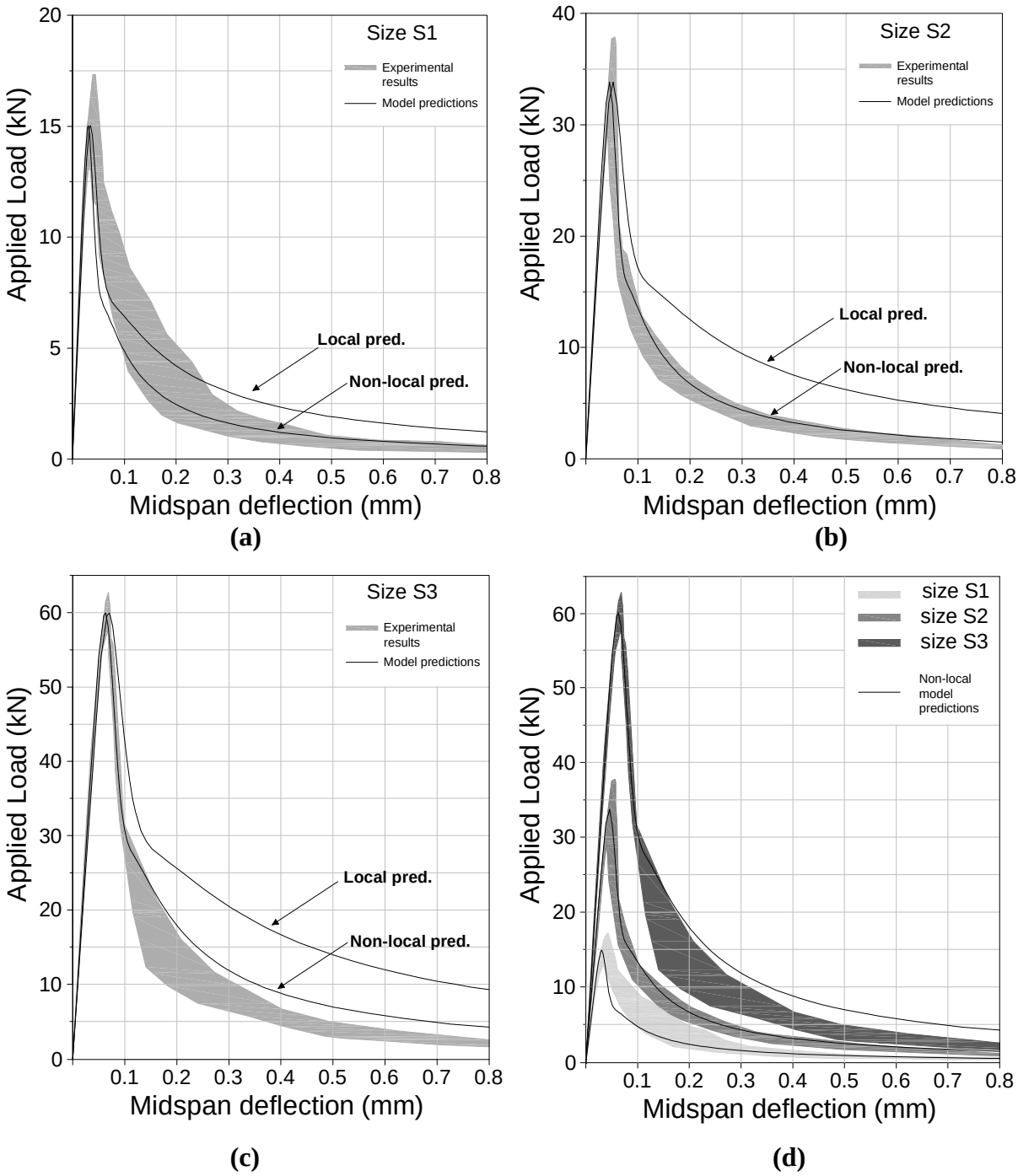

Fig. 5 – Comparison of the experimental results with numerical predictions for the MC2 mix: (a) size S1, (b) size S2, (c) size S3 and (d) all sizes.

Institutional Repository - Library & Information Centre - University of Thessaly
15/10/2023 05:52:39 EEST - 167.114.118.212

Unloading path predictions

Unloading/reloading and monotonic (no unloading) tests were performed with the majority of beam specimens being unloaded/reloaded at least three times at different load levels in the post-peak softening branch of response. The unloading path (P, δ) is depicted by an expression of the form, $P = \overline{P} - (1-\overline{D})K_0(\overline{\delta} - \delta)$, where $\overline{P}$ and $\overline{\delta}$ are the values on the load vs. midspan deflection softening branch where unloading starts, $\overline{D}$ is the average cross-section damage parameter at point $(\overline{P}, \overline{\delta})$ and K_0 the initial flexural stiffness for the uncracked concrete. Thus, the inelastic (plastic) midspan deflection upon complete unloading is:

$$\delta_{pl} = \overline{\delta} - \overline{P}/(1-\overline{D})K_0 \tag{7}$$

Three representative experimental P vs. δ curves including the unloading/reloading cycles for the MC2 mix, one for each beam size, are compared with the non-local predictions in Fig. 6. The analytical normalized applied load at unloading with respect to the peak load, $\overline{P}/P_{peak}$, vs. the normalized inelastic midspan deflection, $\delta_{pl}/\overline{\delta}$, and midspan plastic strain, $\varepsilon_{pl}/\overline{\varepsilon}$, curves (see Section VII.5) are plotted in Figs. 7(a) to 7(d) together with the experimental results for all specimen sizes. Both local and non-local predictions are shown in Fig. 7. The unloading estimates depend on the initial flexural stiffness of the material, K_0, and the $\overline{P}$ vs. $\overline{\delta}$ model predictions. These predictions are closer to the experimental findings when the influence of the gradient internal length is considered and this is reflected in the unloading values shown in Fig. 7.

Institutional Repository - Library & Information Centre - University of Thessaly
15/10/2023 05:52:39 EEST - 167.114.118.212

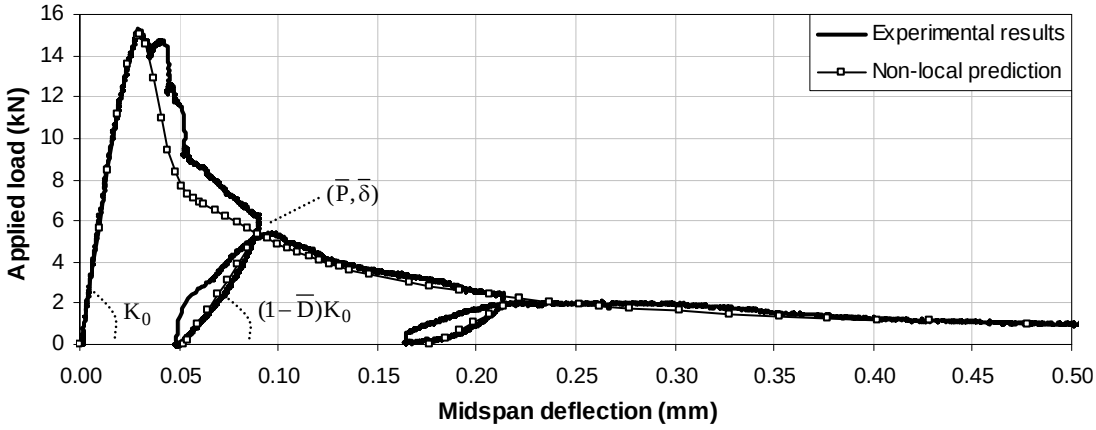

(a)

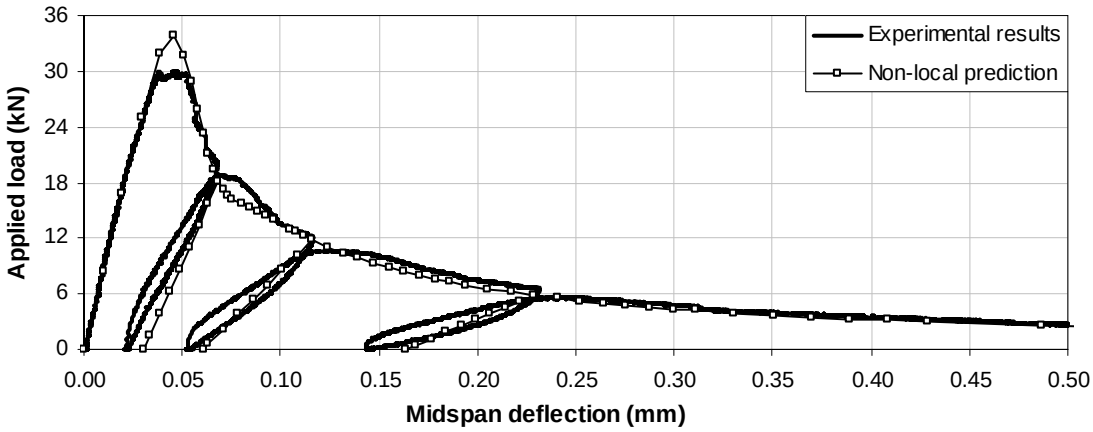

(b)

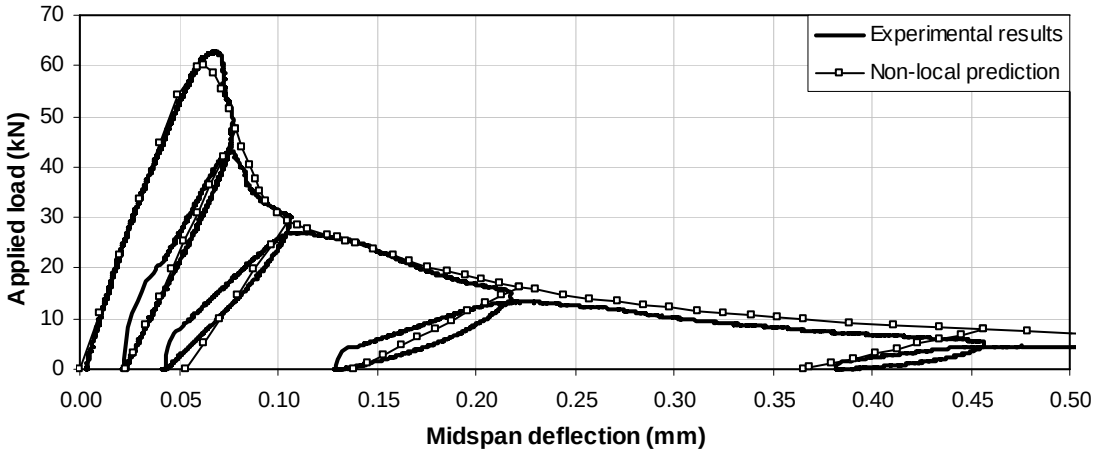

(c)

Fig. 6 – Experimental unloading/reloading curves and non-local numerical predictions for the MC2 mix: (a) beam size S1, (b) beam size S2, and (c) beam size S3.

Institutional Repository - Library & Information Centre - University of Thessaly
15/10/2023 05:52:39 EEST - 167.114.118.212

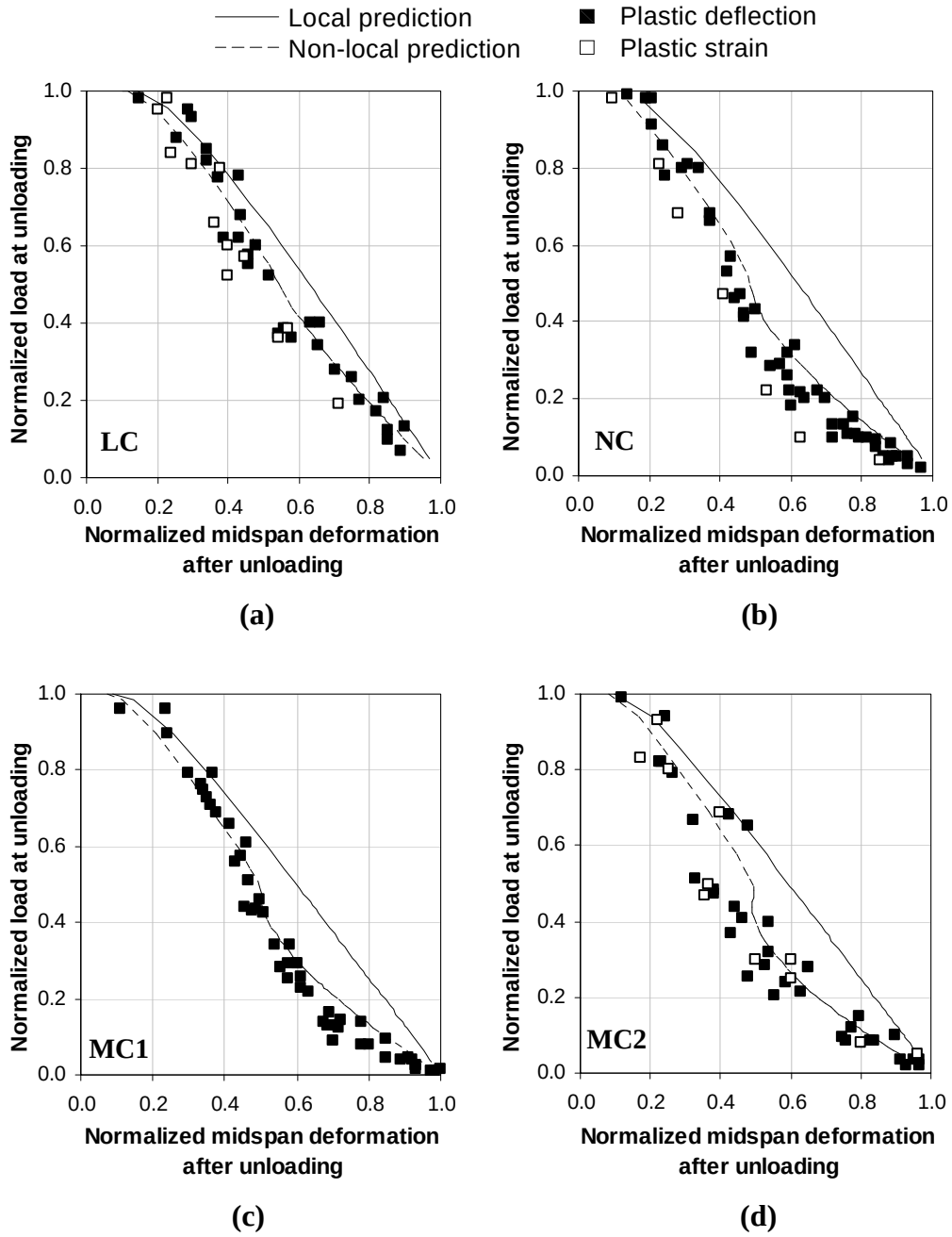

Fig. 7– Inelastic deformation after unloading (experimental results and numerical predictions): (a) LC mix, (b) NC mix, (c) MC1 mix and (d) MC2 mix.

3. DISCUSSION OF RESULTS

The assumption of an increasing internal length

A measure of the difference between the local and non-local predictions is the ratio of predicted midspan deflection, $\delta_{local}/\delta_{non\text{-}local}$, at a given load level in the post-peak softening branch of the flexural response. It can be seen in Figs. 2 to 5 that this ratio increases with increasing damage level or increasing midspan deflection. For example, for the beam specimen NC-S3 (see Fig. 3c), at load

Institutional Repository - Library & Information Centre - University of Thessaly
15/10/2023 05:52:39 EEST - 167.114.118.212

levels of $0.75P_{peak}$, $0.5P_{peak}$ and $0.25P_{peak}$ in the softening branch the predicted deflection ratio $\delta_{local}/\delta_{non\text{-}local}$ is 1.47, 1.74 and 2.26, respectively. This is due to assuming an increasing internal length. On the other hand, the experimental results (see Figs. 2 to 5) clearly show that the accuracy of the local predictions deteriorates with increasing damage level and within the context of gradient theory this is naturally modeled by assuming progressively higher values for the stiffness associated with the strain gradient, that is dg/dD>0. For the stiffness associated with the Cauchy strain it is true that[4] $dK/dD = -K_0 < 0$ (see also Fig. 6) with the difference between the local and non-local predictions being that $K_{0,grad} > K_{0,cl}$, if g_0 is not negligibly small, that is the rate of decrease of the elastic stiffness of the uncracked material is reduced. This "stiffening effect" is revealed upon unloading and it shows that the assumption of an exponential evolution law for the internal length is appropriate yielding predictions for all mixes closer to the present experimental results (see Fig. 7).

Evolution of gradient internal length with damage

The post-peak response in the 4-point bending tests for imposing midspan deflection at a constant rate, right after the peak applied load shows a rather sharp loss of load resistance with a subsequent continuously decreasing rate of loss of resistance. This behavior shows that the relation between damage and midspan deflection is non-linear. In the present strain gradient model, the relation between damage and predicted resisted load is not affected by the value of g since damage characterization is based on the Cauchy stresses and strains[1] through Eq. (39) of Section IV.5. For $g > 0$, however, the predicted strains and hence the curvature and deflection values for the same load level are lower than the predictions of the local model. In addition, consistency of the theory requires the internal length evolution law to be a material property. The cases of a constant internal length ($g = g_0$) and a linear evolution law ($g = g_0(1+\gamma D)$) were examined but in both cases calibration of the associated parameters was not objective. This lack of objectivity was remedied by assuming a nonlinear relation for the evolution law.

Microcracking, which is the source of damage in cementitious materials, is influenced by the composite nature of the materials. Stress redistribution due to microcracking becomes more limited with decreasing brittleness because it is forced to occur in the matrix material. Naturally, localization of microcracking leads to major-crack development and, in that respect, brittleness is related also to the number and size of fractured aggregates along the fracture surface[5-7] (see also Fig. VI.4). Furthermore, it has been shown that microcracking activity becomes more localized for increasing brittleness[8] and this abrupt degradation of the material due to high localization of damage

Institutional Repository - Library & Information Centre - University of Thessaly
15/10/2023 05:52:39 EEST - 167.114.118.212

naturally results to a decrease of its deformation capacity. Therefore, increasing brittleness should affect the rate of increase of the internal length with damage. The present findings support this hypothesis since the non-local parameter, n, for concretes with the same d_{max} was found to increases from 0.9 to 2 for concrete mixes with increasing brittleness (see Fig. 8).

The evolution law assumed in this work, $g = g_0 e^{nD}$, implies that if $g_0 = 0$, then $g(D) = 0$. However, a different evolution law which allows for $g = 0$ at $D = 0$ might be applicable to high-strength concrete and CM mix or concrete mixes with $g_0 \approx 0$. In principle, absence of size effect in elasticity does not necessarily mean no size effect in inelasticity, since microcracking although influenced by the microstructure occurs even in nearly homogeneous quassi-brittle materials like CM. The present experimental results for CM are discussed and compared to the experimental findings of Gettu et al.[9] for high-strength concrete in Section VII.4. Thus, for materials exhibiting practically no size effect in elasticity ($g_0 = 0$), an evolution law of the form, $g = g_1 D^n$, should result in reasonable predictions.

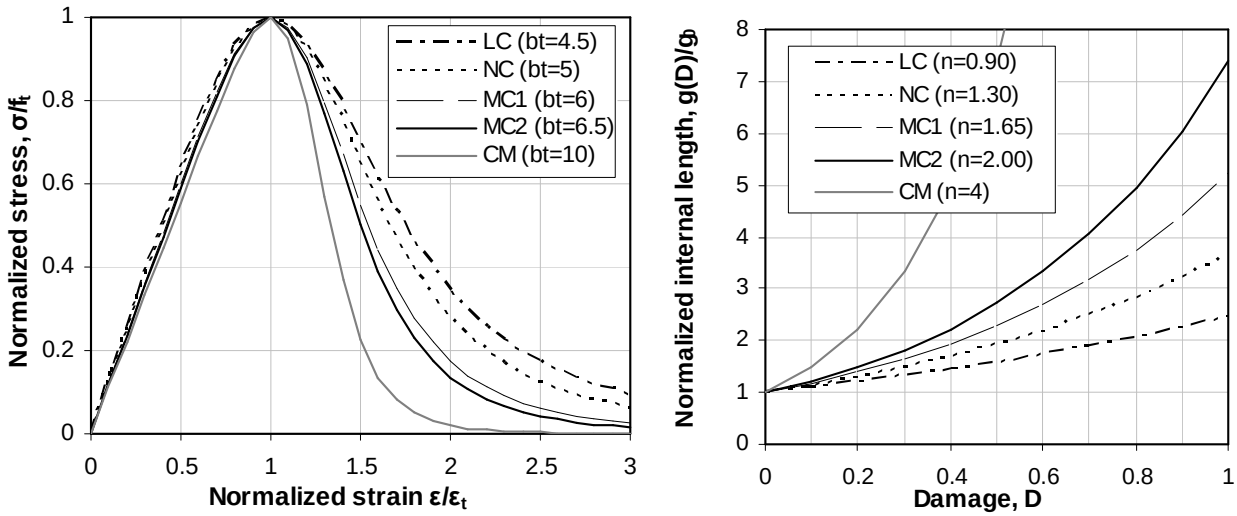

(a) **(b)**

Fig. 8 – (a) Normalized stress-strain law in tension, $\sigma / f_t = (\beta_t(\varepsilon/\varepsilon_t))/(\beta_t - 1 + (\varepsilon/\varepsilon_t)^{\beta_t})$ and (b) Normalized internal length evolution vs. damage D for all mixes based on $g(D) = g_0 e^{nD}$ for the local and non-local numerical predictions.

4. HIGHLY BRITTLE MATERIALS

It was not possible to capture the post-peak softening branch for any of the cement mortar beam specimens due to the extremely unstable crack growth typical of very brittle material. Furthermore, the experimental load vs. midspan deflection, shown in Fig. 9 with the model predictions, showed no sign of non-linearity up to the peak load for all beam sizes. Note that the local and non-local

Institutional Repository - Library & Information Centre - University of Thessaly
15/10/2023 05:52:39 EEST - 167.114.118.212

predictions coincide up to the peak load since elastic behavior is assumed up to the peak tensile strength (see Table 1) and g_0 is negligibly small for this mix.

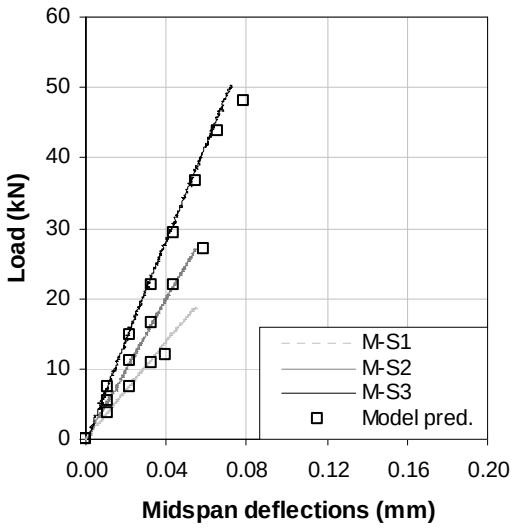

Fig. 9 – Experimental load vs. midspan deflection curves for CM mix up to peak applied load with the numerical predictions.

Gettu et al.[9] investigated size effect in high strength concrete ($f_c = 85$ MPa, $d_{max} = 9.5$ mm) in notched beam specimens subjected to 3-point bending. They reported the midspan deflection recorded at the peak applied load (P_{peak}) and at $0.1P_{peak}$ in the softening branch of the response. The ratio of these two deflections can be seen as a measure of brittleness. The value of this ratio was found to be 2.12 ± 0.63 based on the test results of seven (7) specimens of various sizes. For comparison, the same ratio for the MC2 mix ($f_c = 38$ MPa, $d_{max} = 32$ mm) was 7.58 ± 1.92. If an evolution law of the form $g = g_1 D^n$ with g_1=54.6 mm and n=4 (or g_0=1 mm and n=4 using Eq. 7) is assumed for the gradient internal length and applied to the cement mortar mix, then the local estimate of the deflection ratio is 6.80, whereas the non-local one is 3.09 ($\delta_{local}/\ \delta_{non\text{-}local}$ = 2.2). Although the post-peak softening branch of the cement mortar beam specimens was not recorded, it is reasonable to assume that the brittleness of this material should be similar to the brittleness of high-strength concrete and in that respect the non-local model predictions appear to be more realistic.

5. FLEXURAL STRAIN MEASUREMENTS

Casting of beam specimens in plywood forms unavoidably creates a boundary layer whose properties can differ from the core material[10]. However, it is shown that despite the objections[11]

Institutional Repository - Library & Information Centre - University of Thessaly
15/10/2023 05:52:39 EEST - 167.114.118.212

concerning what is actually being measured on the surface of specimens with strain gages (SG's) due to the complex nature of microcracking, some useful information can be extracted from the SG measurements.

The tensile concrete strain measurements at the bottom side of the midspan cross-section for two LC-S2 specimens are shown in Fig. 10. It can be seen that the axial normal tensile strain value stops increasing before the peak load indicating that certain damage has already occurred before the peak load and that within the elastic deformation range every cross-section experiences a level of strain proportional to the applied load. However, once cracking occurs, tensile strain measurements cannot be fully trusted.

The location of a major crack for un-notched specimens under 4-point bending cannot be predicted neither forced to occur at the midspan cross-section although in some specimens a crack developed nearly at the midspan section. When this occurs, the recordings of the SG's placed on the top extreme compressive fiber of the midspan cross-section show interesting measurements and two examples are shown in Figs. 11 and 12.

The strain values measured on the side face of the beam specimen at a distance of 2 cm from the top compressive fiber for two LC-S3 specimens are shown in Fig. 11. The following sequence of events is observed. Initially compressive strains increase linearly, i.e. the n.a. coincides with the centroid of the cross-section. In the post-peak softening branch, as a consequence of the n.a. shifting upwards towards the fiber where the SG was attached, the strains start to decrease. As damage increases, the measured strain value from compressive turns to tensile indicating that for P/Ppeak=0.33 and P/Ppeak=0.28 for LC-S3-01 and LC-S3-02, respectively, the n.a. should be located at z=80 mm, where the SG is placed. The stress distribution predicted by the present model corresponding to these load levels is shown in Fig. 11c. It can be seen that the location of n.a. is predicted very well.

Representative SG measurements at the extreme top compressive fiber of an MC2-S3 beam specimen are shown in Fig. 12. It can be seen that upon complete unloading a permanent strain (ε_{pl}) is recorded which, however, is not due to inelastic deformations at the top fiber, since that part of the cross-section subjected to compressive stresses should remain elastic. Furthermore, as shown in Fig. 7, the normalized plastic midpsan deflections and strains after unloading are similar for each mix. The strains measurements confirm a "stiffer response" in the inelastic beam's response range and this can be seen as experimental evidence that the adopted constitutive equation[1], $\sigma(\varepsilon, \varepsilon_{,xx}) = (1 - D(\varepsilon))E(\varepsilon - g^2\varepsilon_{,xx})$, is appropriate.

Institutional Repository - Library & Information Centre - University of Thessaly
15/10/2023 05:52:39 EEST - 167.114.118.212

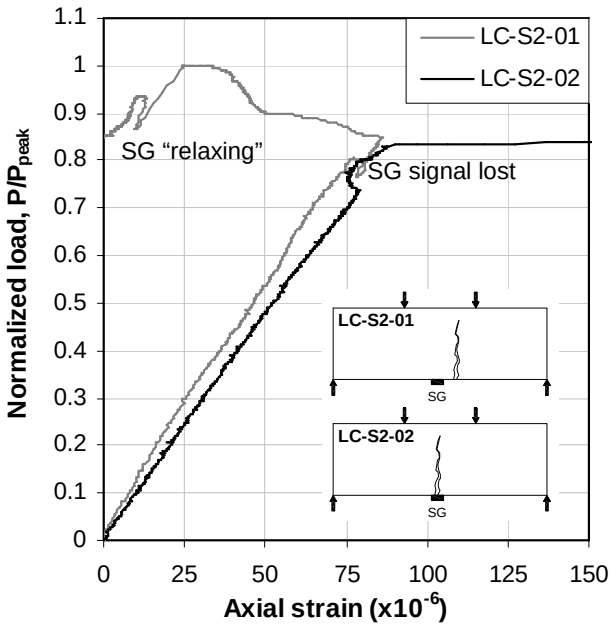

Fig. 10 – Measured longitudinal flexural strains at the extreme bottom (tensile) fiber for two size S2 beams of the LC mix.

Institutional Repository - Library & Information Centre - University of Thessaly
15/10/2023 05:52:39 EEST - 167.114.118.212

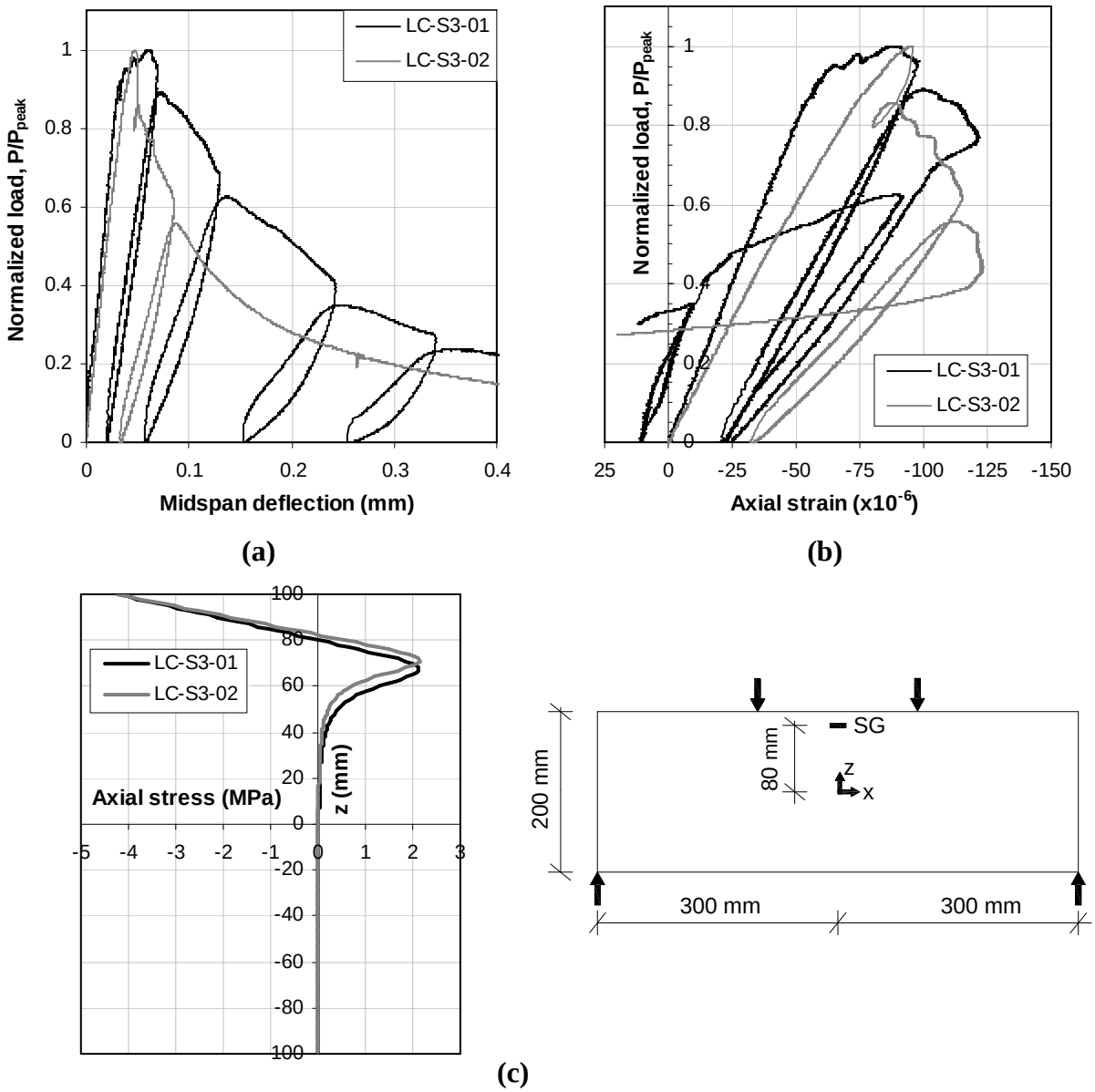

Fig. 11. (a) Normalized applied load vs. midspan deflection, (b) Normalized applied load vs. SG measurements at $z = 80$ mm and (c) numerical predictions of axial stress distribution at midspan along the beam height for load levels in the softening branch P/P_{peak}=0.33 and P/P_{peak}=0.28 for two size S3 beams of the LC mix.

Institutional Repository - Library & Information Centre - University of Thessaly
15/10/2023 05:52:39 EEST - 167.114.118.212

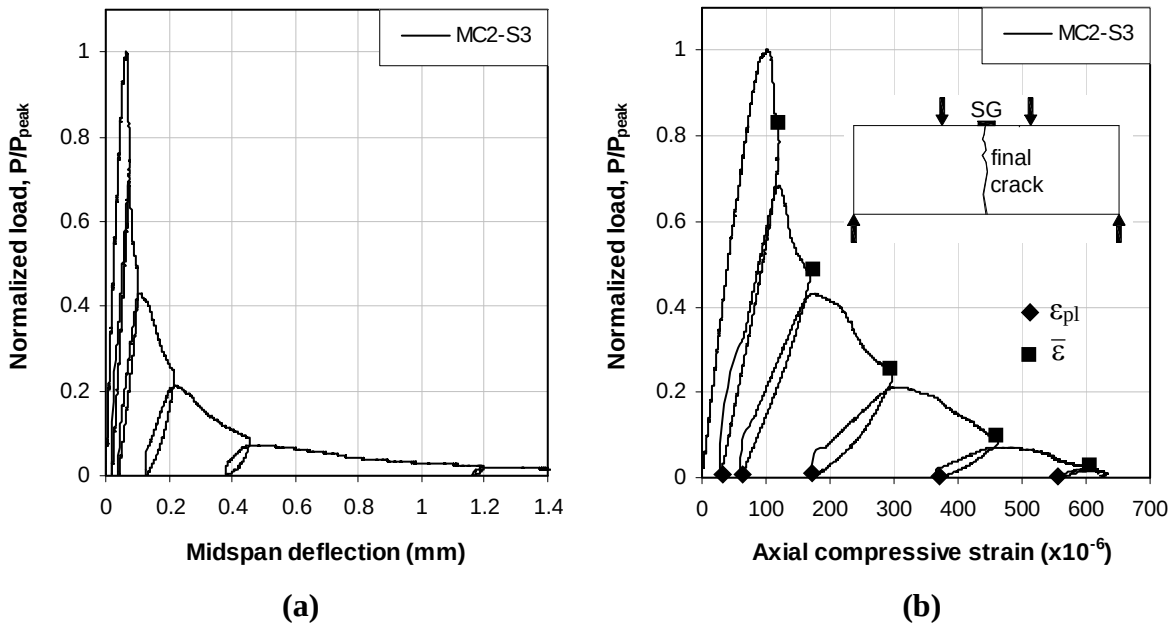

Fig. 12 (a) Normalized applied load vs. midspan deflection, (b) Normalized applied load vs. compressive strain at the extreme top fiber for specimen size S3 of MC2 mix.

6. CONCLUSIONS

The size effect in the inelastic flexural deformation range of the concrete beam specimens tested under 4-point bending was investigated for five (5) cementitious mixes (four concrete mixes with d_{max}=32 mm and one cement mortar mix with d_{max}=1 mm) by testing un-notched geometrically similar beams under midspan displacement control. The key finding of the present study can be summarized as follows:

1. An increasing gradient internal length with damage yields non-local predictions that are in better agreement with the experimental results than the local predictions
2. A non-linear (exponential) relation between damage and the gradient internal length was found to satisfy the objectivity requirement of a size-independent internal length evolution law.
3. The brittleness level of the response for the cementicious mixes studied is found to affect the internal length rate of increase with damage, that is higher rates of increase of the internal length are found for higher brittleness levels.

Institutional Repository - Library & Information Centre - University of Thessaly
15/10/2023 05:52:39 EEST - 167.114.118.212

CHAPTER VIII

SIZE EFFECT ON STRENGTH FOR CEMENTITIOUS MATERIALS

1. INTRODUCTION

Size effect in cementitious materials does not manifest itself only in deformation related parameters such as stiffness but also in tensile or compressive strength such as peak load predictions. In Chapters VI and VII, a strain gradient formulation of the problem was used in order to account for the former, while predicting size effect in strength was not possible. The study on size effect in flexural strength is presented in detail in this chapter and the present experimental results are discussed. The fracture mechanics prediction of size effect in flexural strength for the case of un-notched beam specimens and the statistical size effect are investigated and it is shown that they only partially explain the experimental results. The composite nature of concrete, the boundary layer effects and diffusion phenomena are also discussed and it is argued that the observed behavior can be attributed partially to these factors.

2. SIZE EFFECT ON STRENGTH

Size effect in flexural strength is not possible in the present formulation of the problem which relies on an assumed uniaxial stress-strain law for concrete in tension and compression. However, a size effect in flexural strength is apparent based on the experimental results for some cementitious mixes (see Fig. 1). These results are discussed and are compared with the predictions based on other possible sources of size effect [13,11,12].

Statistical size effect

The statistical size effect predicts[13] that the flexural strength of concrete, σ_N , is affected by size as $h^{-n/m}$, which is $h^{-1/8}$ for n=3 (3D similitude)[3] and Weibull modulus m = 24 according to Bazant and Novak[14].

The measured flexural strength for all concrete mixes is plotted against the beam size in a logarithmic plot in Fig. 2. If statistical size effect was present, the slope of a linear approximation for the σ_N vs. size data plotted in a logarithmic plot should be equal to -3/24= -0.125. If the statistical size effect predictions are compared with the present experimental results it is concluded that the source of the deviations observed cannot be attributed only to statistical reasons and that the main source of the observed behavior is because other sources of size effect are present.

Institutional Repository - Library & Information Centre - University of Thessaly
15/10/2023 05:52:39 EEST - 167.114.118.212

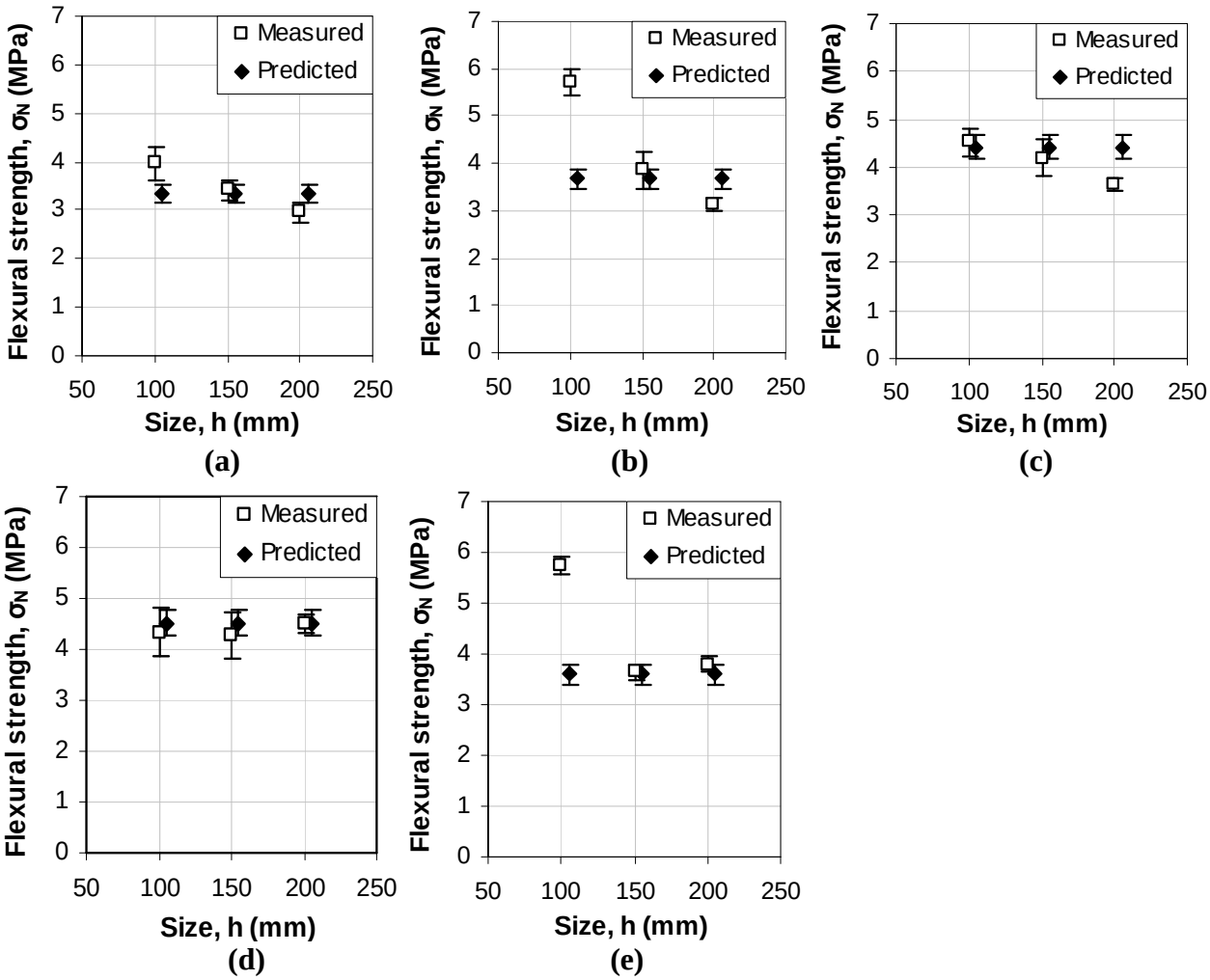

Fig. 1. Comparison of measured flexural strength values vs. size with the present model predictions: (a) mix LC, (b) mix NC, (c) mix MC1, (d) mix MC2, and (e) mix CM.

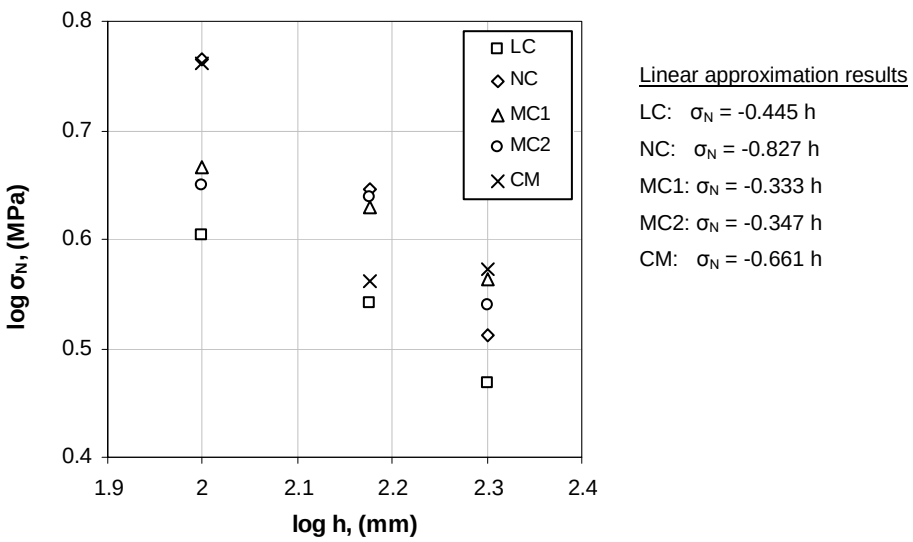

Fig. 2. Measured flexural strength values vs. beam size.

Institutional Repository - Library & Information Centre - University of Thessaly
15/10/2023 05:52:39 EEST - 167.114.118.212

Specific fracture energy

The fracture energy of concrete is typically obtained according to the RILEM method[1] from a 3-point bending test of beam specimens with specific dimensions depending on the maximum aggregate size, d_{max}. For a notch depth, a, and beam height, h, a minimum ratio, $(h-a)/d_{max} = 3.125$ is specified. In the present study, for the un-notched concrete beam specimens tested under 4-point bending the ratio of h/d_{max} is equal to 3.125, 4.69, and 6.25 for beam size S1, S2 and S3, respectively.

The fracture energy per unit fracture surface area is defined as $G_F = W_F / A$, where A is the nominal cross-sectional area of the beam specimen and W_F is the work supplied to statically fracture the beam specimen and is equal to[2]:

$$W_F = \int_0^{\delta_u} P(\delta)d\delta + 2P_q\delta_u = W_P + W_q \tag{1}$$

where P is the applied load, P_q is the equivalent self-weight of the beam and fixtures supported by the beam and δ_u the ultimate midspan deflection. The equivalent concentrated self-weight at each of the two load points, $P_q \cong 0.734qL$ (q= uniformly distributed self-weight), is estimated by equating the midspan deflection for linear elastic behavior in the case of a simply supported beam subjected to a uniformly distributed load, q, to the midspan deflection under 4-point bending and of the same span. Note that, if the equivalent self-weight is determined based on equating the maximum bending moment at midspan an equivalent load, $P_q = 0.75qL$, is found. It is noted that P_q for the un-notched beam specimens tested for this study, was less than 1% of the total peak applied load. For all beam specimens tested, the 4-point bending test was terminated in the softening branch region of response after at least 90% of the maximum load resistance was lost.

The fracture energy per unit fracture surface area results for each concrete mix are plotted against the specimen size in Figs. 3(a) to 3(d). A significant but similar scatter is observed for all beam sizes and no trend of the reduced scatter is apparent with increasing size.

Institutional Repository - Library & Information Centre - University of Thessaly
15/10/2023 05:52:39 EEST - 167.114.118.212

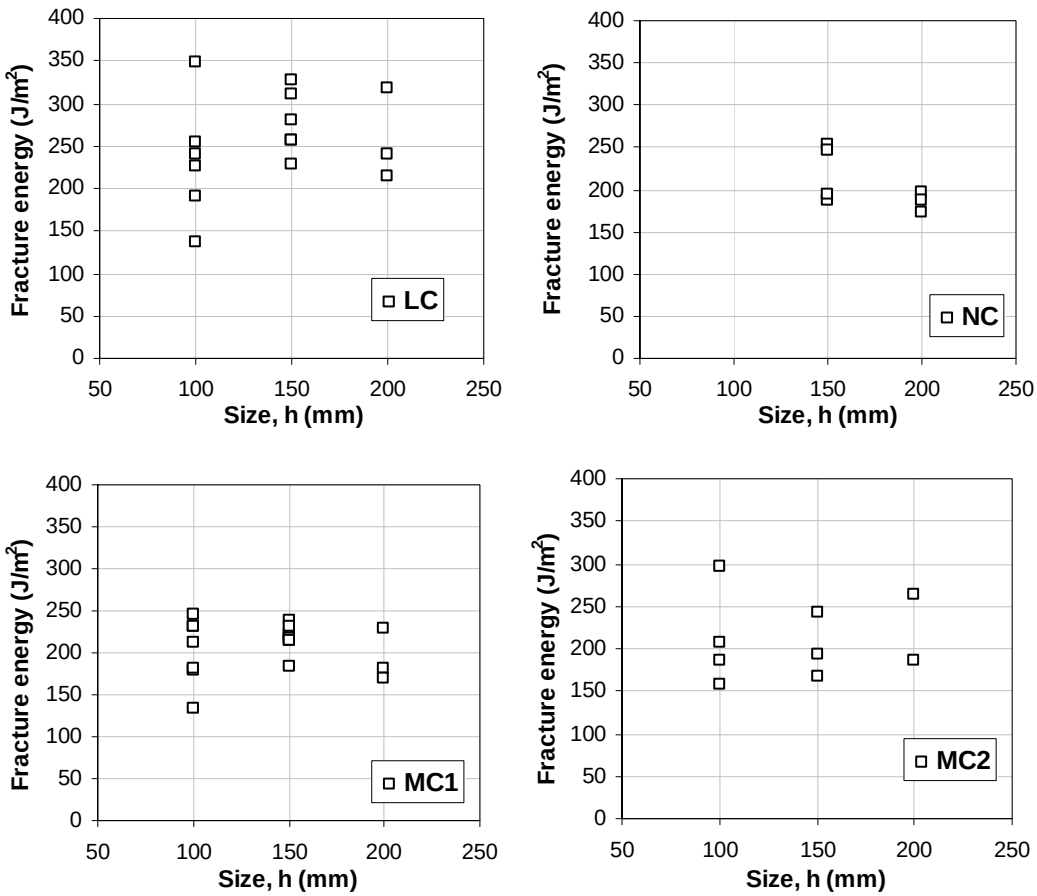

Fig. 3. Fracture energy G_F for all beam sizes: (a) mix LC, (b) mix NC, (c) mix MC1 and (d) mix MC2.

The average value of the specific fracture energy for each size is shown in Table 1. The average value of all tested specimens for each mix is assumed to be the fracture energy of the material and is used in the analysis. This average value for each mix, is similar to values reported by others[4,5,8,9] for concrete mixes with $d_{max} > 20\,\text{mm}$.

Table 1. Measured specific fracture energy values for all concrete mixes and beam sizes.

Mix	Fracture Energy, G_F (J/m^2)			
	S1	S2	S3	Average G_F
LC	232 ± 65	276 ± 37	257 ± 53	255 ± 56
NC	- (*)	220 ± 35	186 ± 13	205 ± 32
MC1	202 ± 39	218 ± 16	193 ± 31	207 ± 29
MC2	212 ± 52	201 ± 38	225 ± 54	211 ± 47

(*) not measured

Institutional Repository - Library & Information Centre - University of Thessaly
15/10/2023 05:52:39 EEST - 167.114.118.212

The specific fracture energy and the characteristic length (l_{ch}) for each concrete mix are plotted against the compressive strength in Figs. 4(a) and 4(b), respectively. The so-called "characteristic" length of a cementicious material is defined as: $l_{ch} = EG_F / f_t^2$ (E=Young's modulus, f_t=tensile strength and G_F=fracture energy), which is a measure of the inverse of the material's brittleness. Note that an increase of the compressive strength does not necessarily result in an increase of the specific fracture energy. This is due to the fact that the fracture energy can not distinguish the different effect on ductility and brittleness resulting from an increase of the compressive strength[10]. However, regarding the brittleness of the concrete mix (see Fig.4), the calibration of the softening parameter b_t yielded 4.5, 5, 6, 6.5 and 10 for mixes LC, NC, MC1, MC2 and CM, respectively. Increasing the softening parameter is equivalent to assigning a steeper softening branch to the material's uniaxial stress-strain law (see Chapter VII). Furthermore, the non-local parameter, n, of the assumed gradient internal length evolution law was found to increase with increasing brittleness.

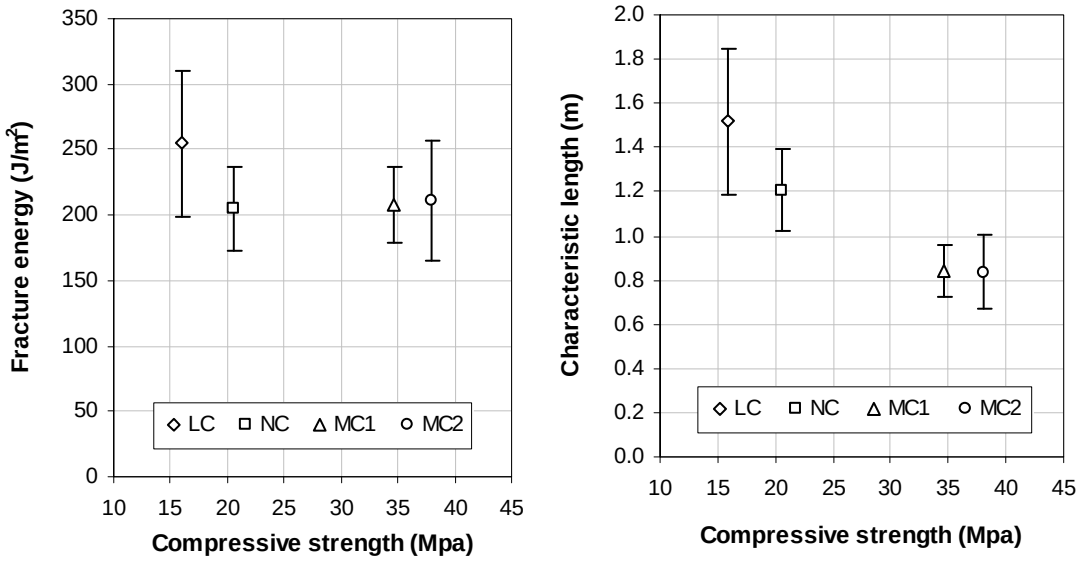

(a) **(b)**

Fig. 4. Fracture parameters vs. compressive strength for mixes NC, LC, MC1 and MC2: (a) Specific fracture energy, G_F (b) Characteristic length, l_{ch}.

Fracture mechanics size effect on flexural strength

Expression (2) [15] for the size effect on the modulus of rupture for the case of un-notched concrete beams based on a cohesive crack model predicts that:

Institutional Repository - Library & Information Centre - University of Thessaly
15/10/2023 05:52:39 EEST - 167.114.118.212

$$\frac{f_r}{f_t} = \varphi + \frac{3 - \varphi + 99(h/l_1)}{(1 + 2.44(h/l_1))(1 + 87(h/l_1))} \tag{2}$$

where f_r is the modulus of rupture ($f_r = \sigma_N$), f_t is the uniaxial tensile strength, $\varphi = 1$ for pure bending and l_1 is a length parameter. The length parameter, l_1, is linked to the characteristic length, l_{ch}, through the relation, $l_1 = c_0 l_{ch}$, where the factor c_0 ranges from 0.4 to 0.6 and is associated with the softening branch of concrete[3] . The steeper the initial softening after the peak load, the smaller the c_0. It is assumed that $c_0 = 0.6$ for mixes LC and NC, and $c_0 = 0.5$ for mixes MC1 and MC2.

The predictions based on Eq. (2) are plotted with the present experimental results in Fig. 5. It is noted that concerning the tensile strength f_t, the values shown in Table VII.1 are used.

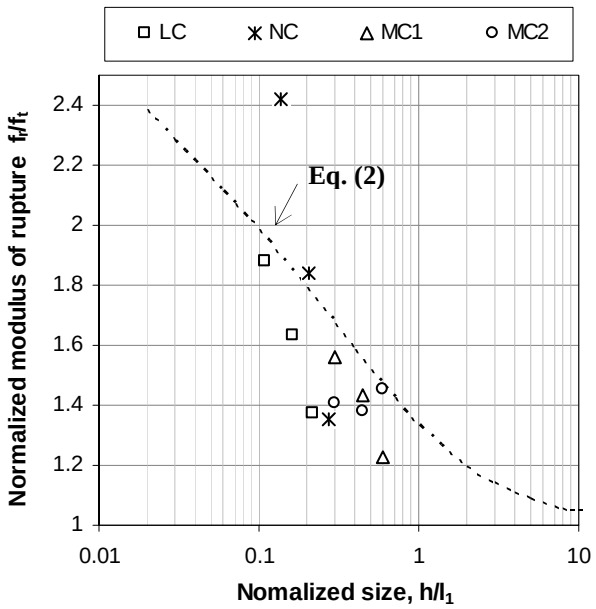

Fig. 5. Normalized measured flexural strength values with respect to the assumed tensile strength of the concrete mixes vs. beam size compared to the cohesive crack model predictions.

Fracture mechanics size effect on splitting strength

For the case of the split cylinder test configuration used in this study (see Chapter V), the splitting to the uniaxial tensile strength ratio can be predicted by the expression (3)[18] :

$$\frac{f_{sp}}{f_t} = 1.0233 + \frac{1}{-6.73 + 26.27\, D_{cyl}/l_1} \tag{3}$$

Institutional Repository - Library & Information Centre - University of Thessaly
15/10/2023 05:52:39 EEST - 167.114.118.212

where f_{sp} is the splitting strength and D_{cyl} is the cylinder diameter. It is noted that Eq. (3) is applicable for $0.4 \le D_{cyl}/l_1 \le 10$ and that it was shown[18] to be in good agreement with the experimental results for cement mortar ($d_{max} = 5\,\text{mm}$) and granite specimens.

The measured splitting strength (see Table V.3) to the assumed uniaxial tensile strength (see Table VII.1) ratios are shown together with Eq. (3) in Fig.6. The predictions of Eq. (3) are good for the concrete mixes with D_{cyl}/l_1<0.4 and the asymptotic behavior predicted is also realistic.

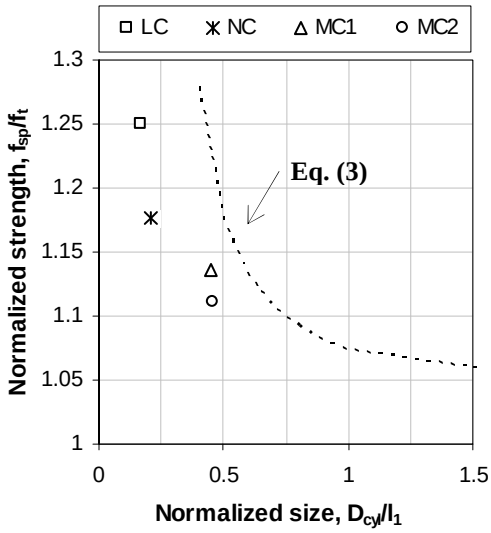

Fig. 5. Comparison of the measured splitting strength, f_{sp}, to the calibrated uniaxial tensile strength, f_t, ratio with the cohesive crack model predictions.

Empirical prediction of size effect in flexural strength

The CEB-FB model[19]code empirical expression (5) can predict the size effect on flexural strength:

$$\frac{\sigma_N}{f_t} = \frac{0.06h^{0.7}}{1+0.06h^{0.7}} \tag{5}$$

where h is the beam height in mm.

The predictions of Eq. (5) are plotted with the present experimental results in Fig. 6. It can be seen that correlation with the present experimental results is good for beam size S3 for all mixes and significant deviations are observed for sizes S1 and S2.

Institutional Repository - Library & Information Centre - University of Thessaly
15/10/2023 05:52:39 EEST - 167.114.118.212

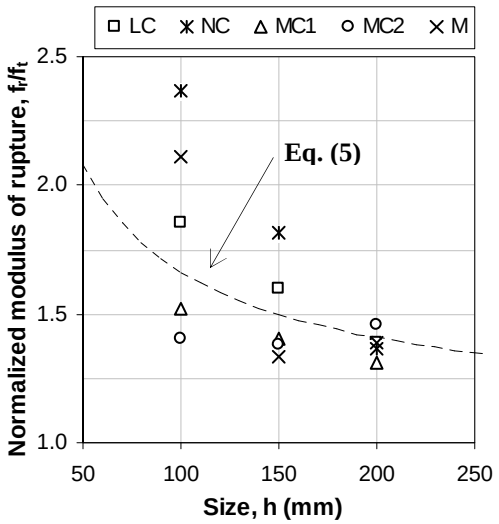

Fig. 6. Comparison of the measured flexural strength, σ_N , and calibrated uniaxial tensile strength, f_t, with the predictions of the CEB-FIB model code empirical Eq. (5).

3. DISCUSSION

The heterogeneity of a material and the relative strength of the different phases of a composite have been shown experimentally to affect the details of macrocrack propagation[5-7]. However, with regard to how microcracking may affect the measured peak load, the issue of propagation of a macrocrack offers little insight for an un-notched beam specimen. Impregnation tests have shown that microcracking in concrete exhibits some random characteristics that a major crack by definition can not include. Any effect microcracking will have on the peak load should be the same for all sizes according to the present model predictions, since damage at peak load is size-independent. However, lattice model simulations[16] have shown that as the scale of concrete specimens is decreased, the detail of the microstructure can significantly affect the predicted peak load. This implies that as the macroscale of specimens decreases, the measured behavior will be less representative of the material. Note that in interpreting uniaxial tension tests for concrete, a ratio of h/d_{max}=3.75 was argued to be too small[12].

Other inherit uncertainties associated with casting and curing of the beam specimens like formation of a boundary layer with different properties[17] and diffusion phenomena[3] due to different cooling times of the core and surface material, can be important for the case of un-notched specimens and their influence cannot be neglected. For example, the reduced flexural strength of size S3 specimen of the MC1 mix could be attributed to induced microcracking due to hydration heat phenomena since relatively very small size effect is observed in sizes S1 and S2. Also, the very

Institutional Repository - Library & Information Centre - University of Thessaly
15/10/2023 05:52:39 EEST - 167.114.118.212

high flexural strength especially for size S1 for the CM mix (h/d_{max}=100) which showed no size effect for sizes S2 and S3, could be the result of a boundary layer rich in cement concentrated at the bottom of the specimen during casting. The same could be argued for the very high peak values measured in specimen size S1 of the NC mix. Also, a size effect on flexural strength was not present for mix MC2. This might be seen as proof of the absence of the material's size effect or as proof that the true material's size effect is shadowed by other factors affecting the results. Finally, the size effect on flexural strength measured for the LC mix can be attributed to material's size effect since a regression analysis of Bazant's two parameter size effect law[3] was possible only for this mix.

A review of the present experimental results collectively does not reveal a single source of size effect which can be identified as the source of the observed behavior. However, considering the relatively small size range of specimens used in this study (1 : 1.5 : 2), other sources[3] not associated with the material size effect on strength are expected to influence the measured peak load values.

Institutional Repository - Library & Information Centre - University of Thessaly
15/10/2023 05:52:39 EEST - 167.114.118.212

MAIN CONCLUSIONS

Given the increasing awareness regarding the usefulness of gradient elasticity theories and the significant amount of theoretical work that has been produced in the last decade or so, it is rather surprising that the discussion concerning the relationship between the internal length and the material's microstructure is more or less limited usually to the vague statement that the internal length parameter of the material is a function of the dominant feature of the material's microstructure. The main aim of this thesis was to investigate the physical correlation of this internal length assumed by dipolar elasticity to the material's microstructure. To the author's knowledge, the estimation of an evolving internal length parameter for cementitious materials based on experimental evidence has not been done in the past. For this to be attempted and in order to investigate a possible size effect in elasticity from flexure tests of concrete beams, the two classical material constants, the Young's modulus and Poisson's ratio, should be determined independently.

A homogenization procedure applied to heterogeneous materials in this study showed that the internal length is best described as a measure of the heterogeneity which cannot be defined only in terms of the dominant feature of the microstructure (size of inclusions) but also of the matrix/inclusions elastic mismatch in the material. This was verified experimentally by testing concrete specimens of various mixes with similar microstructural details but with different matrix/aggregate elastic mismatch. The internal length estimate determined based on this model was found to decrease with decreasing level of elastic mismatch.

A gradient enhanced elasto-damage model applicable to the case of concrete beams under flexure, which relies heavily on the elasticity solution of the boundary value problem for the case of a dipolar elastic Timoshenko beam, is presented in this work. A closed-form solution of this problem and a methodology for solving more complex beam problems, such as indeterminate beam configurations, is described. This model reduces to the gradient Bernoulli-Euler solution and the classical Timoshenko solution if the necessary simplifications and limits are considered. The elasticity solution of the boundary value problem was used in conjunction with an assumed stress-strain law applicable to semi-brittle materials in order to produce numerical predictions for the inelastic response of the beams tested. The model proposed is shown to lead to an objective (mesh-independent) damage characterization.

In this study, the presence of size effects in elasticity and inelasticity of cementitious materials was investigated based on midspan deflection and axial strain measurements of un-

Institutional Repository - Library & Information Centre - University of Thessaly
15/10/2023 05:52:39 EEST - 167.114.118.212

notched concrete beam specimens tested under true displacement-controlled 4-point bending for concrete with a compressive strength of up to 40 MPa. The geometrically similar un-notched beam specimens tested had a beam height to maximum aggregate size ratio of up to about 6.5. Since concrete possesses rather complex microstructural details due to the presence of different aggregate sizes with specific volume fractions (aggregate gradation), the internal length estimate for a given mix is compared with its average inclusion size, which describes its inherent heterogeneity. The average inclusion size for the concrete mixes considered in this study with a maximum aggregate size of 32 mm, obtained by mapping the actual microstructure on cross-sectional cuts of the specimens, ranged between 10 and 20 mm. An estimate of the internal length for a given concrete mix was obtained based on the applied load vs. midspan deflection and curvature measurements of the beam tests. A stiffer response than that predicted by the classical elasticity theory is measured in the flexural elastic response range of the beams tested. The proposed model predicted an internal length estimate of about 15 ± 5 mm in the case of the concrete mixes with a significant elastic mismatch for which cracking occurs predominantly in the matrix material (lower-strength concrete). It should be noted, that the same internal length estimate was obtained independently of the use of either the midspan deflection or the axial strain measurements. These concrete mixes are representative of a composite with inclusions much stiffer than the matrix material. It is important that the internal length parameter in this case appears to be practically equal to the average inclusion size of such a microstructure. On the other hand, lower internal length estimates of about 12 ± 2 and 8 ± 4 mm (about one-half the average inclusion size), were found for the two concrete mixes with a higher compressive strength. The lower internal length estimates for the higher-strength concrete is attributed to the lower elastic mismatch in the microstructure of these mixes, due to which a significant number of aggregates were fractured along the crack path. As expected, the size effect in elasticity is found to be insignificant in the case of the cement mortar mix with a maximum aggregate size of 1 mm, which can be viewed as a completely homogeneous material.

Furthermore, it is argued that microcracking in semi-brittle materials, which is the source of material softening, should also affect the initial internal length parameter value, g_0, which is associated with the given heterogeneity of the material. If a microstructural internal length is related to the level of damage, a thermodynamic formulation of the problem showed that this length should be either increasing or remaining constant with damage. An experimental investigation of the particular form of the gradient internal length evolution law verified this theoretical finding since it was shown that an increasing gradient internal length with damage yields non-local predictions that

Institutional Repository - Library & Information Centre - University of Thessaly
15/10/2023 05:52:39 EEST - 167.114.118.212

are in better agreement with the experimental results than the local predictions. Finally, a non-linear (exponential) relationship between damage and the gradient internal length was found to satisfy the objectivity requirement of a size-independent internal length evolution law for the cementicious mixes considered in this study. Also, it was found that the rate of increase in the internal length value with damage is increasing with increasing brittleness level of response.

Institutional Repository - Library & Information Centre - University of Thessaly
15/10/2023 05:52:39 EEST - 167.114.118.212

REFERENCES

CHAPTER II

1. Mindlin RD, Tiersten HF. Effects of couple-stresses in linear elasticity. Arch. Rational Mech. Anal. 1962; 11: 415-448.
2. Koiter WT. Couple-stresses in the theory of elasticity. Part I. Proc. Ned. Akad. Wet. 1964; B67: 17-29, II: 30-44.
3. Toupin RA. Perfectly elastic materials with couple stresses. Arch. Rational Mech. Anal. 1962; 11: 385-414.
4. Mindlin RD. Micro-structure in linear elasticity. Arch. Rational Mech. Anal. 1964; 16: 51-78.
5. Mori T, Tanaka K. Average stress in matrix and average elastic energy of materials with misfitting inclusions. Acta Metall. 1973; 21: 571-574.
6. Budiansky B. On the elastic moduli of some heterogeneous materials, J. Mech. Phys. Solids 1965; 13: 223-227.
7. Hill R. A self-consistent mechanics of composite materials, J. Mech. Phys. Sol. 1965; 13: 213-222.
8. Christensen RM, Lo KH. Solution for the effective shear properties in three phase sphere and cylindrical models, J. Mech. Phys. Sol. 1979; 27: 315-330, Erratum 34: 639.
9. McLaughlin R. A study of the differential scheme for composite materials, Int. J. Eng. Sci. 1977; 15: 237-244.
10. Norris AN. A differential scheme for the effective moduli of composites, Mech. Metall. 1985; 21: 1-16.
11. Christensen MR. A critical evaluation for a class of micro-mechanics models, J. Mech. Phys. Solids 1990; 38: 379-404.
12. Hashin Z, Rosen BW. The elastic moduli of fiber-reinforced materials, J. App. Mech. 1964; 31: 223-232.
13. Kachanov M, Shafiro B, Tsukov I**.** Handbook of Elasticity Solutions, Kluwer Academic Publishers, Dordrecht, 2003.
14. Timoshenko S, Goodier JN. Theory of Elasticity, 2nd Ed., McGraw-Hill Book Company, New York, 1951.
15. Eshelby JD. The determination of the elastic field of an ellipsoidal inclusion, and related problems, Proc. R. Soc. 1957; A241: 376–396.
16. Eshel NN, Rosenfeld G. Axi-symmetric problems in elastic materials of grade two, Journal of the Franklin Institute 1975; 299: 43-51.
17. Aravas N. Plane-strain problems for a class of gradient elasticity models-A stress function approach, J. Elast. 2011; 45: 100-110.
18. Gao XL, Park SK. Variational formulation of a simplified strain gradient elasticity theory and its application to a pressurized thick-walled cylinder problem, Int. J. Solids Stuct. 2007; 44: 7486-7499
19. Bigoni D, Drugan WJ. Analytical derivation of Cosserat moduli via homogenization of heterogeneous materials, J. App. Mech. 2007; 74: 741-753.

Institutional Repository - Library & Information Centre - University of Thessaly
15/10/2023 05:52:39 EEST - 167.114.118.212

20. Abramowitz M. and Stegun A.I. Handbook of Mathematical Functions, 7th Ed., Dover Publications, INC., New York, 1970.
21. Budiansky, B., Carrier, G.F., 1984. High shear stresses in stiff fiber composites. J. Appl. Mech. 51, 733–735.
22. Aravas N. Private communications.
23. Papatheocharis T. Experimental study of fiber-reinforced concrete beams response to static and cyclic bending, MSc Thesis, University of Thessaly, Dept. of Civil Engineering, Volos, Greece, 2007.
24. Ben-Amoz M. A dynamic theory for composite materials, J App. Math. Ph. (ZAMP) 1976; 27: 83-99.

CHAPTER III

1. Mindlin, RD. Micro-structure in linear elasticity. Arch. Rat. Mech. An. 1964; 16: 51-78.
2. Cosserat E, Cosserat F. (1909) Theories des Corps Deformables. Hermann et Fils, Paris.
3. Koiter WT. Couple-stresses in the theory of elasticity. Part I. Proc. Ned. Akad. Wet. 1964; B67: 17-29, II: 30-44.
4. Eringen AC. Linear theory in micropolar elasticity. J. Math. Mech. 1966; 15: 909-923.
5. Senturia SD. Microsystem Design. Kluwer Academic Publishers, Boston, 2001.
6. Salvetat JP, Briggs AD, Bonard JM, Basca RB, Kulik AJ, Stockli T, Burnham NA, Forro L. Elastic and shear moduli of single-walled carbon nanotube ropes. Phys. Rev. Lett. 1999; 82 (5): 944-947.
7. Poncharal P, Wang ZL, Ugarte D, de Heer AW. Elecrostatic deflections and electromechanical resonances of carbon nanotubes. Sc.1999; 283: 1513-1516.
8. Ding JN, Meng YG, Wen SZ. Specimen size effect on mechanical properties of polysilicon microcantilever beams measured by deflection using a nano-indenter. Mat. Sc. Eng.:B.2001; 83: 42-47.
9. Lam DCC, Yang F, Chong ACM, Tong P. Experiments and theory in strain gradient elasticity. J. Mech. Phys. Sol. 2003; 51: 1477-1508.
10. Morgan RJ, O'Neal JE. The microscopic failure processes and their relation to the structure of amine-cured bisphenol-A-diglycidyl ether epoxies. J. Mat. Sc. 1977; 12: 1966-1980.
11. Vanlandingham MR, Eduljee RF, Gillespie Jr. Relationships between stoichiometry, microstructure, and properties for amine-cured epoxies. J. Appl. Polym. Sc. 1999; 71 (5): 699-712.
12. McFarland AW, Colton JS. Role of materials microstructure in plate stiffness with relevance to microcantilever sensors. J. Micromech. Microeng. 2005; 15: 1060-1067.
13. Vianna JC, Cunha AM, Billon N. The thermomechanical environment and the microstructure of an injection moulded polypropylene copolymer. Polymer 2003; 43: 4185-4196.
14. Hong SH, Kim KS, Kim Y-M, Hahn J-H, Lee C-S, Park J-H.. Characterization of elastic moduli of Cu thin films using nanoindentation technique. Comp. Sc. Tech. 2005; 65: 1401-1408.
15. Perez-Prado MT, Vlassak JJ. Microstructural evolution in electroplated Cu thin films. Scripta Mater. 2002; 47: 817-823.
16. Yang L, Van der Werf KO, Fitie CFC, Bennink ML, Dijkstra PJ, Feijen J. Mechanical properties of native and cross-linked type I collagen fibrils. Biophys. J. 2008; 94: 2204-2211.

Institutional Repository - Library & Information Centre - University of Thessaly
15/10/2023 05:52:39 EEST - 167.114.118.212

17. Jager I, Fratzl P. Mineralized collagen fibrils: a mechanical model with staggered arrangement of mineral particles. Biophys. J. 2000; 79: 1739-1746.

18. Namarazu T, Isono Y, Tanaka T. Evaluation of size effect on mechanical properties of single crystal silicon by nanoscale bending test using AFM. J. Microelectromech. Syst. 2000; 9 (4): 450-459.

19. Liu H-K, Pan CH, Liu P-P. Dimension effect on mechanical behavior of silicon micro-cantilever beams. Measur. 2008; 41: 885-895.

20. Timoshenko SP, Goodier JN. Theory of Elasticity, 3rd Ed. McGraw-Hill, New York, 1970

21. Papargyri-Beskou S, Tsepoura KG, Polyzos D, Beskos DE. Bending and stability analysis of gradient elastic beams. Int. J. Sol. Str. 2003; 40: 385-400. Erratum: 42, 4911-4912.

22. Vardoulakis I, Sulem J. Bifurcation Analysis in Geomechanics. Blackie/Chapman & Hall, London, 1995.

23. Giannakopoulos AE, Stamoulis K. Structural analysis of gradient elastic components. Int. J. Sol. Str. 2006; 44: 3440-3451.

24. Wang B, Zhao J, Zhou S. A micro scale Timoshenko beam model based on strain gradient elasticity theory. Eur. J. Mech. A/Sol. 2010; 29: 591-599.

25. Lazopoulos KA, Lazopoulos AK. On the strain gradient Timoshenko beam model. J. Appl. Math. Mech. 2011; 91 (11): 875-882.

26. Reddy JN. Non-local theories for bending, buckling and vibration of beams. Int. J. Eng. Sc. 2007; 45: 288-307.

27. Ma HM, Gao X-L, Reddy JN. A microstructure-dependent Timoshenko beam model based on a modified couple stress theory. J. Mech. Phys. Sol. 2008; 56 (12): 3379-3391.

28. Asghari M, Kahrobaiyan MH, Rahaeifard M, Ahmadian MT. Investigation of the size effects in Timoshenko beams based on the couple stress theory. Arch. App. Mech. 2011; 81: 863-874.

29. Ramezani S, Naghdabadi R, Sohrabpour S. Analysis of micropolar elastic beams. Eur. J. Mech. A/Sol. 2009; 28: 202-208.

30. Kaneko T. On Timoshenko's correction for shear in vibrating beams. J. Phys. D: Appl. Phys. 1975; 8: 1927-1936.

31. Giannakopoulos AE, Amanatidou E, Aravas N. A reciprocity theorem in linear gradient elasticity and the corresponding Saint-Venant principle. Int. J. Sol. Str. 2006; 43: 3875-3894.

32. Schwaiger R, Kraft O. Size effect in the fatigue behavior of thin Ag films. Acta Materialia 2003; 51: 195-206.

33. Hocheng H, Hung J-N, Guu Y-H. Various fatigue testing of polycrystalline silicon microcantilever beam in bending. Jap. J. Appl. Phys. 2008; 47 (6): 5256-5261.

34. Hocheng H, Kao KS, Fang W. Fatigue life of a microcantilever beam in bending. J. Vac. Sci. Technol. B 2004; 22 (6): 3143-3146.

35. Liu H-K, Lee BJ, Liu P-P. Low cycle fatigue of single crystal silicon thin films. Sens. Act. A 2007; 140: 257-265.

36. Ni H, Li X. Young's modulus of ZnO nanobelts measured using atomic force microscopy and nanoidentation techniques. Nanotech. 2006; 17: 3591-3597.

37. Ding JN, Meng YG, Wen SZ. Size effect on the mechanical properties and reliability analysis of microfabricated polysilicon thin films, Reliability Physics Symposium. Proc. Int. Rel. Phys. Symp. 2001; 106 – 111.

Institutional Repository - Library & Information Centre - University of Thessaly
15/10/2023 05:52:39 EEST - 167.114.118.212

38. Huang H, Spaepen F. Tensile testing of free standing Cu, Ag and Al thin films and Ag/Cu multilayers. Acta Mater. 2000; 48: 3261-3269.

39. Kulkarni AJ, Zhou M, Ke FJ. Orientation and size dependence of the elastic properties of zinc oxide nanobelts. Nanotech. 2005; 16: 2749-2756.

40. Son D, Jeong JH, Kwon D. Film-thickness considerations in microcantilever-beam test in measuring mechanical properties of metal thin film. Thin Sol. Films 2003; 437: 182-187.

CHAPTER IV

1. Bazant ZP, Planas J. Fracture and size effect in concrete and other quasibrittle materials, CRC Press, Florida, 1997

2. Bazant ZP. Why continuum damage is nonlocal: Micromechanics arguments. J. Eng. Mech., 1997; 117(5): 1070-1086.

3. Pijaudier-Cabot G, Bazant Z. Non-local damage theory. J. Eng. Mech., 1997; 113(10): 1512-1533.

4. Mazars J, Pijaudier-Cabot G, Saouridis C. Size effect and continuous damage in cementitious materials. Int. J. Fract. 1991; 51: 159-173.

5. Peerlings RHJ, de Borst R, Brekelmans AM, de Vree HHP. Gradient enhanced quasi-brittle materials. Int. J. Num. Meth. Eng. 1996; 39: 3391-3403.

6. Fremond M, Nedjar B. Damage, gradient of damage and principle of virtual power. Int. J. Sol. Struct. 1996; 33(8): 1083-1103.

7. de Borst R, Gutierrez MA. A unified framework for concrete damage and fracture models including size effects. Int. J. Fract. 1999; 95: 261-277.

8. Commi, C. Computational modelling of gradient-enhanced damage in quasi-brittle materials. Mech. Coh.-Frict. Mat. 1999; 4: 17-36.

9. Peerlings RHJ, Geers MGD, de Borst R, Brekelmans WAM. A critical comparison of nonlocal and gradient-enhanced softening continua. Int. J. Sol. Struct. 2001; 38: 7723-7746.

10. Addessi D, Marfia S, Sacco E. A plastic nonlocal damage model. Comp. Meth. Appl. Mech. Eng. 2002; 191: 1291-1310.

11. Benvenuti E, Borino G, Tralli A. A thermodynamic consistent nonlocal formulation for damaging materials. Eur. J. Mech. A: Sol. 2002; 21: 535-553.

12. Borino G, Failla B, Parrinello F. A symmetric nonlocal damage theory. Int. J. Sol. Struct. 2003; 40: 3621-3645.

13. Nguyen GD. A thermodynamic approach to non-local modelling of concrete. Int. J. Sol. Struct. 2008; 45: 1918-1934.

14. Poh LH, Swaddiwudhipong S. Gradient-enhanced softening material models. Int. J. Plast. 2009; 25: 2094-2121.

15. Desmorat R, Catuingt F, Ragueneau F. Non-standard thermodynamics framework for robust computations with induced anisotropic damage. Int. J. Dam. Mech. 2011; 20: 1073-1093.

16. Geers MGM, de Borst R, Brekelmans WAM, Peerlings RHJ. Strain-based transient-gradient damage model for failure analysis. Comp. Meth. Appl. Mech. Eng. 1998; 160: 133-153.

17. Pijaudier-Cabot G, Haidar K, Dube JF. Non-local damage model with evolving internal length. Int. J. Numer. Anal. Meth. Geomech. 2004; 28, 663-652.

Institutional Repository - Library & Information Centre - University of Thessaly
15/10/2023 05:52:39 EEST - 167.114.118.212

18. Aggelis DG, Shiotani T. Experimental study of surface wave propagation in strongly heterogeneous media, J. Acoust. Soc. Am. 2007; 122(5): 151-157.

19. Aggelis DG, Shiotani T. Surface wave dispersion in cement-based media: inclusion size effect. NDT & E Intern. 2008; 41: 319-325.

20. Georgiadis HG, Vardoulakis I, Velgaki EG. Dispersive Rayleigh-wave propagation in microstructured solids characterized by dipolar gradient elasticity. J. Elast. 2004; 74: 17-45.

21. Li J. A micromechanics-based strain gradient damage model for fracture prediction of brittle materials – Part I: Homogenization methodology and constitutive relations. Int. J. Sol. Struct. 2011; 48: 3336-3345.

22. Li J, Pham T, Abdelmoula R, Song F, Jiang CP. A micromechanics-based strain gradient damage model for fracture prediction of brittle materials – Part II: Damage modelling and numerical simulations. Int. J. Sol. Struct. 2011; 48: 3346-3358.

23. Stamoulis K, Giannakopoulos AE. A second gradient elasto-plastic model for fatigue of small-scale metal components. Int. J. Struct. Int. 2010; 1(3): 193-208.

24. Voyiadjis ZG, Abu Al-Rub RK. Gradient plasticity theory with a variable length scale parameter. Int. J. Sol. Struct. 2005; 42; 3998–4029.

25. Mazars J, Pijaudier-Cabot G. Continuum damage theory –Application to concrete. J. Eng. Mech. 1989; 115(2): 345-365.

26. Murakami S, Kamiya K. Constitutive and damage evolution equations of elastic-brittle materials based on irreversible thermodynamics. Int. J. Mech. Sc. 1997; 39(4): 473-486.

27. Wu JY, Li J, Faria R. An energy release rate-based plastic-damage model for concrete. Int. J. Sol. Struct. 2006; 43: 583-612.

28. Ortiz M. A constitutive theory for the inelastic behaviour of concrete. Mech. Mat. 1985; 4: 67-93.

29. Mindlin RD. Micro-structure in linear elasticity. Arch. Rat. Mech. Anal. 1964; 16: 51-78.

30. Georgiadis HG, Grentzelou CG. Energy theorems and the J-integral in dipolar gradient elasticity. Int. J. Sol. Struct. 2006; 43: 5690-5712.

31. Budiansky B, O'Connell RJ. Elastic moduli of cracked solids. Int. J. Sol. Struct. 1976; 12: 81-97.

32. Kachanov M. Continuum model of medium with cracks. J. Eng. Mech. 1980; 106: 1039-1051.

33. Horii H, Nemat-Nasser S. Overall moduli of solids with microcracks: load-induced anisotropy. J. Mech. Phys. Sol. 1983; 31: 155-171.

34. Simone A, Askes H, Sluys L. Incorrect initiation and propagation of failure in non-local and gradient-enhanced media. Int. J. Sol. Struct. 2004; 41: 351-363.

35. Bui QV. Initiation of damage with implicit gradient-enhanced damage models. Int. J. Sol. Struct. 2010; 47: 2425-2435.

36. Rodriguez-Ferran A, Bennett T, Askes H, Tamayo-Mas E. A general framework for softening regularisation based on gradient elasticity. Int. J. Sol. Struct. 2011; 48: 1382-1394.

37. Chen L, Shao JF, Zhu QZ, Duveau G. Induced anisotropic damage and plasticity in initially anisotropic sedimentary rocks. Int. J. Rock Mech. Min. Sc. 2012; 51: 13-23.

38. Tada H, Paris PC, Irwin GR. (1973) The stress analysis of cracks handbook. Del Research Corporation, Hellertown, Pa.

39. Bowie OL, Freese CE. On the “overlapping” problem in crack analysis. Eng. Fract. Mech. 1976; 8: 373-379.

Institutional Repository - Library & Information Centre - University of Thessaly
15/10/2023 05:52:39 EEST - 167.114.118.212

40. Stallybrass MP. A crack perpendicular to an elastic half-plane. Int. J. Eng. Sc. 1970; 8: 351-353.

41. Huang H, Detournay E. Discrete element modelling of tool-rock interaction II: rock indentation. Int. J. Num. Anal. Meth. Geomech. 2013; 37(13): 1930-1947.

42. Popovics SA. A numerical approach to the complete stress-strain curve of concrete. Cem. Concr. Res. 1973; 33(4): 583-599.

43. Li F, Li Z. Acoustic emission monitoring of fracture of fiber-reinforced concrete in tension." ACI Mater. J. 2000; 97(6): 629–636.

44. Le Bellego C, Dube JF, Pijaudier-Cabot G, Gerard B. Calibration of nonlocal damage model from size effect test. Eur. J. of Mech. A: Sol. 2003; 22: 33-46.

45. Triantafyllou A, Giannakopoulos AE. Derivation of strain gradient length via homogenization of heterogeneous elastic materials. Mech. Mat., 2013; 56: 23-37.

46. Zhu WC, Zhao XD, Kang YM, Wei CH. Tian J. Numerical simulation on the acoustic emission activities of concrete. Mat. Struct. 2010; 43(5): 633-650.

47. Li Z, Shah SP. Localization of microcracking in concrete under uniaxial tension. ACI Mat. 1994; 91(4): 372-381.

48. Chen B, Liu J. Effect of aggregate on the fracture behavior of high strength concrete. Constr. Build. Mat. 2004; 18: 558-590.

49. Triantafyllou A, Giannakopoulos AE. Structural analysis using a dipolar elastic Timoshenko beam. Eur. J. Mech. A: Sol. 2013; 39: 218-228.

CHAPTER V

1. ASTM C39M -14, Standard test method for compressive strength of cylindrical concrete specimens, ASTM International, West Conshohocken, PA, USA, 2014.

2. ASTM C469M-10, Standard test method for static modulus of elasticity and Poisson's ratio of concrete in compression, ASTM International, West Conshohocken, PA, USA, 2010.

3. Hung KM, Ma, CC, Theoretical analysis and digital photoelastic measurements of circular discs subjected to partially distributed compressions, Exp. Mech. 2003; 43: 216-224.

4. Ma, CC, Hung, KM, Exact full-field analysis of strain and displacement for circular discs subjected to partially distributed compressions, Int. J. Mech. Sc. 2008; 50: 275-292.

5. Rocco C, Guinea GV, Planas J, Elices M, Size effect and boundary conditions in the Brazilian test: Experimental verification, Mat. Struct., 1999; 32 (3): 210-217.

6. Noguchi T, Tomosawa F, Nemati KM, Chiaia M, Fantilli AP, A practical equation for the elastic modulus of concrete, ACI Struct. 2009; 106 (5): 1-7.

7. Lydon FD, Balendran RV, Some observations on elastic properties of plain concrete, Cem. Concr. Res. 1986; 16: 314-324.

8. Plowman JH, Young's modulus and Poisson's ratio of concrete cured at various humidities, Mag. of Concr. Res., 1963; 15 (44): 77-82.

9. Allos AE, Martin LH., Factors affecting Poisson's ratio for concrete, Build. Envir. 1981; 16(1): 1–9.

10. Logan A, Choi W, Mirmiran A, Rizkalla S, Zia P, Short-term mechanical properties of high-strength concrete, ACI Mat. 2009; 106 (5): 1-7.

11. Gercek H, Poisson's ratio value for rocks, Int. J. Rock Mech. Min. Sc. 2007; 44: 1-13.

Institutional Repository - Library & Information Centre - University of Thessaly
15/10/2023 05:52:39 EEST - 167.114.118.212

12. Popovics S, A numerical approach to the complete stress-strain curve of concrete, Cem. Concr. Res. 1973; 3: 583-599.
13. CEB-FIB Model Code for Concrete Structures 2010, FIB bulletin 65, Comite European du Béton /Fédération Internationale du Béton , Lausane, 2012, 350 pp.
14. van Mier JGM, Fracture processes of concrete, CRC press, NY, 1996, 422 pp.
15. Jianhong Y, Wu FQ, Sun, JZ, Estimation of the tensile elastic modulus using brazilian disc by applying diametrically opposed concentrated loads, Int. J. Rock Mech. Min. Sc. 2009; 46: 568-576.
16. Liu, C, Elastic constants determination and deformation observations using Brazilian disc geometry, Exp. Mech. 2010; 50: 1025-1039.
17. Exadaktylos GE, Kaklis KN, Applications of an explicit solution for the transversely isotropic circular disc compressed diametrically, Int. J. Rock Mech. Min. Sc. 2001; 38: 227-243.
18. Castro-Montero A, Jia Z, Shah SP, Evaluation of damage in Brazilian test using holographic interferometry, ACI Mat. 1995; 92 (3): 268-275.
19. Tedesco JW, Ross CA, Kuennen ST, Experimental and numerical analysis of high strain rate splitting tests, ACI Mat. 1993: 90 (2): 162-169.
20. Grosse C, Finck F, Kurz J, Reinhardt HW, Brazilian test of concrete evaluated by AE, Earthquakes and Acoustic Emission (selected papers from the 11th International Conference on Fracture, Turin, Italy, March 20-25, 2005), Ed. by A. Carpinteri and G. Lacidogna, Taylor & Francis, 2007: 139-146.
21. Anoglou N, Canan Girgin Z, Anoglou E. Evaluation of ratio between splitting tensile strength and compressive strength for concretes up to 120 MPa and its application in strength criterion, ACI Mat. 2006: 103 (1): 18-24.
22. Gardner NJ, Sau PL, Cheung MS, Strength development and durability of concretes cast and cured at 0º C, ACI Mat. 1988; 85 (6): 529-536.
23. ACI Committee 363, State-of-the-art report on high-strength concrete (ACI 363R-92), ACI, Farmington Hills, Michigan, 1992, 55 pp.
24. Gettu R, Mobasher B, Carmona S, Jansen DC, Testing of Concrete under Closed-loop Control, Ad. Cem. Bas. Mat., 1996; 3 (2): 54–71.
25. MTS Model Flex-40 Controller Manual, MTS Systems Corporation, Minnesota, 2000, 350 pp.

CHAPTER VI

1. Grassl P, Gregoire D, Solano LR, Pijaudier-Cabot G, Meso-scale modelling of size effect on the fracture process zone of concrete, Int. J. Sol. Struct. 2012; 49: 1818-1827.
2. Lilliu G, van Mier JGM, 3D lattice type fracture model for concrete, Eng. Fract. Mech. 2003; 70: 927-941.
3. Mindlin, RD, Micro-structure in linear elasticity, Arch. Rat. Mech. Anal. 1963; 16 (1): 51-78.
4. Ma HM, Gao X-L, Reddy JN, A microstructure-dependent Timoshenko beam model based on a modified couple stress theory, J. Mech. Phys. Sol. 2008; 56 (12): 3379-3391.
5. Triantafyllou A, Giannakopoulos AE, Derivation of strain gradient length via homogenization of heterogeneous elastic materials, Mech. Mat. 2013; 56: 23-37.
6. Triantafyllou A, Giannakopoulos AE, Structural analysis using a dipolar elastic Timoshenko beam,

Institutional Repository - Library & Information Centre - University of Thessaly
15/10/2023 05:52:39 EEST - 167.114.118.212

Eur. J. Mech. A/Sol. 2013; 39: 218-228.

7. Bigoni D, Drugan WJ, Analytical derivation of Cosserat moduli via homogenization of heterogeneous materials, J. Appl. Mech. 2007; 74: 741-753.
8. van Mier, JGM, Mode I fracture of concrete: Discontinuous crack growth and crack interface grain bridging, Cem. Concr. Res. 1991; 21: 1-15.

CHAPTER VII

1. Triantafyllou A, Perdikaris PC, Giannakopoulos AE, Gradient elasto-damage model for quassi-brittle materials with an evolving internal length, ASCE J. Eng. Mech.
2. Van Vliet MRA, van Mier JGM., Experimental investigation of size effect in concrete and sandstone under uniaxial tension, Eng. Fract. Mech. 2000; 65: 165-188.
3. CEB-FIB Model Code for Concrete Structures 2010, FIB bulletin 65, Comite European du Béton /Fédération Internationale du Béton , Lausane, 2012, 350 pp.
4. Li J, A micromechanics-based strain gradient damage model for fracture prediction of brittle materials – Part I: Homogenization methodology and constitutive relations, Int. J. Sol. Struct. 2011; 48: 3336-3345.
5. Rosello C, Elices M, Guinea GV, Fracture of model concrete: 1. Types of fracture and crack path, Cem. Conc. Res. 2004; 34: 1441-1450.
6. Rosello C, Elices M, Guinea GV, Fracture of model concrete: 2. Fracture energy and characteristic length, Cem. Concr. Res. 2006; 36: 1345-1353.
7. Chen B, Liu J, Effect of aggregate on the fracture behavior of high strength concrete, Constr. Build. Mat. 2004; 18: 585–590.
8. Zhu WC, Zhao XD, Kang YM, Wei CH, Tian J, Numerical simulation on the acoustic emission activities of concrete, Mat. Struct. 2010; 43 (5): 633-650.
9. Gettu R, Bazant ZP, Karr ME, Fracture properties and brittleness of high-strength concrete, ACI Mat. 1990; 87 (6): 608-618.
10. Kreijger PC, The skin of concrete: Composition and properties, Mat. Struct. 1984; 17 (4): 275-283.
11. Duan K, Hu X-Z, Wittmann FH, Thickness effect on fracture energy of cementitious materials, Cem. Concr. Res. 2003; 33: 499-507.

CHAPTER VIII

1. RILEM TC-50-FMC. Determination of fracture energy of mortar and concrete by means of three-point bend tests on notched beams. Mat. Struct. 1985; 18(106): 285-290.
2. Hillerborg A. Theoretical basis of a method to determine fracture energy G_F of concrete. Mat. Struct. 1985; 18(106): 291-296.
3. Bazant ZP, Planas J. (1998) Fracture and Size Effect in Concrete and Other Quassi-Brittle Materials, CRC Press, NY.
4. Duan K, Hu X.-Z, Wittmann FH. Thickness effect on fracture energy of cementitious materials. Cem. Concr. Res. 2003; 33: 499-507.
5. Perdikaris PC, Romeo A. Size effect on fracture energy of concrete and stability issues in three-point bending fracture toughness testing, ACI Mat. 1995; 92(5): 483-496.

Institutional Repository - Library & Information Centre - University of Thessaly
15/10/2023 05:52:39 EEST - 167.114.118.212

6. Rosello C, Elices M, Guinea GV. Fracture of model concrete: 1. Types of fracture and crack path. Cem. Concr. Res. 2004; 34: 1441-1450.
7. Rosello C, Elices M, Guinea GV. Fracture of model concrete: 2. Fracture energy and characteristic length. Cem. Concr. Res. 2006; 36: 1345-1353.
8. Zhang J, Leung CKY, Xu S. Evaluation of fracture parameters of concrete from bending test using inverse analysis approach. Mat Struct. 2010; 43(6): 857-874.
9. Wu K-R, Chen B, Yao W, Zhang D. Effect of coarse aggregate type on mechanical properties of high-performance concrete. Cem. Concr. Res. 2001; 31: 1421-1425.
10. Karihaloo B. (1995) Fracture mechanics and structural concrete, Longman Scientific and Technical, Essex, UK.
11. Zech B, Wittmann FH. A complex study on the reliability assessment of the container of a PWR. Part II: Probabilistic approach to describe the behavior of materials. Nucl. Eng. Des. 1978; 48: 575-584.
12. van Vliet MRA, van Mier, JGM. Effect of strain gradients on the size effect of concrete in uniaxial tension. Int. J. Fract. 1999; 95: 1145-219.
13. Weibull W. A statistical theory of the strength of materials. Royal Sw. Ac. Eng. Sc. Proc. 1938; 151: 1-45.
14. Bazant ZP, Novak D. Energetic-statistical size effect in quassi-brittle failure at crack initiation. ACI Mat. 2000; 97(3): 381-392.
15. Planas J, Guinea GV, Elices M. Rupture modulus and fracture properties of concrete. Fracture Mechanics of Concrete Structures, V. 1, F. H. Wittmann, ed., Edification Publishers, Freiburg, Germany, 1995
16. van Vliet MRA. Size effect of tensile fracture in concrete and rock,'' PhD thesis, Delft University Press, Delft, Netherlands, 2000.
17. Kreijger PC. The skin of concrete: composition and properties. Mat. Struct. 1984; 17(4): 275-283.
18. Rocco C, Guinea GV, Planas J, Elices M. Size effect and boundary conditions in the Brazilian test: Theoretical Analysis. Mat. Struct. 1999; 32: 437-444.
19. CEB-FIB Model Code for Concrete Structures 2010, FIB bulletin 65, Comite European du Béton /Fédération Internationale du Béton , Lausane, 2012

Institutional Repository - Library & Information Centre - University of Thessaly
15/10/2023 05:52:39 EEST - 167.114.118.212

Last page

Institutional Repository - Library & Information Centre - University of Thessaly
15/10/2023 05:52:39 EEST - 167.114.118.212